Diagnostic Features of the Rocks and Minerals Peripheral to the Highland Valley Copper District, British Columbia, Canada: Implications for the genesis of porphyry Cu systems and their footprints

by

Kevin Byrne

A thesis submitted in partial fulfillment of the requirements for the degree of

Doctor of Philosophy

Department of Earth and Atmospheric Sciences

University of Alberta

Abstract

The Highland Valley Copper (HVC) porphyry Cu (±Mo) district is Canada's largest and longest operating mine. Globally, exploration expenditure has been increasing, yet very few new resources have been discovered, despite the anticipated Cu demand for the future. Hosted in the Triassic Guichon Creek batholith (GCB) in the Cordillera of British Columbia, the HVC district is an excellent site to study the distal expression of porphyry Cu systems, integrate disparate data sets, and develop new exploration tools and models to aid the discovery of porphyry Cu deposits for the next generation.

This study aimed to determine the diagnostic features of the rocks and minerals peripheral to the prolific HVC porphyry Cu centers– the footprint. Specifically, how, to what degree, and to what distance are the rocks outside of the porphyry centers affected by hydrothermal processes? Can vein mineral chemistry be used to vector to Cu mineralization and identify the presence of a porphyry system? Was there an external fluid entrained in the magmatic-hydrothermal systems in the porphyry Cu centers, and what was its origin? Whole-rock lithogeochemistry, mineral geochemistry, and a combination of stable (H, O, C and B) and radiogenic (Sr) isotope techniques are used to address these questions.

The HVC district is hosted in calc-alkalic plutonic rocks of the GCB. Well-developed, feldspar-destructive, white-mica–chlorite alteration is indicated by (2Ca+Na+K) /Al values <0.85, Ca-depletion, K-enrichment, and quartz addition and is spatially limited to within ~200 m of porphyry Cu mineralization. Localized K, Fe, and Cu-depletion and Na-addition occurs in

sodic-calcic domains that form a large (~34 km^2) non-concentric footprint peripheral to Cu mineralization and K-enriched alteration (potassic and white-mica–chlorite). Water- and calcite-enriched rocks form the largest coherent lithogeochemical footprint (~60 km^2). The porphyry centers generally contain >0.75 wt. % calcite and have measured $\delta^{13}C_{total}$ values > -10 ‰. Up to 6 km away from Cu mineralization, propylitic, sodic-calcic, and a few least-altered rocks have $\delta^{13}C_{total}$ values between -11 and -7 ‰ that contrast with lower whole-rock $\delta^{13}C_{total}$ values (-25 and -21 ‰) in more distal propylitic alteration and fresh rocks. Calcite is interpreted to have formed via CO_2 degassing from a late-stage magmatic volatile phase that contained ~1.6 mol. % CO_2 in H_2O.

Estimates of $\delta^{18}O_{fluid}$ and δD_{fluid} values derived from epidote and tourmaline in sodic-calcic domains range from 3.0 to 8.2 ‰ and -40.6 to -3.9 ‰, respectively, which contrasts with the dominantly magmatic fluid values from Cu-mineralized potassic and white-mica–chlorite alteration facies. Tourmaline $\delta^{11}B_{fluid}$ values range from 4.2 to 18.3 ‰. The highest $\delta^{11}B_{fluid}$ values occur in albite-altered rocks and indicate a fluid source rich in ^{11}B, such as seawater or seawater-derived formation water in country rocks. Sodic-calcic alteration is interpreted to be caused by the inflow and heating of seawater-derived fluid along regional-scale fracture-sets at low water–rock ratio (~0.01–0.1), and locally mixed with magmatic fluids in and adjacent to the porphyry centers.

Epidote veins from the fertile HVC porphyry district can be discriminated from the epidote occurring in non-prospective geological environments by a combination of compositional features: large positive Eu anomaly, low sum HREE concentration, moderate negative REE_N slope, and principally by analyses of >30 ppm As and Ge, and >10 ppm Sb.

A coherent domain of epidote veins with a Ge anomaly (>30 ppm) forms a halo around the porphyry centers for ~ 5 km. Epidote veins with the highest As and Sb values (~ >20 ppm) occur within ~4 km of the porphyry Cu centers. The elements Mn (>6000 ppm) and Zn (> 25 ppm) are most enriched in epidote between 1.5 and 4 km of the porphyry centers, whereas Pb enrichment (~>120 ppm) occurs between ~ 4–6 km away. Prehnite veinlets are enriched in Mn (>2500 ppm) between 3 and 6 km away from the porphyry centers, and enriched in Pb (~>130 ppm) within a window of ~ 5.5–8 km. The pathfinder metals in epidote are interpreted to be primarily sourced from outflowing H_2S-depleted, cooling, magmatic volatile phase emanating from the porphyry Cu centers or from the fringes of the subjacent cupola.

Collectively, these results demonstrate methodologies and approaches that will be useful in elucidating hydrothermal footprints in porphyry Cu systems globally.

Preface

This research is part of the Natural Sciences and Engineering Research Council (NSERC)-Canadian Mining Innovation Council Mineral (CMIC) Exploration Footprints Research Network. The network includes 42 researchers from 24 universities across Canada and 45 industry collaborators from 27 mining, exploration and service companies (https://cmic-footprints.laurentian.ca/). Mineral exploration in Canada is increasingly focused on concealed and deeply buried targets, requiring more effective tools to detect large-scale ore-forming systems and to vector from their most distal margins to their high-grade cores. This network has been formed to aid the mining industry in discovering the next generation of mineral deposits. The site sponsor for the Porphyry Cu sub-project, the focus of this thesis, was Teck Resources Limited (Teck). My research peers at the study site were primarily Guillaume Lesage (University of British Columbia), Philip Lypaczewski (University of Alberta) and Mike D'Angelo (Lakehead University).

Guillaume and I divided the study site into domains in which we were individually responsible for mapping and sampling. We integrated our mapping results to produce internally consistent district-scale geological maps. Additionally, we agreed to focus on different components of the porphyry footprint and pursue disparate hypotheses. Samples were portioned for down-stream geochemical, mineralogical and physical property testing. Subsequent rock sample data was utilized by various members of the Footprints Network for their own research.

Chapter 2 has been submitted to a Special Issue of Economic Geology on the green rock environment. The study was devised by me, S.J. Piercey and S.A. Gleeson. G. Lesage and I mapped and collected the CMIC rock samples, and developed the alteration framework for the district. P. Lypacewski collected and interpreted SWIR spectral data. I interpreted, collated, and tabulated feldspar staining results, SWIR mineralogy and textures, and petrographic observations. K. Kyser guided us through the whole-rock C isotope sampling rationale and facilitated data collection. Whole-rock carbon isotope ($\delta^{13}C_{total}$) analyses were completed at the Queen's Facility for Isotope Research (QFIR), Queen's University, Canada. I completed all other the data analysis and wrote this manuscript. S. Gleeosn and S. Piercey edited the manuscript.

Chapter 3 will be submitted to the journal Economic Geology, once approved by sponsor companies for release to the public domain. Samples were collected by me and G. Lesage. I developed the hypothesis tested in this manuscript with S. Gleeson. R. Trumbull and I collected the boron isotope data, and R. Trumbull critically assessed early version of my interpretations the boron isotope data and the manuscript. Hydrogen and O isotopes were analyzed at the QFIR. Electron microprobe analyses (EPMA) was performed using the CAMECA SX100 at the Electron Microprobe Laboratory at the University of Alberta.

Chapter 4 is intended to be submitted to the Journal of Geochemical Exploration when the material clears the project disclosure period. Samples for this study were collected by me, and provided by G. Lesage and J. Glodny. Research objectives for this manuscript were devised by myself and S. Gleeson. Trace geochemical data was collected by M. Oelze and I at the LA-ICP-MS lab at GFZ, Potsdam. I processed and interpreted the data and wrote the paper. S. Gleeson edited the paper.

Chapter 5 was submitted to a special issue on Special Issue on "Spatial modelling and analysis of ore-forming processes in mineral exploration targeting" in the journal Ore Geology Reviews, it is currently in revision. I devised this study with G. Lesage and R. Lee. Data in this paper was compiled from several CMIC and Teck sources, and new measurements were also taken by me. W.A. Morris and R.J. Enkin advised with data presentation and interpretations. S. Gleeson reviewed this paper.

Acknowledgements

Funding for this study was provided by the Natural Sciences and Engineering Research Council of Canada (NSERC) and the Canadian Mining Innovation Council (CMIC) through the NSERC Collaborative Research and Development Program. The Porphyry Cu Subproject research would have not been possible without significant financial, material and informational support from Teck Resources Limited (Teck). I am also very grateful for the individual financial support which I received from Teck, and to Andrew Davies and Lucas Marshall for championing me and the CMIC research. Early in my career as an exploration geoscientist I was inspired and mentored by several people, some of whom married academic knowledge with a practical understanding of ore systems. Thank you Pete Rowgowski, Scott Manske, Patrick Redmond, and Jo Lipski– you set me on this path. Subsequent influencers, mostly positive, include John Dilles, Dick Tosdal, Scott Halley and Claire Chamberlain. Your ceaseless efforts to educate and inform are much appreciated. Particular thanks to my supervisor Dr. Sarah Gleeson who agreed to take me on as her student, and from whom I have learnt a tremendous amount about the nature of research. I truly appreciate the efforts of Dr. Andrew Locock in ensuring only quality data leaves his lab, and I appreciate his patience with my sometime fruitless experimentation. Thank you Immigration Canada for allowing me to first enter Canada in 2007, subsequent work permits, and my permanent residence status. There are no decent porphyry Cu deposits in Ireland. Thank you Beverly Quist for sticking with me on this– you had not realized you would be married to a mature student.

Table of Contents

List of Tables

List of Figures

List of Appendices

List of Supplemental data files provided in the Education and Research Archive

Supplemental data 2-A: Lithogeochmical and rock slab alteration data.

Supplemental data 2-B: Material-transer / element gain and loss calculations.

Supplemental data 2-C: Whole-rock C isotope data (CF-IR-MS).

Supplemental data 3-A: Boron isotope data (SIMS).

Supplemental data 3-B: Radiogenic Sr isotope data (TIMS).

Supplemental data 3-C: Chlorite EMPA.

Supplemental data 3-D: Feldspar EMPA.

Supplemental data 3-E: Amphibole EMPA.

Supplemental data 4-A: Epidote and prehnite EMPA.

Supplemental data 4-B: LA-ICP-MS results.

Supplemental data 4-C: LA-ICP-MS QAQC analysis.

1 Introduction

Copper is a critical metal for present and future civilization (Radetzki, 2009; Elshkaki et al., 2016). Porphyry Cu systems supply nearly 75 % of the world's Cu, 50 % of the Mo, around 20 % of the Au, most of the Re, and minor amounts of other metals such as W, Ag, Zn, Pb, and Bi (Seedorff et al., 2005; Sillitoe, 2010). These magmatic-hydrothermal systems typically form above subducted oceanic lithosphere at convergent plate margins (Richards, 2015). Porphyry Cu systems manifest as large volumes (10-100km^3) of hydrothermally altered rocks ("the footprint") that locally host ~100-200 times crustal abundance of metals and S as sulfide minerals in veins and disseminations in wall-rock(s) overlying feeder cupolas in the roofs of upper crustal magma chambers (Seedorff et al., 2005; Sillitoe, 2010). Opinion varies on how Cu will be utilized and whether demand will outstrip supply over the next ~50 years (Tilton and Lagos, 2007; Elshkaki and Graedel, 2013; Elshkaki et al., 2016). What is clear, however, is that a pipeline of environmentally and socially responsible resource projects is needed to replace decreasing inventories and meet near-term demand expectations (Sillitoe, 2010; Jennings and Schodde, 2016; Thompson, 2016; Ali et al., 2017). Exploration costs and expenditures have increased approximately three-fold over the last 12 years (Wilburn et al., 2015; Wood, 2016), yet discovery rates are down and very few new, economic, deposits have been found (Sillitoe, 2013; Jennings and Schodde, 2016; Wood, 2018). As a result, exploration is focusing on porphyry plays that are deeper, or with little or no surface expression (blind), in known productive belts, and in under-explored, high-risk, jurisdictions necessitating more effective and efficient exploration methodologies (Sillitoe, 2013; Schodde, 2014; Wood, 2016). The Natural Sciences and Engineering Research Council (NSERC)-Canadian Mining Innovation Council Mineral (CMIC) Exploration Footprints Research Network aimed to meet these challenges by developing tools to detect large-scale ore-forming systems and to vector from their most distal margins to their high-grade cores (Lesher et al., 2017).

Four major porphyry Cu-(Mo) centers occur in the Highland Valley Copper (HVC) district, which is hosted in Guichon Creek batholith (GCB) in the island-arc Quesnel terrane of the Canadian cordillera (Figs. 1A and B; McMillan, 1976; Nelson et al., 2013). The HVC district has produced 1615 million tonnes of ore grading 0.40% Cu and 0.010% Mo as of 2013 (Fig. 1C; Byrne et al., 2013), has current total reserves of 589.5 million tonnes of ore grading 0.30% Cu and 0.007% Mo (Teck, 2018), and is Canada's largest and longest operating Cu mine (Ydon, 2007). The HVC porphyry systems are unusual in that some of them formed at depths of at least 4–5 km in plutonic host rocks (D'Angelo, 2016; D'Angelo et al., 2017). The concentration of Cu, Mo, Ag and many pathfinder elements (e.g., As, Bi, W, Te) decrease sharply within ~400 m of Cu mineralization in the porphyry centers (Olade and Fletcher, 1976a; Olade and Fletcher, 1976b; Lesage et al., 2016). Additionally, alteration in the plutonic host rocks is restricted to mostly narrow 1–3 cm halos around a low density of prehnite and/or epidote veinlets outside of the porphyry centers (Lesage et al., 2016; Byrne et al., 2017). Furthermore, the geophysical response of the porphyry systems is subdued (Bergey et al., 1971; Ager et al., 1972; Ager et al., 1973; Casselman et al., 1995; Roy and Clowes, 2000). This is a particularly challenging style of footprint to explore. Exposure and airborne magnetic data indicate that the batholith has an oval shape, elongate to the northwest, with a long axis of approximately 60 km and a short axis of 25 km. Due to its size and low degree of exposure (~3%), the HVC district is a realistic natural laboratory in which to investigate the large-scale footprint of a porphyry Cu system, integrate disparate geological and geochemical datasets, and develop new methodologies and genetic understanding to aid modern exploration. The broad topics addressed in this thesis therefore are, what are the diagnostic features of the rocks and minerals peripheral to the porphyry Cu centers, and what processes led to their formation?

This thesis is organized into four main chapters (stand-alone papers) that focus on different components of the porphyry Cu footprint. In Chapter 2, feldspar staining, shortwave infrared spectral imaging, and petrography is used to characterize vein and alteration mineralogy in rock slabs resulting in an "alteration facies" classification. This framework is then used to interrogate corresponding whole-rock lithogeochemical data collected on the same sample suite. By linking observed alteration mineralogy to lithogeochemical data, the sensitivity of the whole-rock determinations in detecting changes in mineralogy and material-transfer in the porphyry footprint are evaluated. Specifically, does a measurable material-transfer accompany the fracture-controlled alteration peripheral to the porphyry Cu centers? If so, what components were added / removed from the rock, by what alteration process, and can they be used to vector to Cu mineralization?

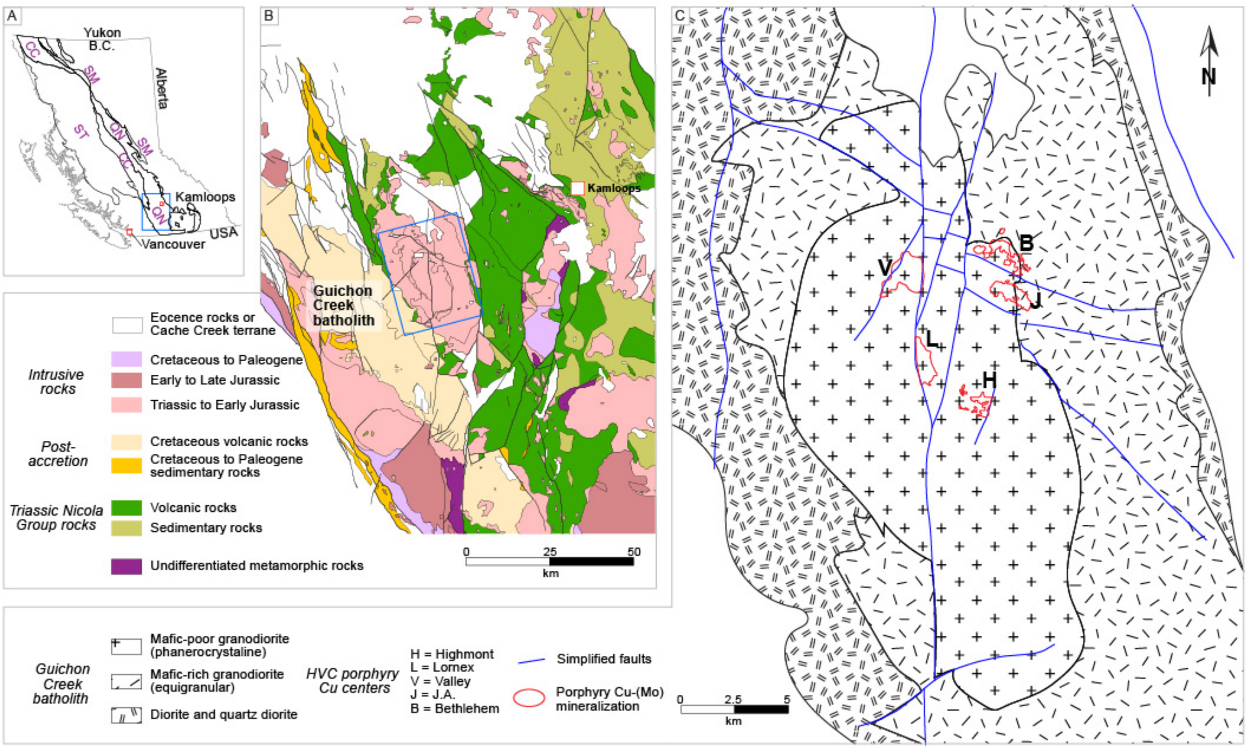

Figure 1-1. Location Maps. A. Cordilleran terranes in British Columbia: ST =Stikine, QN = Quesnel, CC= Cache Creek, SM = Slide Mountain. The blue frame indicates area in Fig. 1-1B. B. Southern Quesnel terrane rocks and the location of the Guichon Creek batholith (after Massey et al., 2005). The blue frame indicates the area in Fig. 1-1C. C. Simplified Guichon Creek batholith geology showing Cu mineralization in the Highland Valley Copper district (modified from McMillan et al., 2009 and Byrne et al., 2013).

Chapter 3 focuses on the source of the fluids that caused hydrothermal alteration in the HVC porphyry system. District-scale sodic-calcic alteration has only recently been recognized in the GCB (Byrne et al., 2017), despite the site being the focus of exploration and research over several decades (e.g., Olade, 1974; McMillan, 1976; McMillan, 1985; Casselman et al., 1995). The hypothesis being tested is that the ingress of seawater caused sodic-calcic alteration that is temporally linked to porphyry Cu genesis in the GCB. A combination of stable (D, O and B) and radiogenic Sr isotope techniques, and mineral geochemistry, integrated with a robust geological paragenesis is used to determine fluid sources and their contribution to the porphyry footprint.

Chapter 4 builds on the vein and alteration framework established in the earlier chapters, and uses quantitative multi-element trace geochemistry techniques to analyze epidote and prehnite veins. Innovative application of trace mineral chemistry has shown that the concentration of some elements in epidote and chlorite define a footprint up to 1.5 km away from the pyrite zones surrounding porphyry Cu centers (Cooke et al., 2014; Wilkinson et al., 2015). We test if the trace element composition of epidote and prehnite veins surrounding the prolific HVC mining district vary systematically with respect to distance from Cu mineralization. If so, what are principal controls on the composition of the epidote veins in the GCB? Additionally, are there compositional characteristics that can be used to discriminate epidote formed in porphyry systems from epidote occurring in other, non-prospective, geological environments?

Chapter 5 is a short and practical examination of the relationship between outcrop (n = 1610) magnetic-susceptibility measurements and vein and alteration intensity in the porphyry Cu footprint. Magnetic-susceptibility data is routinely collected for rock identification in exploration programmes (Clark and Emerson, 1991), but can it be leveraged to elucidate features related to hydrothermal alteration? Specifically, what does the variability in outcrop magnetic-susceptibilities indicate, and do changes in this attribute vary systematically with respect to distance from the porphyry Cu centers, i.e., define a footprint?

The thesis concludes (Chapter 6) with a synthesis of the diagnostic features of the rocks and minerals peripheral to the HVC porphyry system. Collectively the results reveal the underlying processes that generated the footprints, which can be used to inform geological models and aid in the exploration of porphyry Cu systems globally.

2 Linking mineralogy to lithogeochemical changes and C isotope composition in rocks around the Highland Valley Copper porphyry district– *Implications for porphyry Cu footprints*

2.1 Introduction

Calc-alkalic porphyry systems typically exhibit a predictable spatial and temporal distribution of alteration minerals that is the result of the common thermal and chemical evolution of porphyry magmatic-hydrothermal systems (Seedorff et al., 2005; Sillitoe, 2010). Alteration zones are depicted as volumes in, and around, Cu mineralization that are diagnostic of the fluid composition and temperature under which they formed. The deep and central part of the hydrothermal system is characterized by potassic alteration that zones upwards to sericitic (white-mica–chlorite and white–mica), and then into advanced argillic alteration (Seedorff et al., 2005; Sillitoe, 2010). Additionally, at deep levels potassic alteration can zone laterally to sodic-calcic or propylitic alteration (Seedorff et al., 2008; Halley et al., 2015), whereas at intermediate and shallow levels the peripheral alteration comprises propylitic and intermediate argillic assemblages, respectively (Seedorff et al., 2005; Sillitoe, 2010). Thus, the plan-view distribution of the alteration facies, the porphyry footprint, is partly a function of erosional level. A challenge for explorationists is that the peripheral parts of porphyry Cu systems are most commonly characterized by “green rock” propylitic alteration that lacks diagnostic pathfinder element enrichment that occurs with sulphide mineralization and/or white-mica alteration (Halley et al., 2015). Propylitic alteration can comprise low- to moderate-intensity replacement of primary feldspars and mafic minerals by epidote–calcite–chlorite ± albite, actinolite, pyrite, hematite, prehnite, and zeolites that occurs with and without epidote ± chlorite ± carbonate veins (Meyer and Hemley, 1967; Cooke et al., 2014a; Cooke et al., 2014b). Propylitic alteration can extend laterally and upwards for several kilometres away from the well mineralized potassically and hydrolytically altered zones (Seedorff et al., 2005; Cooke et al., 2014b) and, thus, forms the largest footprint. Sodic-calcic or sodic alteration is also recognized in the peripheral and deep (root) parts of several Laramide porphyry systems in the western part of the US (Dilles and Einaudi, 1992; Seedorff et al., 2008), and in some B.C. porphyry Cu systems (Jago et al., 2014; Chapman et al., 2015; Byrne et al., 2017). Sodic-calcic alteration is characterized by the replacement of K-feldspar with albite, and the alteration of mafic minerals to actinolite ± epidote, chlorite, and titanite, that generally occurs with veins of epidote or actinolite (Dilles and Einaudi, 1992; Seedorff et al., 2005).

Few studies have tested for lithogeochemical changes in the altered rocks peripheral to Cu centers and pyrite halos, particularly at the district scale (e.g., Greenlaw, 2004; Urqueta et al., 2009), nevertheless, some commonalities emerge. By many definitions, propylitic alteration involves material-transfer of H_2O, CO_2, and localized S to the altered rock, but limited hydrolysis or alkali-exchange metasomatism (Meyer and Hemley, 1967; Ulrich and Heinrich, 2001; Urqueta et al., 2009). Furthermore, in the Collahuasi epithermal and porphyry district, Northern Chile, C isotope and concentration measurements were applied to successfully distinguish propylitic alteration from background regional lower greenschist alteration (Djouka-Fonkwe et al., 2012). In contrast to propylitic facies, sodic-calcic and sodic alteration is defined by the exchange of K for Na, with varying degrees of Ca addition, and can be accompanied by formation of hydrous minerals, and calcite addition (Carten, 1986; Dilles and Einaudi, 1992).

Four major porphyry Cu-(Mo) systems, hosted in the Late Triassic Guichon Creek batholith (GCB), occur in the Highland Valley Copper (HVC) district in British Columbia, Canada's largest and longest operating Cu mine (Fig. 2-1; Ydon, 2007; Byrne et al., 2013; Sillitoe, 2013). The HVC porphyry systems are unusual in that some of them formed at depths of at least 4–5 km in co-genetic plutonic host rocks (D'Angelo, 2016; D'Angelo et al., 2017). Furthermore, ore (Cu, Mo, Ag) and pathfinder element (e.g., As, Bi, W, Te) concentrations diminish to background levels just a few 100 m beyond porphyry Cu mineralization, and alteration in the plutonic host rock is restricted to generally narrow 1–3 cm halos around a low density of prehnite and/or epidote veinlets (Olade and Fletcher, 1975; Olade and Fletcher, 1976a; Lesage et al., 2016; Byrne et al., 2017). This is a particularly challenging style of footprint to explore because outside of the mine pit areas the geophysical response of the porphyry systems is subdued (Bergey et al., 1971; Ager et al., 1972; Ager et al., 1973; Casselman et al., 1995; Roy and Clowes, 2000). The question then, is how to use lithogeochemistry to the best effect in such a challenging environment? As part of the NSERC-Canadian Mining Innovation Council (CMIC) Mineral Exploration Footprints Research Network (Lesher et al., 2017) the footprint of the HVC porphyry district has been investigated. We use feldspar staining, shortwave infrared spectral imaging, and petrography to characterize vein and alteration mineralogy in rock slabs and to categorize corresponding lithogeochemical samples. We apply molar element ratio diagrams (Stanley and Madeisky, 1994), normative mineralogy, and calculate element gains and losses (Grant 1986) that allows us to quantify and map mineralogical changes and material-transfer, and thus evaluate alteration processes.

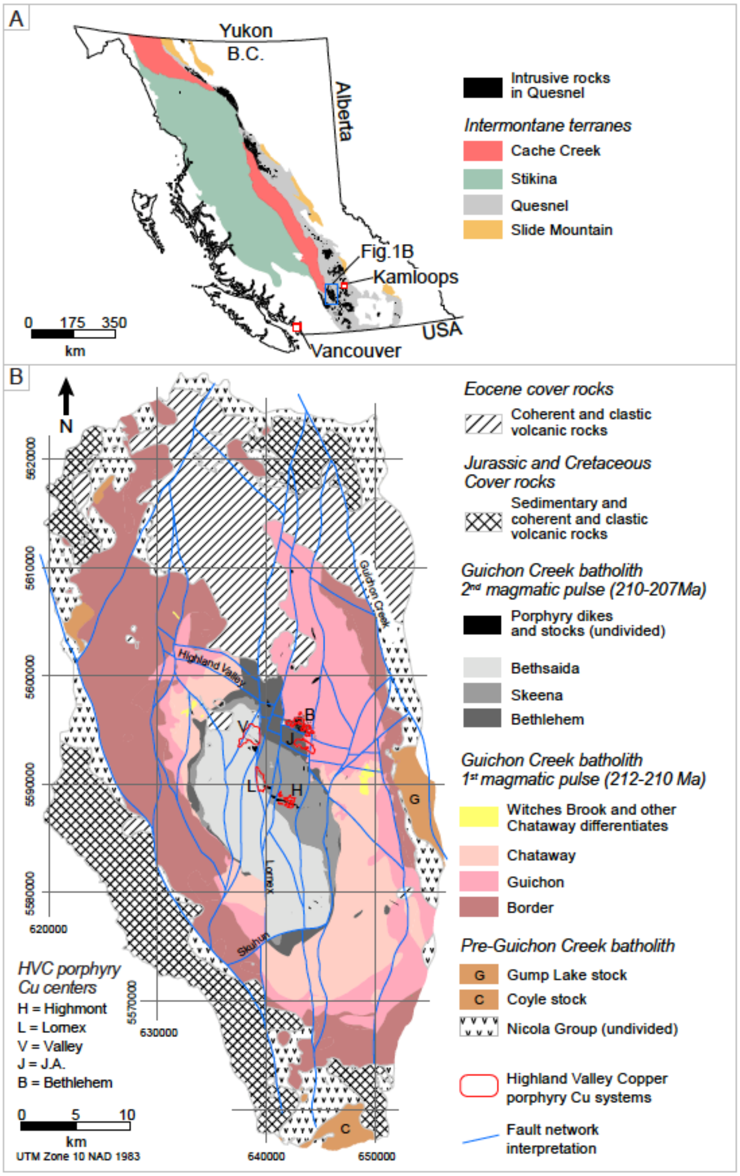

Figure 2-1. Location Maps. A. Terranes of the Intermontane belt in British Columbia (B.C.), and the location of the Guichon Creek batholith in the Triassic Quesnel terrane. B. Guichon Creek batholith geology showing the location of the Highland Valley Copper porphyry systems (modified after McMillian 2009, and D'Angelo et al., 2017). Fault network modified from Lesage et al. (2019). Note the off-set of the Bethsaida granodiorite contact across the Lornex fault, and the segmented Valley–Lornex porphyry center. Highmont is spatially associated with an elongate composite dike complex.

By linking observed alteration mineralogy to lithogeochemical data we test how sensitive the whole-rock determinations are in detecting changes in mineralogy and material-transfer in the porphyry footprint. We show that host rock composition influences alteration mineralogy, material-transfer occurred in the green rocks outboard of mineralization, and that feldspar staining identified weak and subtle alteration that cannot be identified by lithogeochemistry. Additionally, we show how the paragenesis of calcite impacts the porphyry footprint, and demonstrate the effectiveness of whole-rock C isotope analysis in detecting the outer limit of magmatic-hydrothermal fluid-flux related to the porphyry centers. Collectively, these results will demonstrate methodologies and approaches that will also be useful in elucidating hydrothermal footprints in porphyry Cu systems globally.

2.2 Background Geology

2.2.1 Regional geology

The Quesnel terrane in the Canadian Cordillera is characterized by Mesozoic island-arc assemblages consisting of volcanic and sedimentary rocks and associated intrusions (Coney et al., 1980). The Triassic Guichon Creek batholith (GCB) is an I-type composite batholith (D'Angelo et al., 2017) that intruded Nicola Group rocks along the western margin of the Quesnel terrane (Logan and Mihalynuk, 2014). Nicola Group rocks directly adjacent the GCB (Fig. 2-1B) comprise mafic to intermediate volcaniclastic and volcanogenic sedimentary rocks, sandstone, limestone, layered siltstone, calcareous siltstone, and several chert horizons that were predominantly deposited in a submarine setting (McMillan, 1976; McMillan, 1977; McMillan et al., 2009).

2.2.2 District-scale geological framework

The GCB formed from multiple pulses of magmatism and is compositionally, and concentrically, zoned with an oval shape measuring approximately 60 km by 25 km, elongate to the northwest (Fig. 2-1). The initial magmatic pulse consists of melanocratic quartz-diorite, monzogabbro, and granodiorites (Border, Guichon and Chataway), which occur at the margin of the batholith. The second pulse comprises leucocratic quartz-rich granodiorites and monzogranite facies (Bethlehem, Skeena and Bethsaida; Fig. 2-1B; D'Angelo et al., 2017). A third pulse of syn- to late-mineralization stocks and dikes occur at some of the porphyry centers

(Lee et al.). The HVC district is situated within the younger more felsic facies in the core of the batholith and comprises the Bethlehem, J.A., Valley-Lornex, and Highmont porphyry Cu-(Mo) systems (Fig. 2-2A). Post-mineral faulting along the Lornex fault off-set mineralization at the once contiguous Valley-Lornex system (McMillan, 1974; Hollister et al., 1975; Lesage et al., 2019).

At least two main stages of porphyry Cu mineralization are evident in the HVC district (Byrne et al. 2013). The first occured at the Bethlehem center at ~209 Ma and is associated with magmatic-hydrothermal breccia and cogenetic porphyry dikes emplaced in a dome-shaped feature in the Guichon-Bethlehem granodiorite contact (Briskey and Bellamy, 1976; Briskey, 1980; Byrne et al., 2013; D'Angelo et al., 2017). Late to post-mineral stocks, compositionally similar to Skeena facies, cross-cut mineralized breccia at depth in the Bethlehem porphyry center (Byrne et al., 2013). Mineralization at Bethlehem was followed by intrusion and crystallization of the Skeena and Bethsaida facies, and subsequently the formation of the Valley-Lornex and Highmont porphyry centers between 208 and 207 Ma (D'Angelo et al., 2017). The Valley-Lornex porphyry is hosted in Skeena and Bethsaida granodiorite. Main-stage Cu mineralization occurred with quartz–bornite–chalcopyrite ± molybdenite veins with halos of coarse-grained, grey colored, paragonitic muscovite (Table 2-1; Alva-Jimenez, 2011). The coarse-grained muscovite exhibit bowtie morphology and are locally inter-grown with quartz and secondary K-feldspar (Alva-Jimenez, 2011), and are thus interpreted to be early-halo (EH) type veins (e.g. Proffett, 2009; Riedell and Proffett, 2014). Late-stage intermediate-argillic alteration occurs throughout the Valley-Lornex system (Table 2-1). The timing of alteration and mineralization at J.A. is undefined; however, the mineralization and alteration style suggests it is akin to Bethlehem (McMillan, 1985b).

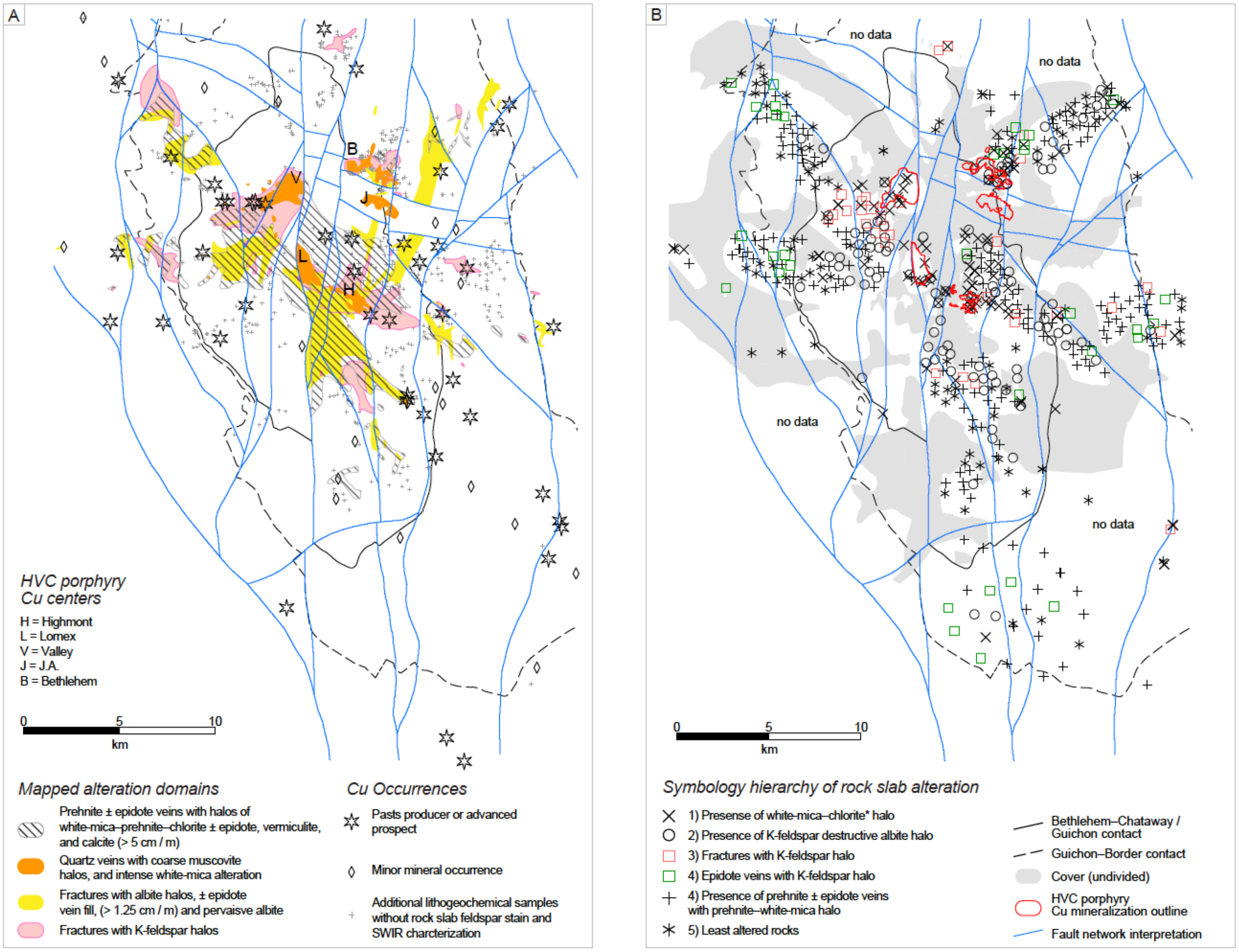

Figure 2-2. A. Mapped alteration in the Guichon Creek batholith (modified from McMillian et al., 2009 and Lesage et al., 2016) and the location of select Cu occurrences in the region (data from http://aris.empr.gov.bc.ca and http://minfile.gov.bc.ca). Fault network modified from Lesage et al. (2019). Additionally, the locations of supplemental lithogeochemical samples, provided by Teck Resources Limited, are indicted. B. Sample (CMIC data) location map showing simplified alteration facies based on feldspar staining, shortwave infrared spectral response, and visual inspection. Some overlapping samples have been removed for clarity.

Table 2-1. Summary of vein and alteration facies in the Highland Valley Copper district and Guichon Creek batholith

Alteration facies and sub-facies[2]		Fracture fill minerals	Alteration halo minerals	Description	White-mica SWIR Al-OH response[3]	Paragenesis	Location in system	Inferred temperature range[4]	Equivalent alteration types in Sillitoe (2010) and Seedorff et al. (2005)
Barren quartz[5]		Qz,	Weak Ksp, qz	Sugary texture qz veins 1-3cm wide with localized poorly developed Ksp halos. Locally associated with vein-dikes and unidirectional solidification textures at depth in Valle	NA	Cut by syn-mineral qz–(musc) veins	Absent in Bethlehem and Highmont. Deep and centrally located in Valley and Lornex	[a]400-500°C	K-Silicate; potassic. "A"-veins with silicic or Ksp halo; secondary bt alteration
(K-feldspar)		Qz, cp, tour	Ksp, bt, {cp}	Fracture halos (0.2-1 cm) of Ksp associated with discontinuous qz and cp fill. Hbl altered to secondary bt	NA	Possibly coeval with the barren qz vein facies and are cross-cut by well mineralized qz–(musc) facies	Bt and Ksp within Cu zones at Bethlehem, Valley, Lornex and Highmont. Extends outboard of Valley and Highmont for several km as weakly mineralized narrow Ksp fracture halos	[a]350-550°C	
Epidote-(albite)		Ep, act, diop, tour	Ab, chl, ep, act, wm, gt {tit}	Ep veins with irregular and diffuse vein walls and Ksp-destructive halos of ab, ab–wm or ab–ep. Mafics strongly altered to chl ± act within halo. Mt typically altered to Ti-oxides. Plag is also ab altered in intense alteration. Turbidity in altered feldspars caused by micro-porosity and mineral inclusion.	Short-λ	Post-mineral timing at Bethlehem, pre-mineral at Valley and Lornex, and pre and post main mineral at Highmont	Pervasive ab and act ± diop are more common proximal to the HVC porphyry centers. Domains of ep-(ab) extend up to 7 km away from the porphyry centers	[a]300-450°C	Sodic-calcic; sodic
White-mica–chlorite*[6]	Quartz-(muscovite)	Qz, bn, cp, anh	Coarse-grained gray colored musc, bn, Ksp, qz {hem, rt}	Vitreous qz veins with distinctive coarse-grained 0.3-1.5 cm gray colored musc, ± inter-grown fine-grained Ksp, that exhibit bowtie and "sericite-island" textures[e,f]. Primary Ksp and bt generally stable and plagioclase is replaced	Dominantly short-λ. Localized intermediate-λ	Cross-cuts ep-(ab) veins and is overprinted by younger faulted hosted qz-ca-mo-py-(wm-chl) veins	Intimately associated with bn and cp mineralization at Valley, Lornex and locally at Highmont centers. Coarse-grained and green colored musc occurs at some Cu occurrences in the district	[a]350-450°C	Transitional potassic-sericitic; early-halo veins (EH)[d]; early-micaceous (EM)[e]
	(White-mica–chlorite)	Qz, cp, tour, py, mo, ca, wm	Fine-grained white to green colored wm, chl, cp, py, ca, {hem, tit, rt}	Fracture controlled and pervasive fine-grained white to green colored wm in feldspar sites and chl in mafic sites. Locally associated with qz and sulfide veins	Intermediate and long-λ	Mostly cross-cuts ep-(ab), and overprints qz-(musc) domains	Intimately associated with Cu mineralization at Bethlehem and J.A., and Highmont. Occurs peripheral to and cross-cuts qz-(musc) facies at Valley and Lornex. Common at Cu-occurrences throughout the district	[a]250-350°C	Chlorite-sericite; sericite-chlorite-carbonate (SCC); phyllic
(Clay / argillic)[4]			Fine-grained wm, kaol, mont, chl,	Primary bt replaced to brown colored mixture of wm-mont. Plag altered to mixtures of wm-kaol-mont[g]. Selective replacement of relict plag in previously altered rocks	Kaol interference common	Appears to be late to post mineral. Most intense in the barren qz vein core, and locally within qtz-(musc) domains, of Valley	Generally limited to the Cu mineralized portions of the J.A. and Valley, and parts of Lornex and Highmont. Occurs in and around structures hosting late ca, qz, py, mo-(wm-chl) veins	[a]100-200°C	Intermediate argillic
Epidote–(K-feldspar)		Ep, prh, pump, ca, qz	Weak to moderate Ksp, wm, ep, chl, prh, verm, ab	Weak to moderately developed Ksp ± ep halos (0.5-1 cm) associated with ep ± prh veins. Irregular and diffuse vein walls. White-micas dominantly have a short-λ Al-OH absorption feature. Primary Ksp stable. Some zoned halos of inner Ksp and outer wm. Mafics altered to chlorite	Short-λ	Pre to syn prh-(wm-prh) facies	Mostly occurs in the more mafic Guichon and Border granodiorites	[a,b,c]200-350°C	Propylitic
Prehnite–(white-mica–prehnite)		Prh, ep, pump, ca, qz	Prh, wm, ab, chl, ep, pump, verm, ca {cp, mt, hem, tit}	Veinlets (0.1-0.2 cm) of prh ± inter-grown ep and ca, ± late pump, with plag-destructive halos of wm-prh and accessory ab. Ksp stable. Turbid feldspar in halos. Hbl incompletely replaced by chl ± act, ep within halo. Primary bt locally altered to chl or verm with prh along cleavage planes Generally sharp vein walls. Mt altered to ilm ± hem. Localized reddening in the halo.	Dominantly short-λ. Localized intermediate-λ proximal to the Cu centers.	Cross-cuts earlier formed veins and alteration	Highest density of veins centered on the HCV porphyry systems but occurs throughout the batholith at lower vein density	[a,b,c]200-250°C	

[1] based on descriptions in McMillian (1985), Byrne et al. (2013), Lesage et al. (2016), and Byrne et al. (2017). [2] Parentheses "( )" indicate minerals in the halo. [3] The wavelength (λ) position of the Al-OH absorption feature is classified as short (2190–2199 nm), intermediate (2199–2204 nm), and long (2204-2214 nm). Prehnite is identified from the SWIR image based on a distinct absorption feature between 1470 and 1480 nm. [4] Temperature range estimates based on mineral stabilities presented in [a]Seedorff et al. (2005), [b]Bird and Spieler (2004), and [c]Digel and Gordon (1995). [d]Proffett (2009). [e] Alva-Jiminez (2011), [f]Riedell and Proffett (2014). [g]Jambor and Delabio (1978). [5] not assessed in this study. [6] Quartz-(muscovite) and white-mica–chlorite sub-facies are grouped together as white-mica–chlorite* alteration facies in this study. {} = accessory minerals. Mineral abbreviations: ab = albite; bn = bornite; act = actinolite; anh = anhydrite; bt = biotite; ca = carbonates; chl = chlorite; cp =chalcopyrite; diop = diopside; ep = epidote; gt = garnet; hm = hematite; ill = illite; kaol = kaolinite; Ksp = K-feldspar; mont = montmorillonite; musc = muscovite (coarse grained); Mt = magnetite; plag = plagioclase; prh = prehnite; pump = pumpellyite; py = pyrite; qz = quartz; rt = rutile; tit = titanite; tour = tourmaline; verm = vermiculite; wm = white-mica undifferentiated between illite, fine-grained muscovite, paragonite, phengite, and montmorillonite. White-mica is synonymous with sericite.

2.3 Methodologies

2.3.1 Mapping and sample work-flow

Outcrop mapping, core logging, and lithogeochemical sampling was conducted between 2013 and 2016. Mapped alteration captures domains of specific assemblages with similar vein densities or alteration intensity (Fig. 2-2A). The fault network interpretation used in this contribution was constructed by Lesage et al. (2019) and is based on the integration of airborne magnetic response and lineaments, topographic lineaments, and structural measurements.

Approximately 500–1000 cm^3 size rock samples of representative vein and alteration were taken per outcrop, 0.5–1.5 km apart (Fig. 2-2B). The samples were portioned and slabbed using a rock saw to ensure weathered and organic material was removed before analyses. A total of 850 samples (average weight of 1.4 kg) underwent coupled lithogeochemical analysis, feldspar staining, and shortwave infrared spectral imaging. Lithogeochemical data for an additional 181 samples (average weight 2.5 kg) were provided by Teck Resources Limited ("Teck"). and are utilized in maps in this contribution.

Observations made from rock slabs, feldspar staining, and shortwave infrared spectral imaging were integrated to define the alteration assemblages present in each sample (Fig. 2-2B). Results were tabulated and linked to the corresponding lithogeochemical analysis (Supplemental data 2-A).

2.3.2 Lithogeochemical analysis

Lithogeochemical analysis was completed at the Bureau Veritas Laboratories, Vancouver, Canada. A crushed sample split was fused with a lithium metaborate/tetraborate mix. The fused bead was digested using a 4-acid solution and the major element oxides were analyzed by inductively coupled plasma emission spectroscopy (ICP-ES). Trace elements were measured on an inductively coupled plasma mass spectrometer (ICP-MS). Loss on ignition (LOI) is reported as % weight loss on a 1 g split ignited at 1000°C. Carbon and S were measured by LECO. Sample preparation, analytical digestion methods, and quality assurance and control procedures are provided in Appendix 2-A.

2.3.3 Shortwave infrared spectral imaging and feldspar staining

Rock slabs were analyzed using a Specim SisuROCK imaging spectrometer at the University of Alberta, which acquires reflectance data in the shortwave infrared (SWIR) wavelength (λ) range of 1000–2500 nm, at a variable spatial resolution of 0.2-1 mm/pixel (DR2). Absorption positions were retrieved from the second derivative of interpolated spectra, as described in Lypaczewski and Rivard (2018). The term "white-mica" as used herein encompasses the minerals and compositional varieties of muscovite and illite. In this study, the λ absorption position of the white-mica Al-OH feature is classified as short (2190–2198 nm), intermediate (2198–2204 nm), and long (2204-2214 nm), see Appendix 2-A for more details. This classification is based on the response of white-mica in fracture halos, or the background response if no discrete vein halo is present. Prehnite was identified from the SWIR spectra based on a distinct absorption feature appearing at 1476 nm, and kaolinite is identified by the presence of an absorption around 2160 nm.

Rock slabs were etched with hydrofluoric acid and stained with sodium colbaltinitrite to detect K-feldspar, and with amaranth to test for plagioclase, calcite and prehnite (Appendix 2-A).

2.3.4 Normative mineralogy

Total C (wt. %) measurements were converted to CO_2 and then, using molecular mass proportions, the amount of CO_2 present was equated to $CaCO_3$. Subsequently, the weight percent CaO corresponding to $CaCO_3$ was subtracted from the CaO_{total} analysis to calculate the residual, non-carbonate, CaO in the sample. The residual CaO value is used in subsequent molar element ratio diagrams. This conversion assumes that the C present in the rock is CO_3 and that the carbonate mineral is calcite (see below). The amount of CO_2 and S in each analysis was subtracted from the LOI measurement to estimate the total mineral-hosted H_2O and OH in the sample: calculated H_2O. The calculated H_2O term assumes all S is as sulfide minerals in the rock—a reasonable assumption for the district samples (Appendix 2-B).

2.3.5 Molar element ratio diagrams and element gains and losses

Molar element ratios (MERs) are used to reduce the effects of closure and cast lithogeochemical data in terms that can be related to variations in mineral formulae, chemical reaction stoichiometries, and to test for material-transfer (Madeisky and Stanley, 1993; Stanley, 2011). More specifically, Pearce element ratio (PER) diagrams use a denominator element that did not participate in material-transfer processes (conserved element), which creates a simple proportionality with material-transfer (Madeisky and Stanley, 1993; Stanley and Madeisky, 1994).

To assess and visualize element gains, losses, and immobility, in select sample pairs, isocon diagrams were constructed (Grant 1986; Grant 2005). Element gains and losses for each alteration facies, based on median values in the data populations, were calculated on a weight basis following Grant's approach (Grant 1986; Warren et al., 2007) and using Al_2O_3 as the conserved element:

$$\Delta C = (\text{CP immobile}/\text{CA immobile}) \cdot \text{CA} - \text{CP}, \qquad \text{(Eq. 1)}$$

where CP and CA are the concentrations of the conserved element in the protolith (P) and altered (A) sample, respectively, and ΔC denotes the gain or loss in grams per 100 g of rock for major elements or in parts per million for trace elements, and parts per billion for Au, Ag, and Hg (Supplemental data 2-B). By plotting calcite instead of CO_2, the CaO term is inferred to isolate changes in aluminosilicate minerals.

2.3.6 Whole-rock C isotope analysis

A total of 119 whole-rock carbon isotope ($\delta^{13}C_{total}$) analyses were completed at the Queen's Facility for Isotope Research (QFIR), Queen's University, Canada (Supplemental data 2-C). For C isotope compositions and C concentrations, 15 to 80 mg of powdered whole-rock sample was analyzed using a Costech ECS 4010 Elemental Analyzer coupled to a Thermo-Finnigan DeltaPlus XP Continuous-Flow Isotope Ratio Mass Spectrometer (CF-IRMS). One outlier with a $\delta^{13}C$ value of -39‰ appears to be contaminated with surficial organic matter and this data point was discarded; all other data were utilized herein. Additional analytical information is in Appendix 2-A.

2.4 Protolith compositions

Critical to the use of PER diagrams is to test whether the chosen denominator is conserved. Figure 2-3 plots the immobile elements Al versus Ti and Zr for GCB rocks. Samples from an originally homogeneous protolith will form a linear array that passes through the origin if the plotted elements are immobile, and disparate protoliths will form additional linear arrays and trend lines (Barrett and McLean 1999; Bushchette and Piercey, 2016). Based on Figure 2-3, Al, Ti and Zr are conserved (immobile) with respect to alteration (i.e., each linear array has a homogeneous protolith). There is some variation between sample suites in terms of Ti, Zr, and several other incompatible elements due to magmatic differentiation in the GCB intrusive suite (D'Angelo et al., 2017). There is a failure to reject the cogenetic igneous hypothesis for GCB for Ti and Zr, and thus application of PER plots *sensu stricto* to understand magmatic fractionation is not possible (Russell and Stanley, 1990). We will demonstrate, however, that by grouping and plotting data by rock types defined from a combination of mapping, mineralogical and textural criteria, and Al-Ti composition, that Ti can be used in the denominator to elucidate alteration processes.

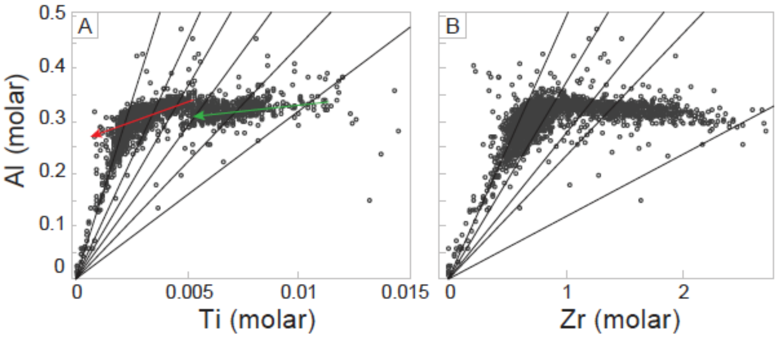

Figure 2-3. Immobile element test cross-plots. A. Al vs. Ti (molar). B. Al vs. Zr (molar). The green and red lines represent magmatic evolution trends.

Least altered samples (Table 2-2) were identified on the basis of the absence of veins, halos, or aplite dikes, and have unaltered primary plagioclase, K-feldspar and hornblende. The GCB formed from two magmatic pulses that fractionated from high to low Ti at a relatively constant Al content (Fig. 2-4A). The decrease in Ti corresponds to a decrease in Mg-number (Fig. 2-4B), and an increase in Si (Fig. 2-4C). On a plot of 2Ca+Na+K/Ti versus Al/Ti (molar) the mineralogical control on the composition of a sample is indicated by the slope of the line made between the origin and the sample (Madeisky and Stanley, 1993). The theoretical slopes of lines on the plot are 1, 0.3 and 0 for feldspar, muscovite and chlorite/kaolinite control, respectively. (Stanley and Madeisky, 1994). By plotting the 2Ca+Na+K/Ti versus Al/Ti (2CNK/Al) slope value against the Al/Ti value, the initial Ca, Na, and K content can be evaluated with respect to magmatic evolution (Fig. 2-4D). Guichon Creek batholith rocks evolved from high 2CNK/Al values towards compositions controlled by feldspar (Fig. 2-4D). Least altered Border, Guichon and Chataway rocks have 2CNK/Al values > 1, because of high Ca concentrations (Table 2-2) associated with hornblende content in excess of 5% (McMillan, 1985b; D’Angelo, 2016). Unaltered Bethlehem granodiorite has 2CNK/Al between ~1.1 and 1, whereas Skeena and Bethsaida granodiorite cluster between 1 and 0.95 (Fig. 2-4D).

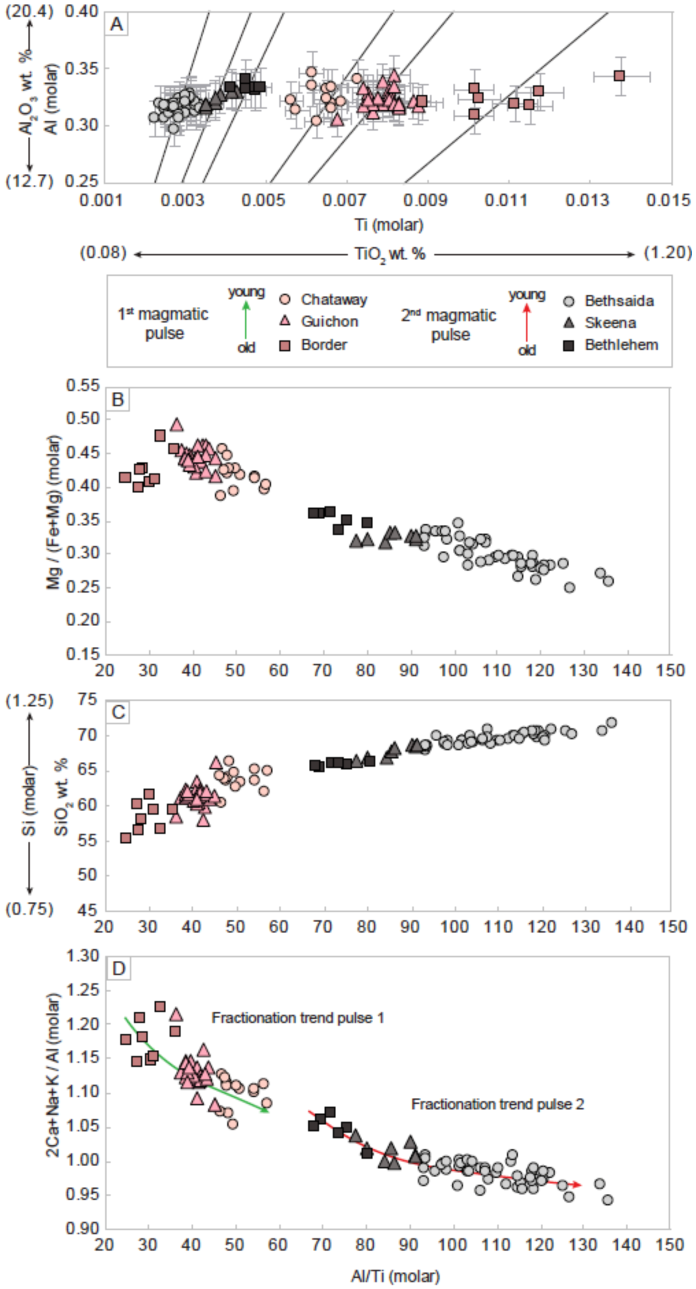

Figure 2-4. Least altered host rock discrimination diagrams. A. Al vs. Ti (molar), the analytical error bars shown are 6% of the value. B. Mg / (Mg + Fe) vs. Al/Ti. The GCB magmatic suite evolved towards lower Mg#. C. Si vs. Al / Ti. Rocks evolve towards higher Si content through time. D. 2Ca+Na+K / Ti vs. Al/Ti. Rocks in the GCB show two fractionation trends towards decreasing 2CNK/Al associated with each pulses of magmatism. The least altered, or precursor, mean 2CNK/Al values for the host rocks are: ~1.20 (Border); 1.12 (Guichon); 1.10 (Chataway); 1.05 (Bethlehem); 1.00 (Skeena); and 0.97 (Bethsaida).

A subset of 119 whole-rock samples, mostly from south and east of the Lornex and Highmont deposits, were analyzed for their C isotope composition (Table 2-3; Fig. 2-5). The $\delta^{13}C$ values have a bimodal distribution with modes at approximately -25 and -5 ‰ (Fig. 5B). There is a wide range in $\delta^{13}C$ values between -30 to -5 ‰, but some systematic variation with respect to alteration facies is evident and discussed below. The least altered samples labeled A (2015GL082) and B (2015GL071) in Figure 2-5A lack veins and alteration halos detectable by staining or spectral imaging but do contain approximately 0.05 wt. % C each. The C in these samples is interpreted to be related to secondary carbonate micro-veinlets because GCB rocks do not contain primary carbonate inclusions or phenocrysts (D'Angelo et al., 2017). Excluding samples 2015GL082 and 2015GL071, least altered rocks have a median and mean $\delta^{13}C$ values of -21.3 and -21.9 ‰, respectively (Fig. 2-5; Table 2-3).

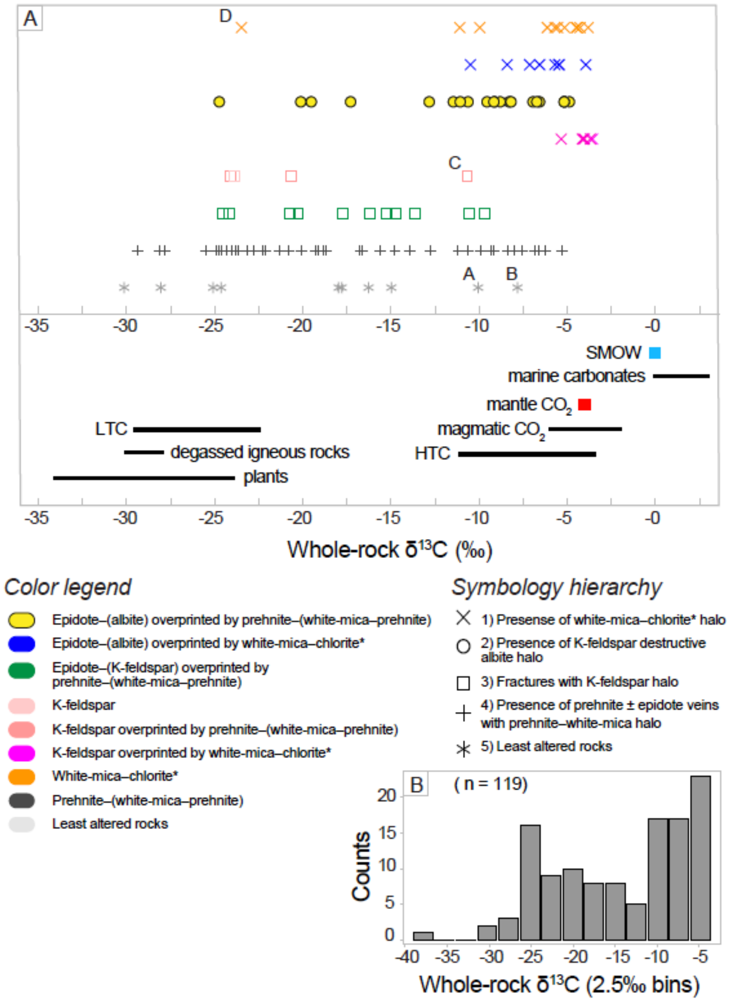

Figure 2-5. Whole-rock $\delta^{13}C$ ‰ data. A. Whole-rock $\delta^{13}C$ ‰ values organized by alteration facies, and common C isotope reservoirs (Taylor, 1986 and references therein). LTC = low temperature carbon and HTC = high temperature carbon. Range of values of degassed intrusive rocks is from Collahuasi district (Djouka-Fonkwe et al., 2012). Sample labels are explained in the main body text. B. Histogram of whole-rock $\delta^{13}C$ values in 2.5 ‰ bins.

2.5 Carbonate composition

By plotting the molar ratios of $Ca_{(total)}$/Ti against CO_2/Ti the composition of carbonate present in whole-rock samples can be estimated (Fig. 2-6). Most GCB samples plot close to the anorthite trend line but some extend towards, and form an array along, the calcite control line. Samples with a slope between vertical and 1 contain some carbonate that is interpreted to be calcite; this is supported by electron probe microanalysis results (Figs. 2-6B-D; Appendix 2-A).

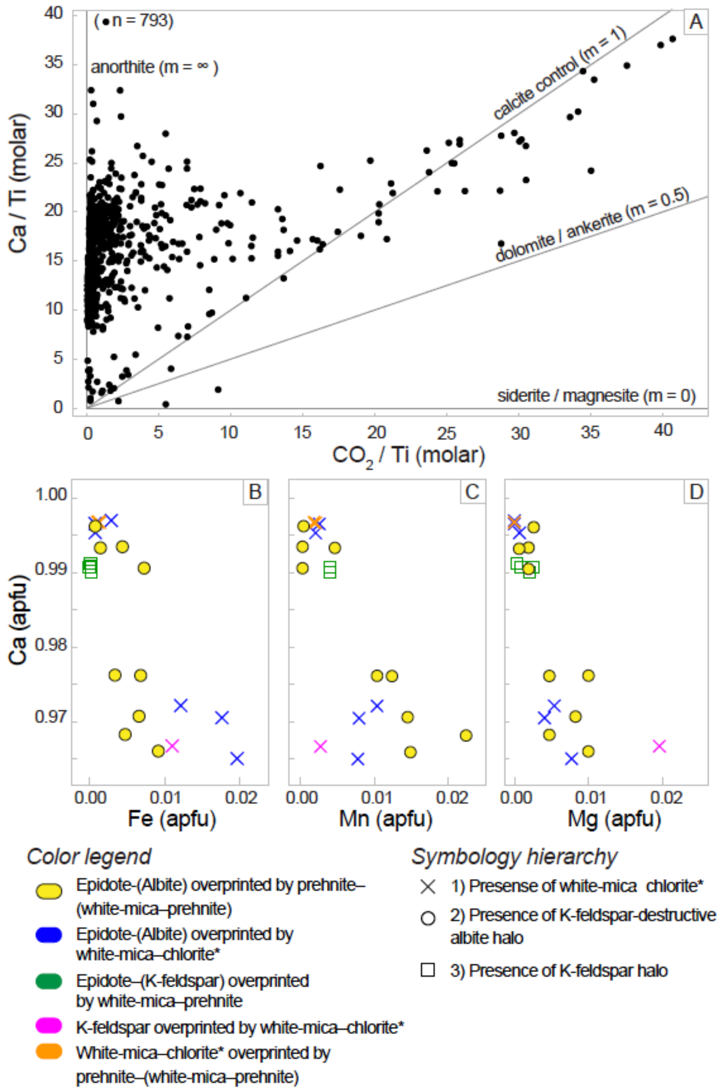

Figure 2-6. Carbonate mineral compositional diagrams. A. Ca / Ti vs. CO_2 / Ti. B-D. Electron microprobe analysis (EMPA) of carbonate minerals in the Guichon Creek batholith symbolized by alteration facies. EMPA indicate that the carbonate analyzed in GCB samples are >96% calcite in composition, and typically contains only trace amounts of Fe, Mn or Mg. Abbreviations: apfu = atoms per formulae unit. Microprobe data is provided in Appendix 2A.

Table 2-2. Representative lithogeochemical data for the Guichon Creek batholith[1]

	Border diorite		Guichon and Chataway granodiorite						
	Least altered	σ	Least altered	σ	Epidote-(albite)	K-feldspar	White-mica-chlorite*	Epidote-(K-feldspar)	Prehnite-(white-mica-prehnite)
n	10		39		31	7	14	26	126
SiO_2 (wt. %)	58.60	*2.11*	61.82	*1.50*	63.42	63.05	60.34	61.10	62.71
Al_2O_3	16.40	*0.54*	16.42	*0.52*	15.94	15.81	16.84	16.49	16.30
Fe_2O_3	7.06	*0.74*	5.39	*0.37*	3.97	5.14	5.62	5.60	5.02
MgO	3.54	*0.50*	2.75	*0.33*	2.22	2.40	2.75	2.83	2.37
$CaO_{(total)}$	6.30	*0.74*	5.15	*0.50*	5.23	3.40	4.32	5.21	4.86
Na_2O	3.56	*0.23*	4.00	*0.20*	4.83	3.81	3.93	4.03	4.05
K_2O	1.98	*0.39*	2.20	*0.27*	0.68	3.17	2.21	1.94	2.14
TiO_2	0.86	*0.12*	0.61	*0.03*	0.57	0.54	0.62	0.61	0.56
P_2O5	0.18	*0.05*	0.16	*0.01*	0.14	0.11	0.16	0.15	0.15
MnO	0.11	*0.02*	0.08	*0.01*	0.07	0.06	0.09	0.09	0.08
Cr_2O_3	0.00	*0.00*	0.00	*0.00*	0.00	0.00	0.00	0.00	0.00
S	0.01	*0.00*	0.01	*0.00*	0.01	0.01	0.01	0.01	0.01
C	0.02	*0.01*	0.01	*0.01*	0.10	0.01	0.05	0.02	0.01
LOI	1.3	*0.4*	1.0	*0.3*	1.9	1.2	1.6	1.5	1.4
CO_2^*	0.07	*0.03*	0.04	*0.03*	0.37	0.04	0.18	0.07	0.04
Calcite*	0.17	*0.06*	0.08	*0.08*	0.84	0.08	0.42	0.17	0.08
$CaO^*_{residual}$	6.21	*0.70*	5.11	*0.46*	4.76	3.36	4.09	5.12	4.81
H_2O^*	1.2	*0.3*	1.0	*0.3*	1.5	1.1	1.4	1.4	1.4
Sc (ppm)	18	*2*	11	*1*	10	11	11	12	10
Ba	632	*73*	699	*55*	151	841	700	634	694
Cs	1.7	*1.2*	1.1	*0.4*	0.9	1.0	0.8	0.8	1.1
Ga	16.9	*1.1*	17.2	*1.0*	16.5	16.4	17.5	16.7	17.0
Hf	3.9	*11.3*	3.7	*0.8*	3.8	3.3	3.3	3.5	4.1
Nb	3.3	*1.1*	2.6	*0.6*	2.8	2.6	2.7	2.5	2.6
Rb	56.9	*17.2*	57.5	*11.7*	17.5	91.2	52.6	50.3	54.4
Sn	0.5	*0.2*	0.5	*0.0*	0.5	1.0	0.5	0.5	0.5
Sr	544.3	*112.4*	657.0	*67.9*	588.8	497.2	645.6	668.3	639.3
Ta	0.3	*0.1*	0.1	*0.1*	0.2	0.2	0.2	0.2	0.2
Th	3.6	*1.8*	4.8	*1.6*	5.9	5.9	4.8	4.2	4.8
U	2.0	*0.8*	2.2	*0.6*	2.5	2.9	2.4	1.9	2.2
V	184	*30*	138	*13*	117	117	137	141	128
W	0.6	*0.4*	0.3	*0.3*	0.6	0.7	1.3	0.3	0.3
Zr	135.9	*480.3*	128.9	*31.7*	135.9	116.4	104.4	119.2	139.6
Y	16.9	*3.6*	11.6	*1.9*	13.2	11.4	10.6	11.3	11.9
La	14.3	*2.5*	14.0	*2.0*	14.7	15.4	14.1	13.5	14.3
Ce	31.5	*6.1*	29.5	*4.4*	31.8	32.7	31.0	30.3	31.0
Pr	4.07	*0.77*	3.74	*0.54*	3.86	4.11	3.83	3.71	3.88
Nd	17.1	*3.5*	15.6	*2.2*	15.3	16.3	15.9	15.1	16.1
Sm	3.75	*0.80*	2.98	*0.47*	3.28	3.15	3.14	3.09	3.18
Eu	0.94	*0.15*	0.79	*0.07*	0.76	0.77	0.81	0.83	0.80
Gd	3.61	*0.64*	2.61	*0.44*	2.82	2.60	2.49	2.63	2.70
Tb	0.53	*0.09*	0.38	*0.06*	0.41	0.40	0.36	0.37	0.40
Dy	3.07	*0.49*	2.16	*0.40*	2.51	2.14	2.02	2.11	2.25
Ho	0.56	*0.13*	0.43	*0.07*	0.47	0.41	0.41	0.41	0.43
Er	1.77	*0.36*	1.19	*0.21*	1.31	1.37	1.13	1.17	1.25
Tm	0.27	*0.07*	0.19	*0.03*	0.21	0.19	0.17	0.18	0.19
Yb	1.66	*0.36*	1.22	*0.24*	1.30	1.30	1.15	1.21	1.26
Lu	0.28	*0.07*	0.19	*0.03*	0.19	0.21	0.18	0.19	0.20
Mo	1.05	*0.83*	0.58	*0.42*	0.45	0.63	0.63	0.63	0.59
Cu	148.50	*98.31*	106.62	*49.18*	23.19	456.53	359.09	115.92	111.28
Pb	2.00	*0.81*	1.42	*1.56*	1.01	1.72	1.23	1.75	1.71
Zn	46.7	*3.9*	33.2	*6.7*	33.3	26.0	37.9	37.2	32.6
Ag (ppb)	55	*41*	40	*17*	24	208	187	43	42
Ni	15.5	*2.4*	13.4	*2.8*	9.2	12.3	15.3	14.6	11.8
Co	14.7	*2.3*	10.0	*1.1*	6.5	8.5	10.9	11.3	9.8
Mn	309.0	*35.9*	252.0	*23.8*	323.5	238.0	408.5	305.0	283.0
As	2.2	*0.6*	1.1	*0.6*	3.9	1.5	1.5	1.2	1.0
Au (ppb)	1.5	*0.8*	0.9	*0.9*	0.1	0.1	1.9	1.0	0.8
Cd	0.05	*0.03*	0.03	*0.04*	0.01	0.02	0.03	0.03	0.02
Sb	0.11	*0.05*	0.06	*0.04*	0.45	0.12	0.16	0.07	0.07
Bi	0.05	*0.03*	0.04	*0.03*	0.01	0.06	0.08	0.02	0.03
Cr	20.90	*10.76*	16.70	*5.39*	11.75	15.20	16.10	14.75	13.10
B	7	*3*	3	*2*	3	6	7	4	4
Tl	0.08	*0.03*	0.06	*0.02*	0.02	0.01	0.02	0.02	0.03
Hg (ppb)	9	*5*	3	*2*	3	3	4	3	3
Se	0.05	*0.02*	0.05	*0.00*	0.05	0.05	0.05	0.05	0.05
Te	0.01	*0.02*	0.01	*0.00*	0.02	0.03	0.03	0.01	0.01
Ge	0.05	*0.05*	0.05	*0.02*	0.05	0.05	0.08	0.05	0.05
In	0.01	*0.01*	0.01	*0.00*	0.01	0.01	0.01	0.01	0.01
Re (ppb)	0.50	*0.00*	0.5	*0.22*	0.5	0.5	0.5	0.5	0.5
Be	0.2	*0.1*	0.2	*0.1*	0.3	0.3	0.2	0.3	0.3
Li	8.8	*1.2*	8.1	*1.9*	6.9	7.5	7.5	9.0	8.6

[1] Median oxide and elemental values and σ is the standard deviation of the sample series

* = Calculated fields based on S, C and LOI analysis and on the assumption that all CO_2 is associated with $CaCO_3$.

Table 2-2 continued.

	Bethlehem and Skeena granodiorite						
	Least altered	σ	Epidote-(albite)	K-feldspar	White-mica-chlorite*	Epidote-(K-feldspar)	Prehnite-(white-mica-prehnite)
n	17		39	5	23	1	35
SiO_2 (wt. %)	66.58	*1.24*	67.16	68.12	67.00	67.16	67.25
Al_2O_3	16.85	*0.45*	16.49	16.33	16.38	16.74	16.44
Fe_2O_3	3.30	*0.44*	2.88	2.88	3.15	3.09	3.08
MgO	1.04	*0.18*	1.00	0.92	0.97	0.96	0.96
CaO $_{(total)}$	4.15	*0.44*	4.31	3.37	3.10	3.82	3.89
Na_2O	4.74	*0.16*	4.85	4.70	4.57	4.72	4.78
K_2O	1.73	*0.24*	0.75	2.14	1.87	2.02	1.84
TiO_2	0.33	*0.04*	0.33	0.29	0.30	0.30	0.30
P_2O5	0.13	*0.01*	0.12	0.11	0.12	0.11	0.11
MnO	0.06	*0.02*	0.04	0.06	0.05	0.07	0.05
Cr_2O_3	0.00	*0.00*	0.00	0.00	0.00	0.00	0.00
S	0.01	*0.00*	0.01	0.01	0.02	0.01	0.01
C	0.01	*0.02*	0.08	0.01	0.09	0.01	0.02
LOI	0.8	*0.7*	1.9	1.0	1.9	0.8	1.2
CO_2*	0.04	*0.06*	0.29	0.04	0.33	0.04	0.07
Calcite*	0.08	*0.14*	0.67	0.08	0.75	0.08	0.17
CaO*$_{residual}$	4.11	*0.36*	3.93	3.33	2.68	3.78	3.79
H_2O*	0.7	*0.6*	1.6	0.9	1.6	0.8	1.2
Sc (ppm)	4	*1*	4	4	4	4	4
Ba	815	*217*	372	954	702	884	850
Cs	0.6	*0.6*	0.5	1.1	1.0	0.3	0.6
Ga	17.0	*2.1*	17.0	2.8	15.9	18.9	16.5
Hf	2.2	*0.5*	2.3	16.0	2.2	2.8	2.2
Nb	1.6	*0.6*	1.9	2.3	1.5	1.8	1.7
Rb	27.4	*8.2*	17.5	39.7	29.3	34.4	30.5
Sn	0.5	*0.5*	0.5	1.8	1.0	2.0	1.0
Sr	712.5	*92.1*	759.3	647.8	650.5	685.9	662.7
Ta	0.1	*0.1*	0.1	0.8	0.1	0.1	0.1
Th	1.7	*0.7*	1.6	0.1	1.4	1.7	1.6
U	0.8	*0.5*	1.0	1.6	1.0	1.0	1.0
V	62	*12*	62	57	58	58	58
W	0.3	*0.4*	0.6	0.7	1.8	0.3	0.3
Zr	72.1	*17.5*	79.0	1.3	70.5	88.2	72.7
Y	6.1	*0.8*	6.3	72.6	5.8	5.9	6.0
La	9.3	*1.0*	9.0	5.7	9.0	9.6	9.5
Ce	18.2	*2.2*	18.1	0.3	18.0	17.9	18.3
Pr	2.26	*0.33*	2.22	9.55	2.17	2.11	2.16
Nd	8.9	*1.7*	9.0	18.6	8.5	8.8	8.7
Sm	1.66	*0.32*	1.70	2.17	1.60	1.67	1.60
Eu	0.52	*0.08*	0.52	8.00	0.51	0.54	0.52
Gd	1.40	*0.20*	1.45	1.51	1.30	1.41	1.35
Tb	0.20	*0.03*	0.21	0.48	0.19	0.20	0.19
Dy	1.08	*0.26*	1.12	1.25	1.08	1.13	1.07
Ho	0.21	*0.04*	0.22	0.19	0.20	0.22	0.21
Er	0.61	*0.15*	0.64	0.97	0.58	0.60	0.61
Tm	0.09	*0.02*	0.10	0.20	0.08	0.10	0.09
Yb	0.65	*0.13*	0.68	0.54	0.64	0.72	0.64
Lu	0.10	*0.02*	0.11	0.08	0.10	0.12	0.10
Mo	0.07	*0.91*	0.50	0.48	1.43	0.34	0.28
Cu	17.50	*43.12*	19.91	193.63	133.06	71.75	14.43
Pb	1.00	*0.43*	1.86	1.74	1.74	0.73	1.46
Zn	23.0	*13.6*	20.2	24.0	22.4	20.0	21.9
Ag (ppb)	13	*16*	23	48	56	22	20
Ni	2.5	*0.6*	2.7	2.3	2.4	2.3	2.3
Co	4.3	*1.0*	4.3	4.1	4.6	4.1	4.4
Mn	258.5	*87.2*	204.0	278.0	274.0	314.0	267.0
As	0.7	*1.3*	1.2	0.1	0.9	0.5	0.7
Au (ppb)	0.2	*1.7*	0.4	0.5	0.4	0.5	0.2
Cd	0.01	*0.07*	0.02	0.02	0.02	0.01	0.01
Sb	0.04	*0.07*	0.15	0.04	0.10	0.11	0.05
Bi	0.01	*0.02*	0.01	0.03	0.05	0.01	0.01
Cr	4.00	*3.46*	2.80	1.78	2.90	2.80	3.00
B	2	*2*	2	1	2	1	2
Tl	0.01	*0.02*	0.01	0.55	0.02	0.01	0.01
Hg (ppb)	3	*3*	3	3	5	3	3
Se	0.05	*0.02*	0.05	0.05	0.05	0.05	0.05
Te	0.01	*0.00*	0.01	0.02	0.01	0.01	0.01
Ge	0.05	*0.00*	0.05	0.01	0.05	0.05	0.05
In	0.01	*0.00*	0.01	0.05	0.01	0.01	0.01
Re (ppb)	0.5	*0.00*	0.5	0.0	0.5	0.5	0.5
Be	0.1	*0.2*	0.2	0.5	0.3	0.2	0.3
Li	5.7	*6.4*	5.6	8.8	5.5	3.1	5.3

Table 2-2 continued.

	Bethsaida granodiorite							
	Least altered	σ	Epidote-(albite)	K-feldspar	White-mica-chlorite*	Prehnite-(white-mica-prehnite)		
						All samples	Distal	Proximal
n	45		65	30	50	71		
SiO_2 (wt. %)	69.33	0.62	69.21	70.25	70.35	69.17	69.02	69.24
Al_2O_3	16.16	0.22	15.93	15.86	14.44	16.03	16.06	16.03
Fe_2O_3	2.32	0.17	2.25	2.14	2.03	2.30	2.40	2.27
MgO	0.60	0.07	0.62	0.55	0.42	0.61	0.69	0.58
$CaO_{(total)}$	3.05	0.24	3.09	2.67	1.70	2.92	3.05	2.95
Na_2O	4.96	0.17	5.11	4.95	1.65	4.96	4.80	5.00
K_2O	1.89	0.19	1.25	2.09	2.55	1.85	1.92	1.82
TiO_2	0.23	0.01	0.22	0.22	0.17	0.23	0.24	0.22
P_2O5	0.08	0.01	0.08	0.07	0.07	0.08	0.09	0.08
MnO	0.06	0.01	0.06	0.04	0.04	0.06	0.07	0.05
Cr_2O_3	0.00	0.00	0.00	0.00	0.00	0.00	0.00	0.00
S	0.01	0.00	0.01	0.01	0.19	0.01	0.01	0.01
C	0.01	0.01	0.07	0.01	0.35	0.01	0.01	0.03
LOI	0.9	0.4	1.8	0.9	3.4	1.3	1.4	1.4
CO_2*	0.04	0.02	0.26	0.04	1.28	0.04	0.04	0.09
Calcite*	0.08	0.06	0.58	0.08	2.92	0.08	0.08	0.21
$CaO^*_{residual}$	3.01	0.21	2.77	2.63	0.06	2.88	3.01	2.84
H_2O*	0.8	0.4	1.6	0.9	2.0	1.3	1.4	1.3
Sc (ppm)	3	0	2	2	2	2	3	2
Ba	977	134	732	1040	744	939	881	949
Cs	0.7	0.3	0.5	0.6	1.5	0.6	0.6	0.6
Ga	16.3	1.0	16.0	16.4	14.9	16.2	15.8	16.4
Hf	2.0	0.2	2.0	2.0	1.8	2.0	2.1	2.0
Nb	1.8	1.3	1.8	2.0	1.7	1.8	1.7	1.9
Rb	30.5	4.0	21.3	32.7	46.2	30.9	31.2	30.7
Sn	0.5	0.1	0.5	0.5	0.5	0.5	0.5	0.5
Sr	635.0	45.6	672.0	615.1	237.7	631.8	629.1	633.2
Ta	0.1	0.1	0.1	0.2	0.1	0.1	0.1	0.1
Th	1.2	0.3	1.1	1.1	0.8	1.3	1.4	1.3
U	0.6	0.2	0.7	0.6	0.6	0.7	0.9	0.7
V	39	5	36	33	31	40	42	38
W	0.3	0.3	0.6	0.6	3.3	0.3	0.3	0.4
Zr	65.4	6.8	66.0	67.0	58.7	66.3	65.8	66.4
Y	5.3	0.9	5.3	5.5	5.0	5.3	5.4	5.3
La	9.4	0.9	9.1	9.9	7.7	9.6	9.9	9.5
Ce	17.4	2.0	17.5	17.7	15.5	17.9	18.9	17.3
Pr	2.03	0.27	2.02	2.04	1.82	2.04	2.11	1.98
Nd	7.8	1.3	7.8	7.9	6.8	8.0	8.5	7.7
Sm	1.33	0.27	1.34	1.35	1.21	1.38	1.42	1.31
Eu	0.44	0.05	0.42	0.41	0.32	0.43	0.45	0.43
Gd	1.13	0.18	1.12	1.15	1.00	1.15	1.21	1.13
Tb	0.16	0.03	0.16	0.16	0.14	0.16	0.16	0.16
Dy	0.93	0.17	0.89	0.88	0.83	0.93	0.96	0.89
Ho	0.18	0.04	0.18	0.18	0.17	0.18	0.18	0.18
Er	0.51	0.10	0.53	0.55	0.51	0.53	0.55	0.52
Tm	0.08	0.02	0.08	0.08	0.08	0.08	0.09	0.08
Yb	0.60	0.09	0.61	0.62	0.58	0.61	0.63	0.60
Lu	0.10	0.01	0.10	0.10	0.10	0.10	0.10	0.10
Mo	0.17	0.33	0.22	1.85	7.11	0.26	0.18	0.33
Cu	6.24	45.41	4.54	370.47	1632.74	8.68	5.65	15.28
Pb	0.95	0.51	1.70	1.00	1.76	1.63	2.03	1.44
Zn	25.0	6.1	27.6	16.6	14.6	24.4	31.3	22.4
Ag (ppb)	12	39	17	114	614	21	19	21
Ni	1.1	0.3	1.0	1.0	0.6	1.2	1.5	1.1
Co	2.9	0.5	2.8	2.6	1.2	2.8	3.5	2.7
Mn	339.0	52.7	343.0	276.5	302.5	341.0	367.5	327.5
As	0.3	0.4	0.7	0.3	1.7	0.5	0.6	0.4
Au (ppb)	0.4	0.9	0.1	3.0	2.8	0.3	0.1	0.5
Cd	0.01	0.01	0.01	0.01	0.04	0.01	0.01	0.01
Sb	0.02	0.03	0.09	0.03	0.05	0.03	0.04	0.03
Bi	0.01	0.05	0.01	0.07	0.20	0.01	0.01	0.03
Cr	2.40	2.02	2.40	2.10	4.05	2.30	2.75	2.10
B	1	1	1	1	2	2	2	2
Tl	0.01	0.01	0.01	0.02	0.03	0.01	0.01	0.01
Hg (ppb)	3	2	3	4	6	3	3	3
Se	0.05	0.00	0.05	0.05	0.05	0.05	0.05	0.05
Te	0.01	0.01	0.01	0.01	0.03	0.01	0.01	0.01
Ge	0.05	0.04	0.05	0.05	0.05	0.05	0.05	0.05
In	0.01	0.00	0.01	0.01	0.01	0.01	0.01	0.01
Re (ppb)	0.5	0.15	0.5	0.5	2.0	0.5	0.5	0.5
Be	0.2	0.1	0.3	0.2	0.2	0.3	0.4	0.3
Li	6.1	2.7	4.7	4.9	0.9	6.5	8.7	5.5

2.6 Alteration facies

Vein and halo mineralogy, spectral characteristics, and paragenesis of the alteration facies present in the HVC porphyry centers and GCB are summarized in Table 2-1 and Figure 2-7. The results below are grouped by alteration facies and form the basis for assessing lithogeochemical data. To reduce the effects of fractionation-related chemical trends (i.e., Fig. 2-4), altered samples are organized by host rock, which also helps to declutter data points and visualize the results. Samples are colored by the alteration facies and any overprint present, and symbolized hierarchically based on the presence of: 1) coarse-grained muscovite and / or fine-grained white-mica–chlorite halos; 2) albite halos; 3) K-feldspar halos; and 4) prehnite–white-mica halos.

2.6.1 K-feldspar: potassic

Petrography / mineralogy: Veinlets and discontinuous fracture fill of quartz and chalcopyrite with 1–2 cm K-feldspar halos compose the K-feldspar alteration facies (Fig. 2-7A). Calcite veins and alteration do not commonly occur with K-feldspar facies.

Mapped distribution: The highest density (~ 5cm/m) of veinlets with K-feldspar halos are located over the Valley deposit. The presence of K-feldspar halos continues, at a lower density, for ~2 km west of mineralization, beyond which distance they are absent (Figs. 2-2A and 2-7A). A second K-feldspar halo domain occurs over Lornex and Highmont that extends asymmetrically up to 1 km to the northeast in narrow structures, and ~2 km to the southeast (Fig. 2-2A).

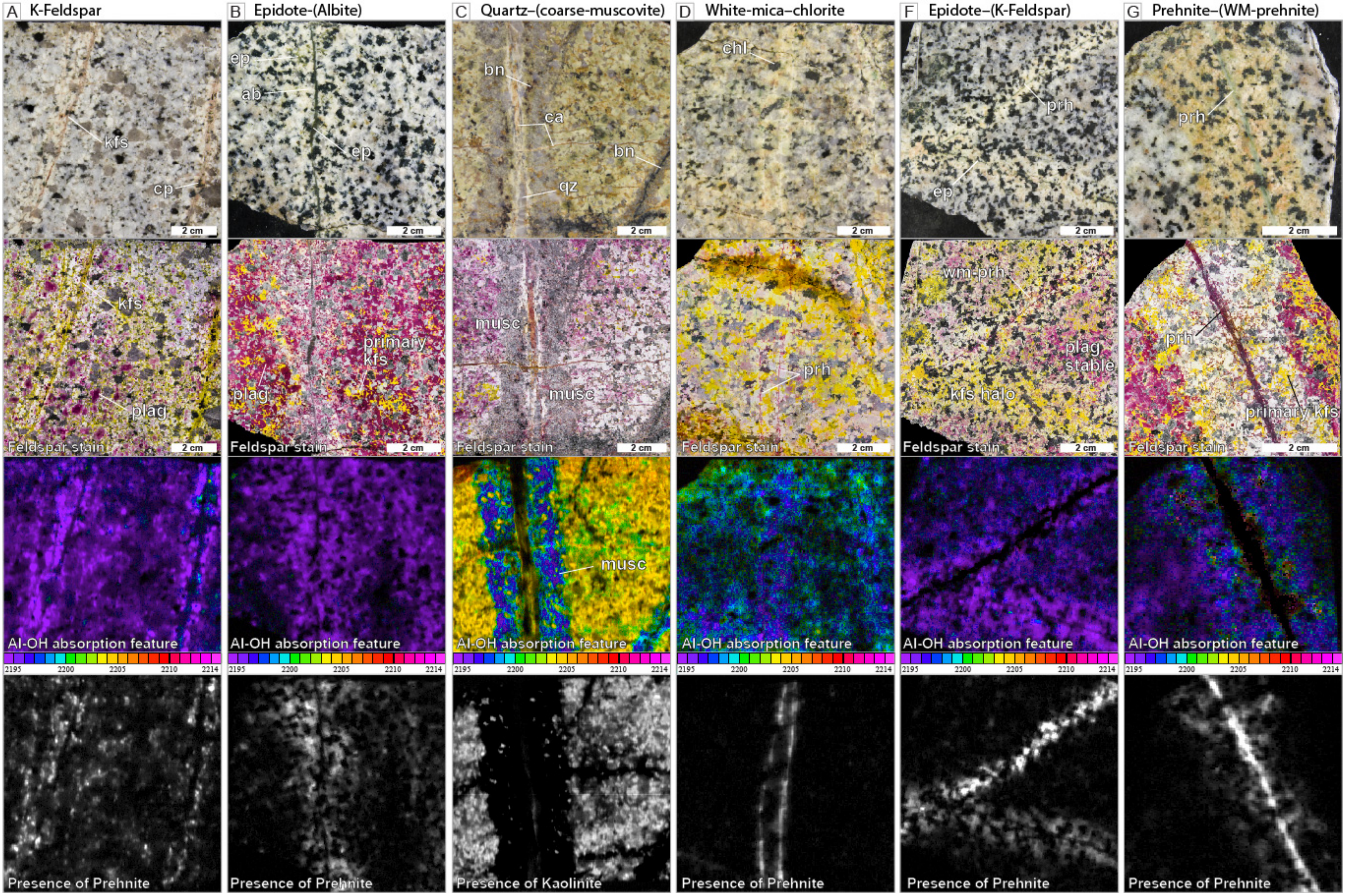

Figure 2-7. Examples of the alteration facies in the Guichon Creek batholith. A. K-feldspar fracture-halo; *K-feldspar facies*. Patchy K-feldspar alteration of plagioclase within halos around fractures with trace chalcopyrite fill. Trace, short-λ white-mica and prehnite present throughout. B.

Epidote vein with K-feldspar destructive albite halo and patchy epidote in the plagioclase sites; *epidote-(albite) facies*. Note the whitening of the feldspars and the absence of the yellow-stain that defines the K-feldspar-destructive albite halo around the epidote vein fill. Trace, short-λ white-mica and prehnite also present in the halo. C. Quartz ± bornite veins with diagnostic coarse-grained grey-colored muscovite halos; *quartz-(muscovite) facies*. Pervasive trace kaolinite alteration of feldspar results in ineffective staining of the feldspar sites. The coarse muscovite is characterized by short to intermediate-λ spectral response. D. Pervasive fine-grained white-mica–chlorite; *white-mica–chlorite facies*. K-feldspar is mostly stable but plagioclase is pervasively altered to fine-grained white-mica with intermediate-λ spectral response. Mafic minerals are selective pervasively altered to chlorite. Note the late prehnite veinlets (pink stained). E. Epidote vein with K-feldspar halo; *epidote-(K-feldspar) facies*. Plagioclase is partially altered to K-feldspar within the halo, whereas mafic minerals are selective pervasively altered to chlorite. Note, the prehnite veinlet with plagioclase-destructive short-λ white-mica and prehnite halo which possibly cross-cuts the epidote veinlet. D. Prehnite ± pumpellyite veinlet with fine-grained white-mica–prehnite halo; *prehnite–(white-mica–prehnite) facies*. Note the prehnite veinlet stains pink and the reddening within the alteration halo. K-feldspar is stable, whereas plagioclase has been selectively and incompletely replaced by short-λ white-mica and accessory prehnite (small pink-stained grains within the halo). Spectral criteria used are provided in Data Repository 2. Mineral abbreviations: ab = albite, bn = bornite, ca = calcite, cp = chalcopyrite, chl = chlorite, ep = epidote, kfs = K-feldpsar, musc = muscovite, plag = plagioclase, prh = prehnite, qz = quartz.

Table 2-3. Alteration facies and C_{total} isotope results and statistics.

Facies	Least altered			K-feldspar			Epidote–(albite)			White-mica–chlorite*			Epidote–(K-feldspar)			Prehnite–white-mica		
n	8			4			22			25			11			46		
	m	μ	σ	*m*	μ	σ	*m*	μ	σ	*m*	μ	σ	*m*	μ	σ	*m*	μ	σ
$\delta^{13}C$ (‰ VPDM)	-21.31	-21.87	5.8	-23.87	-22.88	1.92	-9.12	-10.55	5.51	-5.5	-5.87	2.11	-16.19	-17.06	4.99	-19.69	-17.95	7.26
Calcite (wt. %)	0.08	0.1	0.06	0.08	0.11	0.05	0.58	0.77	0.59	2.17	3.37	3.95	0.17	0.3	0.27	0.12	0.33	0.36
H_2O (wt. %)	0.91	1.27	1.35	1.36	1.25	0.35	1.53	1.57	0.45	1.61	1.68	0.8	1.42	1.39	0.46	1.37	1.45	0.51
Cu (ppm)	120	102	69	1243	1548	1285	10	28	47	510	6603	10822	78	111	130	51	479	2044
2CNK/Al	1.04	1.05	0.08	0.78	0.82	0.1	0.92	0.95	0.09	0.77	0.68	0.27	1.11	1.14	0.19	1.07	1.09	0.14

VPDM = Vienna Pee Dee Belemnite.
m = median; μ = arithmetic mean; σ = standard deviation.

PER, MER, mobile element, and volatile characteristics: K-feldspar altered rocks plot on the feldspar control line and overlap with other alteration facies in the 2CNK/Al diagram (Fig. 2-8A). In K/Ti vs. Al-2Ca-Na/Ti space the K-feldspar altered rocks plot close to or the on the K-feldspar control line (Fig. 2-8B); data that plot high on the K-feldspar control line contain more K-feldspar than points lower on the K-feldspar control line. K-feldspar altered samples overprinted by a white mica–chlorite* assemblage are shifted towards the muscovite control line (Fig. 2-8B). Consistent with PER diagrams, in K /Al vs. Na/Al space most K-feldspar altered rocks overlap with the least altered rock domains (Fig. 2-8C). In Guichon and Chataway granodiorite, however, a few samples plot parallel to the K-feldspar-plagioclase tie-line towards the K-feldspar node, and have low Ca/Al.

A few K-feldspar altered rocks hosted by Guichon and Chataway granodiorite plot above the least altered rock domain and have high Rb/Sr and low Rb/Ba (Fig. 2-9). In the other host rocks, however, the K-feldspar facies is indistinguishable from least altered and prehnite–(white-mica–chlorite) facies rocks using Sr-Ba-Rb (Fig. 2-9). The K-feldspar facies, however, can be discriminated based on elevated Cu concentrations (i.e., >100 ppm in Bethsaida) and generally high K/Th values compared to the least altered rocks (Fig. 2-10).

K-feldspar altered rocks hosted in Guichon or Chataway granodiorite gained 3.7 g/100g SiO_2, 1.1 g/100g K_2O, and minor H_2O (Fig. 2-11A). Alteration caused a loss of 1.6 g/100g CaO and 0.3 g/100g MgO (Fig. 2-11A). Bethlehem and Skeena units have a similar element gain and loss response compared to the mafic rocks but with greater loss of Fe_2O_3, at 0.3 g/100g (Fig. 2-11B). In the Bethsaida granodiorite, the most common host to K-feldspar fracture halo facies, there is less K_2O (0.2 g/100g) added but still a significant gain in SiO_2 at 2.3 g/100g (Fig. 2-11C). In the Bethsaida granodiorite a gain in Ba (82 ppm), Cu (371 ppm), and Ag (103 ppb), and minor loss of Mn (57 ppm), and possibly some Sr (8 ppm) and Zn (8 ppm) occurs with K-feldspar alteration (Fig. 2-11D). No significant addition of calcite or H_2O occurred during K-feldspar alteration (Table 2-2).

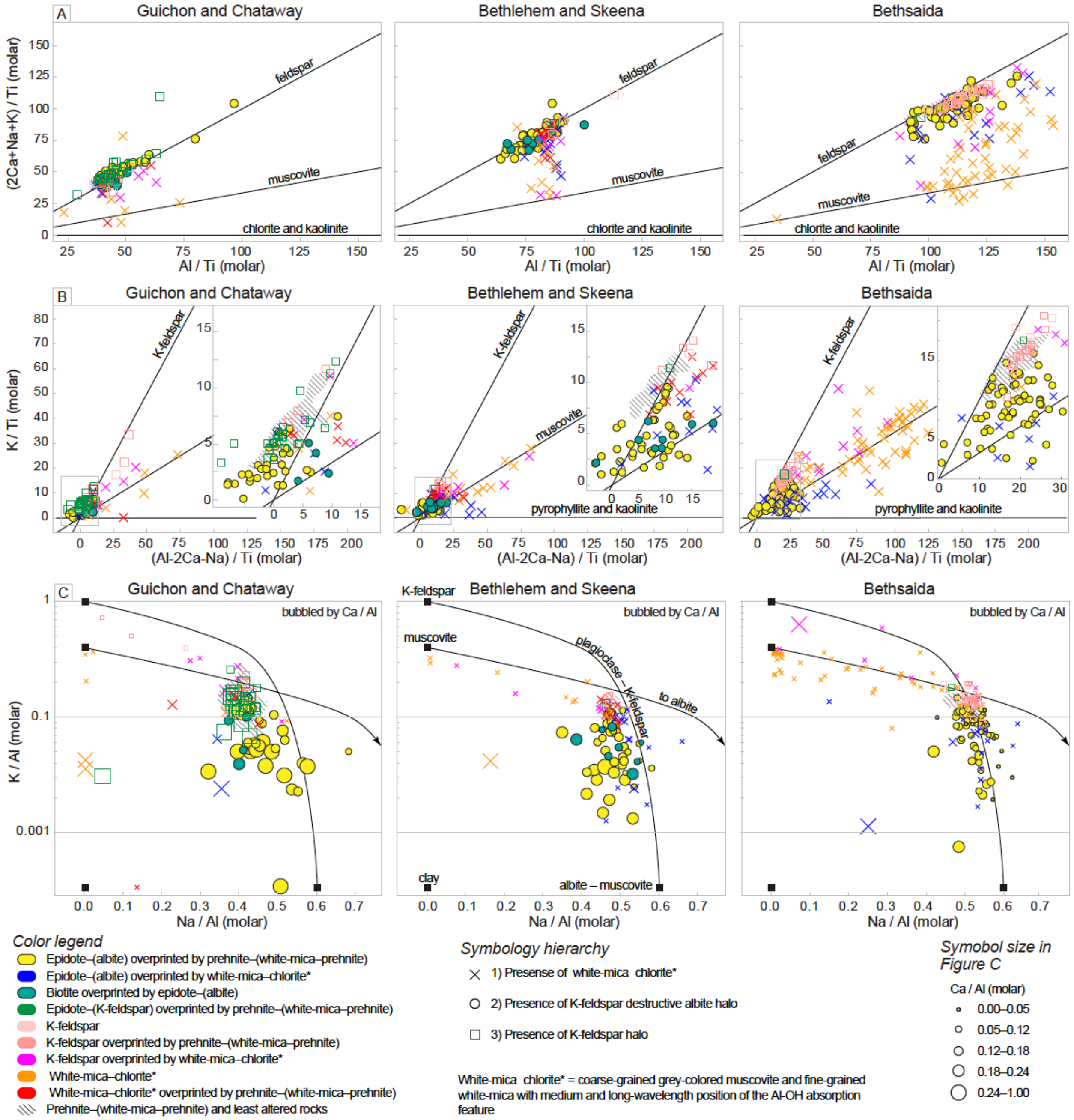

Figure 2-8. PER and GER diagrams for Guichon and Chataway, Bethlehem, and Bethsaida host rocks. A. 2Ca+Na+K / Ti vs. Al / Ti. Mineral control lines are indicated for feldspar, muscovite, and chlorite-kaolinite. B. K / Ti vs. Al-2Ca-Na / Ti. Mineral control lines shown for K-Feldspar, muscovite, and pyrophyllite and kaolinite (projected from anorthite and albite). C. K /Al (log-scale) vs. Na/Al (modified after Davies and Whitehead, 2006). Tie-lines indicate mixing between mineral and mineral-mix nodes. Symbol size indicates the Ca / Al (molar) value. Epidote-(albite) altered rocks are characterized by destruction of K-feldspar, low K/Ti, elevated Na/Al, elevated Ca/Al in mafic host rocks, and a shift towards an end-member composition of albite or an albite–muscovite mix.

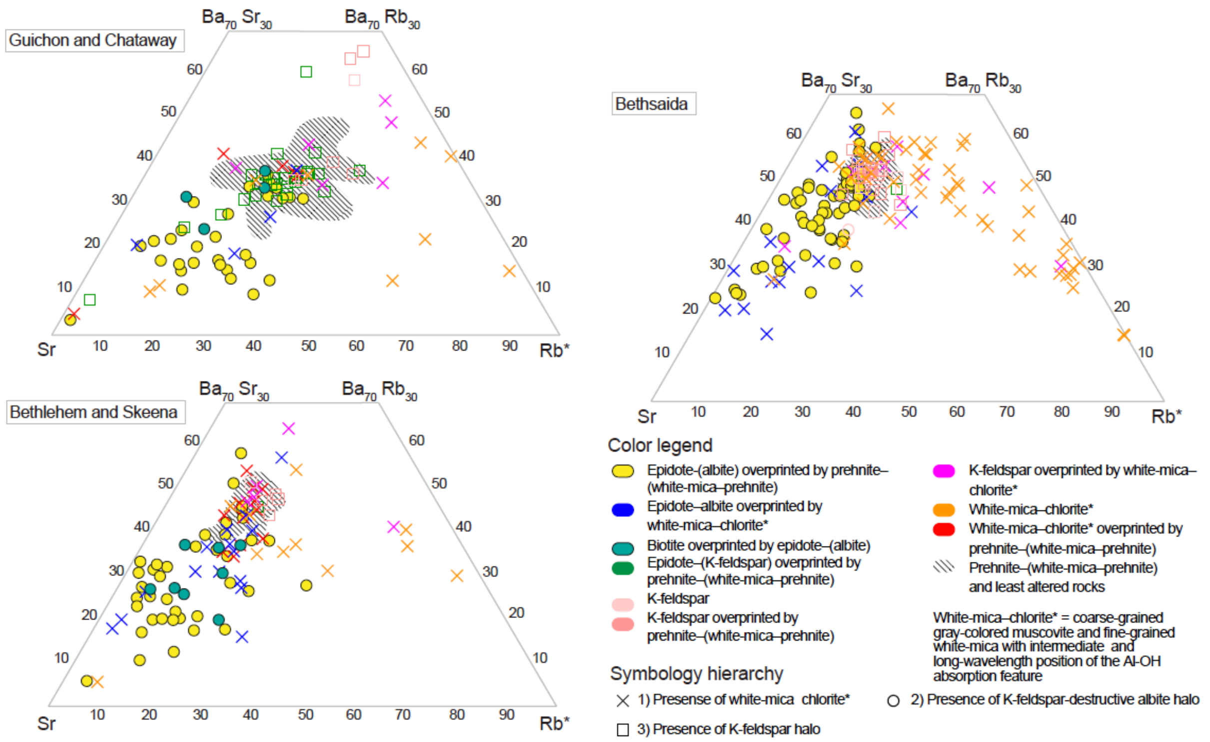

Figure 2-9. Strontium-Ba-Rb ternary diagrams for Guichon and Chataway, Bethlehem, and Bethsaida host rocks. Albite altered rocks show a shift towards high Sr/Ba and Sr/Rb, whereas rocks with white-mica–chlorite* alteration have high Rb/Ba and low Sr/Rb. Prehnite–(prehnite–white-mica) and least altered rocks, and most K-feldspar altered rocks, plot in the same location within the Sr-Ba-Rb ternary system, per host rock group. Albite altered rocks overprinted by white-mica–chlorite* have a range of values but appear to preserve a high Sr/Ba signature.

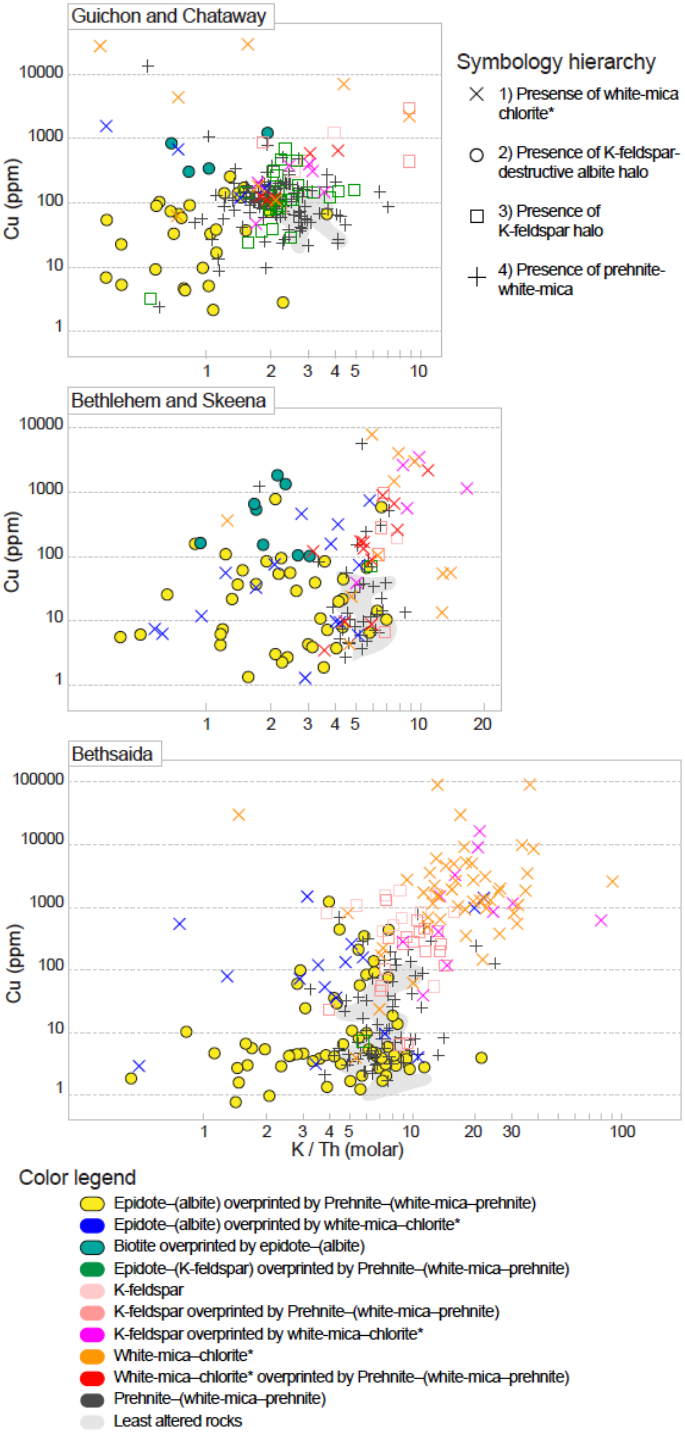

Figure 2-10. Copper concentrations vs. K / Th for Guichon and Chataway, Bethlehem, and Bethsaida host rocks. The epidote-(K-feldspar) alteration facies is predominantly associated with the more mafic host rocks (Guichon and Chataway) and is not elevated in Cu or K/Th relative to least altered rocks, and prehnite–(prehnite–white-mica) facies. K-feldspar alteration facies in Bethsaida partially overlaps with the least altered and prehnite–(prehnite–white-mica) field but some samples extend towards higher K /Th and correspond to samples with high K / Al in Fig. 2-9. Additionally, rocks with K-feldspar halos and no epidote vein fill are distinguished by elevated Cu contents. White-mica–chlorite* altered samples have high K/Th and generally higher Cu than the other facies, the inverse is true for epidote–(albite) facies in each host rock.

Carbon isotopes: The C isotope composition of four K-feldspar altered rocks was analyzed. The sample labelled C in Figure 2-6 (2015KB208; Supplemental data 2-C) is K-feldspar altered but is overprinted by intense prehnite-(white-mica) alteration and contains 0.42 wt. % calcite. Excluding sample 2015KB208, K-feldspar alteration has a mean $\delta^{13}C$ value -22.9 ‰ (Fig. 2-6; Table 2-3).

2.6.2 Epidote–(albite): sodic-calcic

Petrography / mineralogy: Epidote veins with K-feldspar-destructive albite halos compose the epidote-(albite) alteration facies (Fig. 2-7B). Altered feldspars are porous and typically contain inclusions of fine-grained white-mica (Table 1; Byrne et al., 2017). Within albite halos primary mafic minerals are replaced by chlorite with accessory titanite and lesser actinolite (Table 2-1; Byrne et al., 2017). At Valley-Lornex and Highmont, albite alteration is cross-cut by bornite-bearing quartz–coarse-muscovite EH veins (Table 2-1). Calcite veinlets cross-cut re-fractured epidote-(albite) facies veins (Figs. 2-12A and B). Around Valley-Lornex in Bethsaida, epidote–(albite) facies is cross-cut by prehnite veinlets and overprinted by prehnite–(white-mica–chlorite) alteration of varying intensity (Table 2-1; Byrne et al., 2017).

Mapped distribution: Domains of epidote veins (> 1.25 cm/m) with K-feldspar-destructive albite halos have a non-concentric distribution in the GCB (Fig. 2-2A). Epidote-(albite) facies forms a narrow, structurally controlled, ~0.5–1.5 km-wide, north-northeast-elongated domain that that is up to ~8 km long in the northeast portion of the batholith, whereas it forms a ~ 3 km wide domain that extends for ~ 7 km south of Lornex and Highmont (Fig. 2-2). Additionally, actinolite alteration of primary mafic minerals is more common in epidote-(albite facies) within ~500 m of the Highmont and Lornex porphyry centers primary, elsewhere the mafic minerals are more commonly replaced by chlorite. Some isolated domains of epidote–(albite) facies occur in mafic Border facies rocks. At a vein density > 1.25 cm/m the total of area epidote-(albite) facies is ~34 km^2. At the Bethlehem porphyry center albite alteration occurs beneath the breccias overprinting biotite alteration and Cu mineralization (Byrne et al., 2017), in some structures and in some post-mineralization stocks.

PER, MER, mobile element, and volatile characteristics: Epidote-(albite) altered rocks mostly plot on the feldspar control line overlapping with the least altered rocks (Fig. 2-8A). In Bethsaida, however, numerous albite altered samples are shifted towards the muscovite control line (Fig. 2-8A). Albite altered rocks plot beneath the least altered domains on, or close to, the K-feldspar control line (Fig. 2-8B). Epidote-(albite) facies that have been overprinted by white-mica–chlorite* plot on the muscovite control lines, but at low K/Ti values (blue colored X symbol; Figs. 2-8A and B). Variation in the proportions of K-feldspar, muscovite, and kaolinite in epidote-(albite) facies in Bethsaida granodiorite at low K/Ti values is evident (Fig. 2-8B). In the Guichon and Chataway granodiorites, epidote-(albite) altered rocks have elevated Ca/Al relative to the least altered domain, which is interpreted to be caused by the addition of epidote (Fig. 2-8C). Secondary biotite ± K-feldspar ± bornite alteration is cross-cut by albite at some localities in the Bethlehem porphyry center; these rocks have a major element geochemical signature similar to other epidote–(albite) facies samples.

Albite altered rocks form arrays in Sr-Ba-Rb space that extend from least altered host rock compositions towards high Sr/Ba and low Rb/Sr (Fig. 2-9). Similarly, albite altered rocks that were overprinted by white-mica–chlorite* plot in the same field as the epidote-(albite) facies. The high Sr/Ba response corresponds to samples with low K/Al and high Na/Al. Epidote-(albite) facies rocks exhibit a wide range of K/Th that partially overlap with the least altered rocks, but overall have lower K/Th and Cu contents (Fig. 2-10).

Isocon diagrams for epidote–(albite) and white-mica–chlorite* altered Guichon granodiorite (Table 2-4; Fig. 2-13) exhibit Al_2O_3, TiO2, P_2O_5 and Zr concentrations with constant ratios and form a line that projects back to the origin indicating that these elements were conserved during alteration (Fig. 2-13). Zirconium concentrations are more variable in mafic host rocks compared to the felsic ones (Table 2-2), which is likely why Zr deviates slightly from the conserved line for the paired Guichon samples (Fig. 12-3A). Epidote–(albite) alteration in mafic rocks (Fig. 2-11A) exhibits a higher magnitude of major element gains and losses than in the more felsic rocks (Figs. 2-11B and C); this can be observed in the changes Fe_2O_3 and K_2O concentrations. In Guichon granodiorite epidote–(albite) alteration is highly depleted in Fe_2O_3, K_2O, Ag, Au, Ba, Rb, and Li; moderately depleted in Cu, Co, Fe_2O_3, Ni, Pb, and K_2O; and has minor depletion in MgO, CaO, Ce, and Sr concentrations (Fig. 2-13A). In the Bethsaida granodiorite a loss of 0.6 g/100g K_2O, 0.2 g/100g CaO, and 234 ppm Ba, and a gain of 0.2 g/100g Na_2O, 0.9 g/100g SiO_2 and 45 ppm Sr characterizes the median epidote–(albite) alteration response (Figs. 2-11C and E). Epidote–(albite) facies show a gain in H_2O of 0.8 g/100g and 0.5 g/100g calcite in Bethsaida granodiorite (Fig. 2-11C). A similar enrichment in H_2O and calcite for epidote-(albite) facies is indicated in the isocon diagram for Guichon granodiorite (Fig. 2-13A). The K_2O wt. % probability distribution of epidote-(albite) altered Guichon and Chataway granodiorite is considerably lower relative to the probability curve for least altered samples (Fig. 2-14A). A depletion in Fe_2O_3 (Fig. 2-14B is also evident in epidote-(albite) facies relative to least altered samples, but their SiO_2 concentrations are similar (Fig. 2-14C). The probability distribution of Cu in epidote-(albite) samples is lower, and so is the Zn to a lesser extent, relative to least altered samples (Fig. 2-14D and E). The Pb populations, however, are similar for both facies and have a low concentration (Fig. 2-14F).

Calcite and calculated H_2O content generally increase together in altered Skeena and Bethsaida granodiorites that host the Valley-Lornex and Highmont porphyry systems (Fig. 2-15). Least altered Skeena and Bethsaida granodiorite samples predominantly contain <0.2 wt. % calcite, and have calculated H_2O values ranging between 0.25 and ~1.75 wt. % (Fig. 2-15). Numerous epidote–(albite) samples plot within the least altered rock field (Fig. 2-15). A sub-set of epidote–(albite) altered rocks extend to higher values of calcite, H_2O, and to 2CNK/Al values <0.9 (Fig. 2-15). The spatial significance of these samples will be presented below.

Carbon isotopes: Epidote–(albite) alteration has a wide range of $\delta^{13}C$ values between approximately -25 and -5‰, and median and mean $\delta^{13}C$ values of -9.1 and -10.5‰, respectively (Fig. 2-5; Table 2-3). The average calcite content of this facies is 0.77 wt. % (Table 2-3).

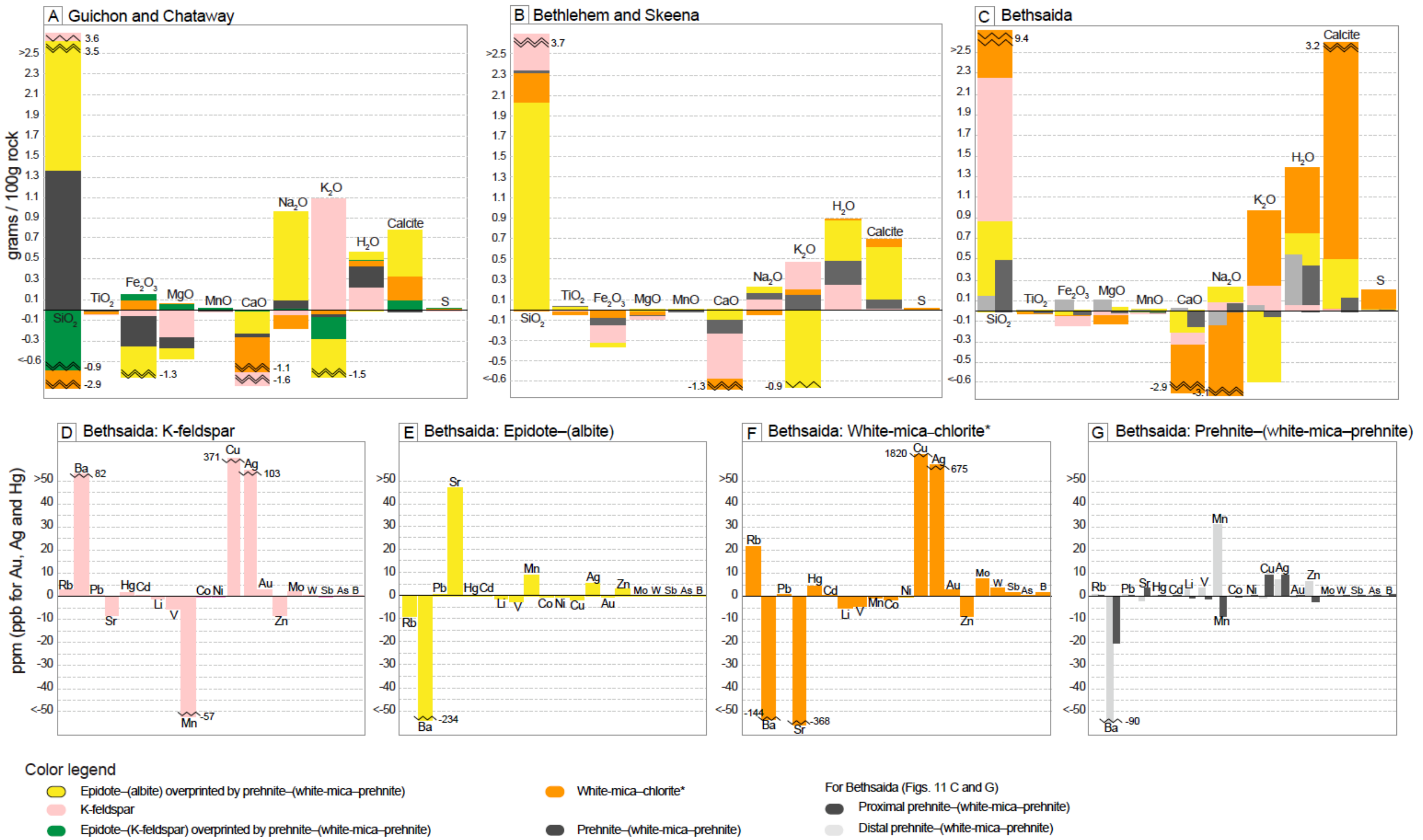

Figure 2-11. Elemental gain and loss diagrams for the main alteration facies in the A. Guichon and Chataway; B. Bethlehem, and C. Bethsaida intrusive phases. Median element values for each protolith (fresh rock) and alteration facies population were used in the calculations with Al as the conserved element. Major element gains and loss expressed as grams per 100 gram of rock. D-G. Minor and trace element gains and loss for alteration facies hosted in Bethsaida granodiorite. Changes are expressed in ppm, except for ppb for Au and Ag.

2.6.3 Quartz–(muscovite) and white-mica–chlorite: White-mica–chlorite*

Petrography / mineralogy: Coarse-grained (~0.3-1.5 cm) gray colored muscovite, with a mostly short-wavelength Al-OH feature, typically occurs in the halos of quartz ± chalcopyrite and bornite veins (quartz-(muscovite) / EH veins; Table 2-1; Fig. 2-3C). Pervasive, selectively pervasive, and fracture controlled fine-grained (< 1 mm) white-mica with intermediate-wavelength Al-OH features compose white-mica–chlorite alteration (Table 2-1; Fig. 2-7D). Veinlets of Cu-Fe-sulfide are intimately associated with white-mica–chlorite alteration (Table 2-1). In this paper, quartz–(muscovite) and white-mica–chlorite alteration facies are grouped together as “white-mica–chlorite alteration*” because of their mineralogical similarity and close spatial association to mineralization in the porphyry Cu centers (Table 2-1). Calcite most commonly occurs as micro-veinlets with white-mica–chlorite* alteration but also formed irregular blebs in well mineralized Cu-rich veins, and in clay-altered fault zones (Table 2-1). Additionally, carbonate is locally inter-grown with fine-grained white-mica, chlorite, and Cu-Fe-sulphide in white-mica–chlorite* alteration halos (Figs. 2-12C and D). Variable amounts of kaolinite and montmorillonite typically overprint relict feldspars outside of white-mica–chlorite* alteration halos within the Cu centers (i.e., intermediate argillic alteration; Table 2-1).

Mapped distribution: Quartz-(muscovite) facies occurs with the main-stage Cu mineralisation at Valley-Lornex and locally at Highmont (Table 2-1; Fig. 2-2). White-mica–chlorite alteration occurs with sulfide mineralization at Bethlehem, J.A., and Highmont, and on the fringes and overprinting quartz–(muscovite) domains at Valley and Lornex (Table 2-1; Fig. 2-2). The distribution of white-mica–chlorite* alteration is overall limited to the sulfide-bearing and well mineralized domains within the porphyry Cu centers, but is recognized in narrow (1–10m) zones at several Cu-occurrences (Fig. 2-2).

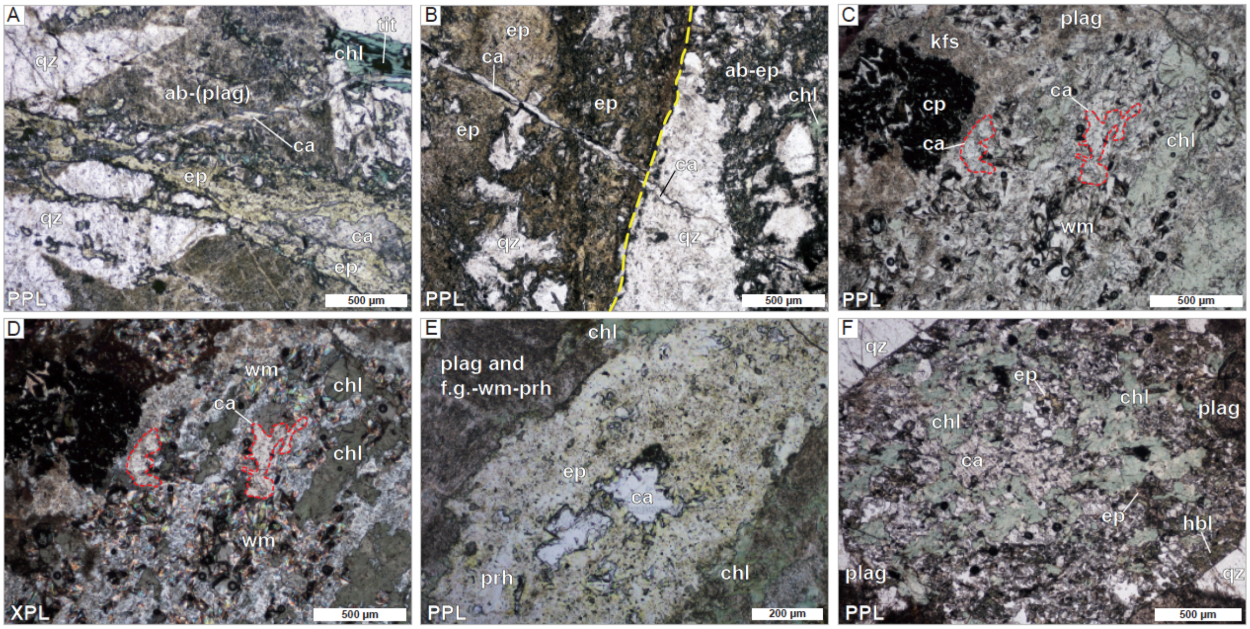

Figure 2-12. Photomicrographs of calcite paragenesis in altered rocks. A. Calcite veinlet cross-cutting and occluding an epidote vein with an albite and chlorite halo. B. Calcite cutting epidote-(albite) vein. The yellow dashed line indicates the epidote vein wall boundary. C. Calcite occluding an epidote vein with a prehnite–fine-grained–white-mica halo associated with prehnite–(prehnite–white-mica) alteration. Note the turbid feldspar in plane polarized light (PPL) is due to porosity and fine-grained secondary mineral inclusions. C. Calcite inter-grown with well-developed white-mica–chlorite alteration and chalcopyrite mineralization associated with white-mica–chlorite* alteration facies. D. Cross-polarized light view of Fig. 2-12C. E. Hornblende phenocryst replaced by chlorite, calcite and epidote associated with the prehnite–(prehnite–white-mica) alteration facies. Mineral abbreviations: Mineral abbreviations: ab = albite, bn = bornite, ca = calcite, cp = chalcopyrite, chl = chlorite, ep = epidote, f.g. = fine-grained, kfs = K-feldpsar, musc = muscovite, plag = plagioclase, prh = prehnite, qz = quartz, tit = titanite, wm = white-mica.

PER, MER, mobile element, and volatile characteristics: Samples identified as being white-mica–chlorite* altered plot between the feldspar and muscovite control lines— the slope of the line between the datum and the origin corresponds directly to the amount of white-mica in the sample (Fig. 2-8A). White-mica–chlorite* facies have a wide range of K/Ti values along the muscovite control line (Fig. 2-8B), and plot towards the muscovite node along the muscovite–albite tie line (Fig. 2-8C). Higher K/Al values correspond to lower Na/Al and Ca/Al values in white-mica–chlorite* facies, which is essentially the inverse of epidote-(albite) alteration (Fig. 2-8C). There appears to be substantial K, Ca, and Na transfer associated with some white-mica–chlorite* alteration.

Rocks affected by white-mica–chlorite*alteration have higher Rb/Sr and higher Rb/Ba than least altered and prehnite–(white-mica–chlorite) altered rocks (Fig. 2-9). This facies is further distinguished by elevated K/Th (Fig. 2-10).

White-mica–chlorite* altered rocks are characterized by loss of CaO, variable gains in K_2O, and some S addition (Figs. 2-11A-C). In the Bethsaida granodiorite, the main host to the Valley-Lornex system, the median response is a gain of 9.4 g/100g SiO_2, 3.2 g/100g calcite, 1.4 g/100g H_2O, 1 g/100g K_2O, 1820 ppm Cu, and a loss of 2.9 g/100g CaO and 144 ppm Ba (Fig. 2-11C and F). Sample 2014GL173 is of white-mica–chlorite* facies and corresponds to the rock shown in Figure 2-7C. This quartz-(muscovite) sample is strongly enriched in Cu, W, Bi, Mo, calcite, Au, Pb, Sb, As, H_2O, and weakly enriched in Rb, SiO_2, and K_2O (Table 2-4; Fig. 2-13B). Calcium oxide and Ba are strongly depleted, and Sr, Zn, Li, Na_2O are moderately depleted in the coarse muscovite altered sample (Fig. 2-13B).

Samples with 2CNK/Al values <0.85 are dominantly associated with white-mica–chlorite* halos and calcite and H_2O in excess of ~2 and 1.0 wt. %, respectively (Fig. 2-15).

Carbon isotopes: White-mica–chlorite* facies have $\delta^{13}C$ values mostly > -7.5 ‰ (Fig. 2-5A). The sample labeled D in Figure 5 (2234425; Highland-1; Supplemental data 2-C) is a tourmaline vein with white-mica-chlorite halo* in the Bethlehem North Cu occurrence area, but it is isolated and appears unrelated to the HVC porphyry centers (see Fig. 2-2B). Excluding this outlier from Bethlehem North, the white-mica–chlorite* facies have an average $\delta^{13}C$ value of -5.9 ‰ and contain 3.4 wt. % calcite (Table 2-3).

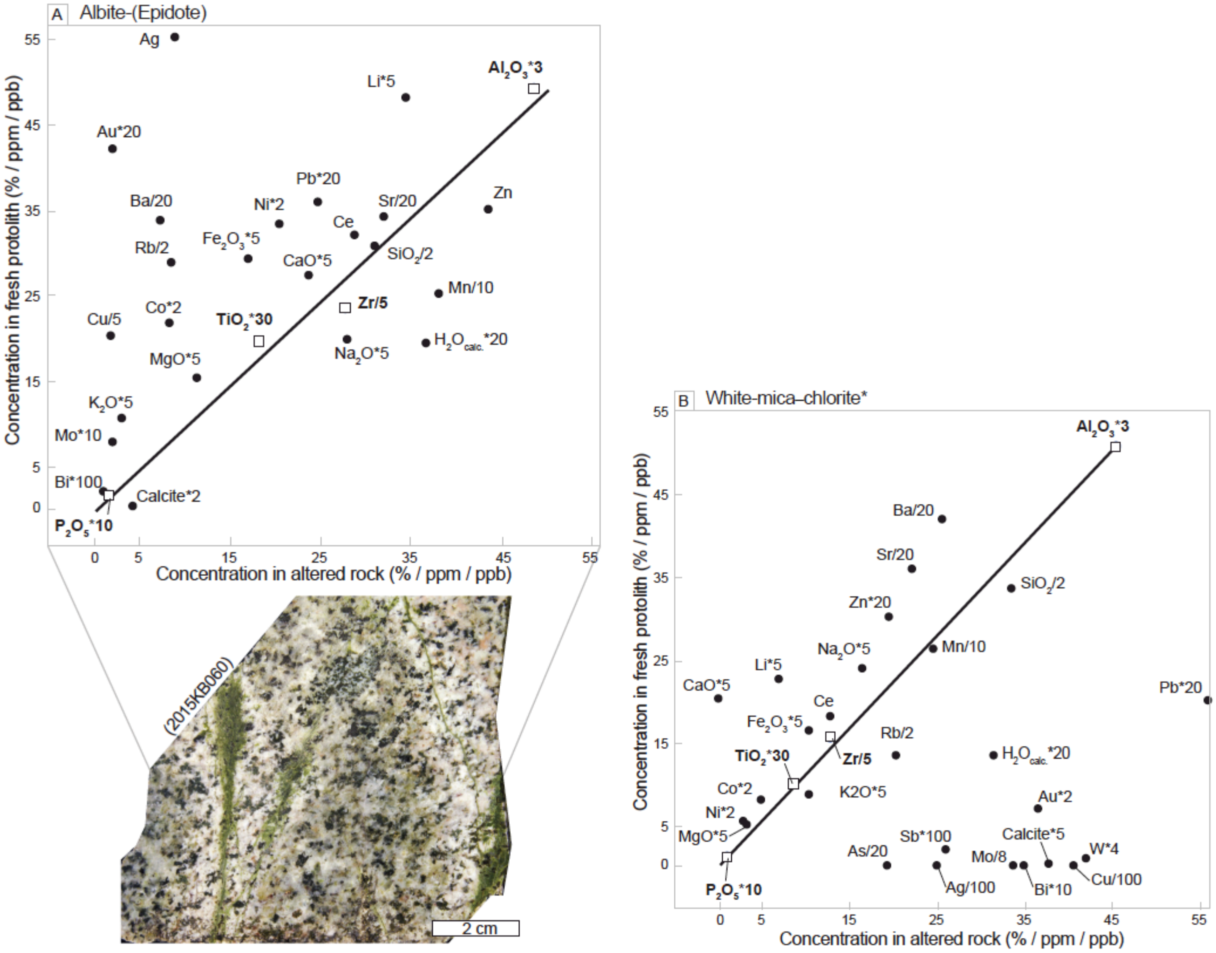

Figure 2-13. Isocon diagrams with selected and weighted elements in which the protolith versus the altered samples are plotted (after Grant 1986). A. Epidote–(albite) altered Chataway (sample 2015KB60 shown). B. Quartz-muscovite altered (white–mica-chlorite* facies) Skeena (sample 2014GL173 in Fig. 2-7D). Elements plotting above the conservation line are depleted in the altered rock, whereas elements below the line are enriched relative to the protolith.

Table 2-4. Samples pairs used in the isocon diagrams in Figure 2-13

Sample	2015KB019	2015KB060	2014GL173	2013MD035
Rock name	Guichon	Guichon	Skeena	Skenna
Alteration	Least altered	Epidote-albite	Least altered	White-mica-chlorite*
SiO_2 (wt. %)	61.15	62.00	66.87	67.00
Al_2O_3	16.33	16.28	16.86	15.17
Fe_2O_3	5.83	*3.43*	3.27	*2.07*
MgO	3.05	*2.30*	1.00	0.68
CaO $_{(total)}$	5.49	**5.99**	4.08	3.51
Na_2O	3.92	**5.59**	4.78	*3.32*
K_2O	2.10	*0.60*	1.74	**2.08**
TiO_2	0.65	0.61	0.33	0.29
P_2O5	0.15	0.16	0.12	0.12
MnO	0.09	0.07	0.07	0.03
Calcite*	0.08	**2.17**	0.08	**7.58**
$CaO^*_{residual}$	5.44	*4.78*	4.03	0.00
H_2O^*	0.96	**1.84**	0.66	**1.58**
Ba	673	*145*	835	*512*
Rb	57.5	*17.1*	26.8	40.7
Sr	682.7	*643.8*	715	*445.9*
W	0.5	1	0.25	**10.5**
Zr	117	138.8	77.2	64
Ce	32	28.8	18	12.8
Mo	0.8	0.2	0.5	**270.6**
Cu	100.8	*9.2*	17.0	**4064.3**
Pb	1.79	1.24	1	**2.81**
Zn	35	**43.7**	30	**19.6**
Ag (ppb)	55	*9*	15	**2504**
Ni	16.6	*10.3*	2.7	1.5
Co	10.8	*4.2*	4	2.5
Mn	250	**381**	262	*247*
As	1.1	**9.5**	0	**388.1**
Au (ppb)	2.1	*0.1*	3.5	**18.3**
Sb	0.05	**0.72**	0.02	**0.26**
Bi	0.02	0.01	0.01	**3.5**

Text in bold indicates elements that were gained and text in italics that were lost.
* = calculated terms

2.6.4 Epidote–(K-feldspar): propylitic

Petrography / mineralogy: Epidote–(K-feldspar) alteration facies comprise epidote veins with weakly developed K-feldspar ± epidote halos and selective replacement of mafic minerals by chlorite (Fig. 2-7F; Table 2-1; Fig. 2-2B). Primary K-feldspar appears stable within the halos. Minor prehnite occurs inter-grown with epidote in some veins, whereas pumpellyite is a late or cross-cutting phase. Additionally, some veins exhibit zoned halos of inner K-feldspar and outer white-mica alteration. Calcite does not commonly occur with epidote–(K-feldspar) alteration.

Mapped distribution: Epidote–(K-feldspar) altered rocks are restricted to the more mafic host rocks (i.e, Guichon and Chataway granodiorite) towards the margin of the batholith (Fig. 2-2B).

PER, MER, mobile element, and volatile characteristics: Epidote–(K-feldspar) altered rocks plot on the feldspar control line in Guichon and Chataway granodiorite (Fig. 2-8A), but have a variable response that mostly overlaps with the least altered rocks in the other compositional diagrams (Figs. 2-8B and C). There does not appear to be any significant K-transfer or white-mica formation associated with epidote–(K-feldspar) altered rocks.

In terms of Rb-Sr-Ba concentrations, epidote–(K-feldspar) facies are mostly indistinguishable from other alteration facies (Fig. 2-9), though a few samples have high Sr/Ba and low Rb/Sr. Similarly, it is difficult to discriminate the epidote–(K-feldspar) facies from least altered rocks based on K/Th value (Fig. 2-10).

Compared to K-feldspar facies, the median response for epidote–(K-feldspar) veins and alteration in Guichon and Chataway show no significant change in CaO or K_2O. A gain of 0.47 g/100g H_2O, and a loss of ~1 g/100g SiO_2 is apparent (Fig. 2-11A), although the latter change might be an artifact due to the greater background variation of SiO_2 in the fresh host rocks (Table 2-2). There is no significant difference in the trace element composition of the epidote–(K-feldspar) facies compared to the least altered rocks (Table 2-2). Epidote–(K-feldspar) alerted rocks contain on average 0.13 wt. % calcite (Table 2-2).

Carbon isotopes: Epidote–(K-feldspar) alteration facies have a wide range in $\delta^{13}C$ values between -25 ‰ and -11 ‰ and a mean value of -17 ‰ (Table 2-3).

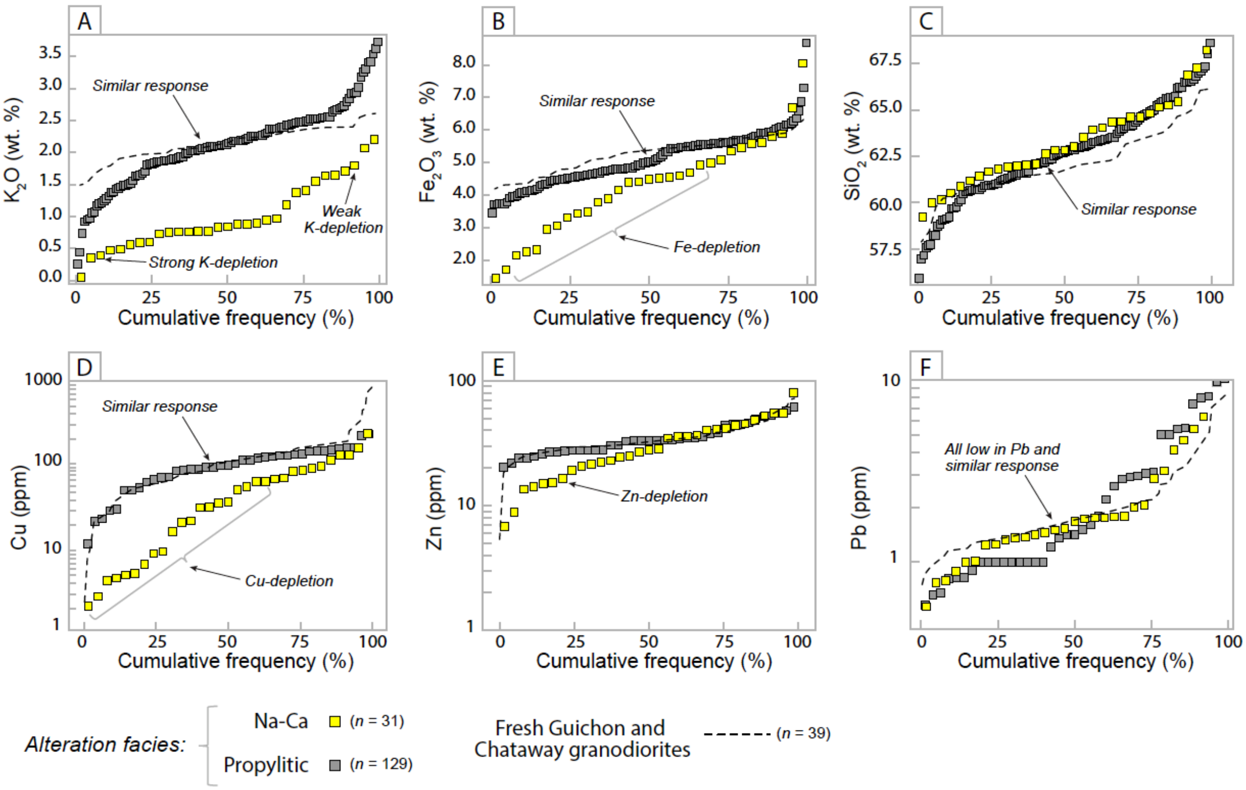

Figure 2-14. Compositional cumulative frequency plots for least altered, epidote-(albite), and prehnite–(prehnite–white-mica) alteration facies in Guichon and Chataway granodiorite. A. K_2O, B. Fe_2O_3, C. SiO_2. D. Cu. E. Zn. F. Pb.

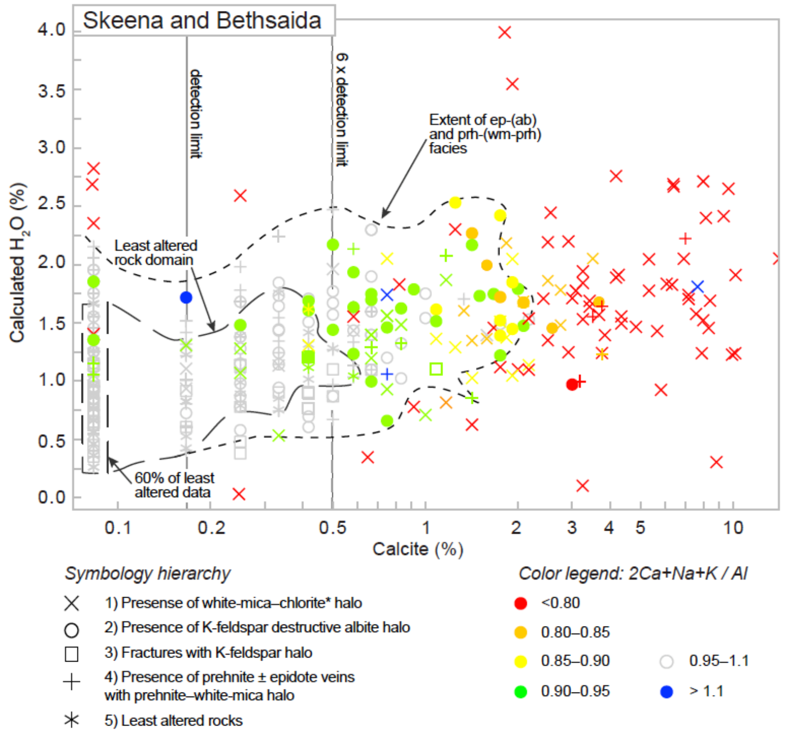

Figure 2-15. Calcite (%) vs. calculated H_2O (%) for Skeena and Bethsaida granodiorites. Data are symbolized by the associated rock slab alteration (shape) and 2CNK/Al value (color).

2.6.5 Prehnite–(white-mica–chlorite): propylitic

Petrography / mineralogy: Veinlets of prehnite ± epidote and calcite with plagioclase-destructive white-mica–prehnite halos compose the prehnite–(white-mica–chlorite) facies (Fig. 2-7F). White-mica in the halos of prehnite ± epidote veins mostly have a short-wavelength Al-OH feature. Mafic minerals are weak to moderately altered to chlorite ± carbonate, prehnite, and vermiculite within the halo, but are generally fresh between fractures (Table 2-1). Prehnite–(white-mica–chlorite) alteration overprinted epidote-(albite), and locally cross-cut mineralized veinlets with white-mica–chlorite* halos. In Bethsaida granodiorite, prehnite is more abundant than epidote in veinlets of this facies, compared to the other host rocks (Lesage et al., 2016). Textural relationships indicate that prehnite veinlets mostly cross-cut epidote–(K-feldspar) veins, but are locally coeval. Calcite infills vug spaces (occludes) in some epidote–prehnite veins (Figs. 2-12E) and locally replaced hornblende along with chlorite and epidote in prehnite–(white-mica–chlorite) altered rocks (Fig. 2-12F).

Mapped distribution: Prehnite–(white-mica–chlorite) facies is the most common and widely distributed alteration in the batholith. The highest density of this vein type is centered on the porphyry systems (Fig. 2-2A), but veins also occur out to the margins of the batholith (c.f. Fig. 2-2B).

PER, MER, mobile element, and volatile characteristics: Compositional changes caused by prehnite–(white-mica–chlorite) alteration are within the range of the natural variability for K, Na and Ca, and background white-mica content, in each protolith (Fig. 2-8).

The fields for least and prehnite–(white-mica–chlorite) altered rocks in the Sr-Ba-Rb system are larger for Guichon and Chataway granodiorite compared to the other host rocks (Fig. 2-9). Prehnite–(white-mica–chlorite) alteration is indistinguishable from least altered rocks and most K-feldspar alteration in Bethsaida granodiorite (Fig. 2-9). Similarly, it is difficult to discriminate prehnite–(white-mica–chlorite) facies from least altered rocks based on K/Th, a few examples, however, do have elevated Cu concentrations and high K/Th relative to the least altered domain and albitized rocks (Fig. 2-10).

Addition of 1.35 g/100g SiO_2 and 0.4 g/100g H_2O characterizes the median prehnite–(white-mica–chlorite) hosted in Guichon and Chataway granodiorite (Fig. 2-11A). The probability distributions of K_2O, Fe_2O_3, SiO_2, Cu, Zn and Pb concentration in prehnite–(white-mica–chlorite) and least altered rocks are very similar (Fig. 2-14). In Bethlehem and Skeena granodiorite the gains in H_2O and calcite, 0.5 g/100g and 0.1 g/100g respectively, are minor (Fig. 2-11B). To further assess element changes occurring with prehnite–(white-mica–chlorite) alteration, samples hosted in Bethsaida granodiorite were sub-divided based on distance from the Valley-Lornex Cu center (Figs. 2-11C and G). Samples within 2.5 km of Valley mineralization and 6 km of Lornex are proximal and samples beyond those distances are grouped as distal. The median response of proximal prehnite–(white-mica–chlorite) alteration in Bethsaida granodiorite is a gain of 0.4 g/100g H_2O and 0.13 g/100g calcite, and minor CaO loss of 0.15 g/100g, whereas the distal response shows no change or gain in calcite, and a similar H_2O gain of 0.5 g/100g (Fig. 2-11C). In proximal prehnite–(white-mica–chlorite) alteration there is perhaps very minor gain in Cu (9 ppm) and Ag (9 ppb), and minor Ba loss of 90 ppm, but these values are within one standard deviation of the least altered rock response (Table 2-2).

Numerous prehnite–(white-mica–chlorite) altered samples have calculated H_2O and calcite contents similar to least altered rock composition, but critically a sub-set of samples extend to higher values of both calcite and H_2O and 2CNK/Al values of 0.9–0.85 (Fig. 2-15), the spatial distribution of these samples will be reviewed below.

Carbon isotopes: Prehnite–(white-mica–chlorite) alteration has the widest range in $\delta^{13}C$ values with median and mean $\delta^{13}C$ values of -19.7 and -18 ‰, respectively (Fig. 2-5; Table 2-3), and median and mean calcite content of 0.12 and 0.33 wt. %, respectively (Table 2-3).

2.7 Spatial distribution of alteration intensity and material-transfer

In order to compare the intensity of feldspar-destructive white-mica alteration between the different host rocks in the GCB, the 2CNK/Al value for each sample was normalized to its host rock. The delta values (Δ) between the least altered host rock 2CNK/Al value (Fig. 2-4D) and 1 (the feldspar control line) were subtracted from the 2CNK/Al value for each sample and plotted spatially (Fig. 2-16A). The symbol size in Figure 2-16A is generated from the slope of the line made between the origin and the sample on a (Al-Ca)/Ti versus (Si-2Ca-3Na-3K)/Ti PER diagram (Moss, 2010), in which samples with a value >1.9 likely contain secondary quartz (Appendix 2-C). The porphyry Cu centers have moderate to intense white-mica alteration and quartz addition (Fig. 2-16A). West and SW of the Valley Cu center, quartz addition without significant white-mica alteration forms a ~1 km wide domain. For approximately 5 km S of Lornex and Highmont, weak white-mica alteration and intermittent quartz addition occurs proximal to interpreted structures, but overall the footprint in this area is heterogeneous and subdued (Fig. 16A). Moderately and highly white-mica altered rocks, without quartz addition, can be discerned in rocks up to 1 km NE of Bethlehem. Isolated anomalies of low 2CNK/Al with quartz addition characterize some Cu-occurrences (Fig. 2-16A).

The bubble size in Figure 2-16B is generated from the calculated $H_2O/Ti_{(molar)}$ value. Using Ti (molar) in the denominator has the additional effect of normalizing the data to the host rock composition because the initial mafic mineralogy (i.e., Mg number), and thus the H_2O–OH, content, is proportional to the Ti concentration (Fig. 2-4). Significant calcite and H_2O addition occurs in, and directly adjacent, to the porphyry Cu centers (Fig. 2-16B). The least altered host rocks contain <0.1% calcite (Table 2-2), thus the >0.75 wt. % contoured calcite domain in Figure 2-16B represents an area where significant calcite has been added to the host rocks. Samples with calcite/$Ti_{(molar)}$ >0.85 occur in areas up to 500m west and ~ 2km southwest of the Valley deposit. The response around the Lornex and Highmont deposits is more variegated, and has a range of calcite and H_2O values. Nevertheless, numerous samples within ~6 km of Lornex have calcite/$Ti_{(molar)}$ >0.85 (approximately equivalent to >0.4% wt. % calcite) and elevated $H_2O/Ti_{(molar)}$ that are distinct from the composition of the more distal rocks (Fig. 2-16B). Calcite addition with weak hydration characterizes the domain NE of mineralization at the Highmont deposit, whereas calcite addition at Bethlehem is mostly limited to the Cu zone. Also within the district, there are a few isolated calcite-enriched samples that are spatially associated with structures and some Cu-occurrences (Fig. 2-16B). These isolated anomalies appear disconnected from the response around the HVC porphyry centers described above.

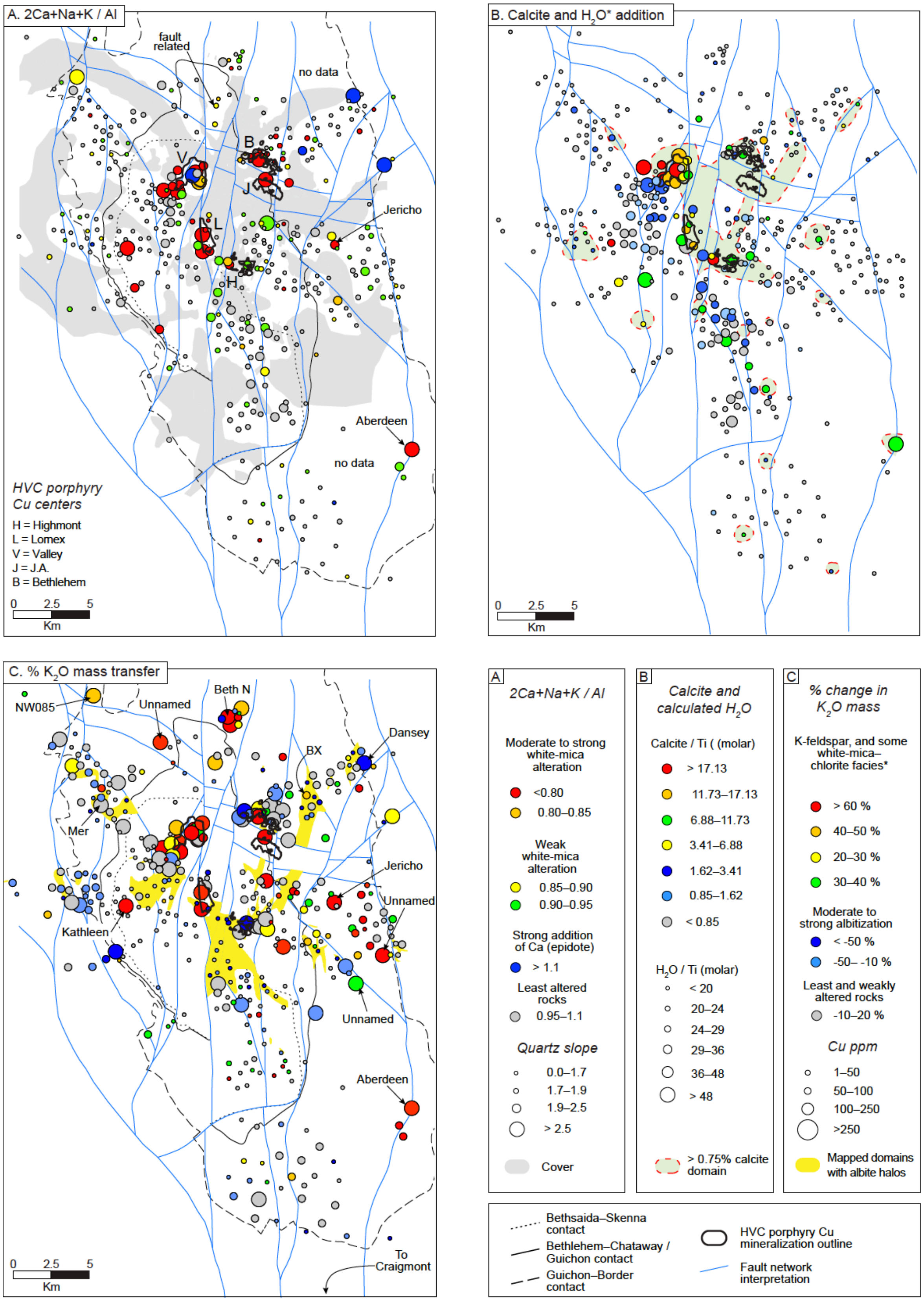

Figure 2-16. Alteration intensity maps. A. Map of (2Ca+Na+K)/Al values normalized per host rock (color) and the (Al-Ca)/(Si-2Ca-3Na-3K) value (symbol size). Warm colors indicate a decrease in slope

angle from the feldspar control line (m = 1) towards muscovite (m = 0.3). An Al-Ca / Si-2Ca-3Na-3K (quartz slope) value of 0 is pure feldspar and 1 is pure quartz, thus an increase in bubble size corresponds to addition of quartz. Fresh Guichon rocks have a quartz slope of ~ 1.9. There is more abundant white-mica and quartz in and around the HVC porphyry systems. At distances >~1.5 km from mineralization white-mica alteration is more restricted to structures (e.g., south of Lornex) B. Calcite/Ti (color) and calculated H_2O/Ti (bubble size) map. Numerous samples within 3km of the HVC porphyry centers are characterized by calcite addition and high H_2O/Ti values. The 0.75 wt. % calcite domain was contoured using all the rock slab characterized samples, and Teck data (Fig. 2-2A). C. Map of % K_2O mass transfer (color) and Cu ppm concentration (bubble size). The K_2O mass transfer value is the change in grams / 100 grams relative to the protolith concentration expressed as a percentage. Addition of K_2O is mostly positively correlated with Cu content. The sample points in all maps were automatically thinned to approximately 400m spacing for clarity.

Mineralization at the Valley deposit is characterized by >30% increase in K_2O relative to least altered Bethsaida granodiorite, whereas the response at Lornex and Highmont is more mixed due to the presence of albite alteration (K_2O-depletion), and because of the structurally controlled distribution of intense alteration (Fig. 2-16C). Potassium addition also occurred in the rocks south of Lornex at the southernmost fringes of the mapped albite halo domain. Transfer of K_2O to the rock is evident at several Cu-occurrences (Fig. 2-16C). The cluster of K_2O-depleted samples west of the Kathleen Cu-occurrence (Fig. 2-16) do not appear to be albite altered (based on feldspar staining) and are interpreted to be a false negative caused by lower initial K_2O in the host rock in this area compared to the least altered median value used in the mass-transfer calculations (Table 2-2). The background Cu concentration in the mafic-rich host rocks at the margin of the batholith is higher, and more varied, than in the inner host rocks (Table 2-2; Fig. 2-16B).

The distribution of whole-rock $\delta^{13}C$ values shows that although variable, altered rocks overlapping with porphyry Cu mineralization and the >0.75 wt. % calcite domains at HVC have $\delta^{13}C$ values greater than -10 ‰ (Fig. 2-17). Critically, however, epidote–(albite), prehnite–(white-mica–chlorite), and a few least altered rocks, with $\delta^{13}C$ values > -10 ‰ occur outboard of Cu mineralization for approximately 6 km, and contrast with the low $\delta^{13}C$ values in more distal expressions of these alteration facies (Fig. 2-17). Isolated outcrops with $\delta^{13}C$ values > -10 ‰ are mostly associated with white-mica–chlorite* alteration at Cu occurrences unrelated to the HVC porphyry centers (Fig. 2-17).

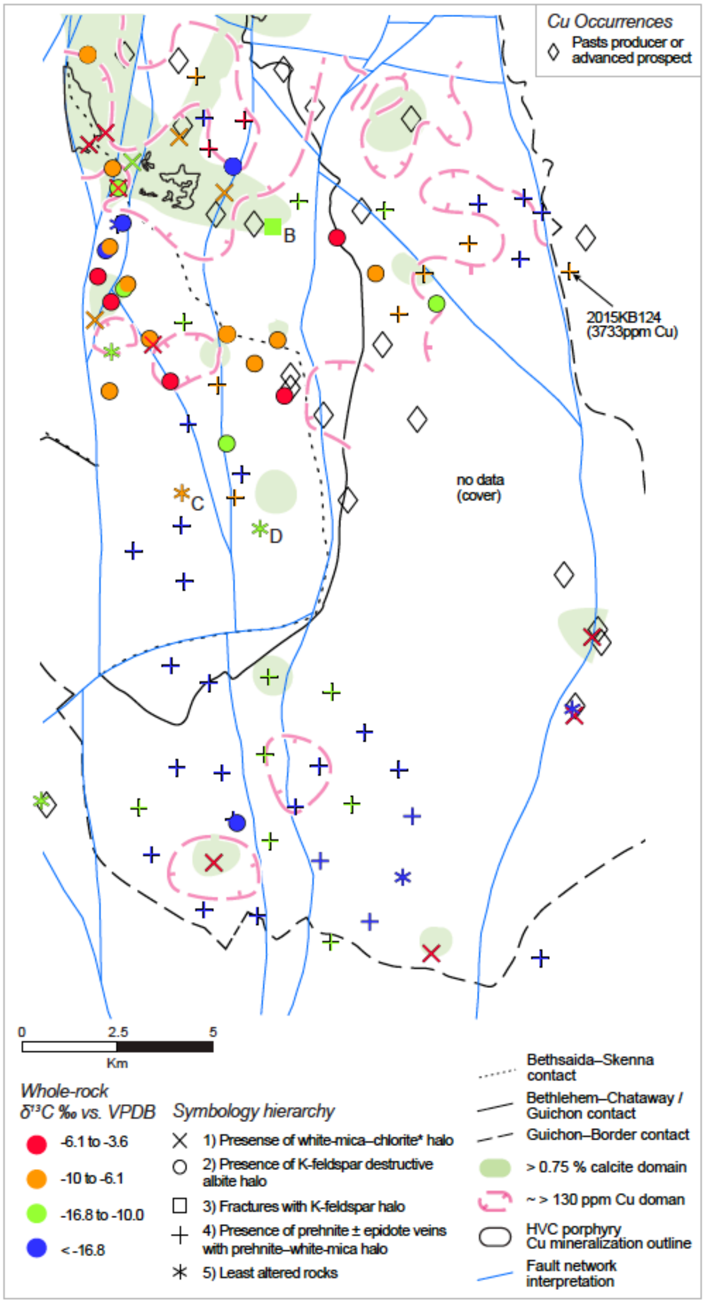

Figure 2-17. Whole-rock $\delta^{13}C$ value (‰) map with 0.75 wt. % calcite and 130ppm Cu ppm contours. Sample labels correspond to the samples indicated in Figure 5A and are explained in the main body text.

2.8 Discussion

2.8.1 Host-rock control on altered rock mineralogy and composition

The ability to predict alteration products and chemical changes during fluid-rock interaction is important for recognizing alteration peripheral to porphyry Cu centers.

Hydrothermal alteration mineralogy is largely dependent on the host-rock bulk composition and the water–rock ratio during exchange (Berger and Velde, 1992; Reed, 1997). Whereas the later can only be inferred, host-rock composition can be estimated. Prehnite is not commonly reported in propylitically altered rocks around porphyry Cu deposits. Exceptions include propylitic alteration in basaltic and andesitic host rocks in the Cadia (NSW, Australia) and Collahuasi (N Chile) districts, respectively (Wilson et al., 2003; Djouka-Fonkwe et al., 2012). Epidote most commonly forms from 350–200°C during propylitic alteration (Bowman et al., 1987; Norman et al., 1991). Prehnite and epidote can coexist over a limited temperature range around 250°C, however, the stability field of prehnite extends down to a temperature of ~150°C, below which zeolites predominate (Bird et al., 1984; Digel and Gordon, 1995; Bird and Spieler, 2004). In the temperate range of 350–200°C the more important control on the stability of epidote and prehnite in the system $CaO-Al_2O_3-Fe_2O_3-SiO_2-H_2O-HCl$ is the activity of Ca, Fe and Si, although high activities of CO_2 in the fluid can inhibit prehnite formation (Wheeler et al., 2001; Bird and Spieler, 2004). At a fixed temperature, the epidote stability field is larger at higher activities of Fe and lower activities of Ca and Si relative to prehnite (Bird et al., 1984; Digel and Gordon, 1995). So, on a mineral-stability basis, and in rocks with similar Ca content, epidote formation is favored in a more Fe-rich wall-rock. This relationship has been observed at HVC where, excluding the epidote–(albite) facies, epidote is more abundant in the hornblende-dominated mafic host rocks (3.3–5.4 wt. % Fe_2O_3; Table 2), and is subordinate to prehnite in the Fe-poor (2.3 wt. % Fe_2O_3; Table 2-2) and biotite-dominated Bethsaida granodiorite (Lesage et al., 2016).

For the sodic-calcic facies, the gain and loss of major rock-forming elements is more pronounced in the mafic Chataway and Guichon granodiorite rather than in the felsic Skeena and Bethsaida granodiorites (c.f., Figs. 2-11A and C; Table 2-2). Similarly, the removal of Cu ± Zn, presumably by chlorite alteration of Cu-bearing primary hornblende, is pronounced in the mafic-rich rocks compared to felsic rocks (Table 2-2). These phenomena are interpreted to be primarily caused by a larger degree of disequilibrium between the composition of the mafic host rocks and the fluids causing the alteration, relative to the contrast between the more felsic rocks and the fluid.

The observations from HVC imply that in Fe-poor and Ca-rich plutonic or volcanic rocks prehnite veinlets can occur in propylitic alteration zones. Additionally, in the case of epidote–

(albite) alteration, the degree of metasomatism may be limited in Fe- and K-poor rocks relative to host rocks rich in these elements.

2.8.2 Interpretation of C isotope compositions

Carbon dioxide is a major component of magmatic-hydrothermal fluids in arcs (Henley and McNabb, 1978; Giggenbach, 1992; Richards, 2011 and refrences therein). In porphyry Cu systems C sourced from magmatic and / or meteoric fluids typically manifests as carbonate minerals in propylitic zones adjacent to porphyry Cu mineralization (Sheppard et al., 1971; Djouka-Fonkwe et al., 2012; Cooke et al., 2014a; Stevenson, 2015). We aimed to test whether whole-rock C-isotope compositions vary as a function of distance from the HVC porphyry centers (i.e., Fig. 2-17)– by what process this occurs, and whether this technique can be used to identify propylitic alteration associated with porphyry Cu deposits.

Djouka-Fonkwe et al. (2012) demonstrated that the hyperbolic relationship between $\delta^{13}C$ values and C content is caused by mixing of variable proportions of two isotopic sources: 1) carbon that remains in solidified CO_2-degassed intrusive and extrusive rocks that is equivalent to dissolved trace C extracted at low-temperatures (<600°) from MORB glasses (Pineau and Javoy, 1983; Taylor, 1986); and 2) deep-sourced magmatic or mantle CO_2, that is equivalent to the C extracted at high temperatures from MORB glasses (Des Marais and Moore, 1984). Furthermore, Djouka-Fonkwe et al. (2012) show that the degassed whole-rock $\delta^{13}C$ values are largely independent of rock composition, but may relate to emplacement depth. A two-source, concentration dependent, isotopic mixing model was calculated using the following equation (Faure and Mensing, 2005; Djouka-Fonkwe et al., 2012):

$$\delta_M = \delta_X f_X(C_X/C_M) + \delta_Y f_Y (C_Y/C_M), \text{ where } f_Y = 1 - f_X, \qquad \text{(Eq. 2)}$$

where δ_M is the isotopic composition of the mixture, δ_X and δ_Y are the isotopic compositions of the sources X and Y, f_X and f_Y are the proportions of end-members' X and Y in the mixture; and C_X/C_M and C_Y/C_M are the concentration fractions contributed by sources X and Y in the mixture, respectively (Fig. 2-18). The composition of X is that of least altered plutonic rocks in the GCB and in the Collahuasi district (Fig. 2-18), which have $\delta^{13}C$ values of -30 to -20 ‰ and have low total C (Djouka-Fonkwe et al., 2012). The $\delta^{13}C$ value of the magmatic volatile phase (MVP), Y (Fig. 2-18), is based on the composition of white-mica–chlorite* altered rocks and is close to the average C-isotope composition of magmatic CO_2 ($\delta^{13}C$ = -5 ‰; Taylor, 1986; Djouka-Fonkwe et al., 2012). Whereas the concentration of C in MVP, ~1 wt.% (Fig. 2-18), is based on the correlation between C and $\delta^{13}C$ values and the fit of the mixing model curve. In mixtures with an MVP mass fraction of 8–15 %, altered rocks generally contain about 0.85 wt. % calcite and have magmatic-CO_2 dominated $\delta^{13}C$ values greater than ~ -6.5 ‰ (Fig. 2-18). In mixtures with an MVP mass fraction of just 3–5 %, however, altered rocks generally contain <0.4 wt. % calcite yet have $\delta^{13}C$ values between -12 and -8 ‰, approximately twice that of the least altered rock average (Table 2-3) and of the C isotope compositions at lower MVP mass fractions (Fig. 2-18). Thus, the whole-rock $\delta^{13}C$ determinations are a more sensitive measure of the flux of magmatic fluids than the total C added to the rock as calcite. The implications are that low-levels of CO_2-bearing MVP flux can be detected by analyzing whole-rock $\delta^{13}C$, and that the C-isotope composition of propylitically altered rocks adjacent porphyry Cu mineralization can be discriminated from regional or background propylitic facies (e.g., Fig. 2-17).

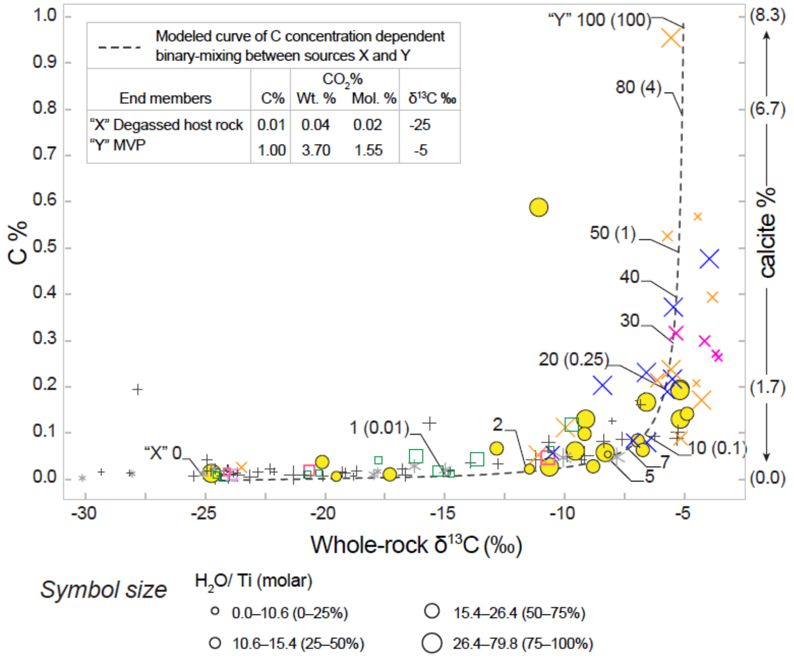

Figure 2-18. Carbon % vs. whole-rock δ^{13}C value and modeled mixing curve between "X' degassed igneous host rock and "Y" magmatic CO_2 in magmatic volatile phase (MVP) modified after Djouka-Fonkwe et al. (2012). Tick marks represent % mass fraction of MVP in the mixture with ~water-rock ratio in parenthesis.

2.8.3 Fluid sources and material-transfer

Most K-feldspar altered samples in Guichon, Chataway, Bethlehem and Skeena host rocks overlap with least altered rock domains indicating only minor amounts of K were added during alteration (e.g., Fig. 2-8). Around the porphyry Cu centers, material-transfer associated with potassic alteration is overall minor, but locally characterized by lower Ca/Al and higher K, K/Th and Cu compared to the least altered rocks. The material-transfer caused by potassic alteration in the HVC porphyry centers is consistent with formation from magmatic-hydrothermal fluids (Ulrich and Heinrich, 2001; Sillitoe, 2010).

Propylitic and sodic-calcic alteration can form from a variety of fluid sources. A common model for the formation of propylitic alteration involves wall-rock reaction with inward-flowing, thermally prograding, meteoric fluids at low water-rock ratio (Meyer and Hemley, 1967; Norman et al., 1991; Reed, 1997). Alternatively, meteoric water with a non-magmatic brine component (Bowman et al., 1987), or the lateral expulsion of cooling and spent magmatic-hydrothermal fluids, can generate propylitic alteration peripheral to Cu-bearing potassic or sericite-chlorite alteration domains (Cooke et al., 2014a; Wilkinson et al., 2015). Sodic-calcic alteration may be caused by the flow of external hypersaline formation waters (Dilles et al., 1992), or potentially from seawater-sourced formation waters (Orovan et al., 2018), heated during inflow into the magmatic cupola region along the margins of potassic alteration and porphyry stocks (Dilles et al., 2000).

A key criterion for the formation of sodic-calcic alteration is the presence of Cl-bearing fluid coupled with a prograding thermal path; this results in an exchange reaction between primary K-feldspar and secondary albite (Carten, 1986; Dilles and Einaudi, 1992):

$$KAlSi_3O_8 + Na^+_{(aq)} = NaAlSi_3O_8 + K^+_{(aq)} \qquad \text{(Eq. 3)}$$

This reaction is consistent with the mineralogical changes demonstrated by the PER plots, and the K loss and concomitant Na gain during epidote–(albite) alteration in the GCB. Additionally, the removal of Fe, Cu, Ag, and Zn associated with intense albitization (e.g., Figs. 2-13A and 2-14B, D-F), is facilitated by the heating of a Cl-bearing fluid because the solubility of these metals increases with increasing temperature (Hemley and Hunt, 1992). Barium and Rb are also lost to the fluid during albitization and are inferred to be primarily derived from K-feldspar, whereas Sr appears to be locally gained and is potentially being sourced from the fluid, and/or from up-flow Sr-depleted zones where primary plagioclase has been altered (Heier, 1962; Rusk et al., 2004). The origin of the fluid causing epidote–(albite) alteration, i.e., whether magmatic or an external brine, cannot be determined using this data set; however, seawater or seawater pore-fluids from submarine Nicola Group sedimentary and volcanic rocks are a plausible external fluid source in the GCB region (see Chapter 3). Furthermore, a $\delta^{18}O_{fluid}$ value of 2.7 ‰ and δD_{fluid} value of -17.6 ‰ derived from a white-mica vein in the Valley Cu center indicates the presence of a seawater-derived fluid in the magmatic-hydrothermal system (Jones, 1974).

There does not appear to be any significant material-transfer of Ca or K occurring with epidote–(K-feldspar) alteration. The alteration is primarily characterized by addition of ~ 0.5 wt. % H_2O. The K required for the patchy replacement of plagioclase by K-feldspar in vein halos of this facies is interpreted to be locally sourced from biotite during chlorite alteration.

Additionally, in order to stabilize secondary K-feldspar over white-mica, more alkaline conditions, and probably higher temperatures of formation, are required for epidote–(K-feldspar) alteration compared to prehnite–(white-mica–chlorite) facies (Hemley and Hunt, 1992). Epidote–(K-feldspar) veins are primarily hosted in Chataway or Guichon granodiorites and their formation may be related to contact metamorphism and hydrothermal circulation caused by intrusion of the second pulse of magma in the GCB.

The prehnite–(white-mica–chlorite) facies in the GCB is associated with the selective replacement of plagioclase by fine-grained white-mica and prehnite, and chlorite alteration of hornblende and biotite, with only localized addition of calcite. These mineral changes are facilitated by the addition of H_2O and CO_2 from the fluid. For discussion purposes, simplified mineral reactions using theoretical mineral compositions are used. Alteration of plagioclase to form albite, white-mica and prehnite can primarily occur by a hydration reaction:

$$4(Na_{0.5},Ca_{0.5})(Al_{1.5}Si_{2.5})O_8 + K^+_{(aq)} + 4H_2O = NaAlSi_3O_8 + Ca_2Al(AlSi_3O_{10})(OH)_2 + KAl_2(AlSi_3O_{10})(OH)_2 + Na^+_{(aq)} + H_4SiO_{4(aq)} \quad \text{(Eq. 4)}$$

The K in aqueous solution required for equation 4 is interpreted to have come from the chloritization of primary biotite via a hydrolysis and hydration reaction:

$$2K(Mg,Fe)_3(AlSi_3O_{10})(OH)_2 + 4H^+ + 2H_2O = (Mg,Fe)_5Al(AlSi_3O_{10})(OH)_8 + (Mg,Fe)^{2+}_{(aq)} + 2K^+_{(aq)} + 2SiO_2 + H_4SiO_{4(aq)} \quad \text{(Eq. 5)}$$

Alternatively, the white-mica formed in equation 4 is mostly paragonite, in which case little addition of K is required and the Na liberated from plagioclase is consumed. The hydration of hornblende and formation of chlorite liberates Ca:

$$Ca_2Mg_4Al(Al_{0.5}Si_{3.5}O_{11})_2(OH)_2 + Mg^{2+}_{(aq)} + 2H^+ + 10H_2O = Mg_5Al(AlSi_3O_{10})(OH)_8 + 2Ca^{2+}_{(aq)} + 4H_4SiO_{4(aq)} \quad \text{(Eq. 6)}$$

The Fe, Mg, Ca, and Si in aqueous solution derived from fluid-mineral interactions (Eqs. 4, 5, and 6) is inferred to be primarily consumed by the formation of prehnite and epidote fracture fills as there is no significant material-transfer associated with this alteration facies (e.g., Figs. 2-

8 and 2-11). Where the requisite Al for vein minerals is sourced from is unclear, but lab experiments have shown that albitization can mobilize Al and Ti from plagioclase (Hövelmann et al., 2010). Additionally, turbidity in feldspars, ubiquitous in the propylitic halos in the GCB, indicates porosity and volume loss (Plümper and Putnis, 2009; Putnis, 2015). Thus, the Al required for minerals precipitated in fractures is inferred to be sourced from feldspars during alteration and concomitant porosity generation. Although not accounted for in mass-balance calculations, propylitic alteration also caused oxidation of primary magnetite to variable mixtures of hematite and ilmenite, and localized reddening within the alteration halo.

Calcite has retrograde solubility, at fixed pressure, and its precipitation is driven by an increase in fluid pH and CO_2 degassing, as opposed to fluid cooling (Rimstidt, 1997). Whole-rock $\delta^{13}C$ values between ~-8 and -3‰ suggest that the CO_2 fixed in the rocks as calcite is magmatic in origin (Taylor, 1986; Djouka-Fonkwe et al., 2012). Calcite alteration occurs in some rocks associated with white-mica–chlorite* facies, but mostly manifests as fracture fills. Hydrolysis reactions of feldspar-forming abundant white-mica and quartz consume H^+ ions and thus promote calcite precipitation:

$$2H_2CO_{3(aq)} + Ca^{2+}_{(aq)} = CaCO_3 + CO_2 + H_2O + 2H^+ \qquad \text{(Eq. 7)}$$

This reaction is a plausible mechanism for calcite formation in white-mica–chlorite* facies, but is a less likely processes to form calcite deposition in veins in the peripheral parts of the porphyry Cu systems (with lower white-mica content). Degassing of CO_2 from a late-stage magmatic volatile phase (MVP), on the other hand, is more consistent with the paragenesis of calcite in the altered rocks around the HVC porphyry systems. The Ca required for the formation of calcite in equation 7 could come from the Ca liberated during chloritization of hornblende in propylitic, and or epidote–(albite) domains, or from Ca removed from Cu mineralized zones associated with quartz–(muscovite) and white-mica–chlorite alteration. Un-mixing of CO_2, and calcite formation, from a MVP would be enhanced by decompression during a transition from early, high temperature, alteration phases (potassic, sodic-calcic, and early-halo type muscovite), to the lower temperature and later alteration phases (white-mica–chlorite and propylitic).

To summarize, propylitic alteration around the HVC porphyry centers is interpreted to have formed from a CO_2-degassing, cooling and spent MVP, or from the circulation of an external fluid, or a mixture of both, at low water-rock ratio. The overlap of early sodic-calcic domains with a high density of younger prehnite–(white-mica–chlorite) veins and alteration (Fig. 2-2A), and the presence of co-genetic MVP-derived calcite in the younger alteration, suggest that both non-magmatic and magmatic fluids were present peripheral to the Cu centers at HVC at different times.

2.8.4 Calcite in porphyry Cu systems

Calcite in the propylitic halo of porphyry systems has been studied at a few other locations, most notably at Bingham (Bowman et al., 1987), Southwest Tintic (Norman et al., 1991), and around Quebrada Blanca in the Collahuasi district (Djouka-Fonkwe et al., 2012). The spatial association between epithermal and porphyry systems of similar ages in the Collahuasi district suggests that the porphyry Cu systems were emplaced at depths in the crust of < 2 km (Masterman et al., 2005). The HVC porphyry centers are estimated to have been emplaced at 4–5 km deep in the crust (D'Angelo, 2016), whereas the Butte porphyry Cu-Mo deposit in Montana is interpreted to have formed at 5–9 km deep (Rusk et al., 2008). Djouka-Fonkwe et al. (2012) document disseminated, replacement-style, calcite in the propylitically altered rocks, outboard of sericite altered domains, which contrasts with the dominantly fracture- fill-style in and around the HVC porphyry centers. At the Butte porphyry, carbonate veinlets occur with distal propylitic alteration and in some fractures with pale-green sericite alteration (Reed et al., 2013). Djouka-Fonkwe et al. (2012) estimate that calcite formed from a magmatic fluid that contained approximately 0.7 mol. % CO_2 in H_2O (~ equivalent to 0.45 wt. % C), much lower than the end-member estimate for HVC of ~1.6 mol. % CO_2 (Fig. 2-15B), and the unmixed parental porphyry fluid at the Butte porphyry contained ~5 mol. % CO_2 (Rusk et al., 2008). Based on the observations from the Collahuasi, HVC and Butte porphyry districts, we propose that the depth of porphyry emplacement and the exposure level influences how calcite manifests in the altered rock package, and that the formation of calcite in fractures in deep systems is the result of CO_2-degassing. An additional factor which controls the distribution of calcite in porphyry systems, is that the disproportionation of acid-forming compounds (SO_2 and HCl) in a cooling MVP is less prevalent at deeper levels in porphyry systems, and thus, it is easier to maintain the pH conditions suitable for calcite precipitation (Ohmoto 1972; Ohmoto and Rye 1979; Meyer and Hemley 1967). Understanding the factors that influence the spatial distribution of calcite and its

C-isotope composition in porphyry Cu systems is important in the interpretation of exploration lithogeochemical data sets, and to allow vectoring to well mineralized domains.

2.9 Conclusions and implications

2.9.1 Evolution of the porphyry footprint from a lithogeochemical perspective

A large area of weak fracture-controlled K-feldspar (potassic) alteration developed around the porphyry stocks and barren quartz vein domain, and is locally characterized by minor gains in Si, K and Cu-Ag (Time 1; Fig. 2-19). Localized K, Fe, and Cu depletion, and Na-enrichment, occurs in albite altered domains that formed a large (~34 km^2) non-concentric footprint outboard of well mineralized and K-enriched zones (Time 2–3; Fig. 2-19). The sodic-calcic alteration is inferred to be caused by the heating and inward-flow of an external brine. Well-developed feldspar-destructive white-mica alteration, indicated by 2CNK /Al values <0.85, quartz, K, and Cu-Ag addition, and Ca and Na-depletion occurs with quartz–(coarse muscovite) and white-mica–chlorite alteration in the Cu-bearing parts of the porphyry system (Time 2–3; Fig. 2-19). Outflow of MVP from the porphyry centers coupled with CO_2-degassing caused incipient calcite precipitation and peripheral white-mica–chlorite alteration (Time 4; Fig. 2-19). An admixture of externally-derived wall-rock equilibrated fluid, and CO_2-degassing MVP depleted in ore elements is inferred to have generated propylitic alteration peripheral to the K-enriched and Cu-mineralized domains (Time 5; Fig. 2-19). Water and calcite–enriched propylitic and sodic-calcic altered rocks form the largest coherent lithogeochemical footprint to the mineralization at HVC (~60 km^2). Furthermore, rocks with high $\delta^{13}C$ values are detected up to 6 km away from porphyry Cu mineralization at Lornex and Highmont and, on this basis, are discernable from background propylitic alteration elsewhere in the district. Although likely formed from a non-magmatic external brine, sodic-calcic altered rocks received a late MVP flux that is recorded as a series of cross-cutting calcite veinlets that is related to porphyry Cu genesis.

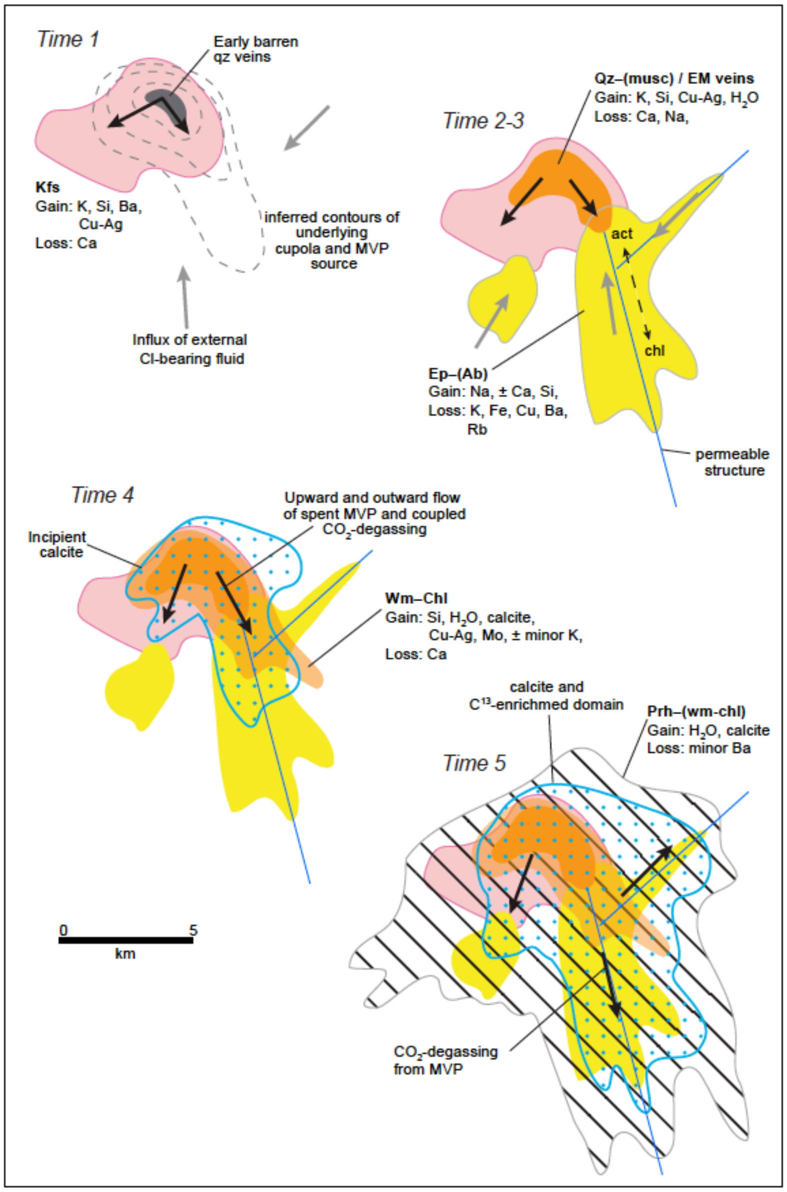

Figure 2-19. Time-integrated plan maps depicting the evolution of the porphyry Cu footprints at HVC from a lithogeochemical perspective.

2.9.2 Study methodology

Linking the feldspar staining and shortwave infrared spectral results to corresponding lithogeochemical analyses revealed several features of interest: 1) staining highlights weak and cryptic albitization that did not cause sufficient material-transfer to be confidently distinguished from protolith compositions; 2) K-feldspar alteration west of Valley is easily detectable with staining, but generally only caused weak alkali metasomatism, however, this facies is characterized by some quartz addition and higher than background Cu and Ag concentrations; 3) shortwave infrared spectral imaging distinguished samples of white-mica–chlorite* alteration with an intermediate-wavelength Al-OH feature that may have otherwise been miss-identified as propylitic; and 4) staining and spectral imaging identified a sub-facies of propylitic alteration, epidote-(K-feldspar), in the GCB that is probably unrelated to porphyry genesis.

2.9.3 Exploration implications

Molar element ratio diagrams are an effective way to assess mineral changes and material transfer caused by alteration processes, but are dependent on correct protolith assignment. We recommend host-rock discrimination using mapping, sample descriptions, and paired immobile elements characteristics. Mineral-normative schemes using loss on ignition, C and S data can be used to calculate rock H_2O and calcite content and potentially help differentiate propylitic alteration in other porphyry districts.

If present, sodic-calcic alteration can deplete the protolith in Fe causing a change in petrophysical properties.

The host-rock composition, emplacement depth, and exposure level of a porphyry system will influence alteration mineralogy, geochemical response, and how carbonate manifests in peripheral alteration. These factors should be considered when assessing exploration lithogeochemical data sets.

The minerals commonly occurring in propylitic alteration can form a variety of processes unrelated to magmatic-hydrothermal systems, i.e., lower greenschist (Hacker et al., 1992) and barren geothermal systems (Bird et al., 1984; Bergbauer and Martel, 1999), however, whole-rock C isotope compositions can be used to discriminate prospective alteration peripheral to porphyry Cu centers, as demonstrated in this study and in the Collahuasi district (Djouka-Fonkwe et al., 2012).

3 Mineralogical and isotopic characteristics of sodic-calcic alteration in the Highland Valley Copper district, British Columbia, Canada– *Implications for fluid sources in porphyry Cu systems*

3.1 Introduction

Porphyry Cu deposits are the largest source of Cu globally and although demand is variable, and recycling is increasing, new projects and resources are needed to replace decreasing inventories (Seedorff et al., 2005; Sillitoe, 2010; Thompson, 2016). An understanding of the fluid types that can be present during porphyry Cu formation, how these fluids manifest in the alteration footprint, and their spatial distribution with respect to Cu-mineralized portions of the system is important for successful exploration.

Isotope and fluid inclusion studies have shown that magmatic (Dilles et al., 1992; Harris et al., 2005; Rusk et al., 2008), meteoric (Sheets et al., 1996; Taylor, 1997; Selby et al., 2000), formation (Dilles et al., 1992), and seawater-derived (Jones, 1974; Chivas et al., 1984; Orovan et al., 2018) fluids of varying salinity can all be present in various proportions at different locations and times in an evolving porphyry system. The diversity in the sources of these fluids, the timing of their ingress and the products of their interactions with host rocks can lead to deviations from generalized genetic models (i.e., Seedorff et al., 2005; Sillitoe, 2010).

By some definitions, propylitic alteration in porphyry systems occurs by material-transfer of H_2O, CO_2, and localized S to the altered rock, but limited hydrolysis or alkali-exchange metasomatism (Meyer and Hemley, 1967; Ulrich and Heinrich, 2001; Urqueta et al., 2009). Models for propylitic alteration commonly invoke heating of meteoric, or formation fluids, around porphyry centers at low water–rock ratio (Meyer and Hemley, 1967; Norman et al., 1991; Reed, 1997). Na-bearing assemblages can occur in a variety of geological environments (Battles and Barton, 1995; Barton et al., 2000; Pollard, 2001; Marshall and Oliver, 2008; Corriveau et al., 2010) and can form from disparate fluid sources (Pollard, 2001; Hunt et al., 2007; Barton, 2014), but may require a particular set of conditions to form over large areas (> ~3 km^2) in porphyry Cu systems. Sodic-calcic (Na-Ca) and sodic (Na) alteration in porphyry systems is defined by the exchange of K for Na with varying degrees of Ca addition (Carten, 1986; Dilles and Einaudi, 1992). Highly oxidized felsic magmas can produce fluids capable of Na-, Fe-, Ca-, or K-rich alteration (Arancibia and Clark, 1996), and fluids evolved from melt compositions atypical of volcanic arcs can cause Na-metasomatism (Lang et al., 1995; Richards and Mumin, 2013), but these tend to cause spatially limited alteration zones (100's m^2 to several km^2) in porphyry systems. Regional-scale Na-Ca alteration in porphyry systems has been attributed to the flow of external brines heated during inflow into the magmatic cupola regions (Dilles et al., 2000). More recent work suggests that some elements lost from potassic zones (e.g. Ca, Fe, Co) are redistributed outwards, producing metasomatic propylitic alteration domains (Pacey et al., 2016), and that the lateral expulsion of cooling magmatic-hydrothermal fluids depleted in ore elements ("spent") can also generate propylitic alteration peripheral to the Cu-bearing portion of porphyry systems (Cooke et al., 2014a; Wilkinson et al., 2015). Thus, Na-Ca and propylitic alteration could both occur around porphyry Cu systems in response to the fluids present, their composition, and respective thermal evolutions. Conceivably, a continuum may also exist between these alteration facies that is dependent on the relative contributions of disparate fluid reservoirs.

Four major porphyry Cu-(Mo) systems, hosted in the Late Triassic Guichon Creek batholith (GCB), occur in the Highland Valley Copper (HVC) district in British Columbia (Figs. 3-1B and C); Canada's largest and longest operating Cu mine (Ydon, 2007; Byrne et al., 2013). The HVC porphyry systems are unusual in that some of them formed at depths of at least 4–5 km in plutonic host rocks (D'Angelo, 2016; D'Angelo et al., 2017). Epidote veins with K-feldspar-destructive albite halos compose extensive domains of Na-Ca alteration in the GCB, and are significant because they potentially formed from non-magmatic fluids during porphyry Cu formation (Byrne et al., 2017). We characterize the distribution and paragenesis of Na-Ca altered rocks in the district. Using stable and radiogenic isotopic data and a robust geological framework, we propose that Na-Ca veins and alteration in the GCB dominantly formed from external seawater-derived saline fluids that were heated along regional-scale, fracture-controlled, flow-paths into the batholith during the formation HVC porphyry systems. Furthermore, we demonstrate that seawater-derived fluids and magmatic-dominated fluids flowed back-and-forth and mixed at one of the porphyry centers. These findings are significant because the ingress of seawater-derived fluids generated a large and asymmetrically-zoned alteration footprint, and modified the host-rock composition and mineralogy in and outboard of the porphyry Cu centers.

Additionally, we suggest that Na-Ca alteration, caused by ingress of seawater-derived fluids, may be more common in porphyry districts hosted in marine deposited rocks occurring in low-lying coastal and island-arcs than is currently recognized.

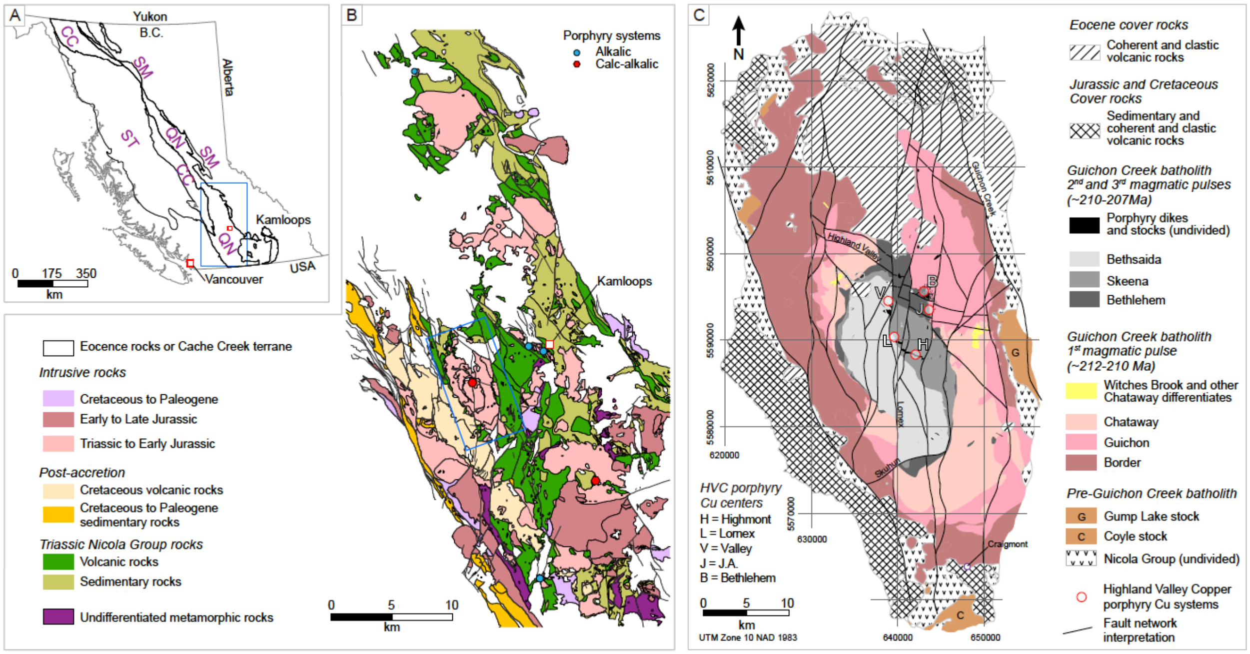

Figure 3-1. Location maps. A. Cordilleran terranes in British Columbia: ST =Stikine, QN = Quesnel, CC= Cache Creek, SM = Slide Mountain. The blue frame indicates area in Fig. 1B. B. Southern Quesnel terrane rocks and the location of the Guichon Creek batholith (after Massey et al., 2005). The blue frame indicates area in Fig. 1C. C. Guichon Creek batholith geology showing the location of the Highland Valley Copper porphyry systems (modified after McMillian 2009, and D'Angelo et al., 2017). Fault network modified from Lesage et al. (2019). Note the off-set of the Bethsaida granodiorite contact across the Lornex fault.

3.2 Background Geology

3.2.1 *Regional geology*

The Canadian Cordillera is a collage of accreted allochthonous oceanic and proximal to distal pericratonic terranes (Coney et al., 1980). Of interest in this paper is the Quesnel terrane which is characterized by Mesozoic island-arc assemblages comprising volcanic and sedimentary rocks and associated intrusions (Fig. 3-1A; Colpron et al., 2007). Relevant to this study is the ~238-202 Ma Nicola Group, which was intruded by the Guichon Creek batholith (GCB) at ~211 to 207 Ma (Coney et al., 1980; Mortimer, 1986; D'Angelo et al., 2017). The Nicola Group rocks form a belt that consists primarily of mafic submarine volcanic and associated volcano-sedimentary rocks (Fig. 1B; Preto, 1979; Mortimer, 1987; Ray et al., 1996) that were deposited in a rifted marine basin above an east-dipping subduction zone (Colpron et al., 2007). The GCB is magnetite-bearing, mostly metaluminous, calc-alkalic in composition (I-type), and is one of many large Mesozoic plutonic bodies associated with porphyry systems within Southern British Columbia (Fig. 1B; McMillan et al., 1995; Logan and Mihalynuk, 2014).

The GCB hosts the HVC porphyry Cu-(Mo) systems and occurs along the western margin of the Quesnel terrane east of the Cache Creek accretionary complex terrane (Fig. 3-1B; Logan and Mihalynuk, 2014). Nicola Group rocks directly adjacent the GCB (Fig. 3-1C) comprise mafic to intermediate volcaniclastic and volcanogenic sedimentary rocks, sandstone, limestone, layered siltstone, calcareous siltstone, and several chert horizons (McMillan, 1976, 1977; McMillan et al., 2009). Some felsic volcaniclastic rocks also occur. The Nicola Group rocks intruded by the GCB appear to be equivalent to assemblage two of Schiarizza (2016) and Western belt rocks of Preto (1979), and were predominantly deposited in a submarine island-arc setting (McMillan, 1976, 1977; Mihalynuk et al., 2016). The region underwent Cretaceous shortening and localized Tertiary extensional deformation (Colpron et al., 2007).

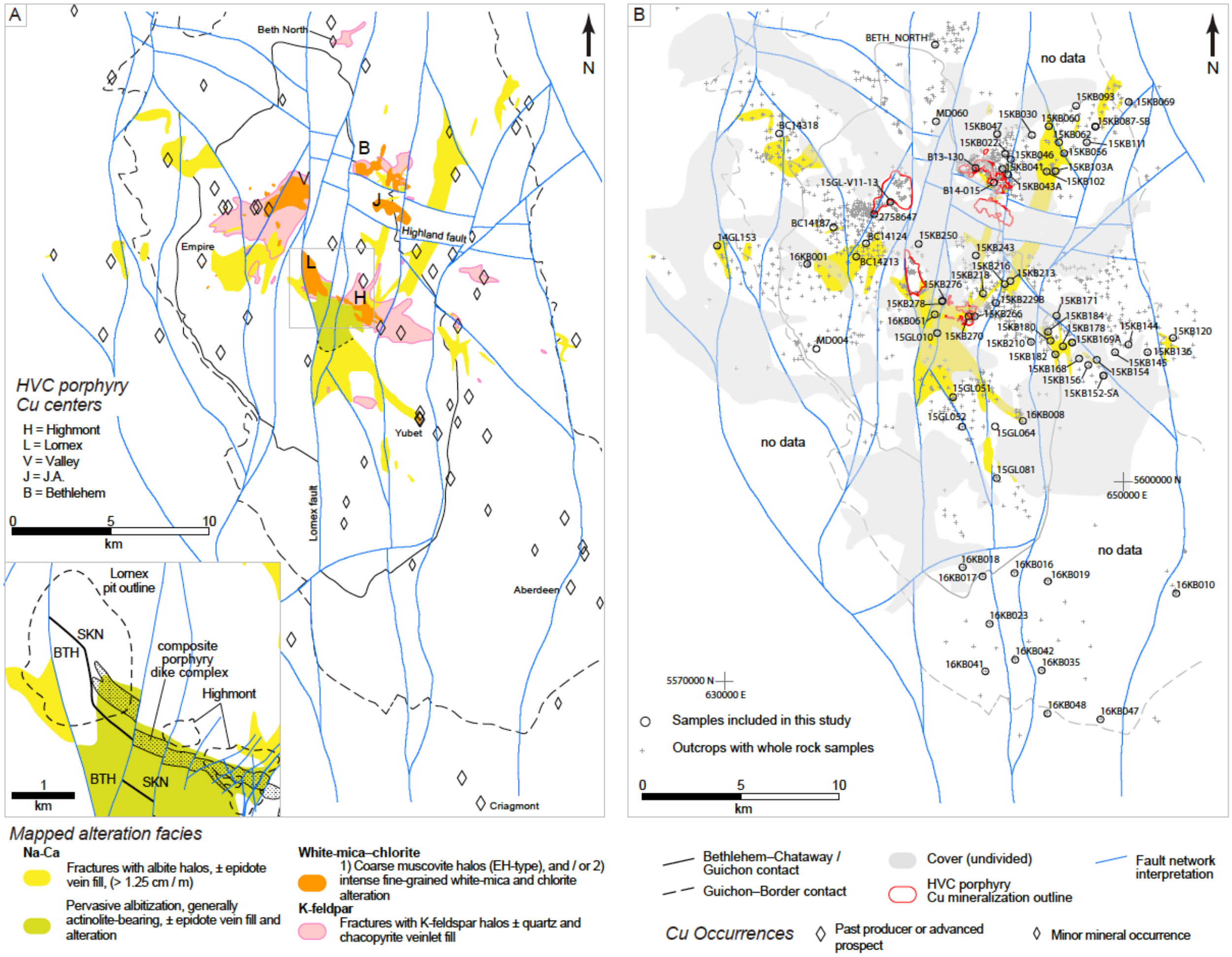

Figure 3-2. A. Simplified mapped alteration domains in the Guichon Creek batholith and the location of select Cu occurrences in the region (occurrence data from http://aris.empr.gov.bc.ca and http://minfile.gov.bc.ca). Excluded from this map is the distribution of propylitic facies, which occurs throughout the batholith with the highest density of veins centered on the porphyry systems (Lesage, 2016). Additionally, the locations of outcrops with whole rock samples that inform the map interpretation are shown. In the northeast portion of the batholith, epidote veins with albite halos trend dominantly NNE and dip steeply to the E or are vertical (Lesage, 2016). Whereas Na-Ca facies veins south of Lornex trend NW and S, and are orientated NE east and northeast of Highmont (Lesage, 2016). B. Distribution of Na-Ca facies, Tertiary and anthropogenic cover, and sample locations specific to this study. Fault network modified from Lesage et al. (2019).

3.2.2 Magmatic evolution and porphyry Cu formation

The GCB has an oval shape measuring approximately 60 km by 25 km, elongate to the northwest (Fig. 3-1C). It formed from multiple intrusive pulses and is concentrically zoned (D’Angelo et al., 2017; Lee et al., *in review*). The initial pulse consists of melanocratic quartz-diorite, monzogabbro, and granodiorites. The second pulse comprises leucocratic quartz-rich granodiorites and monzogranite facies in the interior of the batholith, and a third pulse formed syn- to late-mineralization stocks and dikes at some of the porphyry centers (Table 3-1; Fig. 3-1C; Byrne et al., 2013; D’Angelo et al., 2017; Lee et al., *in review*). Listed from oldest to youngest, the volumetrically significant rocks in the GCB in the first magmatic pulse are the Border quartz-diorite, Guichon granodiorite, and Chataway granodiorite, and in the second pulse are the Bethlehem granodiorite, Skeena granodiorite and the Bethsaida granodiorite and monzogranite (McMillan, 1976; D'Angelo et al., 2017). Dikes and stocks belonging to the second and third magmatic pulses occur at the porphyry centers (Table 3-1) and are genetically related to porphyry Cu formation (D'Angelo et al., 2017). Border diorites at the batholith margin have initial $^{87}Sr/^{86}Sr$ values of 0.70339–0.70356 while overall the first magmatic pulse has an average of 0.703449 (n = 8; D'Angelo et al., 2017). The second magmatic pulse has a slightly lower average $^{87}Sr/^{86}Sr_i$ of 0.703409 (n = 6) and ranges from 0.703367 to 0.703479 (D'Angelo et al., 2017). Chataway granodiorite, belonging to the first magmatic pulse, has the lowest average $^{87}Sr/^{86}Sr_i$ of 0.703380 (n = 2), of the GCB rocks (D'Angelo et al., 2017).

The HVC porphyry Cu-(Mo) systems are situated in the center batholith predominantly within the second magmatic pulse rocks (Bethlehem, J.A., Valley-Lornex and Highmont; Figs. 3-1C and 3-2). At least two main stages of porphyry Cu mineralization are evident (McMillan, 1985a; Byrne et al., 2013). The first was at the Bethlehem system at ~209 Ma and was followed by intrusion and crystallization of the Skeena and Bethsaida granodiorites, and subsequently by the formation of the Valley, Lornex and Highmont porphyry centers between 208 and 207 Ma (D'Angelo et al., 2017). A 5 km long, 100–300 m wide, steeply northeast-dipping and northwest-trending, composite porphyry dike complex consisting primarily of pre- mineralization, and minor syn- to post-mineralization, dikes (Table 3-1) links the Lornex and Highmont porphyry centers (Fig. 3-2A inset; Byrne et al., 2013; D'Angelo et al., 2017). The timing of mineralization of the J.A. system is not clear, however the mineralization and alteration style suggests it is akin to Bethlehem (McMillan, 1985b). A north-trending fault with evidence of post-mineral dextral strike-slip displacement (Lornex fault) cuts the Valley and Lornex deposits (Fig. 3-2A). Restoring approximately 3.5 km of dextral displacement, consistent with off-set in the Bethsaida-Skeena granodiorite rock contact, indicating that the Valley and Lornex deposits were once a single porphyry center (Valley-Lornex; Hollister et al., 1975; McMillian, 1976; Fig. 3-2A).

Table 3-1. Summary of the HVC porphyry Cu centers characteristics

Porphyry system	[1]Host Rocks	*Alteration facies*: fracture fill / halo	[2]Geochronology ± 2σ (Ma)	Additional References
Bethlehem (Huestis, Jersey, and Iona)	Pre: BTHM, GUI Syn to inter: BTHMP, BX Late to post: FQPC, FPC, LS	*Potassic:* qz-bio-bn±cp / bio; bn±cp±tour / ksp *White-mica–chlorite:* qz-cpy-py±ca±tour /wm-chl *Propylitic:* ep-chl±cp / wm-prh-chl±ca *Na-Ca:* ep±diop / ab-wm-chl±act	GUI = 210.77±0.16 BTHM = 209.81±.21	(Briskey and Bellamy, 1976; Briskey, 1981)
J.A.	Pre: BTHM, GUI Syn: Late: QFPM	*Potassic:* / ksp, bio *White-mica–chlorite:* qz-cp±bn±mb / wm *Intermediate argillic:* / wm-kaol-mont±zeo		(McMillan, 1976; McMillan, 1985)
Valley	Pre: BETH, QFPM, BSP Syn: QFP, QFPP Late: QFPP	*Barren quartz (A-vein):* qz. *Potassic:* ±qz±cp */ ksp; / bio* *Early-Halo*: qz-bn±cp±anh / musc±ksp *White-mica–chlorite:* cp±bn±mb±qz±ca/ wm-chl±ca *Late veins (D-vein):* qz-py-mb±ca±cp / wm-kaol *Intermediate argillic:* / wm-kaol-mont±chl	BETH = 208.81±0.21 BSP = 208.15±0.22	(Osatenko and Jones, 1976; McMillan, 1985)
Lornex	Pre: SKN, QFPM Syn: QFP Late: QFPQ	*Barren quartz (A-vein):* Qz. *Potassic*: ±qz±cp / ksp; / bio *Na-Ca:* / ab-wm-act; ep / ab-act±chl *Early-Halo*: qz-bn±cp±anh / musc±ksp *White-mica–chlorite:* cp±bn±mb±qz±ca/ wm-chl±ca *Late veins (D-vein):* qz-py-mb±ca±cp / wm-kaol *Intermediate argillic*: / wm-kaol-mont±chl	SKN = 208.37±0.29 Mb = 208.4±0.9	(Waldner et al., 1976; McMillan, 1985)
Highmont	Pre: SKN, QFPM Syn: QFP (?) Late: QFPQ, BX	*Na-Ca:* ep±act±gt±tour / ab-wm-act; ep / ab-chl *Potassic:* / ksp; / bio *Early-Halo*: qz-bn±cp±anh / musc±ksp *White-mica–chlorite:* cp±bn±mb±qz±ca±tour±spec/ wm-chl±ca *Late veins (D-vein):* qz-py-mb±ca±cp / wm-kaol *Intermediate argillic:* / wm-kaol-mont±chl	QFPQ = 206.95±0.22 Mb = 208.3±1	(Bergey et al., 1971; Reed and Jambor, 1976)

[1] Organized by timing with respect to main-stage Cu mineralization. [2] D'Angelo et al. (2017). Host rock abbreviations: BETH = Bethsaida; BTHM = Bethlehem granodiorite; BSP = salt and pepper–textured stocks and stock; BTHMP = Feldspar-quartz-phyric Bethlehem porphyry dikes; BX = matrix and cemented facies; FPC = feldspar-phyric crowded porphyry dikes; FQPC = feldspar-quartz-phyric crowded porphyry dikes; GUI = Guichon granodiorite; LS = Late to post-mineral stocks at Iona and Jersey equivalent to Skeena granodiorite; QFP = quartz-feldspar-phyric porphyry dikes; QFPM = mafic-bearing quartz-feldspar-phyric porphyry dikes; QFPP = quartz-feldspar-phyric, phenocryst-poor, and mafic-poor porphyry dikelets; QFPQ = quartz-feldspar-phyric, quartz-rich porphyry dikes; SKN = Skeena granodiorite. Mineral abbreviations: ab = albite; bn = bornite; act = actinolite; anh = anhydrite; bt = biotite; ca = carbonates; chl = chlorite; cp =chalcopyrite; diop = diopside; ep = epidote; gt = garnet; hm = hematite; ill = illite; kaol = kaolinite; Ksp = K-feldspar; mont = montmorillonite; musc = muscovite (coarse grained); prh = prehnite; py = pyrite; qz = quartz; spec = specularite, tour = tourmaline; wm = white-mica.

3.2.3 Highland Valley Copper porphyry systems

Mineralization, alteration, and sulfide mineral zonation is centered and focused on porphyry dikes and inter-mineralization, polylithic, matrix-rich magmatic-hydrothermal breccias at Bethlehem (BTHMP and BX; Table 3-1). Three Cu centers with overlapping halos occur at Bethlehem, named Jersey, Huestis and Iona (Briskey and Bellamy, 1976). Bornite and chalcopyrite mineralization primarily occurs with potassic and white-mica–chlorite alteration (Table 3-1). The mineralization and the breccias are truncated by post-mineralization stocks that are interpreted to be a sub-facies of Skeena granodiorite (Byrne et al., 2013). Tourmaline-chalcopyrite-quartz veins with either K-feldspar or white-mica–chlorite alteration halos occur up to 1.5 km north of Bethlehem. The J.A. porphyry system is buried under a thick sequence of post-mineralization cover (Fig. 3-2B). Mineralization at J.A. occurs in quartz veins with fine-grained white-mica halos (Table 3-1; McMillan, 1985b).

At the Valley-Lornex porphyry there is a central domain of abundant Cu-barren, vitreous quartz veins with diffuse vein-wall margins (Byrne et al., 2013). Upward and outboard from the barren quartz veins is a domain of veinlets with K-feldspar halos ± minor chalcopyrite and quartz vein fill extending for up to 3 km away from well-mineralized rock within the pits (Fig. 3-2A; Lesage et al., 2016). Barren quartz veins and K-feldspar-bearing veinlets are cross-cut by well-mineralized quartz–bornite–chalcopyrite ± molybdenite veins with halos of coarse-grained grey colored paragonitic muscovite (Alva-Jimenez, 2011). The coarse-grained muscovite exhibits a bowtie morphology and is locally intergrown with quartz and secondary K-feldspar (Alva-Jimenez, 2011) and, thus, these veins are interpreted to belong to early-halo vein facies (e.g. Proffett, 2009; Riedell and Proffett, 2014). Commonly outboard of, and overprinting, the early-halo veins and halos is a pervasive and fracture controlled assemblage of fine-grained white-mica–chlorite alteration ± chalcopyrite mineralization. Late-stage, intermediate-argillic alteration occurs throughout the Valley-Lornex system (Table 3-1).

The distribution of alteration and mineralization at Highmont is focused primarily above, and on, the northeast side of a steeply NE-dipping composite porphyry dike complex (Fig. 3-2A; Reed and Jambor, 1976). Chalcopyrite, bornite and molybdenite mineralization occurs in quartz veins with coarse-grained early-halo (EH) muscovite halos (McMillan, 1985a). Molybdenite and chalcopyrite ± quartz and carbonate occur in veinlets with fine-grained white-mica–chlorite halos. Late-stage quartz–carbonate–chalcopyrite–molybdenite ± pyrite veins cross-cut and are mostly marginal to the EH vein domains. An igneous and specularite–tourmaline–quartz–Cu-Fe-sulfide cemented breccia is located in the center of the porphyry dike complex at Highmont and is spatially associated with late-mineral dikes of quartz-rich, quartz and feldspar-phyric porphyry (QFPQ; Table 3-1).

Several features indicate that some of the porphyry centers at HVC were emplaced at considerable depth. Cogenetic plutonic host rocks (D’Angelo et al., 2017), hornblende barometry (D’Angelo, 2016), and EH-veins imply that the Valley-Lornex porphyry Cu system was likely emplaced at a depth of 4–5 km (Seedorff et al., 2008; Proffett, 2009; Alva-Jimenez, 2011; Riedell and Proffett, 2014). A 4–5 km emplacement depth for the Valley-Lornex porphyry system is also consistent with stratigraphic thickness estimates of southern Quesnel Nicola Group rocks of ~ 6 km (Sutherland, 1976; Preto, 1979; Schiarizza, 2016), assuming the batholith intruded the base of assemblage 2.

Veinlets of prehnite ± epidote and calcite with plagioclase-destructive white-mica–prehnite alteration halos compose propylitic facies and are the most common and widely distributed alteration in the GCB. The highest density of propylitic veins is focused around the porphyry systems but the facies also occurs out to the margins of the batholith (Lesage et al., 2016).

Outside of the porphyry centers, tourmaline is sparsely distributed. In the northeast part of the batholith, tourmaline occurs locally as fracture patinas without alteration halos. Additionally, tourmaline rosettes occur in some late stage aplitic dikes and pegmatite. A high concentration of tourmaline also occurs in breccias at the South Sea and Krain porphyry Cu occurrences, respectively ~ 10 and 15 km north of Bethlehem (McMillan, 1976; McMillan et al., 2009).

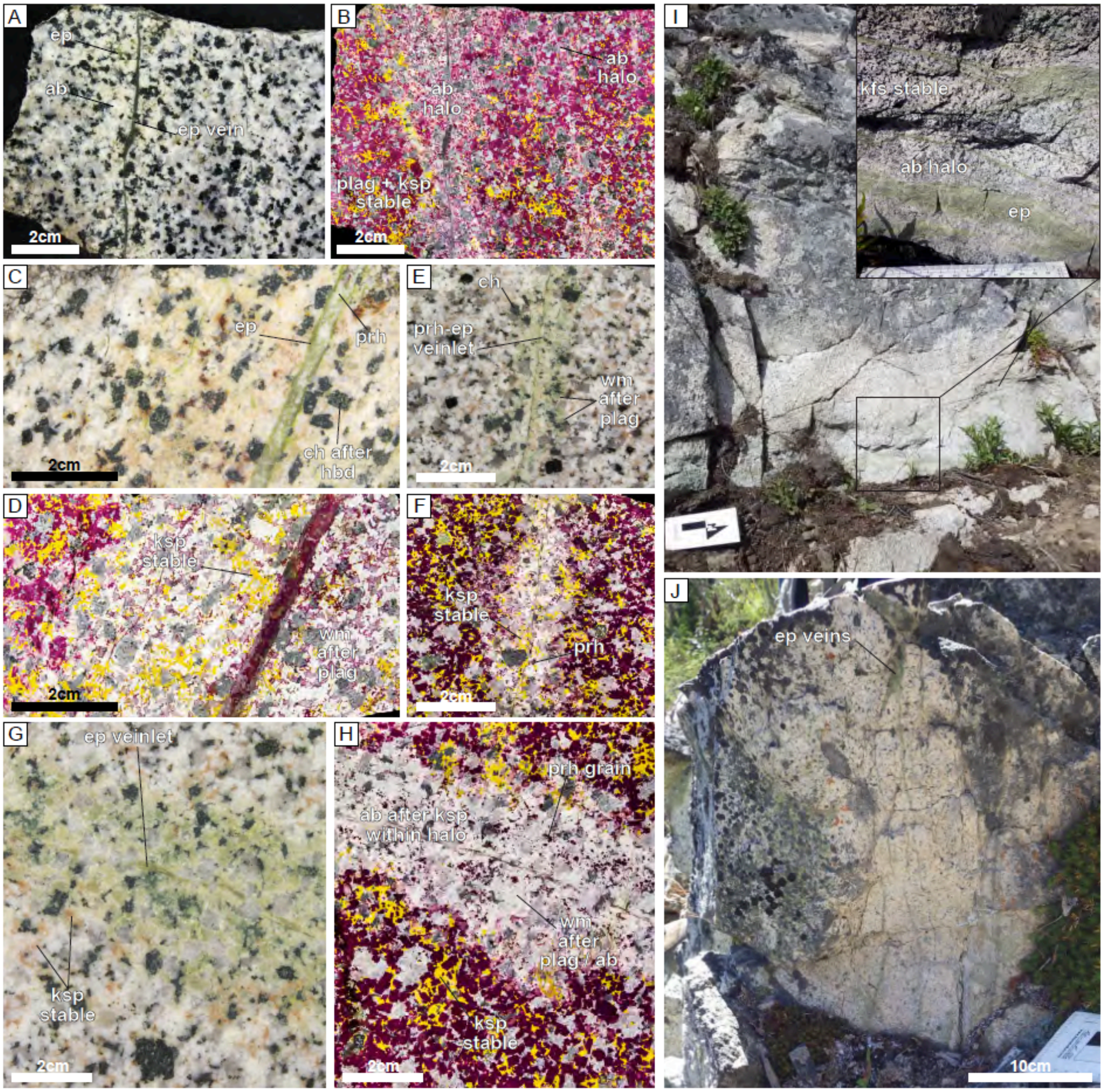

Figure 3-3. Rock slab and field characteristics of Na-Ca and propylitic veins and alteration. A. Unstained and B. stained image pairs of an epidote vein with K-feldspar-destructive albite halo in Skeena (15KB152). Chlorite replaced mafic minerals within the halo and is locally accompanied by epidote. C. Unstained and D. stained image pairs of an epidote–prehnite vein with plagioclase-destructive, K-feldspar-stable, fine-grained white-mica–prehnite halo (15KB156). Mafic minerals are partially altered to chlorite within the vein halo. E. Unstained and F. stained image pairs of a prehnite–epidote veinlet with a plagioclase destructive fine-grained white-mica–prehnite halo in Bethsaida (15GL058). G. Unstained and H. stained image pairs of a discontinuous epidote veinlet with an albite halo overprinted by plagioclase-destructive white-mica–prehnite alteration (15GL038-2247934). I. A low-density of planar to wavy epidote veins with diffuse, irregular, vein wall margins and albite halo in an outcrop of Guichon (15KB057). J. Closely-spaced, high-density, sheeted epidote veins with albite halos (15KB214).

3.3 Methodologies

3.3.1 Mapping and petrography

Outcrop mapping, core logging, and sampling in the GCB was conducted between 2014 and 2016. Detailed bench mapping at the Highmont porphyry center was completed in 2016 and the results were combined with Teck Resources Limited ("Teck") drill log data to produce the map interpretations in this contribution. The maps and section for the Bethlehem porphyry center utilize bench maps from Iona area, but are primarily based on Teck geological interpretations. Approximately 500-1000 cm^3 rock samples of representative vein and alteration zones were taken per outcrop, spaced 0.5–1.5 km apart. The samples were cut and slabbed using a rock saw to ensure weathered and organic material was removed before analyses. A total of 850 samples underwent lithogeochemical analysis and feldspar staining. Rock slabs were etched with hydrofluoric acid and stained with sodium colbaltinitrite to mark K-feldspar, and with amaranth to stain calcic plagioclase, calcite and prehnite (Appendix 3-A). After staining and macroscopic mineralogy identification, the 850 samples were organized into alteration facies. A subset of 77 representative samples (Appendix 3-A; Fig. 3-2B) was further examined with a standard petrographic microscope and imaged with an electron microprobe at the University of Alberta.

3.3.2 Lithogeochemical analysis

Lithogeochemical analysis was completed at the Bureau Veritas Laboratories, Vancouver, Canada. A crushed sample split was fused with a lithium metaborate/tetraborate mix. The fused bead was digested using a 4-acid solution and the major element oxides were analyzed by inductively coupled plasma emission spectroscopy (ICP-ES). Trace elements were measured on an inductively coupled plasma mass spectrometer (ICP-MS). Loss on ignition (LOI) is reported as % weight loss on a 1 g split ignited at 1000°C. Carbon and S were measured by a LECO analyzer. Sample preparation, analytical digestion methods, and quality assurance and control procedures are provided in Appendix 3-A.

3.3.3 Electron microprobe analyses

Electron microprobe analyses (EPMA) was performed using the CAMECA SX100 at the Electron Microprobe Laboratory at the University of Alberta, primarily to determine the major and minor-element composition of silicate alteration minerals in the Guichon Creek batholith. For the wavelength-dispersive spectrometry (WDS) the EPMA beam was operated in spot mode at an accelerating voltage of 20 kV, a probe current of 20 nA, and a beam diameter between 1–5 µm depending on the target mineral. Unknowns were analyzed at a peak count time of 30 s and background count time of 30 s. Standards were analyzed for 20–30 s on peak. Standards used are listed in Appendix 3-A.

3.3.4 Hydrogen and Oxygen isotopes

Hydrogen and oxygen isotope analyses were completed at the Queen's Facility for Isotope Research (QFIR), Queen's University, Canada (see Appendix 3-A for details). Portions of hand samples were crushed in a pestle and mortar. Vein and alteration halo minerals were hand-picked using a fine tweezers and binocular microscope. A total of 42 mineral separates (20-40 mg) and eight whole-rock samples (100 mg) were analyzed.

Hydrogen isotopic composition was measured using a Thermo-Finnigan thermo-combustion elemental analyzer (TC/EA) coupled to a Thermo-Finnigan Delta$^{\mathrm{Plus}}$ XP Continuous-Flow Isotope-Ratio Mass Spectrometer (CF-IRMS). δD values are reported in permil (‰) relative to Vienna Standard Mean Ocean Water (VSMOW) with a precision of 3 ‰.

Oxygen isotopic composition was analyzed via dual inlet on a Thermo-Finnigan Delta$^{\mathrm{Plus}}$ XP Isotope-Ratio Mass Spectrometer (IRMS). $\delta^{18}O$ values are reported in units of permil (‰) relative to Vienna Standard Mean Ocean Water (VSMOW) with a precision of 0.1 ‰.

3.3.5 Boron isotopes

Boron isotope analyses were performed with the Cameca 1280-HR secondary ion mass spectrometry (SIMS) instrument at the GFZ-Potsdam. Flat and polished 1-inch epoxy sample mounts of micro-cored (~ 5 mm diameter) thin-sections were analyses. Prior to analysis, the samples were cleaned with ethanol in an ultrasonic bath, then sputter coated in a vacuum with 35 nm of high-purity gold. Results were obtained in two measurement sessions. Instrument parameters and analytical details are provided in Appendix 3-A and Supplemental data 3-A. To determine instrumental mass fractionation (IMF) and monitor analytical quality we used the tourmaline reference materials Harvard 112566 (schorl, $^{11}B/^{10}B = 3.9931$) and Harvard 108796 (dravite, $^{11}B/^{10}B = 4.0169$). Sixty-four analysis points from eight samples were collected, interspersed with an additional 33 points from the reference materials. The internal precision of each analysis, expressed as the relative standard deviation (RSD) from the mean of 20 cycles, [(standard deviation/$\sqrt{20}$)/mean]·1000, is better than 0.3 ‰ (2 RSD). At the GFZ SIMS lab, the repeatability and external precision, obtained from multiple daily measurements of the reference materials (RM), is calculated by (standard deviation/mean)·1000 and was generally better than 1.6 ‰ (2 RSD). After correction for IMF, the $\delta^{11}B$ values were calculated relative to NIST SRM 951 using the $^{11}B/^{10}B$ ratio of 4.04362 (± 0.00137) from Catanzaro et al. (1970) and the relationship: $\delta^{11}B‰ = \{[(^{11}B/^{10}B)_{sample} / (^{11}B/^{10}B)_{NIST\ SRM\ 951}] - 1\} \cdot 1000$.

3.3.6 Strontium isotopes

The $^{87}Sr/^{86}Sr$ isotope composition of ten whole-rock samples were analyzed by thermal ionization mass spectrometry (TIMS) using a Finnigan Mat 262 mass spectrometer at the Memorial University, Newfoundland, Canada (Appendix 3-A). The mean $^{87}Sr/^{86}Sr$ value for USGS standard reference material NBS-987 was 0.710233 (n=20) with a standard deviation of 0.000013 (1σ): see Supplemental data 3-B.

3.4 Characteristics of Na-Ca and propylitic alteration facies

The defining characteristic of the sodic-calcic (Na-Ca) facies in the HVC district is the selective replacement of primary K-feldspar by secondary albite ± fine-grained white-mica in halos around epidote ± actinolite ± tourmaline veins (sample *n* = 190; Figs. 3-3A and B). The propylitic facies in the district is composed of epidote ± prehnite ± pumpellyite veins with plagioclase-destructive white-mica–prehnite alteration ± hematite-dusted halos in which primary K-feldspar is stable (sample *n* = 265; Figs. 3-3C and D). Hornblende and biotite are generally partially replaced by chlorite ± vermiculite within propylitic vein halos (Figs. 3-3C to F). Within Na-Ca halos, primary mafic minerals are replaced by chlorite, epidote, and localized actinolite, with accessory titanite. Sulfide minerals do not occur with Na-Ca veins and there is typically less magnetite within halos compared to the adjacent wall-rock. Sodic-calcic epidote veins are generally < 0.5 cm wide and have albite alteration halos that range in width from 1–5 cm. Vein margins are typically diffuse and irregular (Fig. 3-3I), but may also be locally planar and sharp. In outcrop, Na-Ca veins form localized sheeted veins (Fig. 3-3I). In addition to the isolated sheeted veins, 1–5 m zones of tightly spaced sheeted vein arrays also occur (Fig. 3-3J), and these typically coincide with the focus of alteration in mapped Na-Ca altered domains. Within more intensely-altered halos plagioclase is replaced by albite, while primary biotite, magnetite, and hornblende are absent (Fig. 3-4A and B). Additionally, some strongly-altered rocks exhibit an inner halo of albite altered primary K-feldspar and plagioclase, and an outer halo in which only the K-feldspar has been albitized. A few samples exhibit an inner halo of albite after K-feldspar, and an outer halo of K-feldspar-stable, plagioclase-destructive, white-mica–prehnite (propylitic) alteration. Epidote veins with albite halos were locally re-fractured and overprinted by white-mica–prehnite alteration in which the plagioclase is most strongly affected, and the halo has a green color (e.g. Figs. 3-3G and H). Detailed paragenetic relationships between rock units and the Na-Ca, propylitic and other alteration facies are presented below.

Depletion in whole-rock K_2O and Fe_2O_3 is evident in epidote-(albite) facies relative to fresh and propylitic altered samples, but their SiO_2 concentrations are similar (Figs. 3-5A-C). The probability distribution of Cu in epidote-(albite) samples is lower, and so is the Zn to a lesser extent, relative to fresh samples and propylitic facies (Fig. 3-5D and E). The Pb populations, however, are similar for each facies and have a low concentration (Fig. 3-5F).

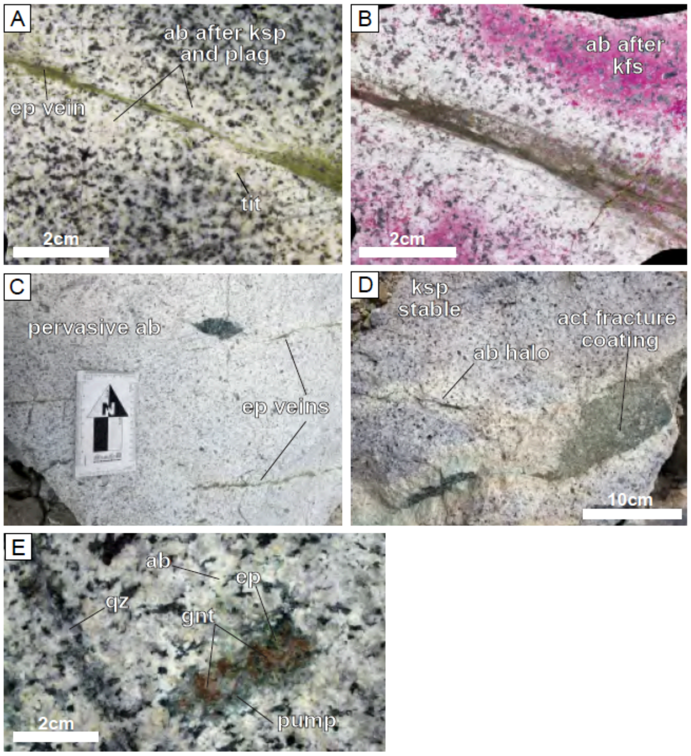

Figure 3-4. Examples of intense and pervasive Na-Ca alteration, and high-temperature calcic mineralogy at the Highmont porphyry center. A. Unstained and B. stained image pairs of an epidote vein with K-feldspar and plagioclase-destructive albite halo. Note the absence of any yellow stain after primary K-feldspar in the Guichon host rock (15KB062). Primary mafic minerals are completely altered to chlorite and accessory titanite. C. Pervasive albitization, and selective actinolite replacement of hornblende, and epidote veins in Skeena at the East Highmont pit (15KB277). D. Actinolite fracture coating / veinlet with

an albite halo (15KB276). E. Patchy tan-colored garnet and epidote alteration in pervasively albitized Skeena from the West Highmont pit. The sample is also cut by a calcite veinlet with a narrow chlorite halo. Abbreviations in Table 3-1.

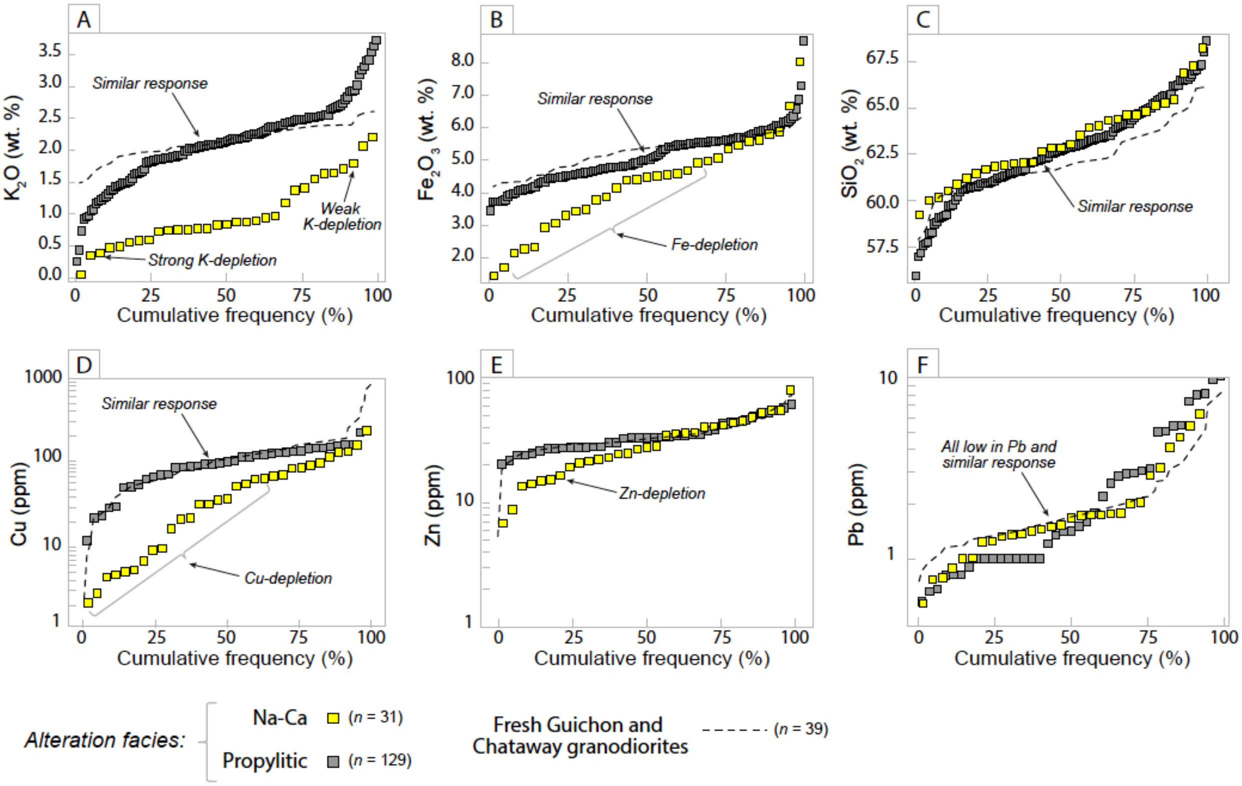

Figure 3-5.Compositional cumulative frequency plots for fresh, sodic-calcic, and propylitic facies in Guichon and Chataway granodiorite. A. K_2O, B. Fe_2O_3, C. SiO_2. D. Cu. E. Zn. F. Pb.

3.5 Spatial and temporal distribution of Na-Ca alteration facies

3.5.1 District-scale distribution

The mapped Na-Ca domains are defined by > 1.25 cm/m of epidote, and localized actinolite, veins with albite and chlorite alteration halos (Fig. 3-2). The wall-rock between the veins and halos is typically fresh. Adjacent to the Lornex and Highmont porphyry Cu centers, pervasive albitization of primary K-feldspar is more common, and actinolite veins can be found (Figs. 3-2A, and 3-4D). A small domain of diopside ± actinolite veins with albite halos occurs in the Bethlehem porphyry Cu center. Outside of the porphyry centers, primary mafic minerals in the halos of Na-Ca veins are typical altered to chlorite. Sodic-calcic facies occur in ~0.5–2 km wide, north- northeast- and northwest-trending domains that extend along trend from the Cu centers for up to 5–7 km in a non-concentric pattern (Fig. 3-2A). The orientation of the mapped Na-Ca domains is predominantly controlled by the strike of the associated epidote veins, which are steeply dipping (~70 to 90°). The widest domain (~2.5 km) of Na-Ca alteration occurs south of Lornex and Highmont and is present up to 5 km away from Cu mineralization (Fig. 3-3A). Small, isolated domains of Na-Ca alteration occur in the more mafic rocks towards the margin of the batholith (Fig. 3-2A), but excluding these, the total area of mapped Na-Ca facies is approximately 34 km^2. The average vein and halo density within this area is ~17 cm per m (Lesage et al., 2016), or ~17 %, thus the estimated aerial extent of Na-Ca altered rocks is approximately 6 km^2.

3.5.2 Deposit-scale distribution and timing relationships

The locus of Cu mineralization and hydrothermal alteration in the Bethlehem porphyry Cu system are syn-mineralization stocks of Bethlehem porphyry and inter-mineralization breccia (Fig. 3-6A; Table 3-1; Byrne et al., 2013). Potassic veins and alteration zone outwards and upwards into domains of quartz-Cu-Fe-sulfide veins with white-mica–chlorite halos (Fig. 3-6B; Table 3-1). The abundance of fracture-controlled and pervasive albitization increases with depth at the Bethlehem porphyry system and is spatially associated with post-mineralization Skeena granodiorite stock (e.g., Fig. 3-6C). Biotite-altered breccia that contains mineralized fragments, exposed in the southeast corner of the Iona pit at approximately 1450 m elevation, was overprinted by texture-destructive albite alteration (Figs. 3-7A-C). Beneath the mineralized magmatic-hydrothermal breccia at Jersey, between 1000-1100 m elevation, Na-Ca alteration is focused in, and around, a post-mineral Skeena granodiorite stock where it overprinted mineralized breccia and potassic alteration (Fig. 3-7D). A significant reduction in Cu to < 0.1 wt. % occurs in the albitized zones relative to the surrounding potassic alteration that hosts > 0.3 wt. % Cu in the breccia beneath Jersey (Fig. 3-7D). The sodic-calcic facies does not appear to form a halo around the Cu-mineralized porphyry stocks and breccias (i.e., Fig. 3-6B).

At the Lornex porphyry center, fracture-controlled and pervasive albite, locally accompanied by actinolite, is focused along the southern fringes of early-halo veins and Cu mineralization and around the composite porphyry dike complex (Fig. 3-2A inset). Albite alteration is largely absent from high levels (~1000 m) in the Valley center but it occurs at depth southwest of the Bethsaida salt and peppered textured granodiorite stock. Albite alteration locally cross-cut quartz veinlets with K-feldspar halos 2–3 km southwest of Cu mineralization on the fringes of the mapped domain of K-feldspar alteration (Figs. 3-2A and 3-7E and F).

At Highmont, albite alteration is focused along the axis of the northwest-trending composite porphyry dike complex (Figs. 3-2A inset, 3-6D and E). Pervasive albite alteration and irregular epidote replacement zones are common in Skeena granodiorite wall-rocks on the southwest side of the porphyry dike complex (Fig. 3-4C). Additionally, actinolite, intense albitization and rare garnet and diopside occur in, and adjacent, to the dike (Fig. 3-4D and E). Quartz-chalcopyrite-pyrite-K-feldspar veinlets are locally observed to cross-cut epidote-veins with albite halos at Highmont (Figs. 3-7G and H). On the northeast side of the composite porphyry dike complex, Skeena granodiorite wall-rock K-feldspar has been pervasively replaced by albite and is cut by discrete white-colored albite replacement veins (Fig. 3-7I). The albite halo veins are in turn cross-cut by EH veins of muscovite with quartz and bornite (Fig. 3-7I).

A late-mineralization magmatic-hydrothermal breccia occurs within the composite porphyry dike complex at Highmont (Fig. 3-6D). The breccia is spatially associated with quartz-phyric leucocratic porphyry dikes that cross-cuts main-stage Cu mineralization (Fig. 3-6D; QFPQ; Table 3-1). Hydrothermal cement minerals in the ellipsoidal and roughly funnel-shaped breccia are zoned (Fig. 3-6E). A mineralized core of specularite > tourmaline–quartz infill with K-feldspar and white-mica alteration, zones outwards to domains where tourmaline and quartz infill is in greater proportions than specularite, Cu mineralization is weak, and white-mica and localized albite alteration occur (Fig. 3-6E). Clasts of quartz and feldspar porphyry (QFP) with truncated quartz-bornite early-halo muscovite veins occur in the late-mineralization breccia (Fig. 3-7J). Additionally, pervasively albitized and actinolite-bearing Skeena granodiorite clasts also occur in the quartz-tourmaline and igneous cemented breccia (Fig. 3-7K). Towards the breccia margin, clast rinds are locally altered to albite adjacent tourmaline and quartz cement (Figs. 3-6E and 3-7L).

East of Highmont, Na-Ca epidote veins are cross-cut by propylitic facies prehnite veinlets with plagioclase-destructive white-mica–prehnite halos (e.g., Figs. 3-7M and 3-N), consistent with observations south of Lornex in Bethsaida granodiorite in which prehnite veinlets cut epidote veins with albite halos (Figs. 3-7O and P). Where observed together, propylitic veins and alteration minerals re-fractured, cross-cut, and overprinted the Na-Ca facies at most localities.

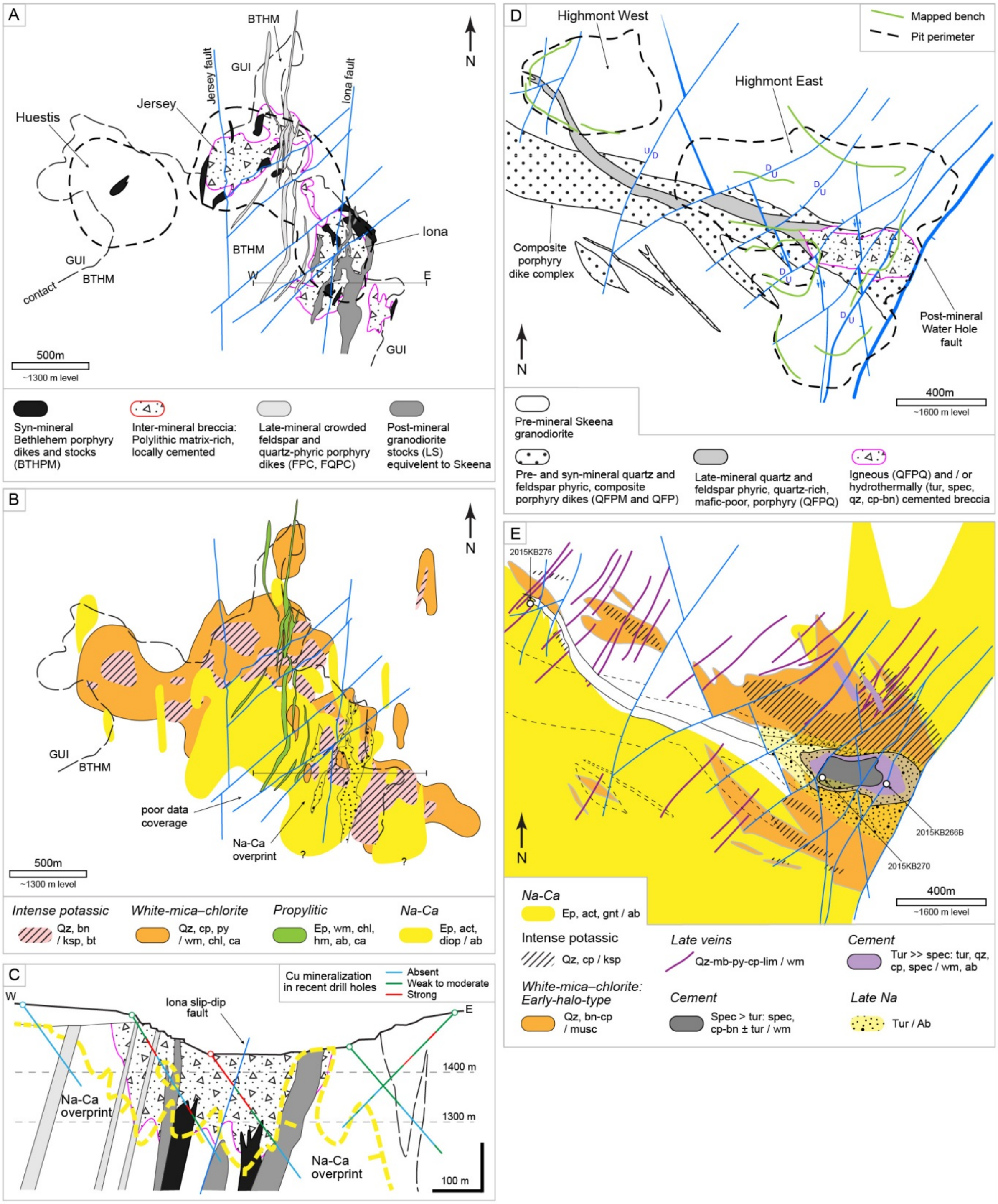

Figure 3-6. A. Simplified Bethlehem lithology and fault map and B. Generalized Bethlehem alteration domains, also shown is the location of the cross-section "W-E" C. Cross-section "W-E" through Iona. The Bethlehem maps and sections are redrafted and modified from internal Teck reports. D. Highmont lithology and fault map from bench mapping and drill hole log compilation. E. Highmont vein, cement and alteration domains. Abbreviations in Table 3-1.

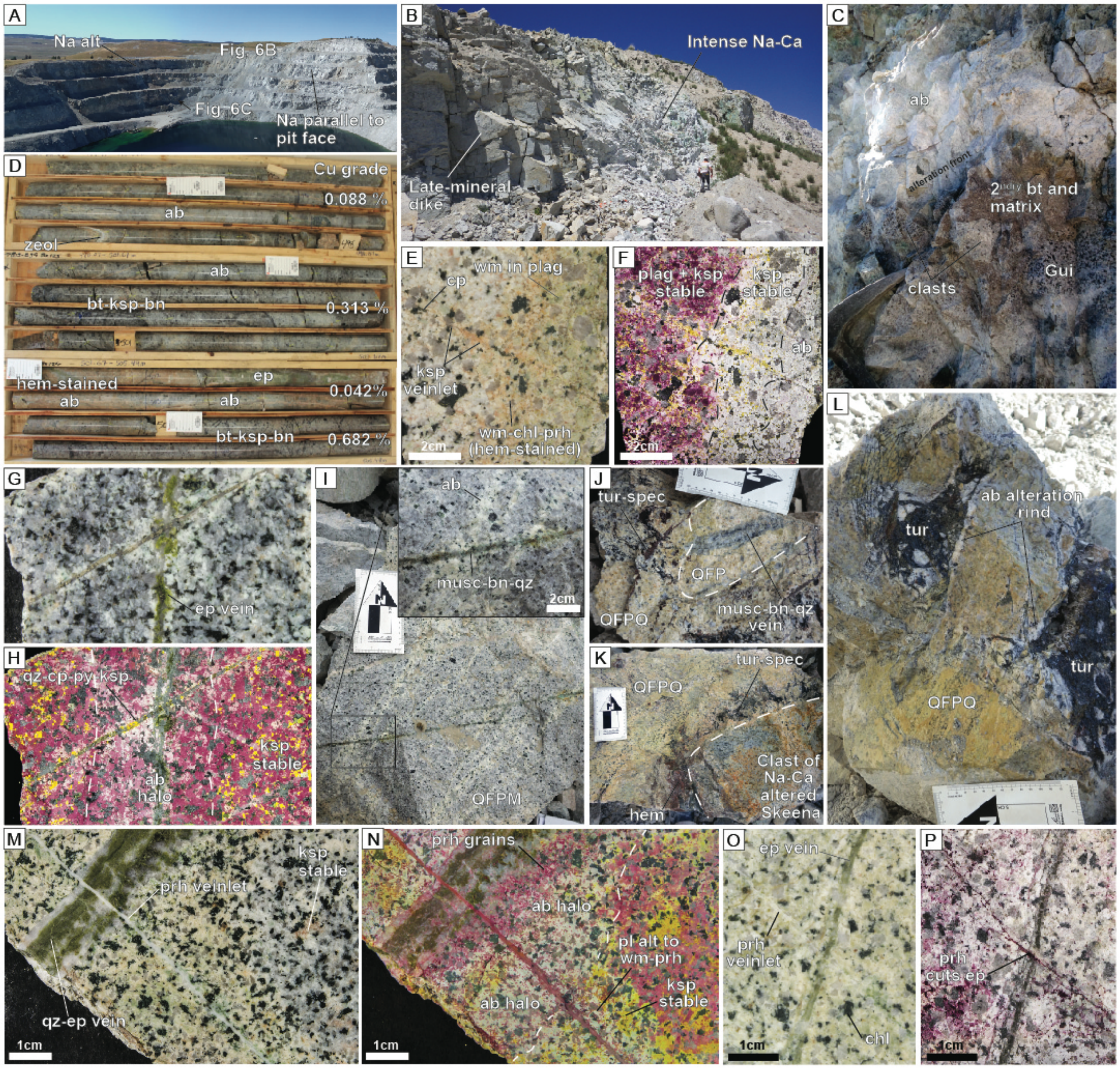

Figure 3-7. Paragenetic relationships from outcrop and hand samples. A. View looking southeast towards the Iona pit at the Bethlehem porphyry system. Labels indicate domains of Na alteration and views in Figs. 7B and C. B. West high wall of the Iona pit. Intensely albitized domain (intensely fractured) adjacent to a late-mineralization crowded feldspar and quartz porphyry (FQPC; blocky fractures). C. Polylithic, biotite altered, matrix infilled breccia overprinted by texturally destructive albite alteration. Note albitization removes mafic minerals and causes a bleached appearance. D. Early Bethlehem porphyry cross-cut by intense biotite bornite veinlets with K-feldspar and biotite alteration, in turn overprinted by epidote veins with albite halos (hematite stained). Critically, Cu and Fe sulfides were removed from the albitized domains (B13-039, ~494–505m). E. Unstained and F. stained image pairs of K-feldspar veinlet overprinted by an albite fracture halo and white-mica–prehnite–chlorite alteration (14GL038). G. Unstained and H. stained image pairs of an epidote vein with an albite halo cross-cut by a quartz-chalcopyrite-pyrite-K-feldspar vein (15KB274). I. Albite fracture halos cross-cut by fractures with EH-type muscovite and bornite fracture halos. J. Clast of quartz and feldspar-phyric porphyry (QFP) with truncated quartz-bornite vein with EH-type coarse muscovite halo in igneous (QFPQ) and hydrothermally cemented (specularite–tourmaline–quartz) breccia in the West Highmont pit. K. Pervasively albite and selectively pervasive actinolite altered Skeena clasts (15KB266) in breccia at Highmont. L. Tourmaline-quartz-specularite cemented breccia with albite alteration rinds at Highmont (15KB270). M. Unstained and N. stained image pairs of an epidote vein with K-feldspar-destructive albite halo re-opened by a quartz veins and cut and off-set by prehnite veinlet with plagioclase-destructive white-mica–prehnite halo in Chataway granodiorite (15KB170). O. Unstained and P. stained image pairs of an epidote vein with intense and pervasive albite halo cross-cut by prehnite veinlet hosted in Bethsaida granodiorite (15GL038-2247933). Abbreviations in Table 3-1.

3.6 Alteration facies and intrusive rock paragenesis

Three distinct stages of Na-Ca alteration occurred in the GCB. These stages have a close spatial and temporal link to some dikes and stocks in the HVC porphyry centers. Texture-destructive and Fe and Cu-leaching albite alteration overprinted potassic alteration at the Bethlehem porphyry centers (e.g. Figs. 3-6C and 3-7D). The most intense fracture controlled and pervasive Na-Ca alteration is focused in and around post-mineralization Skeena granodiorite stocks that intruded the Bethlehem porphyry Cu system. Following emplacement and crystallization of the Bethsaida granodiorite, a large low-density domain of potassic alteration focused on Valley-Lornex and Highmont formed (Figs. 3-2A and 3-8). Sodic-calcic alteration is most intense in and around the contact of the composite porphyry dike that connects the Lornex and Highmont porphyry centers (i.e., Figs. 3-2B and 3-6E). The few examples of Na-Ca and potassic alteration observed together at Valley-Lornex (hosted in Bethsaida granodiorite) indicate that the Na-Ca alteration is younger. The timing between EH veins and Na-Ca alteration at Valley-Lornex is ambiguous. Quartz–K-feldspar–chalcopyrite (potassic) and bornite-bearing EH veins, however, cross-cut the second stage of Na-Ca facies in Skeena granodiorite and porphyry dikes at Highmont (Table 3-1; Fig. 3-8). Fragments in the late-mineralization magmatic-hydrothermal breccia at Highmont record these older alteration events (e.g., Figs. 3-7J and K) as well as a third pulse of Na-Ca alteration as albite altered clast rinds at the breccia margins (e.g., Fig. 3-7L). Breccia formation, and the third pulse of Na-Ca alteration, occurred close in time to intrusion of quartz-phyric leucocratic porphyry dikes at Highmont (Fig. 3-8). Where observed together, propylitic prehnite veinlets cross-cut epidote veins with albite halos (e.g., Fig 3-7M-P). Textural relationships are more ambiguous, however, in re-fractured veins. Several samples occur in which K-feldspar is albite altered (Na-Ca assemblage) and plagioclase is altered to mixtures of fine-grained white-mica and prehnite (propylitic assemblage) within the same halo (e.g., Figs. 3- 3G and H).

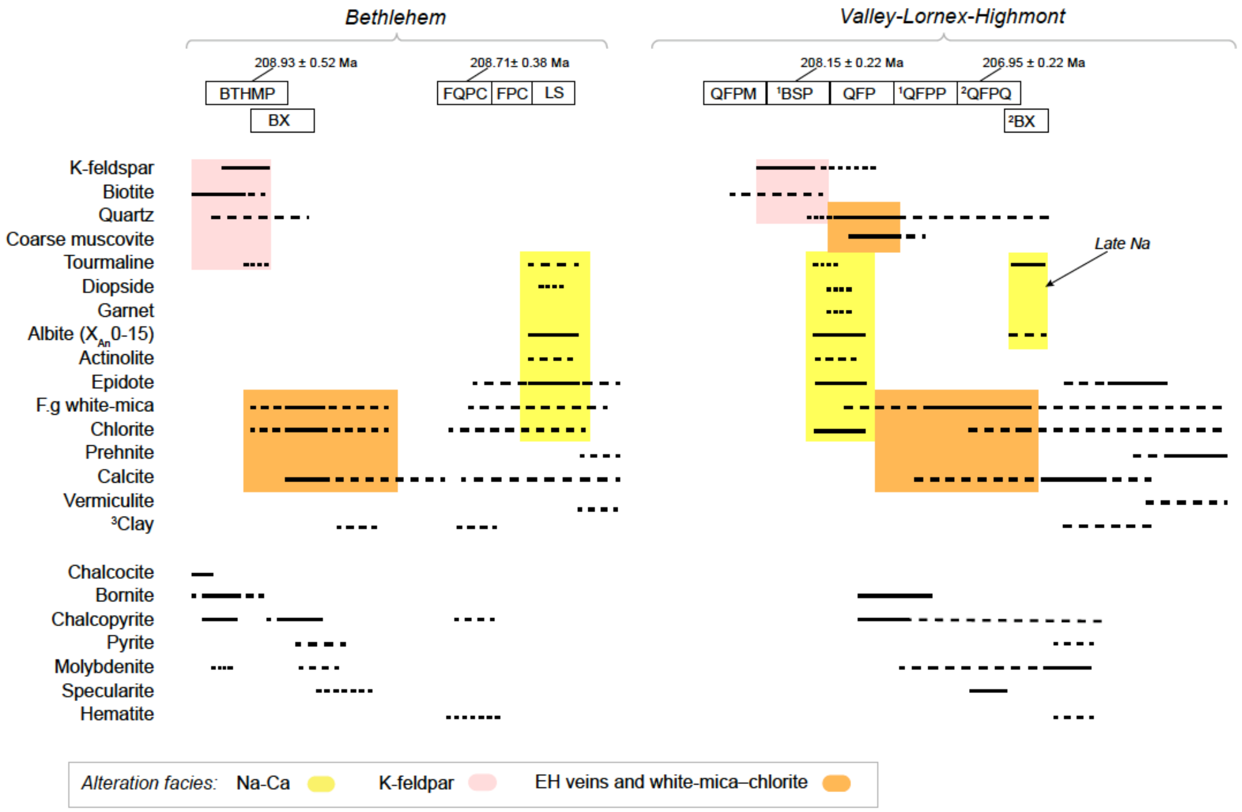

Figure 3-8. Porphyry dike, stock and hydrothermal mineral paragenesis for the Bethlehem and Valley-Lornex-Highmont areas. Abbreviations: BTHMP = Bethlehem porphyry, BSP = Bethsaida salt and pepper texture, BX = breccia undifferentiated, FPC = crowded feldspar-phyric porphyry, FQPC = Crowded feldspar and quartz-phyric porphyry, LS = Late-to-post mineralization Iona and Jersey stocks interpreted to equivalent to Skeena (Byrne et al., 2013), QFP = quartz-feldspar-phyric porphyry dikes; QFPM = quartz-feldspar-biotite-phyric porphyry dikes; QFPP = quartz-feldspar-phyric, phenocryst-poor, and mafic-poor porphyry dikelets; QFPQ = quartz-feldspar-phyric, quartz-rich porphyry dikes. ¹Units present at Valley. ²Units present at Highmont. Geochronology from D'Angelo et al. (2017).

3.7 Petrography and mineral chemistry

3.7.1 Epidote and chlorite

Epidote veins typically display fine-grained (< 20 µm) margins comprising aggregates of subhedral grains that grade to coarser (20–100 µm), locally euhedral, crystals that appear to have grown into open space (Figs. 3-9A and B). Vein centers, and inferred former vugs and interstitial space between crystals, are locally filled by younger quartz or calcite, and trace pumpellyite or clay (Figs. 3-9A and B). Additionally, some veins exhibit micro porosity (Fig. 3-9B). Electron back scatter images show compositional zoning in epidote veins that primarily reflects Fe–Al substitution (Fig. 3-9B) and sector zoning.

Mafic minerals are most commonly altered to chlorite ± epidote with accessory secondary titanite within halos of Na-Ca veins (Figs. 3-9A and F), and magnetite is partially altered to Fe-Ti-oxides or completely removed from halos in more intensely altered rocks. The Mg number of chlorite, hosted in hornblende, in the halos of Na-Ca veins is ~0.65–0.75 (Supplemental data 3-C). Where epidote occurs in the wall-rock it primarily replaced hornblende, but patchy grains also occur in plagioclase. Secondary titanite is ubiquitous with epidote alteration of mafic-minerals in the wall rocks (Fig. 3-9E).

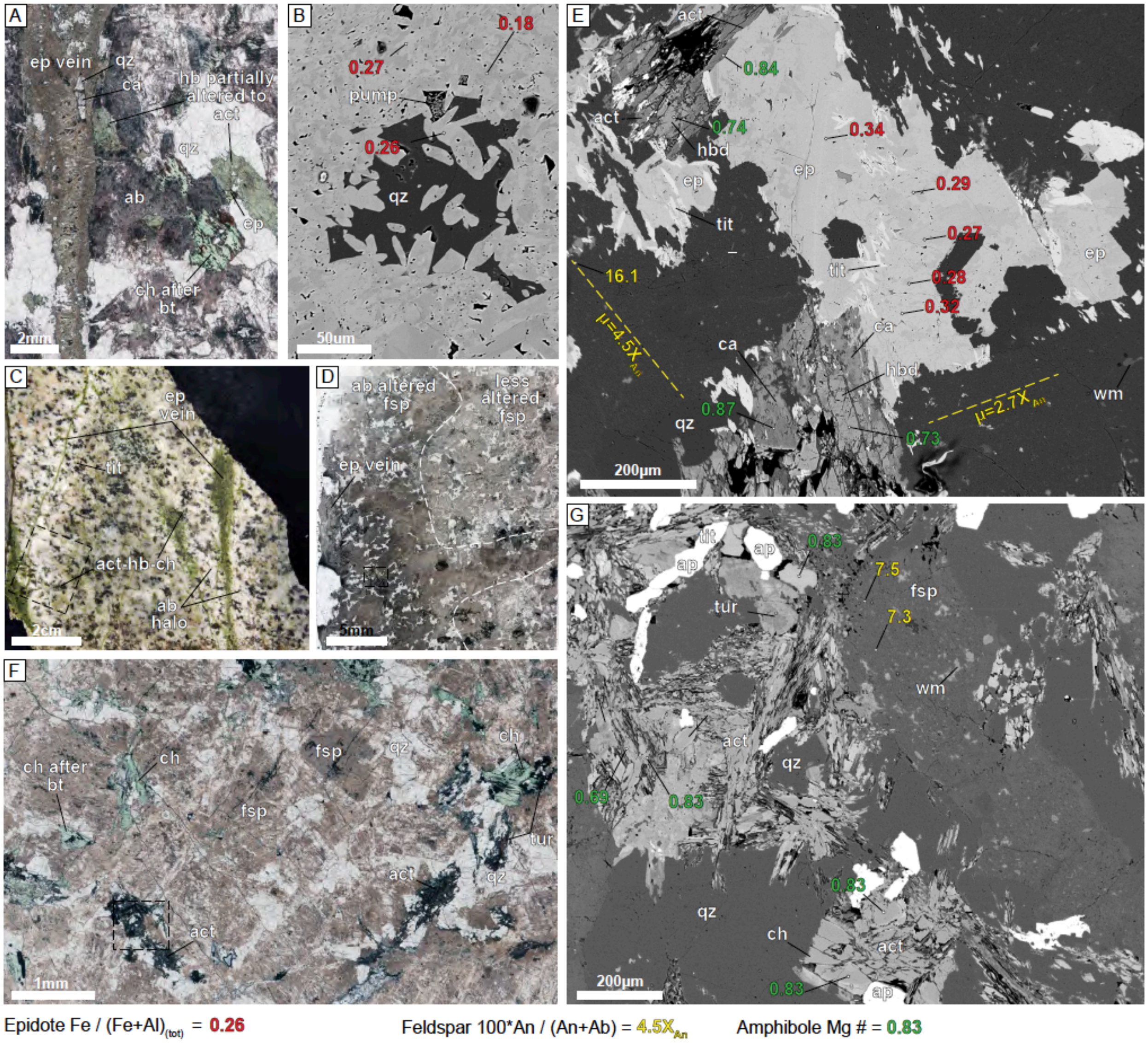

Figure 3-9. Mineral petrography. A. Transmitted light image of an epidote vein with albite, chlorite and actinolite in the halo (15KB184). The epidote vein margin comprises fine-grained (~10-20 μm) anhedral aggregated crystals and coarser subhedral to euhedral crystals in the vein center. B. Back scattered electron image and composition of epidote fill from the vein in Fig. 9A. C. Rock slab showing epidote vein with diffuse and irregular vein wall margin and albite halo (15KB060). The dashed line rectangle indicates

the area in Fig. 9D. D. Transmitted light image of an albite halo. Note that the feldspar within the albite halo adjacent the epidote vein is more turbid than less altered feldspar farther from the halo. E. Back scattered electron image and mineral composition of epidote, amphibole, and feldspar within the alteration halo. Feldspar is pervasively altered to albite and host to micro-porosity and small inclusions of white-mica. Hornblende is partially replaced by fibrous actinolite and altered along fractures. F. Transmitted light image of pervasive albite alteration and selective pervasive replacement of primary hornblende by actinolite (locally overprinted by chlorite) and tourmaline, and primary biotite by chlorite. The dashed line rectangle indicates the area in Fig. 9G. G. Back scattered electron image and composition of actinolite and albite. Actinolite occurs as aggregates of fibrous / acicular crystals interpreted to be replacing hornblende. Abbreviations in Table 3-1.

3.7.2 Feldspar

Feldspars in the halo of Na-Ca epidote veins are turbid in plane-polarized light in contrast with fresher feldspar in adjacent wall rocks (Figs. 3-8C and D). In detail, the turbidity is due to albite alteration, fine-grained inclusions of white-mica ± prehnite, and micro-porosity in pseudomorphs of primary K-feldspar and plagioclase (Figs. 3-9E-G).

In moderately to strongly Na-Ca altered samples, the feldspars in the halo of epidote and actinolite veins have X_{An} values from 1 to 20 (mole % of anorthite), but are mostly albitic and contrast with the feldspar compositions in fresh and propylitically altered rocks (Fig. 3-10; Table 3-2; Supplemental data 3-D). Secondary feldspar in the halos of veins affected by weak Na-Ca alteration have compositions that range from oligoclase to albite, lower X_{An} values than the feldspars in fresh rocks (andesine, see Fig. 3-10). Feldspars with patchy fine-grained white-mica and prehnite alteration in the halos of propylitic prehnite ± epidote veins are mostly oligoclase, but they exhibit a wide range of composition that overlaps with the andesine of fresh host rock and with the albite of Na-Ca zone feldspars. The average X_{An} value of feldspar within propylitic halos is 24, which, excluding plagioclase rims in Bethsaida granodiorite, is lower than the feldspar compositions in fresh rocks and higher than feldspar within Na-Ca halos.

Table 3-2. Representative electron microprobe analysis of feldspar in Na-Ca and propylitically altered samples

Sample	15KB041	15KB060	15KB060	15KB056	15KB056	15KB178	15KB278	15KB229B	15KB169B	15KB047	15KB266	15KB087
Analysis point	4	11	29	54	59	64	70	77	90	99	118	140
Host rock	Guichon	Guichon	Guichon	Guichon	Guichon	Chataway	Skeena	Skeena	Chataway	Guichon	Bethsaida	Guichon
Alteration facies	Na-Ca	Na-Ca	Propylitic	Na-Ca	Na-Ca	Weak Na-Ca	Weak Na-Ca	Propylitic	Na-Ca	Na-Ca	Weak Na-Ca	Na-Ca
Texture	In halo	In halo	Outside halo	In halo	Outside halo	In halo	In halo	Outside halo	In halo	In halo	In halo	In halo
Wt. %												
SiO_2	65.4	65.8	60	65.3	64.1	66.6	64.2	60.8	65.8	63.5	63	68
Al_2O_3	20.6	20.8	24.7	21.7	22.3	21.5	22.3	23.4	21.4	22.3	23.1	20.3
FeO	0	0.1	0.3	0	0.1	0	0	0.1	0	0.1	0.2	0
CaO	0.8	0.5	6.3	1	2.1	1	2	4.3	1.4	2.7	3.8	0.2
SrO	0.1	0.1	0.1	0.2	0.2	0.2	0.1	0.1	0.2	0.3	0.2	0.2
Na_2O	10.8	10.8	7.8	11.2	10.7	11.3	10.4	8.9	10.7	10	9.1	11.2
K_2O	0.2	0.5	0.4	0	0	0.1	0.1	0.1	0.1	0.1	0.3	0
Total	*97.9*	*98.5*	*99.6*	*99.4*	*99.5*	*100.7*	*99.2*	*97.7*	*99.6*	*98.9*	*99.6*	*99.9*
Normalization based on 5 cations												
Si	2.92	2.92	2.68	2.87	2.82	2.89	2.84	2.75	2.9	2.82	2.8	2.98
Al	1.08	1.09	1.3	1.12	1.16	1.1	1.16	1.25	1.11	1.17	1.21	1.05
Z total	*4.01*	*4.01*	*3.99*	*3.99*	*3.98*	*3.99*	*4*	*4*	*4.01*	*4*	*4.01*	*4.03*
Ca	0.04	0.02	0.3	0.05	0.1	0.05	0.09	0.21	0.07	0.13	0.18	0.01
Na	0.94	0.93	0.68	0.95	0.91	0.95	0.89	0.78	0.91	0.87	0.78	0.95
K	0.01	0.03	0.02	0	0	0	0	0.01	0	0	0.02	0
Sr	0	0	0	0	0.01	0	0	0	0.01	0.01	0.01	0.01
X total	*0.99*	*0.98*	*1.01*	*1.01*	*1.02*	*1.01*	*0.99*	*1*	*0.99*	*1*	*0.98*	*0.97*
An%	3.69	2.42	30	4.89	9.54	4.69	9.38	21.15	6.83	12.69	18.43	0.88
Ab%	94.98	94.75	67.78	95	90.23	94.92	90.22	78.04	92.83	86.91	79.94	99.06
Or%	1.33	2.83	2.22	0.11	0.22	0.39	0.4	0.81	0.34	0.4	1.63	0.06
XAn	3.74	2.49	30.68	4.9	9.57	4.71	9.41	21.32	6.85	12.74	18.74	0.88

All analyses provided in Supplemental data 3-D.

3.7.3 Actinolite

Actinolite locally occurs in the halos of Na-Ca veins and is characterized by clusters of acicular and fibrous crystals that are predominantly hosted in primary amphibole (Figs. 3-9F and G). Alteration of primary amphibole along fractures also occurs in some Na-Ca and propylitic altered rocks but lacks the fibrous texture of more intensely actinolite altered samples. Actinolite is intergrown with zoned tourmaline crystals in some samples from the Highmont pit (Fig. 3-9G).

The compositional data for amphibole have been organized by alteration facies and textural characteristics (Table 3-3; Supplemental data 3-E). The compositional diagrams (Fig. 3-11) include amphibole with a fresh appearance from least-altered rocks and grains from altered wall rocks, but no vein fill. Amphibole with a fresh appearance from least-altered rocks are magnesio-hornblende and have C-site values of ($Al+Fe^{3+}+2Ti$) per formulae unit mostly in excess of 0.75. Aggregates of fibrous crystals of secondary amphibole within Na-Ca halos are mostly actinolite or subordinate tremolite, and have lower T-site Si and A-site totals than the other types of amphibole (Fig. 3-11). Amphibole that appears fresh, or formed along fractures in primary mafic minerals within propylitic halos are mostly magnesio-hornblende, and have compositions intermediate to the amphibole in fresh rocks and fibrous actinolite Na-Ca halos.

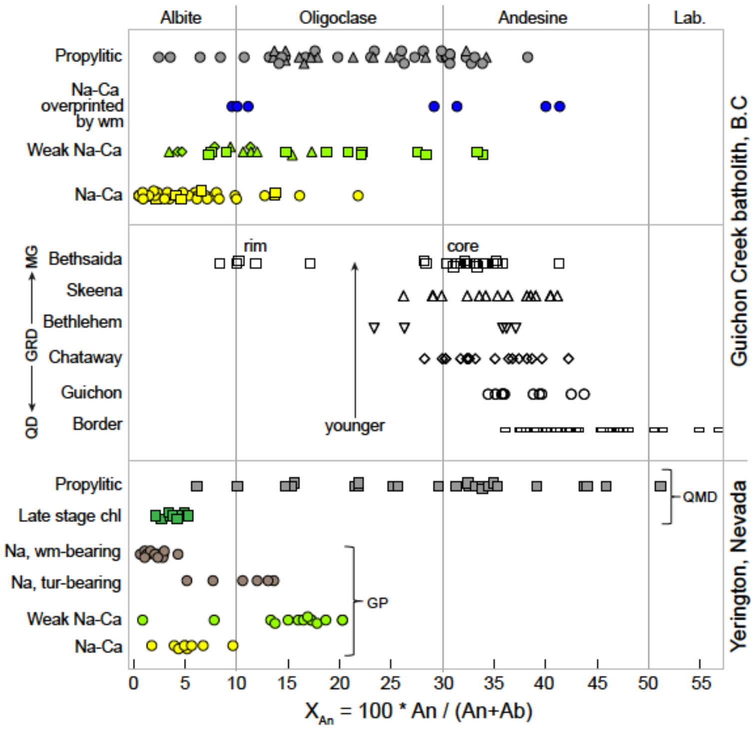

Figure 3-10. Plagioclase composition from altered rocks in the Guichon Creek batholith (modified after Dilles and Einaudi, 1992). Sample n = 12 and analysis points n = 149. Least altered host-rock feldspar composition from D'Angelo (2016). Alteration plagioclase compositions in the Yerington porphyry, skarn, and iron oxide deposit district, Nevada (Dilles and Einaudi, 1992).

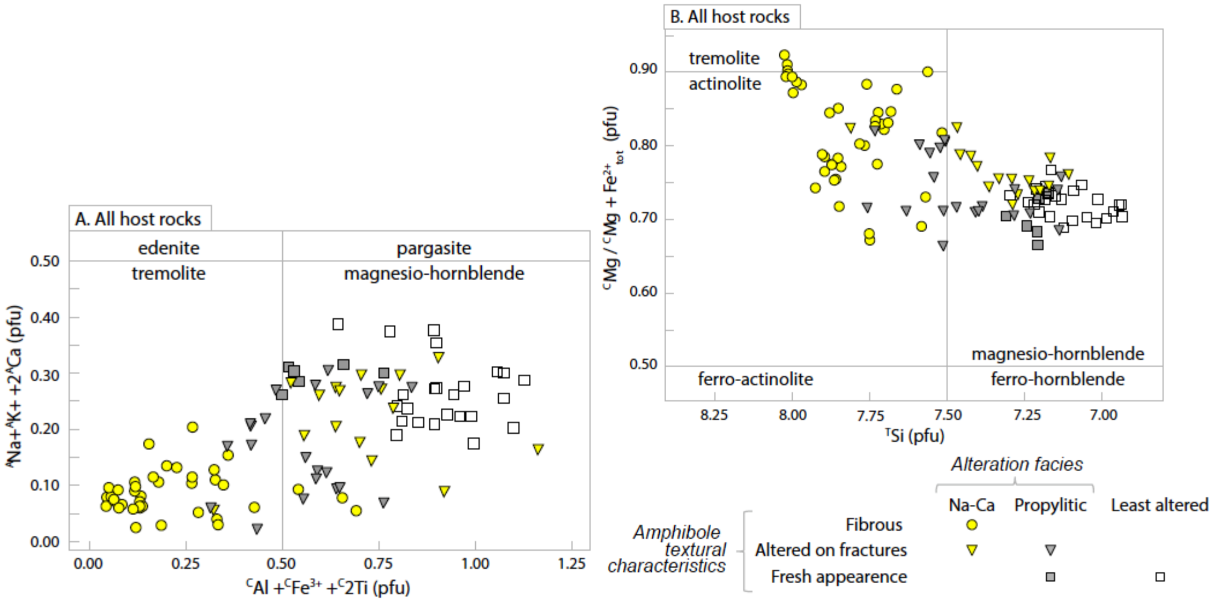

Figure 3-11. Amphibole compositions in the Guichon Creek batholith. A. Na+K+2Ca vs. Al+Fe+2Ti for all host rocks (from Hawthorne et al., 2012). B. Mg / Mg+Fe vs. Si for all host rocks (after Leake et al., 1997). Sample n = 11 and analysis points n = 85. Least altered host-rock amphibole composition from D'Angelo (2016).

Table 3-3. Representative electron microprobe analyses of amphibole

Station	15KB060	15KB056	15KB178	15KB229B	15KB266	15KB087	15KB111	15KB111	15KB022	16KB047	15KB030
Analysis No.	4	17	23	31	36	53	42	46	71	75	80
Host rock	Guichon	Guichon	Chataway	Skeena	Bethsaida	Guichon	Guichon	Guichon	Guichon	Border	Guichon
Facies	Na-Ca	Na-Ca	Na-Ca	Na-Ca	Na-Ca	Na-Ca	Prop	Prop	Prop	Prop	Prop
Texture	PA	FCC	FCC	PA	FCC	FCC	LA	PA	LA	PA	PA
Morphology	In halo	Replacement vein	In vein	In halo	In halo	Adjacent vein	In halo	In halo	In halo	In halo	Adjacent vein
Wt. %											
SiO_2	50.78	54.23	55	52.43	54.38	58.43	49.19	49.6	49.66	48.98	52.79
TiO_2	0.74	0.08	0.04	0.44	0.44	0	1.03	1	0.97	0.88	0.2
Al_2O_3	5.18	1.86	0.87	3.24	2.66	0.27	5.55	5.22	5.53	5.74	2.45
MnO	0.39	0.08	0.59	0.96	0.31	0.02	0.45	0.4	0.43	0.28	0.48
FeO	11.84	8.55	10.41	10.1	6.87	3.23	12.31	11.73	12.12	11.67	13.19
MgO	15.74	18.65	17.1	17.25	18.38	21.85	14.3	14.79	15.45	15.27	15.54
CaO	12.31	13.12	13.3	12.21	12.49	13.74	12	12.19	12.08	12.78	12.15
Na_2O	0.93	0.3	0.06	0.52	0.65	0.07	0.92	0.83	0.97	0.65	0.31
K_2O	0.42	0.11	0.07	0.23	0.27	0	0.52	0.48	0.54	0.51	0.18
Sub Total	98.33	96.98	97.44	97.38	96.45	97.61	96.27	96.24	97.75	96.76	97.29
MnO	0.39	0.08	0.59	0.96	0.31	0.02	0.45	0.4	0.43	0.28	0.48
FeO	10.12	7.19	9.98	6.48	6.87	3.23	11.4	10.98	9.87	9.52	11.2
Fe_2O_3	1.91	1.51	0.47	4.02	0	0	1.01	0.83	2.51	2.39	2.21
H_2O	2.08	2.13	2.11	2.11	2.14	2.19	2.07	2.08	2.07	2.08	2.08
Final Wt.%	100.6	99.26	99.6	99.89	98.59	99.8	98.44	98.4	100.07	99.08	99.59
Normalization is based on the cation and 23O equivalent scheme of Locock (2014)											
Si	7.272	7.705	7.866	7.468	7.734	8.027	7.243	7.284	7.172	7.142	7.632
Al	0.728	0.295	0.134	0.532	0.266	0	0.757	0.716	0.828	0.858	0.368
Ti											
T total	*8*	*8*	*8*	*8*	*8*	*8.027*	*8*	*8*	*8*	*8*	*8*
Ti	0.08	0.009	0	0.047	0.047	0	0.114	0.11	0.105	0.097	0.022
Al	0.146	0.017	0.012	0.012	0.18	0.044	0.206	0.187	0.113	0.128	0.05
Fe^{3+}	0.206	0.161	0.051	0.43	0	0	0.112	0.093	0.273	0.262	0.241
Mn^{2+}	0	0.008	0.071	0.075	0.037	0	0.024	0.023	0	0.033	0
Fe^{2+}	1.208	0.855	1.194	0.773	0.817	0.371	1.404	1.348	1.182	1.161	1.338
Mg	3.36	3.95	3.646	3.663	3.897	4.475	3.139	3.238	3.326	3.319	3.349
C total	*5*	*5*	*4.978*	*5*	*4.978*	*4.892*	*4.999*	*4.999*	*4.999*	*5*	*5*
Mn^{2+}	0.047	0	0	0.041	0	0	0.032	0.026	0.053	0	0.059
Fe^{2+}	0.005	0	0	0	0	0	0	0	0.008	0	0.016
Ca	1.889	1.997	2	1.863	1.903	2	1.893	1.918	1.869	1.997	1.882
Na	0.059	0.001	0	0.095	0.097	0	0.075	0.056	0.07	0	0.043
B total	*2*	*1.999*	*2*	*1.999*	*2*	*2*	*2*	*2*	*2*	*2.001*	*2*
Ca			0.038			0.022					
Na	0.199	0.081	0.017	0.048	0.083	0.019	0.188	0.181	0.202	0.182	0.044
K	0.077	0.02	0.013	0.042	0.049	0	0.098	0.09	0.099	0.095	0.033
A total	*0.276*	*0.101*	*0.106*	*0.09*	*0.132*	*0.063*	*0.286*	*0.271*	*0.301*	*0.277*	*0.077*
OH	2	2	2	2	2	2	2	2	2	2	2
O (non-W)	22	22	22	22	22	22	22	22	22	22	22
$Al+Fe^{3+}+2Ti$	0.638	0.348	0.118	0.919	0.227	0.044	0.544	0.483	0.764	0.749	0.554
Mg # = Mg /(Mg+Fe^{2+})	0.735	0.822	0.753	0.826	0.827	0.923	0.691	0.706	0.736	0.741	0.712
Mineral Species	magnesio-ferri-hornblende	actinolite	actinolite	magnesio-ferri-hornblende	actinolite	tremolite	magnesio-hornblende	magnesio-hornblende	magnesio-ferri-hornblende	magnesio-ferri-hornblende	actinolite

Abbreviations: PA = Partially altered or fracture controlled, FCC = Fibrous, clots, clusters, LA = least altered / fresh appearance. Normalization procedures from Locock (2014).

3.7.4 Tourmaline

In the HVC district tourmaline occurs in veins with 1) K-feldspar, 2) white-mica–chlorite, and 3) albite alteration halos. In plane polarized light, the tourmaline is green or brown, exhibits strong pleochroism (Figs. 3-12A–C), and commonly occurs as rosettes. Tourmaline-chalcopyrite veins with K-feldspar halos and / or white-mica–chlorite alteration occur north of Bethlehem (Figs. 3-12A and B) and around Highmont. In sample 15KB87B, a tourmaline-epidote vein has a halo of actinolite and albite, but in detail, the tourmaline predates the epidote fill and is brecciated (Figs. 3-12C and D). Two other samples also have tourmaline that predates epidote fill and are classified as pre-Na-Ca. Albite-altered clast rinds in tourmaline-cemented breccia occur at Highmont (Figs. 3-12E and F). In this case, the tourmaline is syn-Na-Ca alteration. Two additional samples of tourmaline veins with albite halos that were studied (e.g., Fig. 3-12G) contain tourmaline with inclusions of actinolite, suggesting that the tourmaline replaced actinolite adjacent to vein wall margins (Fig. 3-12H). This tourmaline is classified as post-Na-Ca alteration. Multiple stages of tourmaline growth are evident in the syn-Na-Ca sample from the Highmont breccia. Based on the back scattered electron images, the first stage (T1) tourmaline has two subtle zones comprising large dark cores and slightly lighter margins. The first stage of tourmaline is locally cross-cut by a second stage (T2) overgrowth of zoned tourmaline that is more Fe-rich than the T1 tourmaline (Fig. 3-12F). Additionally, T1 tourmaline is mostly colorless and T2 exhibits green-brown to dark green pleochroism. Sector zoning is the most common style of zoning observed in HVC tourmaline, followed by patchy and rare oscillatory zoning. Furthermore, some samples exhibit more than one zonation style, whereby the core is sector zoned and the margin is oscillatory zoned (Fig. 3-12).

All but a very few tourmaline analyses plot in the alkali group of Henry et al. (2011), with one borderline vacancy-group example and three analyses in the Ca-group field (Fig. 3-13A). The Fe-Mg-Al triangular plots (Figs. 3-13 B and C) shows a considerable range of compositions, but this is mostly related to the Al contents, with a relatively constant Fe/Mg ratio. The Mg contents per formulae unit are between approximately 1.5 and 2 (Table 3-4; Supplemental data 3-F). With the exception of the T1 tourmaline from the Highmont breccia that falls near the Mg-foitite end-member, all tourmaline plots below the schorl (buergerite)-dravite join, i.e. they are Al-deficient with < 6 Al per formula unit and trend toward the povondraite endmember (Figs. 3-13B and C). The charge balance caused by the Al-deficiency is inferred to be compensated by

Fe^{3+} in alkali group tourmaline (Henry et al., 2011). For the HVC tourmaline, the estimated Fe^{3+} per formula unit and Fe^{3+}/Fe^{2+} value, based on normalization to 18 cations (Y, T, Z and B sites) and 31 anions, for the Al-deficient tourmaline is 0.55 and 0.37, respectively (Table 3-4).

Analyses of tourmaline in veins with K-feldspar and white-mica–chlorite halos cluster together along the join between magnesio-foitite and povondraite, with a narrow range of total Al per formula unit between 5.25 and 6 (Fig. 3-13B).

The pre-Na-Ca tourmaline shows a wide compositional range mostly due to $FeAl_{-1}$ substitution that partially overlaps with the composition of tourmaline in veins without any Na-Ca alteration (Fig. 3-13 D). The syn-Na-Ca tourmaline has two distinct compositions related to growth stage. The first stage tourmaline (T1) is magnesio-foitite (Fig. 3-13C), with <6 Si atoms per formula unit and total Al per formula unit of 6.5 – 8 (Fig. 3-12D; Table 3-4). Additionally, T1 tourmaline has higher X-site vacancies compared to the other tourmaline groups (Fig. 3-13A). Second stage tourmaline (T2) is characterized by a higher Fe/Mg ratio compared to tourmaline from the other facies (Fig. 3-13C). Post-Na-Ca tourmalines have compositions that overlap with non-Na-Ca and the pre-Na-Ca tourmaline. Additionally, many analyses of tourmaline occurring in Na-Ca veins have Fe per formulae unit >2, that contrasts with tourmaline from potassic and white-mica–chlorite veins (Fig. 3-13D).

The electron microprobe analysis totals (i.e., excluding B_2O_3 and H_2O) of the tourmaline with < 6 Al per formula unit (~99 % of the data) are normal for that mineral, at around 84–86 wt. % (Henry et al., 2011). However, the exceptional Al-rich and Si-poor T1 tourmaline analyses yielded consistently lower totals of approximately 81 wt. % (Table 3-4). Analyses of all tourmaline samples were done with the same set-up and instrument, and even repeat analyses of the low-total tourmaline with the microprobe at GFZ Potsdam reproduced these results. Furthermore, a scan of energy-dispersion spectrometry (EDS) showed no signs for significant concentrations of elements not analysed (e.g., halogens, S, Sr). Lithium is not in the EDS spectrum but is not expected in significant concentrations in tourmaline from these types of rocks (Henry et al., 2011). Thus, we do not have an explanation for the low totals of the T1 tourmaline.

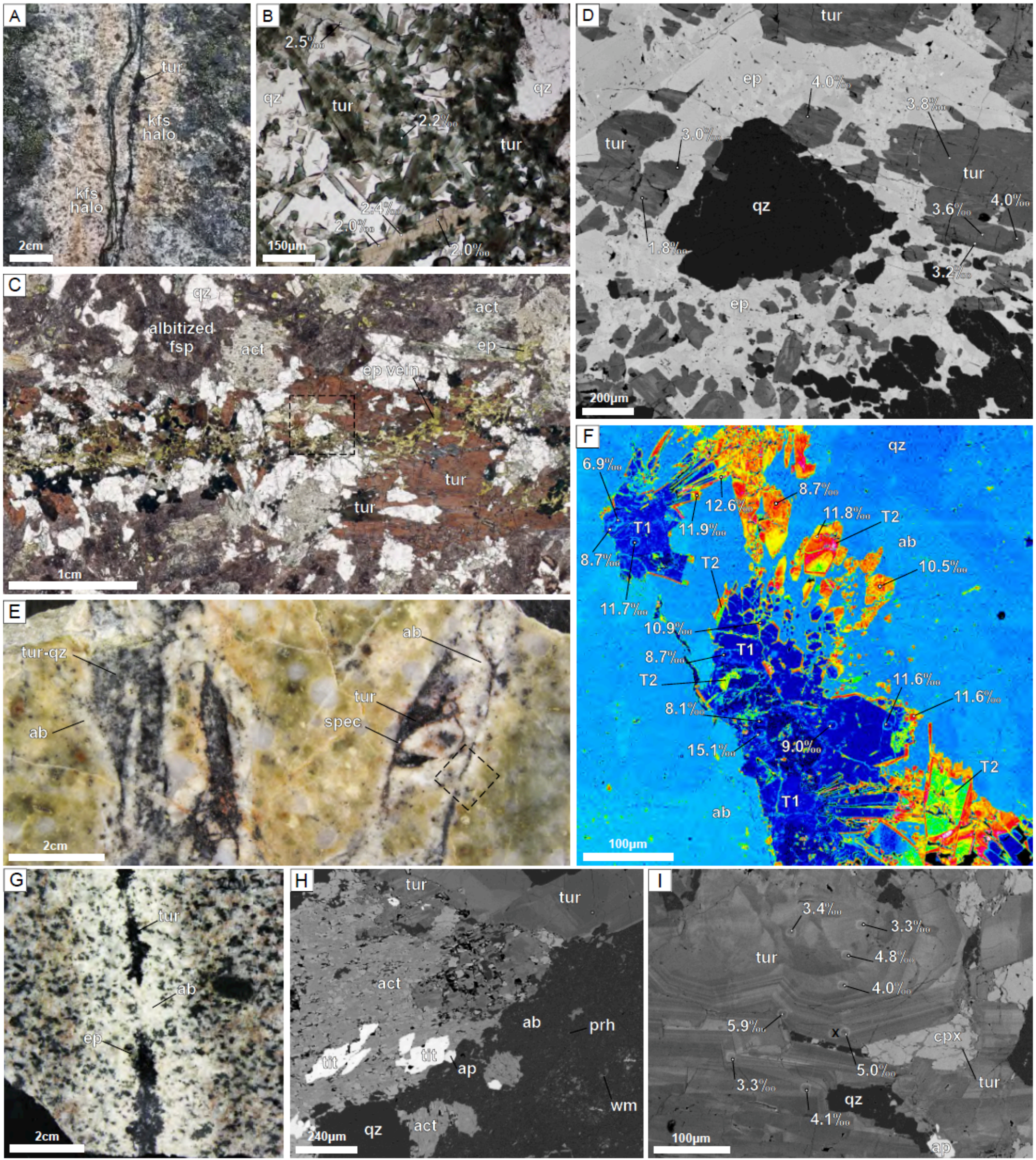

Figure 3-12. Tourmaline petrography and some boron isotope (δ^{11}B‰) results. A. Tourmaline–quartz vein with K-feldspar halo (15KB093). B. Aggregates of elongated green–light-brown pleochroic tourmaline intergrown with quartz. C. Transmitted light image of tourmaline vein fill and alteration cross-cut by epidote vein with an albite, actinolite and chlorite halo. The tourmaline exhibits patchy zoning and dark brown–light brown pleochroism. The dashed line rectangle indicates the area in Fig. 3-12D. D. Back scattered electron image shows zoned epidote vein fill with fragments of older tourmaline. The tourmaline shows some light colored core to darker rim zoning (15KB087-SB). E. Tourmaline-quartz and minor specularite cemented breccia (15KB270). Albite occurs in the alteration rind around the cement fill in the quartz-rich porphyry (QFPQ) at the West Highmont pit. The dashed line rectangle indicates the area in Fig. 3-12F. F. False colored back scattered electron image of two stages (T1 and T2) of radiating

tourmaline in the breccia cement. T1 is Fe poor and Al rich, whereas T2 is Fe-rich and occurs as overgrowths and minor cross-cutting fracture fill in T1 tourmaline. G. Fracture halo of albite, epidote, actinolite and chlorite alteration with late, possibly overprinting, tourmaline occluding the vein. H. Back scattered electron image of the tourmaline vein from Fig. 3-12G, in which the tourmaline appears to be replacing actinolite after hornblende. I. Back scattered electron image of the tourmaline vein from Fig. 3-12G that exhibits a small core domain with sector zoning and a larger domain of oscillatory zoning. Abbreviations in Table 3-1.

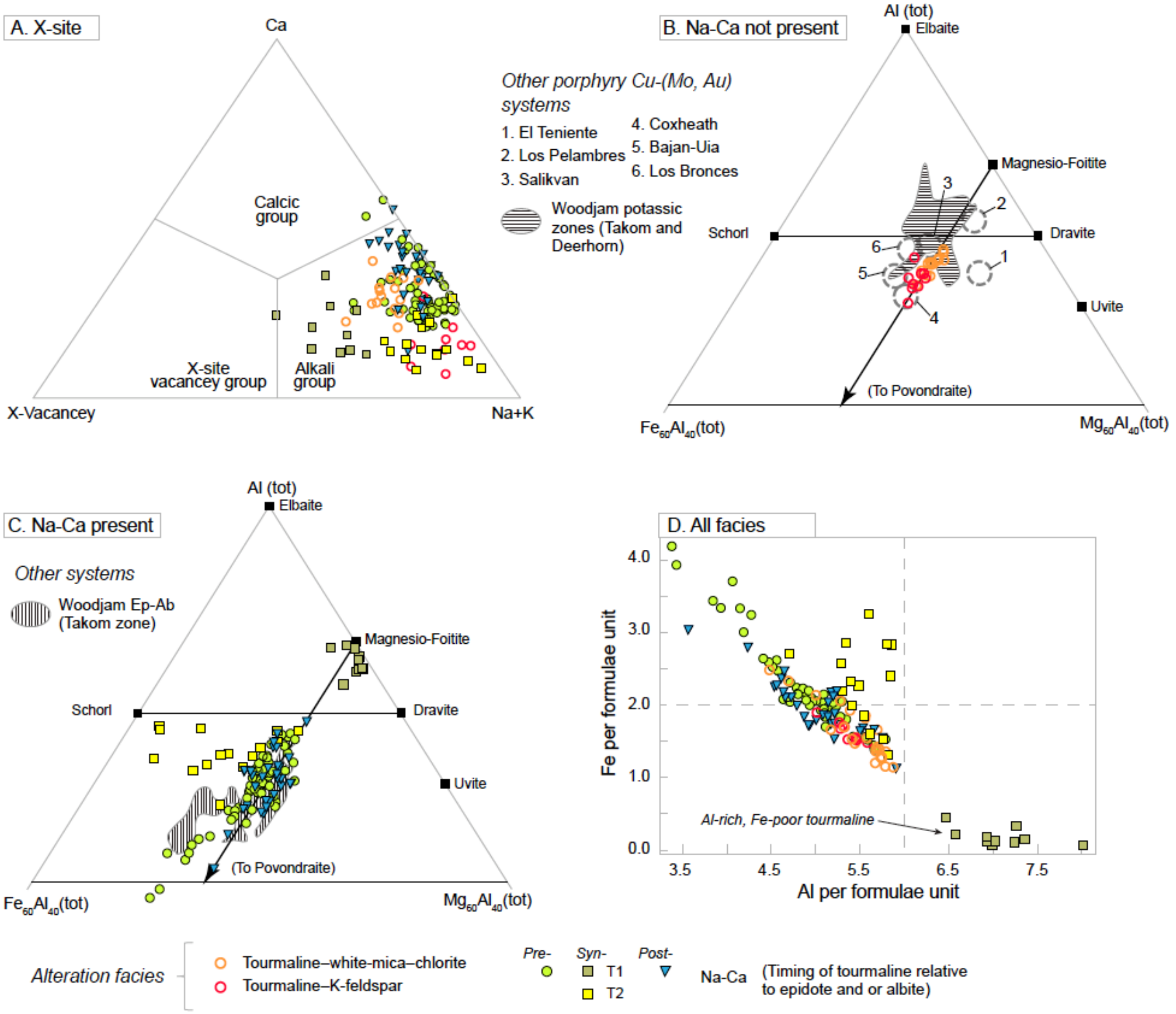

Figure 3-13. Tourmaline composition from altered rocks in the Guichon Creek batholith. A. Cation proportions of total Al, Fe and Mg, after Henry et al. (2011), of tourmaline that occurs with white-mica–chlorite and K-feldspar. B. Cation proportions of total Al, Fe and Mg of tourmaline that occurs with Na-Ca facies organized by the relative timing of tourmaline with respect to epidote and / or albite. C. The composition tourmaline based on the principal constituents at the X site after Henry et al. (2011). Sample n = 10, analysis points n = 141. The tourmaline fields for the Woodjam porphyry Cu occurence in central BC, Canada are from Chapman et al. (2015). The composition of tourmaline in veins and breccia associated with mineralization of other porphyry Cu-(Mo-Au) systems are from Yavuz et al. (1999) and references therein.

Table 3-4. Representative electron microprobe analysis of tourmaline

Sample	16KB010	16KB047	15KB069	15KB103A	15KB266B	15KB087	15KB270	15KB270	15KB270	15KB056	15KB047
Analysis point	95	144	116	76	104	110	127	136	130	155	160
Host Rock	Chataway	Border	Border	Chataway	Bethsaida	Guichon	QFPQ	QFPQ	QFPQ	Guichon	Guichon
Alteration facies: Early / Late	Kfs-Tur / Wm-Chl	Ep-Kfs / Tur-Wm-Chl	Tur-Wm-Chl / Na-Ca	Tur-Wm-Chl / Na-Ca	Tur-Wm-Chl / Na-Ca	Tur-Wm-Chl / Na-Ca	Tur-Ab / Wm-Chl-Kln	Tur-Ab / Wm-Chl-Kln	Tur-Ab / Wm-Chl-Kln	Na-Ca / Tur-Wm-Chl	Na-Ca / Tur-Wm-Chl
Tur timing w.r.t Na-Ca	No Na-Ca	No Na-Ca	Pre Na-Ca	Pre Na-Ca	Pre Na-Ca	Pre Na-Ca	Syn Na-Ca (T1)	Syn Na-Ca (T1)	Syn Na-Ca (T2)	Post Na-Ca	Post Na-Ca
Wt. %											
Na_2O	2.27	1.75	1.31	2.08	1.76	1.97	1.34	1.19	2.01	1.64	1.77
MgO	7.41	7.51	8.82	7	5.78	7.49	7.92	7.19	5.97	7.17	6.09
Al_2O_3	26.45	27.78	25.46	23.62	19.56	28.03	38.07	37.51	22.56	25.1	25.03
SiO_2	35.58	34.6	33.79	35.8	32.79	35.28	30.18	31.83	33.68	33.86	34.04
K_2O	0.04	0.04	0.01	0.02	0.08	0.04	0	0	0.03	0.05	0.05
CaO	0.91	1.69	3	1.73	1.3	1.46	1.96	1.33	1.05	1.92	1.55
TiO_2	0.31	0.56	0.6	0.54	0.4	0.32	0.16	0.07	0.16	0.58	0.59
MnO	0.03	0.03	0.02	0.02	0.07	0.04	0	0	0.12	0	0.06
FeO	9.26	8.84	8.16	12.49	10.08	9.06	1.06	2.36	10.03	9.54	11.19
*Fe_2O_3	3.1	2.24	3.75	2.68	13.43	2.27	0	0.1	9.23	5.04	4.13
SrO	0.06			0.07							
Sub Total	85.42	85.04	84.92	86.05	85.25	85.96	80.69	81.58	84.84	84.90	84.50
*B_2O_3	10.22	10.21	10.09	10.08	9.65	10.32	12.7	12	9.82	10.01	9.92
*H_2O	3.52	3.52	3.48	3.48	3.33	3.56	3.66	3.65	3.39	3.45	3.42
Total	99.16	98.77	98.48	99.6	98.23	99.83	97.05	97.23	98.05	98.36	97.85
Normalization based on 18 cations (Y, T, Z and B) and 31 anions. Site allocations following Henry et al. (2011)											
Na	0.749	0.578	0.438	0.696	0.614	0.643	0.426	0.379	0.69	0.552	0.601
Ca	0.166	0.308	0.554	0.32	0.251	0.264	0.344	0.234	0.199	0.357	0.291
K	0.009	0.009	0.002	0.004	0.018	0.009	0	0	0.007	0.011	0.011
Sr	0.006			0.007							
X-site vacancy	0.07	0.105	0.006	0	0.117	0.084	0.23	0.387	0.104	0.079	0.096
X total	*1*	*1*	*1*	*1.027*	*1*	*1*	*1*	*1*	*1*	*1*	*1*
Mg	1.185	1.377	1.257	0.602	0	1.39	1.936	1.761	0.245	0.88	0.728
Fe^{2+}	1.318	1.26	1.175	1.802	1.516	1.276	0.145	0.324	1.486	1.385	1.641
Mn	0.004	0.004	0.003	0.003	0.011	0.006	0	0	0.018	0	0.009
Al							0.9	0.89			
Fe^{3+}	0.397	0.287	0.486	0.348	1.419	0.288	0	0.012	1.23	0.659	0.545
Ti	0.04	0.072	0.078	0.07	0.054	0.041	0.02	0.009	0.021	0.076	0.078
Y total	2.944	3	3	2.825	2.999	3	3.001	2.996	3	3	3
Al	5.305	5.47	4.992	4.802	4.049	5.509	6	6	4.669	5.023	5.136
Fe^{3+}					0.4						
Mg^{2+}	0.695	0.53	1.008	1.198	1.551	0.491	0	0	1.331	0.977	0.864
Z total	*6*	*6*	*6*	*6*	*6*	*6*	*6*	*6*	*6*	*6*	*6*
Si	6.055	5.894	5.822	6.176	5.9	5.944	4.948	5.229	5.962	5.883	5.966
Al	0	0.106	0.178	0	0.1	0.056	0.46	0.37	0.038	0.117	0.034
B							0.594	0.403			
T total	*6.055*	*6*	*6*	*6.176*	*6*	*6*	*6.002*	*6.002*	*6*	*6*	*6*
B	3.002	3	2.999	3.001	2.997	2.999	3	3	3.001	3.002	3.001
W (OH^{1-})	4	4	4	4	4	4	4	4	4	4	4
Y+T+Z+B	18	18	18	18	18	18	18	18	18	18	18
Al tot	5.31	5.58	5.17	4.8	4.15	5.57	7.36	7.26	4.71	5.14	5.17
Fe tot	1.72	1.55	1.66	2.15	3.33	1.56	0.15	0.34	2.72	2.04	2.19
Mg tot	1.88	1.91	2.27	1.8	1.55	1.88	1.94	1.76	1.58	1.86	1.59
Mg/(Fe+Mg)	0.52	0.55	0.58	0.46	0.32	0.55	0.93	0.84	0.37	0.48	0.42
Ca/(Ca+Na)	0.18	0.35	0.56	0.31	0.29	0.29	0.45	0.38	0.22	0.39	0.33
Vac./(Vac.+Na)	0.09	0.15	0.01	0	0.16	0.12	0.35	0.51	0.13	0.13	0.14
Fe^{3+}/Fe^{2+}	0.3	0.23	0.41	0.19	1.2	0.23	0	0.04	0.83	0.48	0.33

* = calculated terms. Vac = vacancy.

3.8 Hydrogen and oxygen isotopes

Hydrogen and oxygen isotope analysis of alteration minerals and whole-rock samples were undertaken to characterize potential fluid sources and assess the relative influence of magmatic, meteoric, and seawater isotopic reservoirs (Tables 3-5 and 3-6; Appendix 3-B; Supplemental data 3-G). Primarily, minerals from the Na-Ca assemblage were analyzed, but to enable comparison, mineral phases from potassic, white-mica–chlorite, and propylitic assemblages were also analyzed. Results are plotted in Figure 3-14.

3.8.1 Least altered host rocks

Measured whole-rock values for the first, more mafic and barren pulse of intrusions (Guichon and Chataway granodiorite) have an average $\delta^{18}O$ value of 6.6 ‰ ($n = 2$) and δD value of -76.1 ‰ (Table 3-5). Intrusions belonging to the second magmatic pulse (Bethlehem, Skeena, and Bethsaida granodiorite) have a higher average $\delta^{18}O$ value (8.1 ‰; $n = 5$) and lower δD value (-86.2 ‰) compared to the first magmatic pulse (Table 3-5). A quartz and feldspar porphyry dike (QFPM), belonging to the third magmatic pulse has a $\delta^{18}O$ value of 8.6 ‰ and δD value of -87.0 ‰, which is very similar to isotopic compositions for Bethsaida granodiorite (Table 3-5).

Table 3-5. Hydrogen and oxygen isotopic determinations of least altered rocks

Station	Host rock	[1]Measured values		[2]Temp. (C°)	[3]Calculated	
		δD ‰	$\delta^{18}O$ ‰		δD ‰	$\delta^{18}O$ ‰
2013MD044	Guichon	-74.6	6.4	750	-51.5	7.2
2013MD043	Chataway	-77.5	6.7	750	-51.8	7.4
2013MD049	Bethlehem	-86.2	8.3	700	-64.8	8.8
2013MD072	Skeena	-84.1	7.5	700	-58.8	7.9
2013MD034	Skeena	-81.9	8	700	-61.1	8.4
2015GL010	Bethsaida	-99.5	7.1	700	-76.3	7.4
2013MD069	Bethsaida	-79.4	9.4	700	-56.2	9.6
2013MD073	QFPM	-87	8.6	700	-61.7	7.9

[1] δD and $\delta^{18}O$ are reported relative to Vienna standard mean ocean water (V-SMOW).

[2] Solidus temperatures from D'Angelo (2016).

[3] Calculated δD and $\delta^{18}O$ compositions of fluids in equilibrium with host rocks are based on modal mineralogy abundances, formation temperatures, and weighted mineral-fluid 1000lnα (Δ) values presented in Appendix 3-B.

3.8.2 Potassic and white-mica–chlorite facies

Three coarse-grained muscovite separates were analyzed: one from a mineralized EH vein in a deep level (~800 m) of the Valley Cu center, a second from a high-grade Cu-Ag quartz-muscovite-carbonate vein with a muscovite halo (Empire occurrence; Fig. 3-2B; Fig. 3-14A;

Table 3-6), and a third from another high-grade Cu-Ag vein comprising a milky-white quartz-muscovite-chalcopyrite vein and a muscovite ± kaolinite halo (Yubet occurrence; Fig. 3-2B; Table 3-6). The three samples have the same $\delta^{18}O$ value of 8.5 ‰, and have δD values of -48.9, -57.0, and -40.5 ‰ for Valley, Empire and Yubet, respectively. Additionally, Jones (1974) reports that in the Valley-Lonrex porphyry system coarse muscovite in halos and pervasive white-mica have $\delta^{18}O$ values of 6.6 to 7.1 ‰ and δD values of -53 to -64 ‰ ($n = 6$). Tourmaline separates from veins in a pervasively K-feldspar-altered rock at the Bethlehem-North Cu occurrence have a $\delta^{18}O$ value of 6.9 ‰ and δD value of -51.1 ‰, which are similar to the $\delta^{18}O$ (8.0 ‰) and δD (-57.1 ‰) values of tourmaline from a mineralized vein with a white-mica–chlorite halo sampled at the Aberdeen Cu occurrence (Figs. 3-2B and 3-14A; Table 3-6). Epidote from an epidote–white-mica–chalcopyrite–specularite vein and halo (1-2 m wide) on the east side of the Bethlehem pit, adjacent to a Na-Ca altered domain, has a $\delta^{18}O$ value of 3.7 ‰ and δD value of -37.0 ‰ (orange circle; Fig. 3-14A; Table 3-6).

3.8.3 Na-Ca facies

Epidote from veins with albite halos exhibit a wide range of $\delta^{18}O$ values (3.2–9.5 ‰; $n = 13$) and δD values (-45.9–-93.2 ‰). The lowest epidote $\delta^{18}O$ value (3.2 ‰) is from an epidote vein with a strongly albite and epidote altered halo taken from the Na-Ca domain approximately 1.5 km northeast of Highmont, and has a δD value of -82.0 ‰. (Fig. 3-14A; 15KB229B; Table 3-6). The next-lowest epidote $\delta^{18}O$ value of 3.5 ‰ is from a sample collected northeast of the Bethlehem porphyry center (Figs. 3-10G and 3-14A; 15KB056; Table 3-6), and has a corresponding δD value of -61.8 ‰. Albite from the halos of epidote veins have a wide range of $\delta^{18}O$ values from 7.3 to 11.5 ‰ and an average value of 9.1 ‰ ($n = 10$). One fracture coating and two halo actinolite samples have an average $\delta^{18}O$ of 5.4 ‰ and a δD value -85.5 ‰. Chlorite within an intensely albitized vein halo hosted in Bethlehem granodiorite from Iona has a $\delta^{18}O$ of 3.5 ‰ and δD of -47.3 ‰. A second chlorite sample, east of Jersey, from the halo of an albite-diopside-epidote replacement vein has higher $\delta^{18}O$ (5.4 ‰) and lower δD (-88.9 ‰) values. Tourmaline from veins in rocks with albite halos have $\delta^{18}O$ values between 4.8 and 6.9 ‰ ($n = 4$) and δD values from -45.8 to -55.2 ‰. The tourmaline with the lowest $\delta^{18}O$ value (4.8 ‰) occurs in a pervasively albitized rock in which primary plagioclase and K-feldspar have been replaced by albite and all mafic minerals removed; however, the timing of the tourmaline with respect to accompanying epidote vein filling is unclear. Two tourmaline vein samples in which the tourmaline appears to post-date epidote fill (post-Na-Ca), and a third in which the tourmaline is cross-cut by epidote (pre-Na-Ca) have similar $\delta^{18}O$ (~6.8 ‰) and δD (~-50 ‰) values.

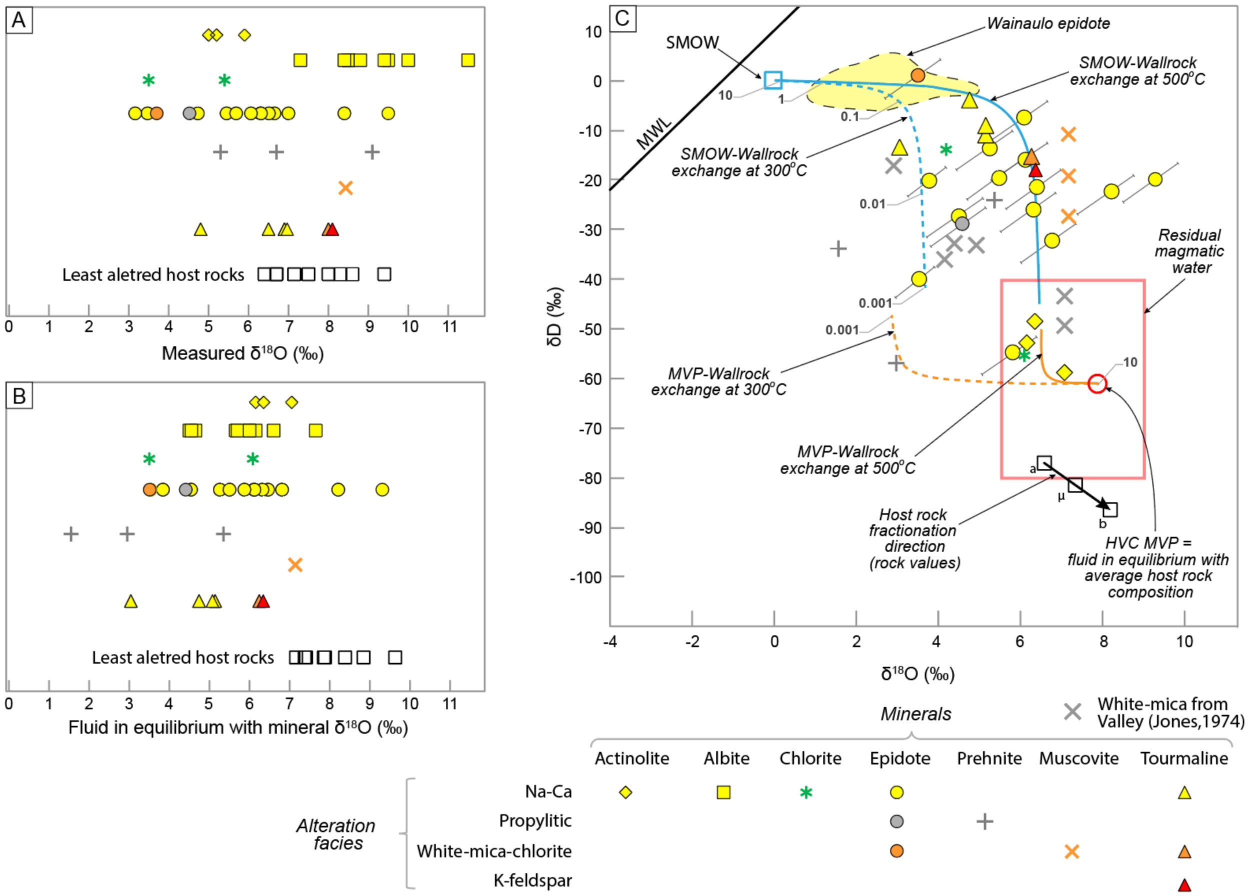

Figure 3-14. A. Hydrothermal mineral and least altered whole rock pulp measured $\delta^{18}O$ values. B. Calculated $\delta^{18}O$ compositions of hydrothermal fluids in equilibrium with hydrothermal minerals based on their temperatures of formation (Tables 8 and 9). C. Calculated δD and $\delta^{18}O$ compositions of hydrothermal fluids in equilibrium with hydrothermal minerals from the GCB. Abbreviations: MWL = meteoric water line, MVP = magmatic volatile phase, SMOW = standard mean ocean water. The black lines associated with epidote vein data points represent the range of possible fluid compositions for that mineral at ± 50C° from the estimated temperature of formation (Table 3-6; Appendix 3-B). The Wainaulo epidote are from a Fijian porphyry Cu-Au systems in Orovan et al. (2018). Also included are the interpreted fluid values in equilibrium with white-mica samples from the Valley Cu center reported by Jones (1974). Residual magmatic water field and MWL from Taylor (1979). Modeled curves show the changes in fluid δD and $\delta^{18}O$ composition of 1) SMOW and 2) MVP through equilibrium isotopic exchange with average GCB host rock at 300C° and 500C° over a range of water–rock (W:R) weight ratios (after Ohmoto and Rye, 1974). The black box labeled “a” is the average measured values for least altered Guichon and Chataway, “b” is the average measured values for least altered Bethlehem, Skeena and Bethsaida host rocks (Table 3-5), and “μ” the average of all the least altered GCB rocks (δD = -81.2 and $\delta^{18}O$ = 7.4).

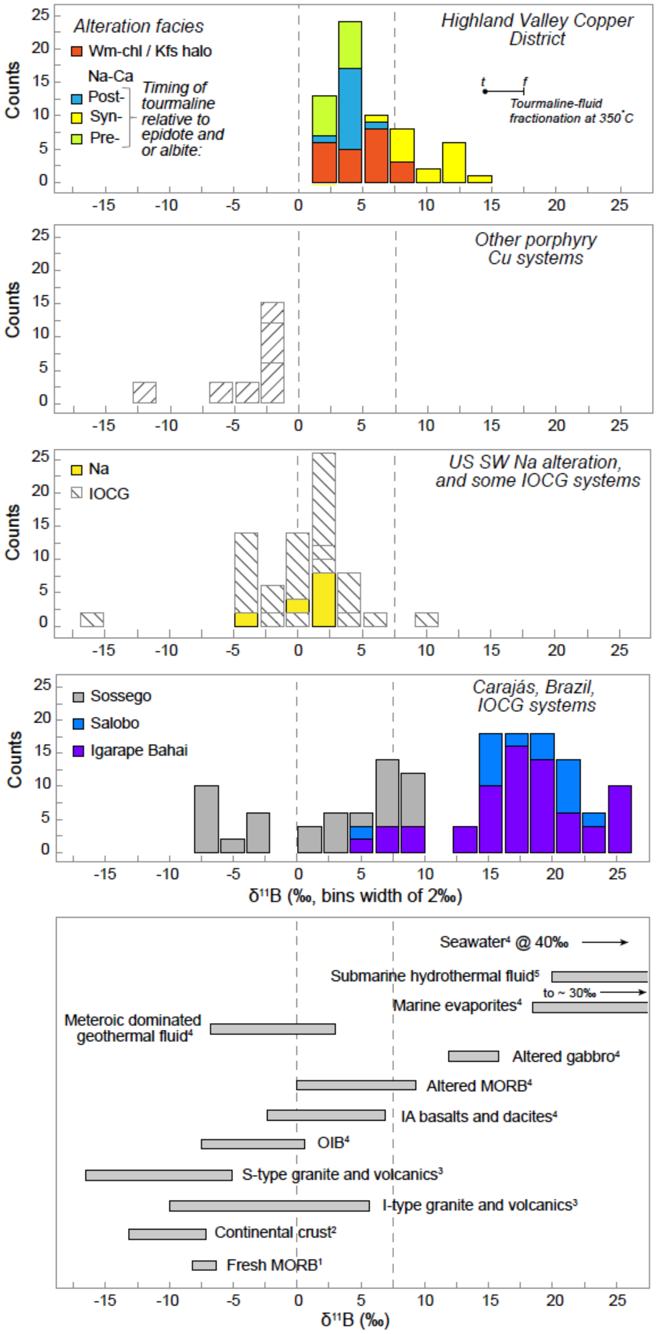

Figure 3-15. Histograms of measured B isotope δ^{11}B‰ values of tourmaline in the GCB, other porphyry Cu systems (Collins, 2010), US Southwest Na altered plutonic rocks (Collins, 2010), and Iron Oxide Copper Gold (IOCG) systems (Xavier et al., 2008; Collins, 2010). The B isotope ratio composition of relevant reservoirs are also presented. Reservoir references: ^{1}(Marschall et al., 2017), ^{2}(Chaussidon and Albarède, 1992), ^{3}(Trumbull and Slack, 2018), ^{4}(Barth, 1993), and ^{5}(Palmer and Swihart, 1996). Note, the δ^{11}B‰ range of I- and S-type granite and volcanic rock is the mean value ± 1.5σ.

Table 3-6. Hydrogen and oxygen isotopic determinations of hydrothermal minerals

Station	Elv.	Alteration facies	Fracture fill	Associated alteration halo	Mineral analyzed	Measured values		Inferred temperature of formation	^{2}Calculated		Comments
						δD‰	δ^{18}O‰		δD‰	δ^{18}O‰	
2015GL010	1644	Na-Ca	Epidote	Albite, chlorite	Albite		8.5	350		4.7	Vein fill sampled. Intense and pervasive albite alteration of wall rock. Highmont west pit.
2015GL010	1644	Na-Ca	Epidote	Albite, chlorite, epidote	Epidote	-59.8	6.7	350	-21.8	6.5	Intense and pervasive albite alteration of wall rock
B14-015_202.6m	1333	Na-Ca	Epidote	Albite, chlorite, epidote	Albite		10	350		6.2	Sample from the Iona area at depth beneath mineralized breccia at the Bethlehem deposit.
B14-015_202.6m	1333	Na-Ca	Epidote	Albite, chlorite, epidote	Chlorite	-47.3	3.5	350	-13.7	4.2	Sample from the Iona area at depth beneath mineralized breccia at the Bethlehem deposit.
B14-015_202.6m	1333	Na-Ca	Epidote	Albite, chlorite, epidote	Epidote	-64.2	6.5	350	-26.2	6.3	Vein fill sampled. Sample from the Iona area at depth beneath mineralized breccia at the Bethlehem deposit.
2015KB056	1371	Na-Ca	Tourmaline	Albite, actinolite, chlorite, epidote	Actinolite	-84.9	5	400	-52.8	6.2	Albite-epidote-actinolite fracture halo with late tourmaline fracture fill.
2015KB056	1371	Na-Ca	Tourmaline	Albite, actinolite, chlorite	Albite		8.5	400		5.7	Albite-epidote-actinolite fracture halo with late tourmaline fracture fill.
2015KB056	1371	Na-Ca	Tourmaline	Albite, actinolite, chlorite, epidote	Epidote	-61.8	3.5	400	-20.4	3.8	Epidote from halo. Tourmaline appears to overprint actinolite.
2015KB056	1371	Na-Ca	Tourmaline	Albite, chlorite	Tourmaline	-45.8	6.5	350	-3.9	4.7	Tourmaline appears to overprint actinolite. Corresponding fluid δ^{11}B = 7.4‰
2015KB062	1399	Na-Ca	Epidote	Albite, chlorite, epidote	Albite		11.5	350		7.7	Epidote vein with albite halo.
2015KB062	1399	Na-Ca	Epidote	Albite, chlorite	Epidote	-57.9	5.7	350	-19.9	5.5	Epidote vein fill sampled
2015KB087	1364	Na-Ca	Tourmaline, epidote	Albite, actinolite, chlorite	Actinolite	-80.5	5.2	400	-48.4	6.4	Epidote veinlet with albite halo cross-cut tourmaline veinlet
2015KB087	1364	Na-Ca	Tourmaline, epidote	Albite, actinolite, chlorite	Albite		7.3	400		4.5	Epidote veinlet with albite halo cross-cut tourmaline veinlet. Corresponding actinolite δ^{18}O is heavier by ~2‰
2015KB087	1364	Na-Ca	Tourmaline, epidote	Albite, chlorite	Tourmaline	-52.9	6.9	350	-11	5.1	Tourmaline cut by epidote. Corresponding fluid δ^{11}B = 6.5‰
2015KB102	1447	Na-Ca	Epidote	Albite, chlorite	Epidote	-45.9	6.3	350	-7.9	6.1	Epidote vein fill sampled
2015KB103A	1423	Na-Ca	Epidote, tourmaline	Albite, chlorite	Tourmaline	-55.2	4.8	350	-13.3	3	Timing of tourmaline fill w.r.t epidote unclear. No B isotope data.
2015KB152	1462	Na-Ca	Epidote	Albite, chlorite	Epidote	-65.4	4.7	350	-27.4	4.5	Epidote vein fill sampled
2015KB171	1501	Na-Ca	Epidote	Albite, chlorite	Epidote	-54.1	6.3	350	-16.1	6.1	Epidote vein fill sampled
2015KB180	1602	Na-Ca	Epidote	Albite, chlorite	Epidote	-93.2	6.1	350	-55.2	5.9	Epidote vein fill sampled
2015KB182	1575	Na-Ca	Epidote	Albite, chlorite, epidote	Albite		8.4	350		4.6	Epidote veinlet with pervasive and intense albite, epidote and chlorite alteration
2015KB182	1575	Na-Ca	Epidote	Albite, chlorite	Epidote	-70.5	7	350	-32.5	6.8	Epidote vein fill sampled
2015KB218	1625	Na-Ca	Epidote	Albite, chlorite	Epidote	-58.4	9.5	350	-20.4	9.3	Epidote replacement vein fill sampled
2015KB229B	1634	Na-Ca	Epidote	Albite, actinolite, chlorite, epidote	Albite		8.8	400		6	Epidote vein fill sampled
2015KB229B	1634	Na-Ca	Epidote	Albite, actinolite, chlorite	Epidote	-82	3.2	400	-40.6	3.5	Epidote vein fill sampled
2015KB276	1563	Na-Ca	Actinolite	Albite, actinolite, chlorite	Actinolite	-90.9	5.9	400	-58.7	7.1	Actinolite fracture coasting with albite and chlorite halo. Highmont west pit.
2015KB276	1563	Na-Ca	Actinolite	Albite, actinolite, chlorite	Albite		8.8	400		6	Albite from halo sampled. Oxygen isotope value is similar to corresponding actinolite result. Highmont west pit.
2015KB278	1593	Na-Ca	Epidote	Albite, actinolite, chlorite	Albite		9.4	400		6.6	Intense and pervasive albite alteration of wall rock. Highmont west pit.
2015KB278	1593	Na-Ca	Epidote	Albite, chlorite, epidote	Epidote	-60.8	8.4	350	-22.8	8.2	Epidote replacement zone with intense and pervasive albite alteration halo. Highmont west pit.
2016KB061	1646	Na-Ca	Epidote	Albite, chlorite, epidote	Epidote	-51.9	5.5	350	-13.9	5.3	Epidote vein fill, with late tourmaline.

Table 3-6 Continued

2016KB061	1646	Na-Ca	Epidote, tourmaline	Albite, chlorite	Tourmaline	-51.1	6.9	350	-9.1	5.1	Tourmaline occludes epidote vein fill. No B isotope data.
B13-130_293m	1452	Na-Ca	Diopside, chlorite	Albite, chlorite	Albite		9.5	350		5.7	Breccia fill of diopside, locally overprinted by chlorite and carbonate, with an albite halo. Sample from the East Jersey area at the Bethlehem porphyry.
B13-130_293m	1452	Na-Ca	Diopside, chlorite	Albite	Chlorite	-88.9	5.4	350	-55.4	6.1	Chlorite sampled. Breccia fill of diopside, locally overprinted by chlorite and carbonate, with an albite halo. Sample from the East Jersey area at the Bethlehem porphyry
2014GL153	1509	Propylitic	Prehnite	Prehnite, white-mica, chlorite	Prehnite	-94.3	6.7	250	-56.8	3	Prehnite vein fill sampled.
2015KB062	1399	Propylitic	Prehnite	Prehnite, white-mica, chlorite	Prehnite	-61.7	9.1	250	-24.2	5.4	Prehnite veinlet cross-cut and infilled epidote vein associated with albite halo.
2015KB111	1390	Propylitic	Prehnite	Prehnite, white-mica, chlorite	Prehnite	-71.3	5.3	250	-33.8	1.6	Prehnite vein fill sampled.
BETH North	1864	Propylitic	Epidote	Epidote, chlorite	Epidote	-67	4.6	350	-29	4.4	Epidote cross-cuts and overprints tourmaline veins with K-feldspar halo. Note, this sample has the highest elevation in the data set and is within ~ 25m elevation of nearby hornfelsed of Nicola volcanoclastic rocks that are interpreted to be roof pendants. (M. Alfaro, pers. comm., 2016)
BETH North	1864	K-feldspar	Tourmaline	K-feldspar	Tourmaline	-59.8	8.1	350	-17.9	6.3	Bethlehem North Cu occurrence. Contrasting isotope values to younger
2015GL-V11-13	1114	White-mica-chlorite	Quartz	Coarse muscovite	Muscovite	-48.9	8.5	400	-19.2	7.1	Valley pit, quartz-bornite vein with early-halo (EH)-type muscovite
2015KB043A	1546	White-mica-chlorite	Epidote, white-mica, specularite	Fine-grained white mica, chlorite	Epidote	-37.4	3.7	350	0.6	3.5	Adjacent albitized zone near the Bethlehem pit. Epidote intergrown with specularite, white-mica, and chalcopyrite
2016KB001	1661	White-mica-chlorite	Quartz	Coarse muscovite	Muscovite	-40.5	8.5	400	-10.9	7.1	Empire occurrence. Intergrown quartz and coarse EH-type grey muscovite. Late carbonate and hematite in sample. High Cu grade bornite mineralization
2016KB008	1606	White-mica-chlorite	Quartz	Coarse muscovite	Muscovite	-57	8.5	400	-27.3	7.1	Yubet occurrence. Intergrown quartz and EH-type green-grey coarse muscovite. High Cu grade chalcopyrite-bornite mineralization.
2016KB010	1056	White-mica-chlorite	Tourmaline	Fine-grained white-mica	Tourmaline	-57.1	8	350	-15.2	6.2	Aberdeen Cu occurrence. White-mica overprinted K-feldspar alteration. No B isotope data

[1] δD and δ^{18}O are reported relative to Vienna standard mean ocean water (V-SMOW).
[2] Calculated δD and δ^{18}O compositions of hydrothermal fluids in equilibrium with minerals are based on inferred temperatures and mineral-fluid 1000lnα (Δ) values presented in Appendix 3-B

3.8.4 *Propylitic alteration*

Prehnite has a wide range of δ^{18}O (5.3–9.1 ‰; *n* = 3) and δD (-61.7–-94.3 ‰) values (Table 3-6). The prehnite vein with the lowest δ^{18}O value (5.3 ‰) is hosted in Guichon granodiorite in the northeast portion of the batholith. Patchy replacement epidote that overprinted tourmaline veins and K-feldspar alteration hosted in Guichon granodiorite at the Bethlehem-North Cu occurrence has a δ^{18}O value of 3.7 ‰ and δD value of -37.4 ‰.

3.9 Sr isotopes

Ten whole-rock samples were analyzed for their Sr isotope composition to test whether Na-Ca altered rocks can be distinguished from HVC magmatic compositions, and whether a shift towards Triassic seawater Sr isotope signature (0.7076; Tremba et al., 1975) can be detected (Table 3-7; Appendix F). Mineralized, weakly K-feldspar altered (potassic) and pervasively white-mica–chlorite altered Bethsaida granodiorite samples have average $^{87}Sr/^{86}Sr_i$ values of 0.703384, which is lower than the average $^{87}Sr/^{86}Sr_i$ value (0.703409) for the second magmatic pulse rocks (Table 3-7). The $^{87}Sr/^{86}Sr_i$ of strongly Na-Ca altered rock samples range from 0.703416 to 0.703508, and have a higher average (0.703450; *n* = 8) compared to the fresh host rocks and potassic and white-mica–chlorite altered rocks (Table 3-7).

Table 3-7. Radiogenic strontium isotope data for whole-rock pulps of altered rocks in the HVC district

Sample	Host rock	Average Age (Ma)[1]	Alteration facies	Whole-rock[2]		Measured[3]		Calculated				
				Rb (ppm)	Sr (ppm)	$^{87}Sr/^{86}Sr$	±2σ	$^{87}Rb/^{86}Sr$	$^{87}Sr/^{86}Sr_i$	Δ magmatic-initial[4]	% seawater[5]	Multiple of 2σ[6]
15GL048	Bethsaida	208.5	WM-Chl	21.9	606.9	0.70369	0.00001	0.105	0.703383	0.000003	0.1	0.3
15GL010-93	Bethsaida	208.5	Potassic	33.6	585	0.70388	1.1E-05	0.167	0.703386	0.000006	0.1	0.5
15GL051	Bethsaida	208.5	Na-Ca	21.1	795	0.703680	0.00001	0.0772	0.703451	0.000071	1.7	7.1
15GL010-92	Bethsaida	208.5	Na-Ca	0.6	865.8	0.70342	0.00001	0.002	0.703416	0.000036	0.8	3.6
15GL036	Bethsaida	208.5	Na-Ca	7.6	761.9	0.7035	1.8E-05	0.029	0.703417	0.000037	0.9	2.1
15KB180	Chataway	210.6	Na-Ca	45.1	630	0.7041	1.1E-05	0.2082	0.703476	0.000096	2.3	8.7
15KB270	QFP	208.5	Na	17.8	353.5	0.70394	1.5E-05	0.1464	0.703508	0.000128	3.0	8.5
15KB250A	Skeena	208.4	Na-Ca	5.7	770.9	0.70353	0.00001	0.0215	0.703464	0.000084	2.0	8.4
15KB218	Skeena	208.4	Na-Ca	9.1	861.3	0.70353	0.00001	0.0307	0.703443	0.000063	1.5	6.3
15KB229A	Skeena	208.4	Na-Ca	13.7	819.5	0.70357	0.00001	0.0486	0.703423	0.000043	1.0	4.3

[1] Average host-rock age from D'Angelo et al. (2017).

[2] Elements were measured on an inductively coupled plasma mass spectrometer (ICP-MS).

[3] Measured $^{87}Sr/^{86}Sr$ corrected to the deviation from NBS-987 (accepted value = 0.710240). Mean $^{87}Sr/^{86}Sr$ value for NBS-987 standard reference material for 20 runs (n=20) was 0.710233 with a standard deviation of 0.000013.

[4] Magmatic fluid $^{87}Sr/^{86}Sr_i$ composition of 0.703384 is based on the average of the white-mica–chlorite and potassic altered samples.

[5] Percentage (%) seawater was calculated using mean $^{87}Sr/^{86}Sr$ for Triassic seawater (0.7076; Tremba et al., 1975) and $^{87}Sr/^{86}Sr_i$ of HVC magmatic fluids (0.703384).

[6] Δ magmatic-initial value divided by the analysis 2σ value

Abbreviations: WM = white-mica, Chl = chlorite.

3.10 Tourmaline boron isotope compositions

Boron isotope measurements were conducted on HVC tourmaline veins to characterize their potential source of the B, and to constrain fluid origins. Tourmaline $\delta^{11}B$ values range from

1.0 to 15.1 ‰ (n = 64) and have a bimodal distribution with a major mode at approximately 4 ‰ and a minor mode at 11 ‰ (Fig. 3-15; Table 3-8).

3.10.1 Potassic and white-mica–chlorite facies

Sample 15KB093 is of a tourmaline vein with a K-feldspar halo hosted in Chataway granodiorite located approximately 5.4 km northeast of Bethlehem (Figs. 3-2B and 3-12A). The tourmaline associated with K-feldspar alteration has an average δ^{11}B value of 2.3 ‰ and a range close to analytical uncertainty of 0.8 ‰ (Fig. 3-12B; Table 3-8). Sample 16KB047 is of a tourmaline vein with a white-mica–chlorite halo, hosted in Border diorite within 5 km of the batholith margin and the Craigmont skarn (Fig. 3-2B). This sample has range of δ^{11}B values of 5.1 to 7.4 ‰ and an average value of 6.2 ‰. The sample also exhibits some internal variations, with lower δ^{11}B values in the core to higher values in rims, but this relationship is not systematic (Table 3-8).

3.10.2 Na-Ca facies

Sample 15KB069A is weakly albite-altered Border diorite, near the eastern margin of the batholith, in which a tourmaline vein is cross-cut by a center line of epidote vein fill and hence is classified as pre-Na-Ca. This pre-Na-Ca tourmaline has δ^{11}B values of 3.3 to 5.1 ‰ (15KB069; Table 3-8). In sample 15KB087B, pre-Na-Ca tourmaline has δ^{11}B values of 1.8 to 4.0 ‰ (Fig. 3-12D; Table 3-8). Some grains in this sample have cores with slightly lower δ^{11}B values compared to the darker rims (Fig. 3-12D). The third pre-Na-Ca tourmaline sample is hosted in an albitized Skeena clast from the breccia at Highmont and has an average δ^{11}B value of 2.5 ‰ (15KB266; Table 3-8). The tourmaline in this sample has cores with an average Mg / (Mg+Fe) value of 0.3 and rims of approximately 0.4, and corresponding δ^{11}B values of around 1 ‰ and 3 to 5 ‰, respectively (Table 3-8). Syn-Na-Ca tourmaline has the highest values and widest range in δ^{11}B, with 6.9 to 15.1 ‰ (Fig. 3-15; Table 3-8). The T1 stage tourmaline is more isotopically heterogeneous compared to T2 tourmaline, however, the compositionally distinct stages (Fig. 3-13C) have similar average δ^{11}B values of around 10 ‰ (Fig. 3-12F; Table 3-8). The highest δ^{11}B value of 15.1 ‰ is from the Al-rich and Si-poor magnesio-foitite T1 tourmaline. There is no apparent core to rim B-isotope zoning in T1 or T2 tourmaline or a correspondence to compositional zoning. Tourmaline in veins with albite halos that appear to have a post-Na-Ca timing have a similar average and range of δ^{11}B values compared to the pre-Na-Ca, potassic and white-mica–chlorite tourmaline (Fig. 3-15). Some weak core to rim B isotopic zoning is evident in the post-Na-Ca tourmaline sample 15KB056 but the pattern is inconsistent (Fig. 3-12I).

3.10.3 Summary

In summary, the tourmaline that formed with K-feldspar alteration has the lowest average δ^{11}B value at 2.3 ‰. The pre-Na-Ca tourmaline in the albitized Skeena granodiorite clast has the same average δ^{11}B value (2.5 ‰) but a moderate range in δ^{11}B values of 3.9 ‰, and a consistent core-to-rim increase in B isotope values that corresponds to changes in chemical composition. The syn-Na-Ca tourmaline of T1 and T2 stages are isotopically similar despite having distinctly different Fe-Al-Mg compositions. Furthermore, relative to the other samples, the syn-Na-Ca tourmaline facies have the highest δ^{11}B values, and the greatest variability in δ^{11}B values of 8.1 ‰.

Table 3-8. B-isotope results for tourmaline in the Highland Valley Copper district

Sample	Host Rock	Area	Alteration facies	Tourmaline timing with respect to epidote or albite	[1]Zoning	Analysis Point	Al (pfu)	Mg #	Measured $\delta^{11}B$ ‰	External precision (1σ) ‰	[2]Fluid $\delta^{11}B$ ‰	Comment
2015KB093	Chataway	5.4km NE of Bethlehem	K-feldspar	No Na-Ca	Sector	15-93@1	5.7	0.51	2.4	0.8	5.6	Rim
						15-93@2	5.28	0.45	2	0.8	5.2	Core
						15-93@3	5.56	0.5	2	0.8	5.2	Rim
						15-93@4	5.56	0.48	2.2	0.8	5.4	Core
						15-93@5	5.39	0.47	2.5	0.8	5.8	Rim
						15-93@6			2.9	0.8	6.2	Core
2016KB047	Border	Southern batholith. 4.5km N of Craigmont skarn and 21km S of Highmont	White-mica-chlorite	No Na-Ca	Sector: Dark to light	16-47-G1@1	5.87	0.64	5.5	0.6	8.7	Dark core
						16-47-G1@2	5.73	0.61	5.5	0.6	8.8	Dark core
						16-47-G1@3	5.68	0.59	6.5	0.6	9.7	Light rim
						16-47-G1@4	5.68	0.59	6.2	0.6	9.4	Light rim
						16-47-G2@1	5.75	0.61	5.1	0.6	8.3	Dark core
						16-47-G2@2	5.75	0.61	5.4	0.6	8.7	Dark core
						16-47-G2@3	5.72	0.58	7.2	0.6	10.4	Light rim
						16-47-G2@4	5.58	0.55	5.8	0.6	9.1	Dark core
						16-47-G3@1	5.7	0.58	7.2	0.6	10.4	Light rim
						16-47-G3@2	5.32	0.53	7.4	0.6	10.6	Dark core
2015KB069	Border	7.6km NE of Bethlehem, batholith margin	Na-Ca	Pre	Patchy	15-69@1	5.41	0.53	4.6	0.8	7.8	Dark zone
						15-69@2	4.48	0.44	4.4	0.8	7.6	Light zone
						15-69@3	5	0.54	5.1	0.8	8.3	Light zone
						15-69@4	5.79	0.59	3.6	0.8	6.8	Dark zone
						15-69@5	5.17	0.55	3.3	0.8	6.5	Dark zone
						15-69@6	5.56	0.46	4.6	0.8	7.8	Light zone
2015KB087B	Guichon	5.6km NE of Bethlehem	Na-Ca	Pre	Patchy: Light to dark	15-87-G1@1	5.59	0.53	3	0.8	6.2	Dark rim
						15-87-G1@2	5.79	0.54	1.8	0.8	5	Light core
						15-87-G2@1	5.09	0.45	4	0.8	7.2	Intermediate
						15-87-G3@1	4.89	0.51	4	0.8	7.2	Dark rim
						15-87-G3@2	5.3	0.46	3.6	0.8	6.9	Light core
						15-87-G3@3	5.57	0.55	3.2	0.8	6.4	Dark rim
						15-87-G3@4	5.3	0.46	3.8	0.8	7	Light core
2015KB266B	Altered Skeena clast in breccia	Highmont east pit	Na-Ca	Pre	Sector: Light to dark	15-266-G1@1	3.38	0.32	1	0.8	4.2	Light core
						15-266-G1@2	4.06	0.27	1	0.8	4.2	Light core
						15-266-G1@3	5.23	0.48	5	0.8	8.2	Dark rim
						15-266-G1@4	4.56	0.39	2.9	0.8	6.1	Dark rim
						15-266-G2@1	4.28	0.33	3.9	0.8	7.1	Intermediate
						15-266-G1@5	4.15	0.32	1.4	0.8	4.7	Core
2015KB270	QFPQ	Highmont east pit	Na-Ca, late stage	Syn-T1	Patchy: Darker cores	15-270-G1@1	6.99	0.97	6.9	0.6	10.2	Core
						15-270-G1@2	7.36	0.93	11.7	0.6	15	Intermediate
						15-270-G1@5	6.57	0.91	8.7	0.6	11.9	Core
						15-270-G2@3	6.93	0.95	10.9	0.6	14.1	Core
						15-270-G2@4	6.93	0.93	8.7	0.6	11.9	Core
						15-270-G3@2	7.02	0.95	11.6	0.6	14.8	Rim
						15-270-G3@1	6.47	0.82	11.6	0.6	14.8	Rim
						15-270-G3@3	7.24	0.95	9	0.6	12.2	Intermediate
						15-270-G3@4	8.01	0.97	8.1	0.6	11.3	Core
						15-270-G3@5	7.26	0.84	15.1	0.6	18.3	Core
				Syn-T2	Sector: Dark to light	15-270-G1@3	5.81	0.6	11.9	0.6	15.2	Rim
						15-270-G1@4	5.34	0.27	12.6	0.6	15.8	Rim
						15-270-G2@2	5.85	0.25	11.8	0.6	15	Rim
						15-270-G2@1	4.71	0.37	8.7	0.6	11.9	Intermediate
						15-270-G2@5	5.3	0.42	10.5	0.6	13.7	Core
2015KB047	Guichon	1.5km N of Bethlehem	Na-Ca	Post	Patchy: Mostly light to dark	15-47@1	5.17	0.42	4.4	0.6	7.6	Light zone
						15-47@2	5.65	0.51	3	0.6	6.2	Dark zone
						15-47@3	4.23	0.4	2.6	0.6	5.8	Dark zone
						15-47@4	5.23	0.42	3.1	0.6	6.3	Intermediate
						15-47@5	5.2	0.44	4.5	0.6	7.7	Intermediate
						15-47@6	5.75	0.55	3.2	0.6	6.5	Intermediate
2015KB056	Guichon	3.9km E of Bethlehem	Na-Ca	Post	Sector and Oscillatory	15-56-G1@1	5.08	0.52	5	0.6	8.2	Rim
						15-56-G1@2	4.61	0.44	3.3	0.6	6.5	Core
						15-56-G1@3	5.21	0.49	3.4	0.6	6.6	Core
						15-56-G1@4	5.14	0.52	5.9	0.6	9.1	Rim
						15-56-G1@5	4.65	0.49	4.8	0.6	8	Intermediate
						15-56-G2@2	4.56	0.48	4	0.6	7.2	Rim
						15-56-G2@1	5.14	0.48	4.1	0.6	7.3	Intermediate
						15-56-G3@1	4.64	0.43	3.3	0.6	6.5	Rim

[1] Zoning in tourmaline based on transmitted light response and back scattered image contrast which primarily reflects variation in concentrations of Fe and Al; brighter is more Fe-rich.

[2] Calculated $\delta^{11}B$ composition of hydrothermal fluid in equilibrium with tourmaline based on tourmaline-fluid $\Delta^{11}B$ of -3.22 ‰ at 350°C (Meyer et al., 2009).

Supplemental data, standard results, and IMF factors applied are provided in Supplemental data 3-A.

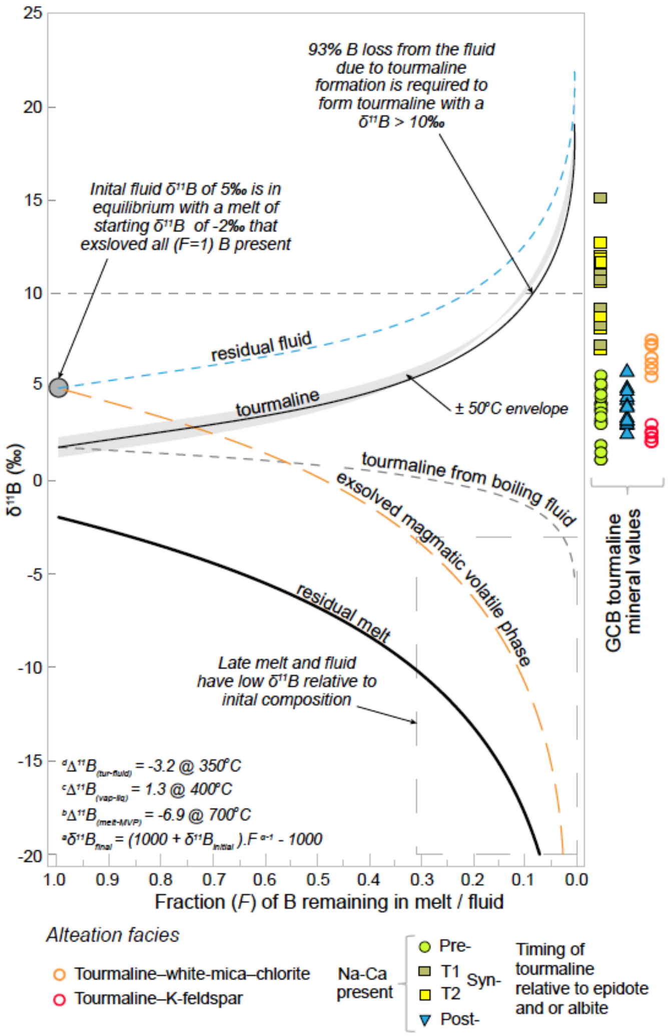

Figure 3-16. Rayleigh fractionation models of the B isotope composition of various phases present in magmatic-hydrothermal systems. [a]Closed system Rayleigh fractionation (distillation) is from Taylor and Sheppard (1986) where *F* is the fraction of melt or fluid remaining and 1 is at the beginning and 0 at the end. [b]Fractionation factor between hydrous fluid (magmatic volatile phase) and silicate melt is from Hervig et al. (2002). [c]Liquid–vapor fractionation factor from Liebscher et al. (2005). [d]Tourmaline–fluid fractionation factor from Meyer et al. (2008). The modeled curves are premised on an starting melt $\delta^{11}B$ value of -2‰ (i.e. average I-type granite reported by' Trumbull and Slack (2018)), which at $F = 1$ forms an MVP with a $\delta^{11}B$ value of 5‰, which would subsequently form a tourmaline with a $\delta^{11}B$ value of 1.8‰, equivalent to the average value of 2.3 ± 0.8‰ for the Cu-mineralized tourmaline–K-feldspar sample in the GCB (Table 3-8; 15KB93). A melt with an initial $\delta^{11}B$ value of 0.5‰ can form a tourmaline, at $F = 1$, with a B isotope composition closer to the median $\delta^{11}B$ value of 4.5‰ for tourmalines in the GCB.

3.11 Discussion

Two possible end-member fluid-source scenarios for the origin of Na-Ca alteration in the GCB will be evaluated below based on the results from this study. In the first scenario, cooled and spent magmatic fluids sourced from deeper, unobserved alteration zones, or injected laterally from the potassic and hydrolytically altered porphyry Cu centers (e.g., Reed et al., 2013; Wilkinson et al., 2015; Pacey et al., 2016), produced the metasomatic Na-Ca alteration in the region. The second scenario invokes an external, progressively-heated fluid (meteoric, formation, or seawater) which is drawn down and inward towards the magmatic-hydrothermal system during porphyry Cu formation, i.e., models for the formation of propylitic alteration at low water–rock ratio (Meyer and Hemley, 1967; Norman et al., 1991; Reed, 1997), and some Na-Ca alteration (Dilles et al., 1992; Dilles and Einaudi, 1992).

3.11.1 Temperatures of formation

The absence of workable fluid inclusions in the Na-Ca veins in the GCB precluded the acquisition of accurate temperature estimates for the system. Studies of analogous, texturally and mineralogically similar sodic-calcic alteration in porphyry systems and in some Permian to Jurassic arc rocks of the western United States estimated moderate temperatures of formation of approximately 300–500°C (Dilles et al., 1992; Battles and Barton, 1995; Jago et al., 2014). Actinolite veins form at the higher end of the Na-Ca temperature range (400-450°C), whereas epidote veins likely form at 400°C or less (Carten, 1986; Dilles et al., 1992; Seedorff et al., 2005). Epidote forms at 200–350°C during propylitic alteration (Bowman et al., 1987; Norman et al., 1991). Prehnite and epidote can coexist over a narrow range of log $(a_{Ca^{2+}})/(a_{H^{+}})^2$ values and temperature of around 9 and 250°C, respectively (Bird et al., 1984; Digel and Gordon, 1995; Bird and Spieler, 2004). Prehnite, however, is stable down to 150°C with increasing log $(a_{Ca^{2+}})/(a_{H^{+}})^2$ (Bird et al., 1984; Bird and Spieler, 2004). Therefore, these ranges of temperature of mineral formation will be used in the stable isotope calculations that follow (Table 3-6).

3.11.2 Distribution and timing of formation of Na-Ca alteration

In the GCB, the distribution of Na-Ca alteration is strongly influenced by near orthogonal northeast and southeast trending fracture sets, and by proximity to the post-mineral stocks at Bethlehem and to the composite porphyry dike complexes at Lornex and Highmont. Based on paragenetic relationships, the first occurrence of Na-Ca alteration in the district post-dated Cu mineralization at Bethlehem and is spatially-, and likely temporally-, linked to post-mineral stocks of Skeena granodiorite. The presence of diopside and actinolite at Bethlehem imply a higher temperature regime than regional veins with chlorite in the halos. The distribution of Na-Ca facies in this area does not by itself help discriminate between fluid-source scenarios, but it does suggest that the post-mineral Skeena stock was a heat source. The composite porphyry dike complex at Lornex and Highmont is the focus of the largest and asymmetrically distributed Na-Ca domains in the GCB (Fig. 3-2A). Albite alteration may have occurred contemporaneously with weak Cu-mineralized K-feldspar alteration, but it preceded the main-stage Cu mineralization and EH coarse-grained muscovite alteration where observed together at the Highmont porphyry. The predominance of higher-temperature actinolite veins and rare garnet and diopside, within and adjacent to the porphyry dike complex, compared to distal chlorite-dominated Na-Ca facies, is also consistent with the dike complex being a heat source. Intrusion of late-mineralization leucocratic porphyry dikes (QFPQ) coincided with breccia formation at Highmont and with a third distinct pulse of albitization at the porphyry center. The distribution of Na-Ca facies around Valley-Lornex and Highmont indicates that regional-scale fracture-controlled permeability in the batholith had developed at this time, but does not discriminate whether the causative fluids were flowing outward / upwards (scenario 1) or inwards (scenario 2) to the porphyry centers. Nevertheless, episodes of Na-Ca alteration appear to be linked to emplacement of stocks and dikes, and for the second and third pulse, these occurred close in time to porphyry Cu mineralization (Fig. 3-8).

3.11.3 Origin and nature of the aqueous phase

Calculated δD and $\delta^{18}O$ values of hydrothermal fluids in equilibrium with hydrothermal minerals from the GCB (Table 3-6) are plotted in Figure 3-14C. The modeled curves show the change in $\delta^{18}O_{fluid}$ and δD_{fluid} values of 1) standard mean ocean water (SMOW) and 2) HVC magmatic volatile phase (MVP) during equilibrium isotopic exchange with average GCB host rocks at 300 and 500C° over a range of water–rock weight ratios (after Ohmoto and Rye, 1974). In comparison with the model curves, the calculated δD_{fluid} values of EH muscovite veins, and of tourmaline veins with white-mica–chlorite or K-feldspar halos, plot above the residual magmatic water field, but have $\delta^{18}O_{fluid}$ values within the range of magmatic water (Fig. 3-14C), and of potassic and hydrolytic alteration in other porphyry systems (Shanks, 2014). Additionally, Jones (1974) interprets the range of $\delta^{18}O_{fluid}$ and δD_{fluid} values derived from white-mica in the Valley porphyry system (e.g., Fig. 3-14C) to reflect mixing between MVP and sweater prior to and during Cu mineralization. Epidote from the white-mica-specularite-chalcopyrite vein has the highest δD_{fluid} (0.6 ‰) and a $\delta^{18}O_{fluid}$ value of 3.5 ‰, which overlaps with the field for Cu-Fe-sulfide-bearing epidote veins with K-feldspar and phengite halos at the Wainaulo porphyry in Fiji (Fig. 3-14C), in which external seawater-derived fluids infiltrated the magmatic-hydrothermal system (Orovan et al. 2018).

Metasomatic replacement of K-feldspar, and locally of primary plagioclase (X_{An} 30–45), by albite (X_{An} 1–10), oligoclase (X_{An} 10–20), and minor epidote implies fluid log $(a_{Na^+})/(a_{H^+})$ values in excess of 4, log $(a_{Ca}2+)/(a_{H}+)^2$ values between roughly 6 and 7, and near neutral pH conditions during Na-Ca alteration at 350–400°C (Beane, 1982; Bird et al., 1984). The composition of secondary feldspars associated with Na-Ca and Na alteration at Yerington is similar to the Na-Ca feldspar compositions in the GCB (Fig. 3-10). A Cl-bearing fluid on a prograde thermal path can cause an exchange reaction between primary K-feldspar and secondary albite (Carten, 1986; Dilles and Einaudi, 1992). Also, the presence of chlorite and / or actinolite and accessory titanite within Na-Ca halos indicates that the fluid had a high $(a_{Mg^{2+}})/(a_{H^+})^2$ and, at 400°C, log $(a_{Ca^{2+}})/(a_{H^+})^2 > \sim 5.5$ (Dilles et al., 1995). Textural evidence (e.g. Figs. 3-4A and 3-7C and D) and lithogeochemical data (e.g. Figs. 3-5B and D) indicates that Fe and Cu within albite halos were locally leached during alteration. The removal of Fe, Cu, and Zn would be facilitated by heating of a Cl-bearing fluid because the solubility of these metals increases with increasing temperature (Hemley and Hunt, 1992). Similarly, a thermally prograding fluid would account for the paucity of quartz in HVC Na-Ca facies veins, because the solubility of quartz increases with increasing temperature up to ~500°C in a 5 wt. % NaCl solutions (Monecke et al., 2018). The rare quartz that occluded cavities in some epidote veins (e.g. Figs. 9A and B), could have precipitated from a cooling residual fluid, or is related to a separate younger event. In other porphyry systems, some elements lost from potassic zones (e.g. Ca, Fe, Co) are redistributed outwards producing metasomatic propylitic alteration domains (Pacey et al., 2016), thus a spent and cooling magmatic fluid could conceivable cause some Ca and Na-metasomatism, but perhaps not deplete the rock in Fe and Cu.

Epidote in Na-Ca facies veins are enriched in D, and over half of the samples are depleted in ^{18}O, relative to residual magmatic water field and the fluids in equilibrium with average GCB host rocks (Tables 3-5 and 3-6). Fluids in equilibrium with actinolite appear to be magmatic in origin (Fig. 3-14C), but perhaps represent the composition of the primary mafic phase due incomplete replacement by secondary actinolite (e.g. Figs. 3-9E and G). The $\delta^{18}O_{fluid}$ and δD_{fluid} values of Na-Ca chlorites from the Bethlehem porphyry area contrast. One chlorite sample appears to be derived from magmatic fluids, while the other is enriched in D and depleted in ^{18}O relative to the residual magmatic water field (Fig. 3-14C). The δD_{fluid} and $\delta^{18}O_{fluid}$ values of prehnite and epidote in propylitic alteration are varied but some samples exhibit ^{18}O-depletion and D-enrichment relative to magmatic water, similar to the Na-Ca facies (Fig. 3-14C).

Tourmaline stability is favored by high to moderate fluid acidity, and with increasing pH and temperature, the minimum aqueous boron concentration required to stabilize tourmaline increases (Morgan and London, 1989). Thus, the optimal pH range for tourmaline precipitation is somewhat at odds with the likely neutral to mildly alkaline conditions of Na-Ca alteration, which may account for the petrographic observation that tourmaline did not typically form contemporaneously with epidote in Na-Ca veins (e.g. Figs. 3-12D, C and H). Tourmaline forming in potassic and white-mica–chlorite veins predominantly contain <2 Fe per formulae unit (Table 3-4), and are compositionally similar to tourmaline in Cu-bearing alteration assemblages from other porphyry Cu systems (Fig. 3-13B). Numerous pre- and post-, and many syn-Na-Ca tourmaline analyses have >2 Fe per formulae unit and overlap with the composition of tourmaline reported from epidote-albite zones in the Takom zone at the Woodjam porphyry Cu system in central British Columbia (Fig. 3-13C). The high Fe-concentration of tourmaline in Na-Ca veins perhaps reflects a local increase in fluid Fe caused by chloritization of mafic minerals and dissolution of magnetite within albite halos. Similarly, the switch from Fe-poor (T1) to Fe-rich (T2) tourmaline in the breccia at Highmont may reflect spatial and temporal fluctuations in fluid Fe-concentration caused by precipitation of specularite cement. The $\delta^{18}O_{fluid}$ and δD_{fluid} values of tourmaline in Na-Ca facies veins have predominantly higher δD_{fluid} values, and are depleted in ^{18}O, relative to the residual magmatic water field, and the fluids in equilibrium with the Cu-mineralized EH muscovite veins (Fig. 3-14; Table 3-6)– implying that the tourmaline formed from a dominantly non-magmatic fluid.

In conclusion, the fluid that caused Na-Ca alteration in the GCB is inferred to have been Cl-bearing, at near-neutral pH, and to have high activities of Na, Mg, Ca, and locally B.

Furthermore, the metasomatic exchange of K for Na, localized removal of Fe and Cu, and paucity of secondary quartz suggest that the fluid was progressively heating, not cooling. The range in $\delta^{18}O_{fluid}$ and δD_{fluid} values of Na-Ca minerals cannot be attributed to a magmatic source alone. The stable isotope modeling demonstrates that isotopic exchange between average GCB host rock and seawater at low water–rock ratio (<0.1) could produce fluid compositions consistent with the fluids in equilibrium with most of Na-Ca facies minerals (Fig. 3-13C). Due to the lower ionic potential of K relative to Fe and Cu (Railsback, 2003), alteration occurring at low water–rock ratio might preferentially remove the more mobile ion (c.f., Figs. 3-5A, B and D). Based on the total range $\delta^{18}O_{fluid}$ and δD_{fluid} values of Na-Ca and propylitic minerals and the D-enrichment of some white-mica–chlorite facies minerals (c.f. this study and Jones, 1974), however, both an external seawater-derived fluid and MVP (or an admixture of both) are interpreted to have been present in and adjacent the porphyry Cu systems at HVC (Jones, 1974; Osatenko and Jones, 1976). Furthermore, based on simple mixing models independent of water–rock ratio, Jones (1974) postulates that the proportion of seawater in the Valley-Lornex magmatic-hydrothermal system decreased through time from up to 69% to between 16 and 44% during the main period of sulfide deposition and MVP flux. Moreover, late gypsum veins at Valley have $\delta^{34}S$ values between 13 and 15 ‰, suggesting precipitation from a solution potentially containing seawater sulfate (Jones, 1974; Osatenko and Jones, 1976).

3.11.4 Source of Sr

The $^{87}Sr/^{86}Sr_i$ of K-feldspar altered (potassic) and pervasively white-mica–chlorite altered Bethsaida granodiorite samples are interpreted to represent the Sr-isotope composition of the MVP at HVC. The percent of seawater Sr in the hydrothermal fluid that caused Na-Ca alteration was calculated based on mixing between Triassic seawater with a $^{87}Sr/^{86}Sr$ of 0.7076 (Tremba et al., 1975) and the $^{87}Sr/^{86}Sr_i$ of HVC MVP (0.70338; Table 3-7). The average seawater Sr component in Na-Ca altered rocks is 1.6 % ($n = 8$), with a maximum of 3 % in the albite altered tourmaline-quartz cemented breccia at Highmont (15KB270; Table 3-7). Thus, most of the Sr in Na-Ca altered rocks is derived from the magmatic precursors.

In zones of low water–rock ratio, Sr in the fluid is able to isotopically equilibrate with the host rocks, resulting in $^{87}Sr/^{86}Sr$ compositions that more closely reflect the host rock signature (Orovan et al. 2018). The low percentage of seawater Sr in the strongly Na-Ca altered samples could be due to dilution by residual primary magmatic Sr in the rock, and / or isotopic equilibration of the fluid with the wall-rock at low water–rock ratio that would be facilitated by the low concentration of Sr in seawater (~10 ppm) relative to GCB host rocks (400–800 ppm). Regardless, there was likely a component of external seawater-derived Sr in the HVC magmatic-hydrothermal system.

3.11.5 Source of B

Tourmaline from all samples in the HVC is significantly ^{11}B-enriched relative to unaltered mid-ocean-ridge-basalt, but they are similar to the range of δ^{11}B values in seawater-altered mid-ocean-ridge-basalt and ophiolite gabbros (Fig. 3-15). The δ^{11}B values also overlap with the range of island-arc basalt, dacite, and I-type granite and volcanic rocks, whose ^{11}B-enriched composition is attributed to subduction of seafloor-altered oceanic crust (Trumbull and Slack, 2018). The HVC tourmaline δ^{11}B values are higher than those currently reported from other porphyry Cu systems, and are closer to the ^{11}B-rich compositions in Na-bearing altered igneous rocks from the southwest United States (Fig. 3-15). The highest tourmaline δ^{11}B values (~11 to 15 ‰) in the HVC district are from the albite-altered breccia at Highmont. These ^{11}B-enriched tourmaline overlap with B-isotope compositions of tourmaline from Salobo and Igarapé iron-oxide-copper-gold systems in the Carajás mineral district in Brazil, in which the ^{11}B-enriched source is interpreted to be marine-derived brines (Fig. 3-15; Xavier et al., 2008).

Calculated δ^{11}B values of the hydrothermal fluids in equilibrium with tourmaline at 350°C (Meyer et al., 2008) are reported in Table 3-8. Fluids in equilibrium with tourmaline in the mineralized vein with a K-feldspar halo have the lowest average $\delta^{11}B_{\text{fluid}}$ of 5.4 ‰, whereas the syn-Na-Ca sample has the highest average $\delta^{11}B_{\text{fluid}}$ of 13.7 ‰ and maximum value of 18.3 ‰ (Table 3-8). The curves in Figure 3-16 are closed system Rayleigh fractionation (distillation) models after Taylor and Sheppard (1986). Progressive exsolution of a B-bearing magmatic volatile phase (MVP) from a crystalizing melt causes the residual melt and subsequent MVP to become increasingly depleted in ^{11}B (Fig. 3-16; Smith and Yardley, 1996; Hervig et al., 2002; Trumbull and Slack, 2018). There is no trend towards lower tourmaline δ^{11}B values with magmatic differentiation or paragenetic stage in the HVC district. Rayleigh-type fractionation of MVP by loss of boron during tourmaline formation causes subsequent fluids to become increasingly enriched in ^{11}B (Marschall et al., 2009), whereas progressive phase-separation (boiling) of the MVP has the opposite but smaller effect of depleting the residual liquid of ^{11}B (Fig. 3-16; Liebscher et al., 2005; Kowalski and Wunder, 2018). A MVP exsolved at 600 °C from a melt with a starting δ^{11}B value of -2 ‰, i.e. average I-type granite (Trumbull and Slack, 2018), will form a tourmaline with δ^{11}B values of 1.8–2.5 ‰ between 0–20% B loss (*F* of 1–0.8) at 350°C– i.e., similar to potassic facies and some pre-Na-Ca tourmaline B-isotope compositions at HVC (Fig. 16). Extensive B-loss (*F* = 0.07, or 93%) from this fluid would be required to form tourmaline with δ^{11}B values > 10 ‰ (Fig. 3-16), and 97% loss to make the most ^{11}B-enriched tourmaline. Such excessive B-loss over a large area and across multiple paragenetic stages is unlikely. A more probable explanation for the HVC tourmaline with high δ^{11}B values is that they formed from an ^{11}B-enriched fluid. Potential ^{11}B-rich source reservoirs are seawater, formation water in submarine volcanic rocks, or marine evaporites (Fig. 3-15). There is no evidence of evaporites in the Nicola Group, but the former two B reservoirs are compatible with the D and O isotope composition of some Na-Ca minerals in the GCB.

3.11.6 Genesis of Na-Ca veins and alteration

The $\delta^{18}O_{fluid}$ and δD_{fluid} values of Na-Ca facies epidote and tourmaline veins, and some halo chlorite and albite, support the inference that seawater-derived fluids caused Na-Ca alteration at most localities, and furthermore indicate that the alteration predominantly occurred at low water–rock ratio (Fig. 3-14C). The total range of fluid D, O and B isotope values of Na-Ca minerals, however, requires involvement of more than one fluid reservoir, i.e. seawater-derived fluid and MVP. Moreover, the high intra-sample δ^{11}B variation of >3 ‰ exhibited by some samples suggests that magmatic and seawater-derived fluids locally mixed and formed tourmaline. The strongest seawater-signal occurs in samples of apparent high paleo-permeability and water–rock ratio in the porphyry centers, e.g. the syn-Na-Ca tourmaline in the Highmont breccia ($\delta^{11}B_{fluid}$ values of ~10–18 ‰ and 3 % seawater Sr), and the epidote in the white-mica–specularite-chalcopyrite vein at Bethlehem (δD_{fluid} of 0.6 ‰ and $\delta^{18}O_{fluid}$ of 3.5 ‰). Taking the isotopic tracers and inferred fluid composition together, the alteration peripheral to the Cu centers was caused predominately by thermally prograding seawater-derived brine at low water–rock ratio that mixed with magmatic fluids in and around the porphyry centers. The limited data for propylitic minerals suggest it also formed from both MVP and seawater-derived fluid but at lower temperature, and post-dating Na-Ca alteration and main-stage Cu-mineralization.

Cross-cutting relationships indicate that the ingress of seawater-derived fluid occurred multiple times in the GCB and that these were temporally related to the emplacement of stocks and dikes, and separate pulses of MVP release, at some of the porphyry centers (Fig. 3-8). Moreover, the paragenetic relationships at the Highmont porphyry center imply fluxing between Cu-bearing MVP and the external seawater-derived fluid that caused albite alteration. Mixing, and back and forth flow, between seawater-derived fluid and MVP is also likely to have occurred in the Valley-Lornex porphyry center (Jones, 1974).

Seawater or seawater-sourced pore fluids in the Nicola Group rocks surrounding the Guichon Creek batholith would provide the salinity (~3.5 wt. %; Chester, 2000) required for Na-Ca alteration, and are consistent with isotopic data and inferred fluid chemistry, but how did this fluid infiltrate the porphyry Cu environment? Mineral-seals formed by the precipitation of calcite and / or anhydrite from heated seawater are thought to isolate external seawater from modern and ancient magmatic-hydrothermal systems (Hedenquist et al., 1993; Vennemann et al., 1993). Circulation of seawater to deep levels in the crust (approximately -7 km), however, occurs at some Mid-Atlantic Ridge hydrothermal fields along steeply dipping segments of detachment faults (de Martin et al., 2007). Accordingly, we propose that thermally driven convection coupled with upwelling of buoyant magmatic-hydrothermal fluids caused the downward and inward flow of seawater-derived fluids through the batholith towards the HVC porphyry cupolas (Fig. 3-17; e.g., Cathles, 1977; Weis, 2014). Several processes could have created permeability in the Nicola Group host rocks during emplacement of the Guichon Creek batholith (Fig. 3-17; e.g., Norton, 1979; Tosdal and Richards, 2001), whereas, the regional-scale permeability in the batholith is likely related to formation of cooling joints in the host intrusions (Bergbauer and Martel, 1999; Lesage et al., 2016). Whether the seawater-derived fluid came directly from the seabed or from pore-waters in Nicola Group rocks cannot be determined based on available data and exposure.

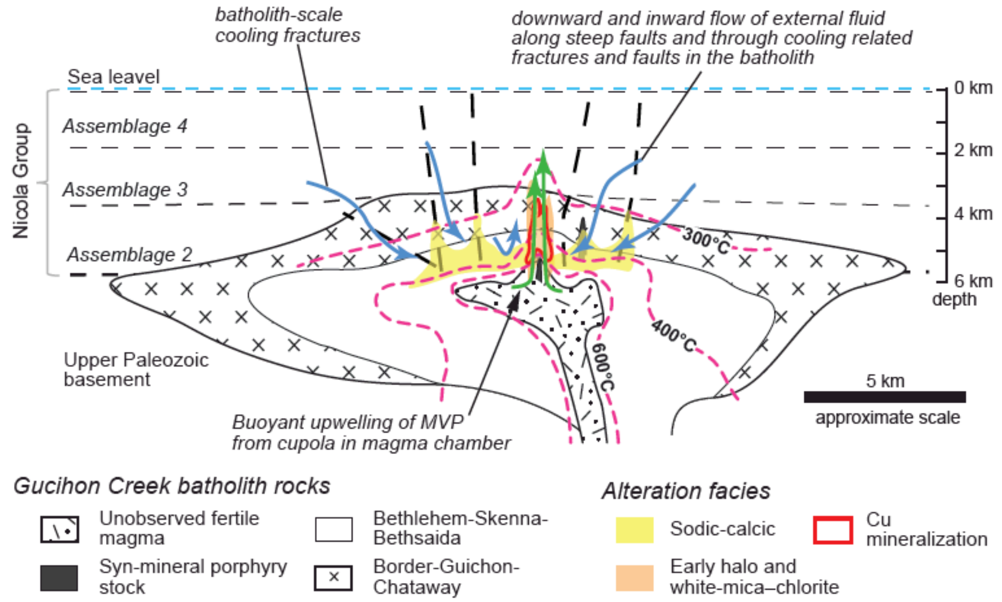

Figure 3-17. Schematic showing the genesis of Na-Ca alteration from the ingress of seawater-sourced pore fluids from Nicola Group country rocks into the GCB. Modified after Dilles et al. (2000) and Tosdal and Richards (2001). Permeability in the Nicola Group rocks is inferred to have formed by piston mechanism roof extension above the expanding batholith as it formed (Tosdal and Richards, 2001). Downward and lateral fluid-flow within the batholith towards the porphyry cupola is interpreted to have been focused along cooling fractures / joints in the older plutonic host rocks. Note, Assemblage 1 of the Nicola Group is thin or absent in the southwestern parts of the Quesnel terrane (Schiarizza, 2016 and 2017).

3.12 Implications for fluid sources in porphyry Cu systems and exploration

The presence of Na-Ca alteration in the GCB demonstrates that seawater-derived fluids can infiltrate batholiths and porphyry systems at deep levels (4–5 km) in the crust, and highlights that complex paleo-hydrology and non-magmatic fluid sources result in atypical porphyry Cu alteration zones (Fig. 3-17). Sodium-bearing alteration assemblages are not unique to the porphyry Cu environment (Dilles and Einaudi, 1992; Williams et al., 2005), and the required fluids can come from a variety of sources (Dilles et al., 1992; Battles and Barton, 1995; Lang et al., 1995; Hunt et al., 2007). Key factors, however, for generating wide-spread Na-Ca assemblages, K-depleted rocks, and local leaching of Fe and Cu, are the presence of permeability and conditions such that the external saline fluid is heated on ingress to the porphyry system.

The effectiveness of porphyry Cu mineral vectoring and fertility indicators (e.g., Cooke et al., 2014; Wilkinson et al., 2015) may be influenced by the relative proportions of MVP to external fluids, and the degree to which these fluids contributed to the alteration patterns peripheral to sulfide-bearing portions of the system. Albite alteration may be more common in rocks peripheral to porphyry Cu systems in the Quesnel and Stikine terranes in the Canadian

Cordillera than currently recognized (e.g., this study; Chapman et al., 2015; Kobylinski et al., 2016). While not strictly an indication of porphyry Cu prospectivity, recognition of Na-Ca facies alteration in island and low-lying coastal arcs can be important because the alteration forms a large footprint that is spatially related to thermal anomalies and potential porphyry centers.

4 The paragenesis and chemistry of epidote and prehnite in the Highland Valley Copper Porphyry Cu district, British Colombia, Canada

4.1 Introduction

Porphyry Cu deposits are the primary source of Cu globally and although demand is variable, and recycling is increasing, new quality projects and resources are needed to replace decreasing inventories (Seedorff et al., 2005; Sillitoe, 2010; Thompson, 2016). Exploration costs and expenditures have increased approximately three-fold over the last 12 years (Wilburn et al., 2015; Wood, 2016), yet discovery rates are down and very few new deposits have been found (Sillitoe, 2013). As a result, exploration is focusing on porphyry plays with little or no surface expression in known productive belts, or in under-explored, high-risk jurisdictions, necessitating more effective and efficient exploration techniques to vector to Cu-rich zones (Sillitoe, 2013; Schodde, 2014; Wood, 2016). Furthermore, for exploration to be successful it is critical to discriminate alteration associated with economic porphyry Cu systems from non-prospective propylitic alteration that can be caused by barren hydrothermal systems (Bird et al., 1984) or by regional metamorphism (Hacker et al., 1992). Studies advancing the use of trace-mineral chemistry have shown that the concentration of some elements in epidote and chlorite vary systematically with respect to porphyry Cu centers (Cooke et al., 2014a; Wilkinson et al., 2015). In the Baguio district, Philippines, Cu, Mo, Au, and Sn were detected in epidote adjacent to Cu mineralization, while distal pathfinder elements (As, Sb, Pb, Zn, Mn) were most enriched in epidote more than 1.5 km from porphyry Cu mineralization (Cooke et al., 2014a). High concentrations of Ti and Zn, and high Ti/Sr and Ti/Pb, characterize chlorite in propylitic rocks up to 1.5 km outboard of the pyrite halo at the Batu Hijau porphyry deposit in Indonesia (Wilkinson et al., 2015). In addition to being pathfinders, As and Sb in high concentrations distinguish epidote formed around porphyry Cu systems from epidote in metamorphic terranes (Wilkinson et al., 2017).

Four major porphyry Cu-(Mo) systems, hosted in the Late Triassic Guichon Creek batholith (GCB), occur in the Highland Valley Copper (HVC) district in British Columbia; Canada's largest and longest operating Cu mine (Fig. 4-1; Ydon, 2007; Byrne et al., 2013; Sillitoe, 2013). Veins of epidote occur with sodic-calcic alteration and form a large footprint (34 km^2) in the HVC district (Byrne et al., 2017; Chapter 2). Prehnite ± epidote veins occur with propylitic alteration around the HVC porphyry centers, overprinting sodic-calcic alteration, and throughout the GCB (Byrne et al., 2017; Chapter 2). We present new trace geochemical data from the epidote and prehnite veins surrounding this prolific mining district. We aim to show that even with widely-spaced samples (up to 2 km) pathfinder elements in epidote and prehnite can detect the presence of porphyry Cu mineralization. Sixty-four samples along two main transects, of ~ 20 and 10 km, from the batholith margins to its center where the porphyry Cu systems occur, were analyzed. We show that the type of alteration influences the major, minor and trace-element composition of epidote. Critically, we add Ge to the previously known suite of pathfinder elements in epidote, and show that Mn, Zn and Pb zoning in epidote and prehnite can be used to vector to Cu-mineralization from up to 8 km away. By comparing HVC epidote to epidote from other geological environments, including the nearby porphyry Cu-barren Nicola Batholith (Fig. 4-1A), we refine the distinguishing characteristics of epidote from porphyry Cu systems. In conjunction with the mineral chemistry vectors and prospectivity criteria, the data processing techniques, and estimates of uncertainty, presented will potentially help geoscientist in the exploration for porphyry Cu deposits.

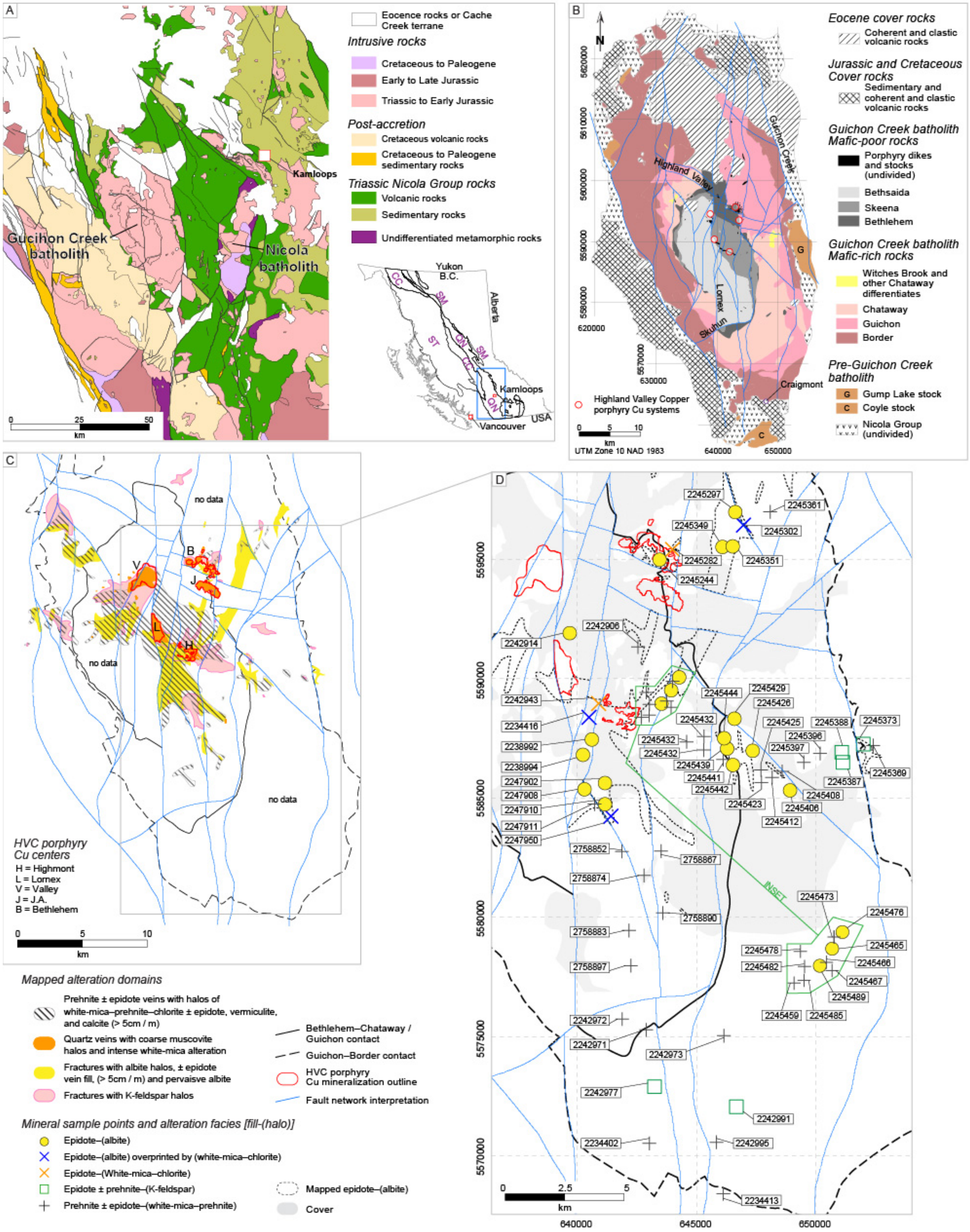

Figure 4-1. Geology and sample location maps. A. Alteration in the Guichon Creek batholith associated with the Highland Valley porphyry Cu systems. B. Location and associated alteration facies of minerals analyzed by EMPA and LA-ICP-MS.

4.2 Epidote, prehnite and porphyry Cu alteration zones

Porphyry Cu occurrences typically exhibit a predictable spatial and temporal distribution of alteration minerals that is the result of a common thermal and chemical evolution (Seedorff et al., 2005). Low- to moderate-intensity replacement of primary feldspars and mafic minerals by an oxidized, hydrous, and Ca-rich assemblage of epidote–calcite–chlorite ± albite, actinolite, pyrite, hematite, prehnite, and zeolites typifies propylitic alteration around porphyry Cu centers (Meyer and Hemley, 1967; Cooke et al., 2014a). Propylitic alteration can extend laterally and upwards for several kilometres away from the well mineralized potassically and hydrolytically altered zones (Seedorff et al., 2005; Cooke et al., 2014b) and, thus, forms the largest footprint for explorationists to recognize. Propylitic alteration commonly involves material-transfer of H_2O, CO_2, and localized S within the pyrite halo, to the altered rock at low water-rock ratio, but limited hydrolysis or alkali-exchange metasomatism (Meyer and Hemley, 1967; Ulrich and Heinrich, 2001; Urqueta et al., 2009; Reed et al., 2013). In some porphyry occurrences, propylitic alteration can be spatially subdivided based on the abundance of actinolite, epidote, and chlorite, calcite and zeolites (Norman et al., 1991; Garwin, 2002; Holliday and Cooke, 2007; Jago et al., 2014).

Epidote can also be observed in sodic-calcic or sodic alteration. These alteration types have been recognized in the peripheral and deep (root) parts of several Laramide porphyry systems in the western part of the US (Dilles and Einaudi, 1992; Seedorff et al., 2008), and in some B.C. porphyry Cu systems (Chapman et al., 2015; Byrne et al., 2017; Chapter 2). Sodic-calcic alteration is characterized by metasomatic replacement of K-feldspar with albite, and the alteration of mafic minerals to actinolite ± epidote, chlorite, and titanite, that generally occurs with veins of epidote or actinolite (Seedorff et al., 2005; Byrne et al., 2017; Chapter 2). Thus, epidote can occur in veins with different alteration halos– propylitic or sodic-calcic.

The epidote group soro-silicates can be divided into three sub-groups– clinozoisite, allanite, and dollaseite– exhibit solid-solution, and have the general formula:

$$A_2M_3(O,F)[T_2O_7][TO_4](OH,O)$$

in which A = Ca, Sr, Mn^{2+} or REE's, M = Al or Fe^{3+} and T = Si (Armbruster et al., 2006). The solid solution between clinozoisite, $Ca_2Al_2AlO[Si_2O_7][SiO_4](OH)$, and epidote,

$Ca_2(Al,Fe^{3+})_2AlO[Si_2O_7][SiO_4](OH)$, is defined by $X_{Fe(total)} = Fe^{3+}/[Fe^{3+} + Al]$ (Armbruster et al., 2006). Epidote from propylitic zones in porphyry Cu systems typically ranges from X_{Fe} of 0.25 to 0.35, but does not consistently vary systematically with distance from Cu-mineralization (Fellows, 1976; Ballantyne, 1981; Norman et al., 1991; Jago, 2008), due to the complex interplay of controls on the major element composition of epidote (Cooke et al., 2014a). Fortunately, however, the crystal-structure of epidote permits incorporation of a wide range of trace elements (Frei et al., 2004). Epidote in propylitic veins most commonly forms at 350–200°C during propylitic alteration (Bowman et al., 1987; Norman et al., 1991), whereas in sodic-calcic veins it is likely forming at a high temperature range of 400–300°C (Carten, 1986; Dilles et al., 1992; Seedorff et al., 2005).

Prehnite is a layered calc-silicate mineral with the general formulae $Ca_2(Al,Fe^{3+})AlSi_3O_{10}(OH)_2$ (Deer et al., 2009). Iron–Al substitution occurs in the octahedral site and the mineral can incorporate Mn (Wheeler et al., 2001; Deer et al., 2009). Prehnite composition is influenced by bulk-rock and fluid compositions, and its stability is dependent on co-existing mineral phases and redox conditions (Liou, 1971; Bird et al., 1984). Prehnite occurs in propylitic halos in mafic-host rocks at the porphyry Cu deposits in Cadia in New South Wales, and in the Collahuasi district, Chile (Wilson et al., 2003; Djouka-Fonkwe et al., 2012). There is a dearth of prehnite trace-element geochemical data in published literature.

Prehnite and epidote can coexist over a limited temperature range around 300–200°C, however, the stability field of prehnite expands with decreasing temperature to ~150°C (Bird et al., 1984; Digel and Gordon, 1995; Bird and Spieler, 2004). At a fixed temperature, the epidote stability field is larger at higher activities of Fe and lower activities of Ca and Si in the fluid than that of prehnite (Bird et al., 1984; Digel and Gordon, 1995).

4.3 Geological setting

4.3.1 Regional geology

The Quesnel terrane in the Canadian Cordillera is characterized by Mesozoic island-arc assemblages comprising of volcanic and sedimentary rocks and associated intrusions (Coney et al., 1980). In southern British Columbia, numerous plutons were emplaced in Nicola Group rocks during the Triassic to Jurassic (Fig. 4-1A; Mortimer, 1986; Mortimer, 1987). The Triassic Guichon Creek batholith (GCB) is a magnetite-bearing I-type composite batholith (D'Angelo et al., 2017) that intruded Nicola Group rocks along the western margin of the Quesnel terrane east the Cache Creek accretionary complex terrane (Fig. 4-1A). The GCB hosts the porphyry Cu-(Mo) systems in the Highland Valley Copper (HVC) district (McMillan, 1976). East of the GCB, Nicola Group volcano-sedimentary rocks occur in a north–south-trending graben (McMillan, 1976; Preto, 1979). Epidote, chlorite, calcite, and albite occur locally as fracture fill and as pervasive alteration throughout mafic Nicola Group rocks in the region (McMillan, 1976; Preto, 1979; Mihalynuk et al., 2016; Schiarizza, 2017). The Nicola batholith horst block occurs on the eastern margins of the Nicola Group graben and comprises multiple Triassic-Jurassic and Eocene aged intrusions (Fig. 4-1A; Moore, 2000). The Nicola batholith was affected by greenschist metamorphism and has no associated porphyry Cu systems (Erdmer et al., 2002; D'Angelo, 2016).

4.3.2 The Guichon Creek batholith

The GCB is compositionally zoned and formed from two main pulses of magmatism (Fig. 1B; McMillan et al., 2009; D'Angelo et al., 2017). The first pulse consists of mafic mineral-rich quartz-diorite, monzogabbro, and granodiorites. The second pulse comprises mafic mineral-poor quartz-rich granodiorites and monzogranites in the interior of the batholith (Fig. 4-1B). Listed from oldest to youngest, the volumetrically significant rocks in the first magmatic pulse are the Border quartz-diorite, Guichon granodiorite, and Chataway granodiorite, and in the second pulse are the Bethlehem granodiorite, Skeena granodiorite and the Bethsaida granodiorite and monzogranite (McMillan, 1976; D'Angelo et al., 2017). There are four porphyry Cu centers in the HVC district– Bethlehem, J.A., Valley-Lornex, and Highmont (Figs. 4-1B and C). However, there are numerous small Cu-occurrences of various size and tenor occur throughout the GCB (McMillan et al., 2009). The HVC porphyry centers formed between ~209 and 207 Ma and are hosted in the mafic-poor granodiorites belonging to the second magmatic pulse of the batholith (D'Angelo et al., 2017). The Valley-Lornex porphyry center has the largest footprint and is the best endowed system in the HVC district (Fig. 4-1C; Byrne et al., 2013). Post-mineralization regional-scale faulting has off-set geological contacts and segmented the once contiguous Valley-Lornex porphyry Cu center (Fig. 4-1C).

4.4 Vein and alteration facies in the Highland Valley Copper porphyry district

The main characteristics of the vein and alteration facies present in the HVC district are summarized in Table 4-1. In the HVC porphyry centers, chalcopyrite, bornite, and localized molybdenite occurs with 1) veinlets and discontinuous fractures filled with quartz; all with K-feldspar alteration halos; 2) early-halo type quartz-coarse-grained muscovite veins and halos; and with 3) pervasive and fracture-controlled fine-grained white-mica–chlorite alteration (Fig. 4-1C; Table 4-1; McMillan, 1985; Byrne et al., 2013; Lesage et al., 2016; Chapter 2). Only minor amounts of pyrite, < 1 vol. %, occur in the HVC porphyry systems and this is, typically, within Cu-mineralized domains (McMillan, 1985a; Casselman et al., 1995). Ore (Cu, Mo, Ag, Zn, Pb) and pathfinder element (e.g., As, Bi, W, Te) concentrations drop to background levels just a few 100 m from the porphyry Cu mineralization (Olade and Fletcher, 1975; Olade and Fletcher, 1976a; Olade and Fletcher, 1976b; Lesage et al., 2016). Distal to Cu mineralization, alteration is restricted to narrow 1–3 cm halos around a low density of prehnite and/or epidote veinlets (e.g., Fig. 4-2; Lesage et al., 2016).

Table 4-1. Alteration and vein facies in the Highland Valley Copper porphyry district

Alteration facies and sub-facies[2]		Fracture fill minerals	Alteration halo minerals	Description	Paragenesis	Location in system	Inferred temperature range[3]	Equivalent alteration type in Sillitoe (2010) and Seedorff et al. (2005)
Barren quartz[5]		Qz,	Weak Ksp, qz	Sugary texture qz veins 1-3cm wide with localized poorly developed Ksp halos. Locally associated with vein-dikes and unidirectional solidification textures at depth in Valle	Cut by syn-mineral qz–(musc) veins	Absent in Bethlehem and Highmont. Deep and centrally located in Valley and Lornex	[a]400-500°C	K-Silicate; potassic. "A"-veins with silicic or Ksp halo; secondary bt alteration
(K-feldspar)		Qz, cp, tour	Ksp, bt, {cp}	Fracture halos (0.2-1 cm) of Ksp associated with discontinuous qz and cp fill. Hbl altered to secondary bt	Possibly coeval with the barren qz vein facies and are cross-cut by well mineralized qz–(musc) facies	Bt and Ksp within Cu zones at Bethlehem, Valley, Lornex and Highmont. Extends outboard of Valley and Highmont for several km as weakly mineralized narrow Ksp fracture halos	[a]350-550°C	
Epidote-(albite)		Ep, act, diop, tour	Ab, chl, ep, act, wm, gt {tit}	Ep veins with irregular and diffuse vein walls and Ksp-destructive halos of ab, ab–wm or ab–ep. Mafics strongly altered to chl ± act within halo. Mt typically altered to Ti-oxides. Plag is also ab altered in intense alteration. Turbidity in altered feldspars caused by micro-porosity and mineral inclusion.	Post-mineral timing at Bethlehem, pre-mineral at Valley and Lornex, and pre and post main mineral at Highmont	Pervasive ab and act ± diop are more common proximal to the HVC porphyry centers. Domains of ep-(ab) extend up to 7 km away from the porphyry centers	[a]300-450°C	Sodic-calcic; sodic
White-mica–chlorite*[6]	Quartz-(muscovite)	Qz, bn, cp, anh, musc	Coarse-grained gray colored musc, bn, Ksp, qz {hem, rt}	Vitreous qz veins with distinctive coarse-grained 0.3-1.5 cm gray colored musc, ± inter-grown fine-grained Ksp, that exhibit bowtie and "sericite-island" textures[e,f]. Primary Ksp and bt generally stable and plagioclase is replaced	Cross-cuts ep-(ab) veins and is overprinted by younger faulted hosted qz-ca-mo-py-(wm-chl) veins	Intimately associated with bn and cp mineralization at Valley, Lornex and locally at Highmont centers. Coarse-grained and green colored musc occurs at some Cu occurrences in the district	[a]350-450°C	Transitional potassic-sericitic; early-halo veins (EH)[d]; early-micaceous (EM)[e]
	(White-mica–chlorite)	Qz, cp, tour, py, mo, ca, wm	Fine-grained white to green colored wm, chl, cp, py, ca, {hem, tit, rt}	Fracture controlled and pervasive fine-grained white to green colored wm in feldspar sites and chl in mafic sites. Locally associated with qz and sulfide veins	Mostly cross-cuts ep-(ab), and overprints qz-(musc) domains	Intimately associated with Cu mineralization at Bethlehem and J.A., and Highmont. Occurs peripheral to and cross-cuts qz-(musc) facies at Valley and Lornex. Common at Cu-occurrences throughout the district	[a]250-350°C	Chlorite-sericite; sericite-chlorite-carbonate (SCC); phyllic
(Clay / argillic)[4]			Fine-grained wm, kaol, mont, chl,	Primary bt replaced to brown colored mixture of wm-mont. Plag altered to mixtures of wm-kaol-mont[g]. Selective replacement of relict plag in previously altered rocks	Appears to be late to post mineral. Most intense in the barren qz vein core, and locally within qtz-(musc) domains, of Valley	Generally limited to the Cu mineralized portions of the J.A. and Valley, and parts of Lornex and Highmont. Occurs in and around structures hosting late ca, qz, py, mo-(wm-chl) veins	[a]100-200°C	Intermediate argillic
Epidote–(K-feldspar)		Ep, prh, pump, ca, qz	Weak to moderate Ksp, wm, ep, chl, prh, verm, ab	Weak to moderately developed Ksp ± ep halos (0.5-1 cm) associated with ep ± prh veins. Irregular and diffuse vein walls. White-micas dominantly have a short-λ Al-OH absorption feature. Primary Ksp stable. Some zoned halos of inner Ksp and outer wm. Mafics altered to chlorite	Pre to syn prh-(wm-prh) facies	Mostly occurs in the more mafic Guichon and Border granodiorites	[a,b,c]200-350°C	Propylitic
Prehnite–(white-mica–prehnite)		Prh, ep, pump, ca, qz	Prh, wm, ab, chl, ep, pump, verm, ca {cp, mt, hem, tit}	Veinlets (0.1-0.2 cm) of prh ± inter-grown ep and ca, ± late pump, with plag-destructive halos of wm-prh and accessory ab. Ksp stable. Turbid feldspar in halos. Hbl incompletely replaced by chl ± act, ep within halo. Primary bt locally altered to chl or verm with prh along cleavage planes Generally sharp vein walls. Mt altered to ilm ± hem. Localized reddening in the halo.	Cross-cuts earlier formed veins and alteration	Highest density of veins centered on the HCV porphyry systems but occurs throughout the batholith at lower vein density	[a,b,c]200-250°C	

[1] based on descriptions in McMillian (1985), Byrne et al. (2013), Lesage et al. (2016), and Byrne et al. (2017). [2] Parentheses "( )" indicate minerals in the halo. [3] Temperature range estimates based on mineral stabilities presented in [a] Seedorff et al. (2005), [b] Bird and Spieler (2004), and [c] Digel and Gordon (1995). [d] Proffett (2009). [e] Alva-Jiminez (2011), [f] Riedell and Proffett (2014). [g] Jambor and Delabio (1978). [5] not assessed in this study. [6] Quartz-(muscovite) and white-mica–chlorite sub-facies are grouped together as white-mica–chlorite* alteration facies in this study. {} = accessory minerals. Mineral abbreviations: ab = albite; bn = bornite; act = actinolite; anh = anhydrite; bt = biotite; ca = carbonates; chl = chlorite; cp =chalcopyrite; diop = diopside; ep = epidote; gt = garnet; hm = hematite; ill = illite; kaol = kaolinite; Ksp = K-feldspar; mont = montmorillonite; musc = muscovite (coarse grained); Mt = magnetite; plag = plagioclase; prh = prehnite; pump = pumpellyite; py = pyrite; qz = quartz; rt = rutile; tit = titanite; tour = tourmaline; verm = vermiculite; wm = white-mica undifferentiated between illite, fine-grained muscovite, paragonite, phengite, and montmorillonite. White-mica is synonymous with sericite.

Two sub-facies of propylitic alteration are recognized in the HVC district (Table 4-1; Figs. 4-2A-F): 1) prehnite–(white-mica–prehnite) and 2) epidote–(K-feldspar). Veinlets of prehnite ± epidote ± pumpellyite with plagioclase-destructive, K-feldspar stable, white-mica–prehnite halos comprise the prehnite–(white-mica–prehnite) sub-facies. This is the most common and most widely distributed alteration facies in the batholith (Figs. 4-2A and B). The proportion of epidote to prehnite in veins of the prehnite-(white-mica–prehnite) sub-facies is generally higher in the mafic-rich host rocks relative to the mafic-poor rocks that host the porphyry Cu centers (c.f. 4-2A and E). The highest density of prehnite-(white-mica–prehnite) veinlets is centered on the porphyry systems, but this sub-facies is present out to the margins of the batholith (c.f. Figs. 4-1C and D). The second propylitic sub-facies comprises epidote veins with weakly developed K-feldspar ± epidote halos in plagioclase, and selective replacement of mafic minerals by chlorite (Figs. 4-2E and F). Epidote-(K-feldspar) sub-facies are restricted to mafic-rich host rocks towards the margins of the batholith (Fig. 4-1D). The mafic minerals in the halos of propylitic facies veinlets are weak to moderately altered to chlorite ± carbonate, prehnite, and vermiculite.

Epidote ± actinolite veins with K-feldspar-destructive albite halos comprise the sodic-calcic facies (epidote-(albite); Table 4-1; Figs. 4-2G to J). Mapped sodic-calcic alteration occurs in a ~0.5–1.5 km-wide north-northeast-elongated domain in the northeast portion of the batholith, and in a ~ 3 km wide domain that extends for ~ 7 km south of Lornex and Highmont (Fig. 4-1C). The sodic-calcic facies in the GCB potentially formed from a seawater-derived fluid (Byrne et al., 2017; Chapter 3). Some sodic-calcic facies epidote veins were re-opened and filled with younger minerals and / or overprinted by white-mica–chlorite alteration (e.g., Fig. 4-2I). Propylitic veins and alteration generally cross-cut sodic-calcic veins (Chapter 4-3).

Rare epidote ± specularite, hematite, chalcopyrite, chlorite, white-mica veins with white-mica–chlorite halos (Figs. 4-2K and L) occur on the fringes of Cu-mineralization at Highmont and Bethlehem (Fig. 4-1D).

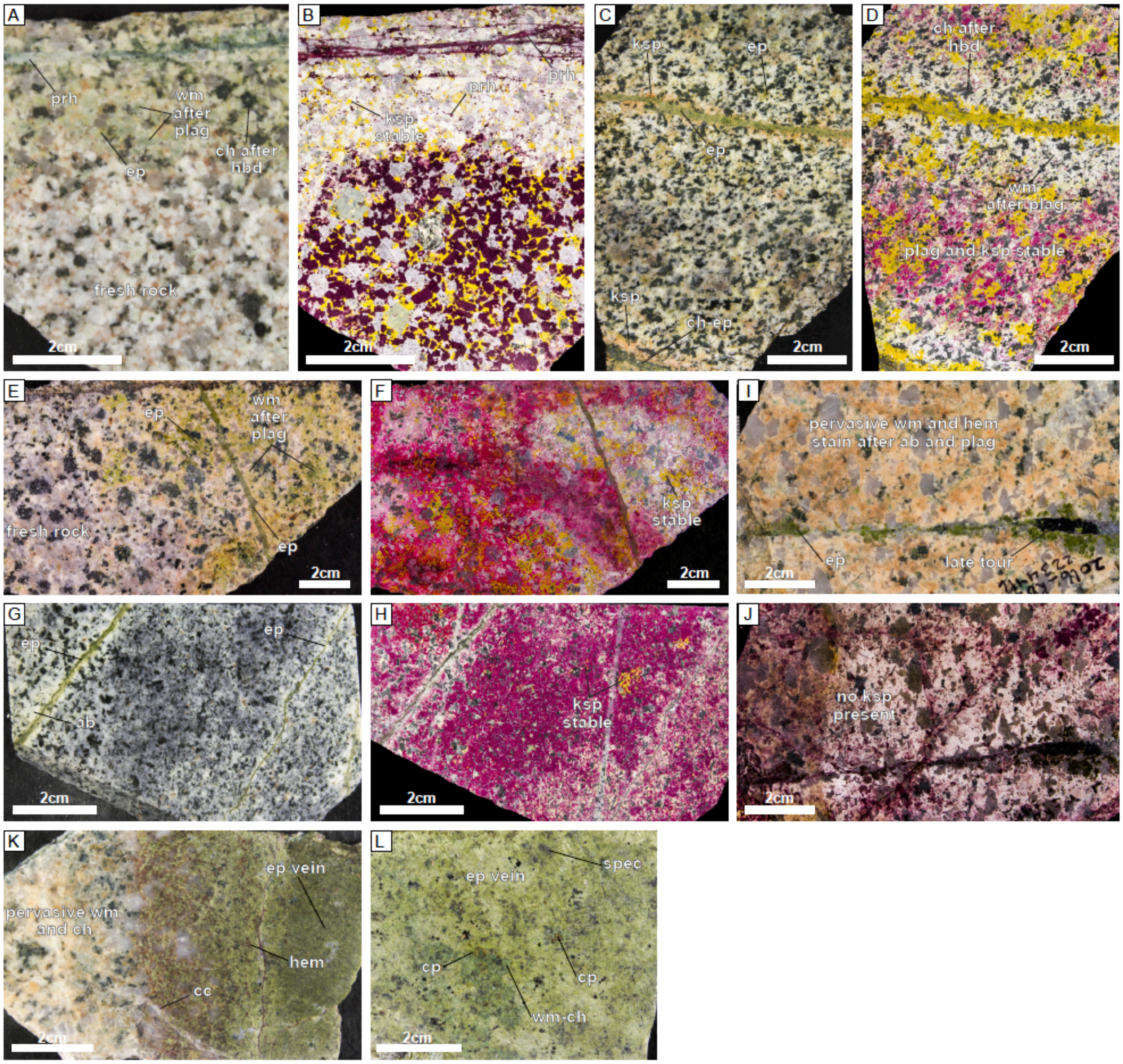

Figure 4-2. Examples of epidote and prehnite-bearing alteration facies in the Guichon Creek batholith. A. unstained and B. stained image pairs of prehnite ± pumpellyite veinlets with plagioclase-destructive, K-feldspar-stable, white-mica–prehnite halo (2758897; propylitic facies). C. unstained and D. stained image pairs of epidote ± chlorite veins with inner K-feldspar halo and outer plagioclase-destructive white-mica halo (2245373; propylitic facies). E. unstained and F. stained image pairs of an epidote vein with an epidote and white-mica–prehnite halo (2242973; propylitic facies). G. unstained and H. stained image pairs of epidote veins with K-feldspar-destructive albite halos (2245429; sodic-calcic facies). I. unstained and J. stained image pairs of a strongly albite altered sample overprinted by pervasive white-mica–chlorite alteration with hematite staining (2234416; sodic-calcic facies overprinted by white-mica–chlorite). The epidote vein is fractured and filled by late tourmaline associated with the white-mica alteration. K. Epidote ± quartz ± hematite vein with pervasive white-mica–chlorite alteration halo (2242943; white-mica–chlorite facies). L. Epidote ± specularite, white-mica, chlorite chalcopyrite vein (2245282; white-mica–chlorite facies). Abbreviations in Table 4-1.

4.5 Methodologies

4.5.1 Sample preparation

Outcrop mapping, core logging, and sampling was conducted between 2014 and 2016 in the GCB. A total of 850 samples were taken from outcrops spaced 0.5–1.5 km apart throughout the district. Approximately 500-1000 cm^3 rock samples of representative vein and alteration zones were cut and slabbed using a rock saw, and underwent lithogeochemical analysis and feldspar staining. Rock slabs were etched with hydrofluoric acid and stained with sodium colbaltinitrite to identify K-feldspar, and with amaranth to stain calcic plagioclase, calcite and prehnite (Appendix 4-A). After staining and macroscopic mineralogy identification, the samples were categorized into alteration facies.

A subset of 64 samples along two main sample traverses was examined at the University of Alberta to characterize the epidote and / or prehnite present (Table 4-2; Fig. 4-1C). One traverse extends 20 km south of Cu mineralization the Lornex and Highmont porphyry centers. The second traverse extends east of Highmont for approximately 10 km. Six epidote samples situated northeast of the Bethlehem porphyry Cu center were also selected for LA-ICP-MS analysis (Fig. 4-1C). Thin-section off-cuts and hand sample vein chips were set in grain mounts for analysis (Appendix 4-A). Paired reflected light and backscattered electron images were collected for each sample in preparation for quantitative analysis.

Epidote from other geological environments were analyzed to test whether specific compositional characteristics can discriminate epidote formed in porphyry Cu systems (Table 4-3; Appendix 4-A). Three samples are from metamorphic terranes in Greece and Chile: epidote from 1) blueschist, 2) blueschist to greenschist transition, and 3) greenschist-facies rocks. A total of four epidote vein samples were collected from the Nicola batholith and adjacent Nicola group volcanic rocks (Table 4-3), that represent a similar geological environment to the GCB, but with no known porphyry Cu mineralization in the vicinity. A sodic-calcic epidote vein in a granite porphyry stock from the Yerington porphyry Cu district (Dilles et al., 2000), Nevada, was also analyzed (Table 4-3). The diverse origins of the epidote in this sample suite provide a good framework for discriminating compositional features related to porphyry Cu systems, and the processes unique to their formation.

Table 4-2. LA-ICP-MS epidote and prehnite samples

Sample ID	Number of Spots	Mineral	Texture	Station	East	North	Host Rock Granodiorite	Alteration Facies
2234402	14	Epidote	Vein	2016KB041	643020	5570520	Guichon	Prehnite-epidote-(white-mica-chlorite)
2234413	17	Epidote	Vein	2016KB048	646119	5568409	Border	Prehnite-epidote-(white-mica-chlorite)
2234416	16	Epidote	Vein	2016KB061	640492	5588376	Bethsaida	Epidote-(albite) overprinted by (white-mica-chlorite)
2234424	9	Epidote	Vein	BETH North	640514	5601872	Chataway	Prehnite-epidote-(white-mica-chlorite)
2238992	10	Epidote	Vein	2015GL010	640611	5587446	Bethsaida	Epidote-(albite)
2238994	8	Prehnite	Vein	2015GL011	640262	5586814	Bethsaida	Epidote-(albite)
2238994	4	Epidote	Vein	2015GL011	640262	5586814	Bethsaida	Epidote-(albite)
2238997	21	Epidote	Vein	2015GL011	640240	5586804	Bethsaida	Epidote-(albite)
2242906	12	Epidote	Vein	2015KB243	642548	5591322	Skeena	Prehnite-epidote-(white-mica-chlorite)
2242914	15	Epidote	Vein	2015KB250A	639686	5591903	Skeena	Epidote-(albite)
2242943	10	Epidote	Vein	2015KB279	640894	5588954	Skeena	Epidote-(white-mica-chlorite)
2242971	10	Prehnite	Vein	2016KB017	642892	5575277	Chataway	Prehnite-epidote-(white-mica-chlorite)
2242971	7	Epidote	Vein	2016KB017	642892	5575277	Chataway	Prehnite-epidote-(white-mica-chlorite)
2242972	3	Prehnite	Vein	2016KB018	641882	5575729	Skeena	Prehnite-epidote-(white-mica-chlorite)
2242972	20	Epidote	Vein	2016KB018	641882	5575729	Skeena	Prehnite-epidote-(white-mica-chlorite)
2242973	13	Epidote	Vein	2016KB019	646143	5575035	Chataway	Prehnite-epidote-(white-mica-chlorite)
2242977	14	Epidote	Vein	2016KB023	643239	5572898	Chataway	Epidote-prehnite-(K-feldspar)
2242991	10	Prehnite	Vein	2016KB031	646669	5572057	Chataway	Epidote-prehnite-(K-feldspar)
2242995	9	Prehnite	Vein	2016KB035	645835	5570571	Chataway	Prehnite-epidote-(white-mica-chlorite)
2245244	15	Epidote	Vein	B14-015_202.6	643452	5594980	Bethlehem	Epidote-(albite)
2245282	17	Epidote	Vein	2015KB043A	643997	5595408	Chataway	Epidote-(white-mica-chlorite)
2245297	13	Epidote	Vein	2015KB056	646965	5596434	Guichon	Epidote-(albite) overprinted by (white-mica-chlorite)
2245302	14	Epidote	Vein	2015KB062	646623	5596976	Guichon	Epidote-(albite)
2245349	17	Epidote	Vein	2015KB102	646085	5595515	Guichon	Epidote-(albite)
2245351	1	Epidote	Vein	2015KB103A	646516	5595539	Chataway	Epidote-(albite)
2245361	19	Prehnite	Vein	2015KB111	648084	5596986	Guichon	Prehnite-epidote-(white-mica-chlorite)
2245369	10	Prehnite	Vein	2015KB120	652400	5587195	Guichon	Prehnite-epidote-(white-mica-chlorite)
2245373	16	Epidote	Vein	2015KB122	651987	5587255	Guichon	Epidote-prehnite-(K-feldspar)
2245387	18	Epidote	Vein	2015KB136	651134	5586490	Chataway	Epidote-prehnite-(K-feldspar)
2245388	10	Prehnite	Vein	2015KB137	651083	5586911	Guichon	Epidote-prehnite-(K-feldspar)
2245396	8	Prehnite	Vein	2015KB144	650179	5586864	Chataway	Prehnite-epidote-(white-mica-chlorite)
2245397	8	Prehnite	Vein	2015KB145	649496	5586489	Chataway	Prehnite-epidote-(white-mica-chlorite)
2245406	10	Epidote	Vein	2015KB152	648917	5585313	Guichon	Epidote-(albite)
2245408	16	Prehnite	Vein	2015KB154	648591	5586106	Guichon	Prehnite-epidote-(white-mica-chlorite)
2245408	2	Epidote	Halo	2015KB154	648591	5586106	Guichon	Prehnite-epidote-(white-mica-chlorite)

Table 4-2 continued

2245412	2	Prehnite	Vein	2015KB156	648164	5585853	Guichon	Prehnite-epidote-(white-mica-chlorite)
2245423	10	Prehnite	Vein	2015KB166	647716	5585645	Chataway	Prehnite-epidote-(white-mica-chlorite)
2245425	11	Prehnite	Vein	2015KB168	647703	5586167	Chataway	Prehnite-epidote-(white-mica-chlorite)
2245426	10	Prehnite	Vein	2015KB169A	647351	5586974	Guichon	Prehnite-epidote-(white-mica-chlorite)
2245429	10	Epidote	Vein	2015KB171	646588	5588317	Chataway	Epidote-(albite)
2245432	10	Prehnite	Vein	2015KB173	645310	5587573	Skeena	Prehnite-epidote-(white-mica-chlorite)
2245439	11	Epidote	Vein	2015KB180	646281	5587062	Chataway	Epidote-(albite)
2245441	9	Prehnite	Vein	2015KB181	646112	5586606	Skeena	Prehnite-epidote-(white-mica-chlorite)
2245442	11	Epidote	Vein	2015KB182	646525	5586377	Skeena	Epidote-(albite)
2245444	16	Epidote	Vein	2015KB184	646156	5587500	Chataway	Epidote-(albite)
2245459	11	Prehnite	Vein	2015KB199	642690	5588377	Skeena	Prehnite-epidote-(white-mica-chlorite)
2245465	19	Epidote	Vein	2015KB205	643936	5589507	Skeena	Epidote-(albite)
2245466	10	Prehnite	Vein	2015KB206	643752	5589063	Skeena	Prehnite-epidote-(white-mica-chlorite)
2245467	19	Epidote	Vein	2015KB207	643937	5588792	Skeena	Prehnite-epidote-(white-mica-chlorite)
2245468	10	Epidote	Vein	2015KB208	644585	5587348	Skeena	Prehnite-epidote-(white-mica-chlorite)
2245471	11	Epidote	Vein	2015KB210	645303	5587005	Bethsaida	Prehnite-epidote-(white-mica-chlorite)
2245473	11	Epidote	Vein	2015KB213	643998	5589888	Skeena	Prehnite-epidote-(white-mica-chlorite)
2245476	15	Epidote	Vein	2015KB216	644272	5590052	Bethsaida	Epidote-(albite)
2245478	14	Epidote	Vein	2015KB218	642894	5589418	Skeena	Prehnite-epidote-(white-mica-chlorite)
2245482	11	Prehnite	Vein	2015KB222	643028	5588921	Skeena	Prehnite-epidote-(white-mica-chlorite)
2245482	3	Epidote	Halo	2015KB222	643028	5588921	Skeena	Prehnite-epidote-(white-mica-chlorite)
2245485	13	Epidote	Vein	2015KB226	643015	5588467	Skeena	Prehnite-epidote-(white-mica-chlorite)
2245489	15	Epidote	Vein	2015KB229B	643531	5588947	Skeena	Epidote-(albite)
2247902	17	Epidote	Vein	2015GL015	641162	5585621	Bethsaida	Epidote-(albite)
2247908	1	Epidote	Vein	2015GL018	640303	5585360	Bethsaida	Epidote-(albite)
2247910	1	Epidote	Halo	2015GL020	641164	5584733	Bethsaida	Epidote-(albite)
2247911	10	Prehnite	Vein	2015GL021	640725	5584742	Bethsaida	Prehnite-epidote-(white-mica-chlorite)
2247911	2	Epidote	Vein	2015GL021	640725	5584742	Bethsaida	Prehnite-epidote-(white-mica-chlorite)
2247950	16	Epidote	Vein	2015GL051	641410	5584234	Bethsaida	Epidote-(albite) overprinted by (white-mica-chlorite)
2758852	10	Prehnite	Vein	2015GL052	641872	5582754	Bethsaida	Prehnite-epidote-(white-mica-chlorite)
2758867	9	Prehnite	Vein	2015GL064	643512	5582769	Bethsaida	Prehnite-epidote-(white-mica-chlorite)
2758867	9	Epidote	Vein	2015GL064	643512	5582769	Bethsaida	Prehnite-epidote-(white-mica-chlorite)
2758874	7	Prehnite	Vein	2015GL070	642800	5581748	Bethsaida	Prehnite-epidote-(white-mica-chlorite)
2758883	12	Prehnite	Vein	2015GL077	642172	5579441	Bethsaida	Prehnite-epidote-(white-mica-chlorite)
2758890	10	Prehnite	Vein	2015GL081	643590	5580180	Bethsaida	Prehnite-epidote-(white-mica-chlorite)
2758890	3	Epidote	Vein	2015GL081	643590	5580180	Bethsaida	Prehnite-epidote-(white-mica-chlorite)
2758897	10	Prehnite	Vein	2015GL088	642245	5577968	Bethsaida	Prehnite-epidote-(white-mica-chlorite)
2758897	6	Epidote	Halo	2015GL088	642245	5577968	Bethsaida	Prehnite-epidote-(white-mica-chlorite)

Table 4-3. Epidote samples from other geological environments

Sample ID	Number of points	Location	Environment	Facies	Comments
SIF 06-6	20	Sifnos, Greece	Metamorphic	Transitional blue- to greenschist	Grain separates from a mobilisate
17 FB05	17	Syros, Greece	Metamorphic	Greenschist	After an eclogite. Grain separates.
AL15-18a	18	Diego de Almagro Island, South Chile	Metamorphic	Blueschist	Minor impurities of garnet and blue amphibole. Grain separates.
2017KB001 and 2017KB002	29	Nicola batholith, southern BC	Epizonal	Greenschist / propylitic	Epidote veins hosted in pervasively chlorite altered and weakly foliated mafic-rich quartz-diorite
2017KB003	13	Nicola Group country rocks, southern BC	Epizonal	Hydrothermal / propylitic	Epidote-calcite vein with Cu-oxides after chalcopyrite in basaltic volcaniclastic rock. Pervasive and weak fine-grained chlorite and white-mica alteration
2017KB004	12	Nicola Group country rocks, southern BC	Epizonal	Hydrothermal / propylitic	Epidote vein in basaltic volcanoclastic rock. Pervasive and weak fine-grained chlorite and white-mica alteration
2017KB007	22	Yerington porphyry Cu district, Nevada, US	Epizonal	Sodic-calcic	Epidote vein with epidote and albite in halo hosted in granite

4.5.2 *Electron microprobe analyses*

Electron microprobe analyses (EMPA) was performed using the CAMECA SX100 at the University of Alberta, primarily to determine the major and minor-element composition of silicate alteration minerals in the GCB. For the wavelength-dispersive spectrometry (WDS) the EPMA beam was operated in spot mode at an accelerating voltage of 20 kV, a probe current of 20 nA, and a beam diameter between 1–5 µm depending on the target mineral. Unknowns were analyzed at a peak count time of 30 s and background count time of 30 s. Standards were analyzed for 20–30 s on peak. Standards used are listed in Appendix 4-A. A total of 572 analyses from 55 samples of epidote veins and alteration halos, and 206 analysis points from 25 prehnite veins were collected (Supplemental data 4-A).

Table 4-4. LA-ICP-MS data summary

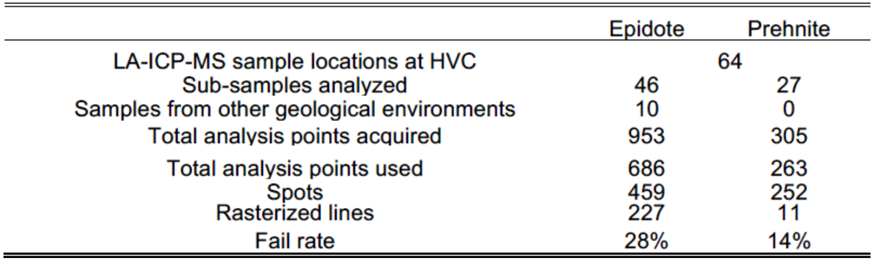

	Epidote	Prehnite
LA-ICP-MS sample locations at HVC	64	
Sub-samples analyzed	46	27
Samples from other geological environments	10	0
Total analysis points acquired	953	305
Total analysis points used	686	263
Spots	459	252
Rasterized lines	227	11
Fail rate	28%	14%

4.5.3 Quantitative multi-element trace geochemistry analysis

Laser ablation inductively-coupled plasma mass spectrometry (LA-ICP-MS) was used to analyze a total of 953 epidote and 305 prehnite spots, and rasterized lines, in 64 samples from the GCB, and eight samples from other geological environments. To analyze the samples a Teledyne Excite 193 nm analyte excimer laser coupled to an iCAP RQ inductively coupled quadrupole mass spectrometer at the German Research Center for Geosciences was used. Very short washout times of the laser aerosol were achieved by the use of a two-volume cell. Quantitative analyses of epidote were performed by ablating 20 μm spots with a laser repetition rate of 10 Hz. For the 193-nm laser the beam fluence at the sample was ~3–5 J/cm^2. A total of 44 elements were analyzed at each spot. Ablation was performed in an atmosphere of pure He (~0.7 L/min). The analysis time for each sample was 50 s, with 20 s for measurement of the baseline with gas background (laser off) and 30 s of signal analysis with laser on. A total of 46 isotopes were measured and used: ^{23}Na, ^{24}Mg, ^{39}K, ^{45}Sc, ^{47}Ti, ^{51}V, ^{52}Cr, ^{55}Mn, ^{57}Fe, ^{59}Co, ^{60}Ni, ^{63}Cu, ^{71}Ga, ^{74}Ge, ^{75}As, ^{85}Rb, ^{88}Sr, ^{89}Y, ^{93}Nb, ^{95}Mo, ^{107}Ag, ^{111}Cd, ^{116}Sn, ^{121}Sb, ^{139}La, ^{140}Ce, ^{141}Pr, ^{146}Nd, ^{147}Sm, ^{153}Eu, ^{157}Gd, ^{159}Tb, ^{163}Dy, ^{165}Ho, ^{166}Er, ^{169}Tm, ^{172}Yb, ^{197}Au, ^{205}Tl, ^{208}Pb, ^{209}Bi, ^{232}Th, ^{238}U. Acquisition time for each mass was set to 0.02 s except ^{23}Na and ^{39}K which was set to 0.01 s, with a total sweep time to analyze all masses ~1.02 s. The NIST-610, 612 and BHVO-2G glass standards were inserted for every 10 unknown analyses and used for calibration. Uncertainty estimates for the elements measured are based on repeated measurement (n=155) of the BHVO-2G reference material and accepted values derived from the GeoReM database (Jochum et al., 2007). An average accuracy (relative error / bias) of 10 % is estimated for most element determinations, except for Co, Ni, Cu, Y, Mo, Sn, Sb, Tm, Pb and U which are ~15 % (Supplemental data 4-B). The average relative standard deviation (precision) for all elements is ~15 %. Calcium concentrations determined by EMPA analyses on the same areas of interest was used as the internal standard.

Time intervals for data reduction were selected by visual inspection of each spectrum using Iolite™ a package for Igor Pro™ (Paton et al., 2011). The major mineral-forming elements K, Na, Mg, and Ca were used as a monitor for epidote and prehnite purity. Parts of the spectrum that show large changes in the major elements and spikes in trace chemistry are inferred to be mineral inclusions and were excluded from the integration– 28 % of epidote and 14 % of prehnite spectra were rejected (Table 4-4). If only samples from HVC are considered, rejection of epidote spectra rose to ~ 35 %. This is primarily attributed to a higher content of mineral-inclusions that occluded volumes (vugs) between epidote grains (see below) in HVC district epidote veins. The mean, median and mode integration times for epidote and prehnite analyses are 24.43 s, 27.09 s, and 27.07 s, respectively. All mineral used LA-ICP-MS data can be found in Supplemental data 4-C.

4.6 Data processing and reproducibility

The limit of detection (LOD) for each element per analysis were calculated based on counting statistics using Igor Pro Iolite™. Experimental conditions being equal, analyses with lower integration times have a higher LOD for each element. The mean, median and mode LOD for each element were calculated for our data-set (Table 4-5). The LOD mode value was chosen to populate element data fields that were below LOD (i.e, null values). The LOD mode was used because it is less susceptible to outliers than the arithmetic mean. Populating below detection null fields with a numeric value facilitates plotting of results, and calculation of mean and median terms for samples comprising multiple analysis points. For Na, K, Cr, Ni, Cu, Rb, Nb, Mo, Ag, Cd, Au and Tl approximately 50% of analyses were below detection in epidote, and >50% in prehnite (Table 4-5). Most elements analyzed are at concentrations between 10 and 100 times LOD for epidote, however, the median concentrations in prehnite are close to the LOD for many elements (Fig. 4-3). Specifically, the median response for the metalloids and REE’s is subdued in prehnite relative to epidote (Fig. 4-3).

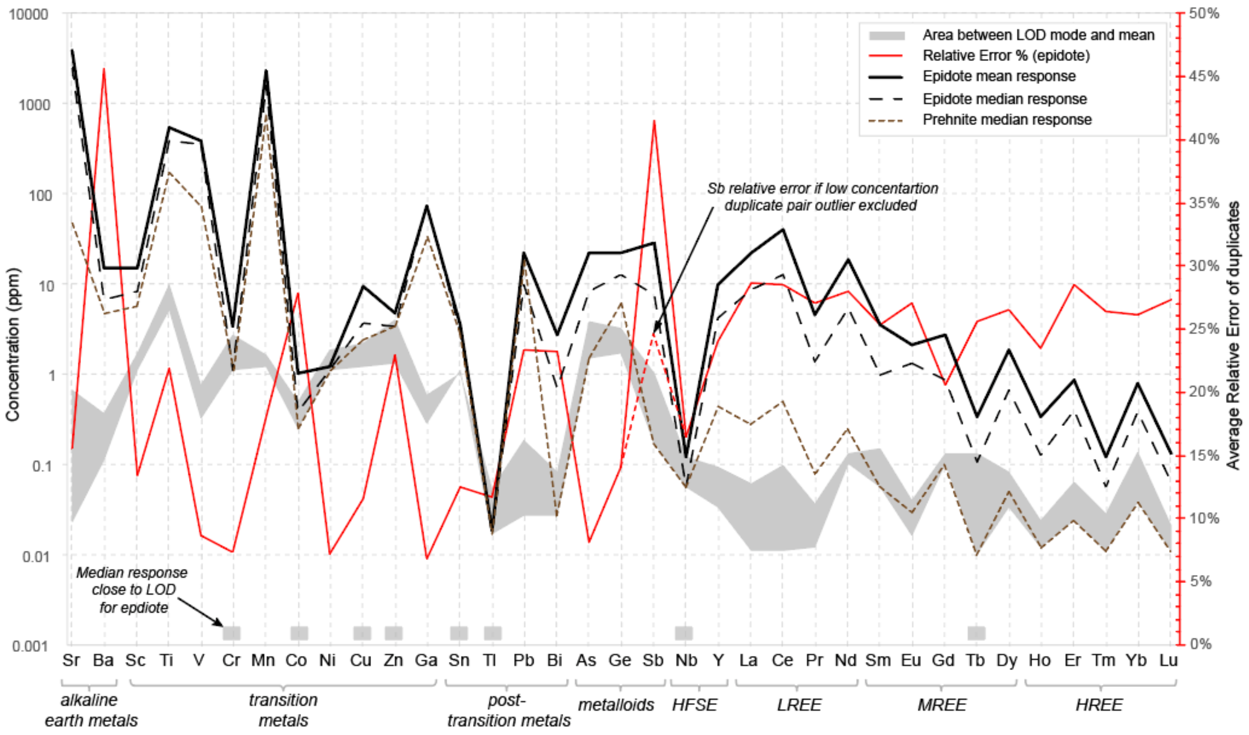

Figure 4-3. Epidote and prehnite LA-ICP-MS geochemical data, limits of detection (LOD), and estimated relative error % for epidote based on duplicate pairs (5 points each). Several elements of interest (Mn, Pb, metalloids and several REE’s) have concentrations >10 times LOD in epidote. Relative error = (absolute difference between A-B) / (mean of A and B) expressed as %.

Table 4-5. Element limits of detection

	Limits of detection (ppm)			Epidote data % >LOD	Prehnite data % >LOD
Isotope	Mean	Median	Mode		
Na_ppm_m23	75.9	33.0	28.0	45%	96%
Mg_ppm_m24	1.9	0.6	0.7	100%	100%
K_ppm_m39	35.7	15.0	15.0	48%	62%
Ca_ppm_m44	505.1	290.0	280.0	100%	100%
Sc_ppm_m45	1.69	0.79	1.10	97%	100%
Ti_ppm_m47	9.89	5.90	5.10	99%	84%
Ti_ppm_m48	0.10	0.05	0.04	100%	100%
V_ppm_m51	0.75	0.42	0.32	100%	97%
Cr_ppm_m52	2.68	1.20	1.10	49%	22%
Mn_ppm_m55	1.64	0.73	1.20	100%	100%
Fe_ppm_m57	33.24	14.00	14.00	88%	51%
Co_ppm_m59	0.50	0.29	0.25	72%	51%
Ni_ppm_m60	1.89	1.10	1.10	37%	13%
Cu_ppm_m63	2.17	1.30	1.20	41%	53%
Cu_ppm_m65	4.87	2.70	2.40	28%	42%
Zn_ppm_m66	4.06	1.70	1.30	75%	76%
Ga_ppm_m71	0.59	0.35	0.29	100%	100%
Ge_ppm_m73	3.29	1.80	1.70	92%	76%
Ge_ppm_m74	1.08	0.47	0.33	100%	97%
As_ppm_m75	3.77	1.70	1.50	80%	29%
Rb_ppm_m85	0.73	0.31	0.30	29%	23%
Sr_ppm_m88	0.67	0.04	0.02	100%	100%
Y_ppm_m89	0.09	0.05	0.03	99%	84%
Nb_ppm_m93	0.12	0.06	0.06	38%	50%
Mo_ppm_m95	0.95	0.47	0.44	6%	71%
Mo_ppm_m98	0.36	0.18	0.11	19%	49%
Ag_ppm_m107	0.22	0.13	0.11	7%	2%
Cd_ppm_m111	1.40	0.57	0.40	19%	11%
Sn_ppm_m116	1.03	0.42	1.10	84%	51%
Sn_ppm_m118	0.56	0.20	0.15	100%	100%
Sb_ppm_m121	1.04	0.28	0.17	81%	18%
Ba_ppm_m137	0.37	0.14	0.11	100%	100%
La_ppm_m139	0.06	0.02	0.01	100%	93%
Ce_ppm_m140	0.10	0.02	0.01	100%	94%
Pr_ppm_m141	0.04	0.02	0.01	99%	83%
Nd_ppm_m146	0.13	0.07	0.10	99%	87%
Sm_ppm_m147	0.15	0.08	0.06	92%	63%
Eu_ppm_m153	0.04	0.02	0.02	100%	82%
Gd_ppm_m157	0.13	0.07	0.10	91%	63%
Tb_ppm_m159	0.13	0.01	0.01	92%	64%
Dy_ppm_m163	0.08	0.04	0.03	93%	66%
Ho_ppm_m165	0.02	0.01	0.01	91%	64%
Er_ppm_m166	0.06	0.03	0.02	92%	71%
Tm_ppm_m169	0.03	0.01	0.01	85%	53%
Yb_ppm_m172	0.14	0.04	0.04	91%	61%
Lu_ppm_m175	0.02	0.01	0.01	89%	60%
Au_ppm_m197	0.07	0.04	0.02	8%	10%
Tl_ppm_m205	0.05	0.03	0.02	15%	13%
Pb_ppm_m208	0.19	0.04	0.03	100%	100%
Bi_ppm_m209	0.08	0.03	0.03	86%	5%
Th_ppm_m232	0.16	0.04	0.18	90%	68%
U_ppm_m238	0.44	0.03	0.01	100%	98%

Epidote is a compositionally diverse mineral that exhibits considerable trace-element heterogeneities on a per sample basis at various scales (Franz and Liebscher, 2004; Frei et al., 2004; Cooke et al., 2014a). Thus, while analytical accuracy and precision contributes to the total error associated with geochemical measurements, the largest source of uncertainty relates to whether multiple analysis points from a single sample are representative of the mineral composition. To establish some limits on how reproducible our epidote measurements were, the relative error of duplicate samples were assessed. Ten samples containing ten analysis spots each were randomly selected from the dataset, and from these five points were randomly partitioned into A and B duplicate sample pairs. Figure 4-4 shows cross-plots between mean and median As, Ge, Sb and sum HREE concentrations in the A and B sample pairs. Arsenic shows excellent reproducibility between A and B duplicate pairs, and the relative error decreases to ~ 10% at concentrations in excess of ~ 30 ppm based on five analysis points (Fig. 4-4A). Germanium shows a similar response to As (Fig. 4-4B). For Sb, however, the residuals between sample pairs and the 1:1 correlation line are greater compared to As and Ge, particularly the mean values (Fig. 4-4C). The internal relative standard deviation of Sb concentrations in individual spectra is on average 13 %, whereas the average relative standard deviation between spots within a single sample is 89% (Supplemental data 4-B). Based on the duplicate pairs, the relative error for Sb is ~ 40 % at concentrations > 25 ppm, however, if only the median term is used and the low concentration outlier (point labeled A in Fig. 4-4C) discarded, the average relative error decrease to ~ 20%, in line with relative error estimates for As and Ge. The HREE's show good reproducibility between duplicate pairs and have an average relative error of ~ 25 % which decreases with increasing concentration (Fig. 4-4D). The average relative error % has been calculated for each element based on the median terms of the duplicate samples (Fig. 4-3; Supplemental data 4-B). These relative error estimates are considered pessimistic because > 85 % of the epidote and prehnite samples were analyzed more than 5 times (Table 4-1).

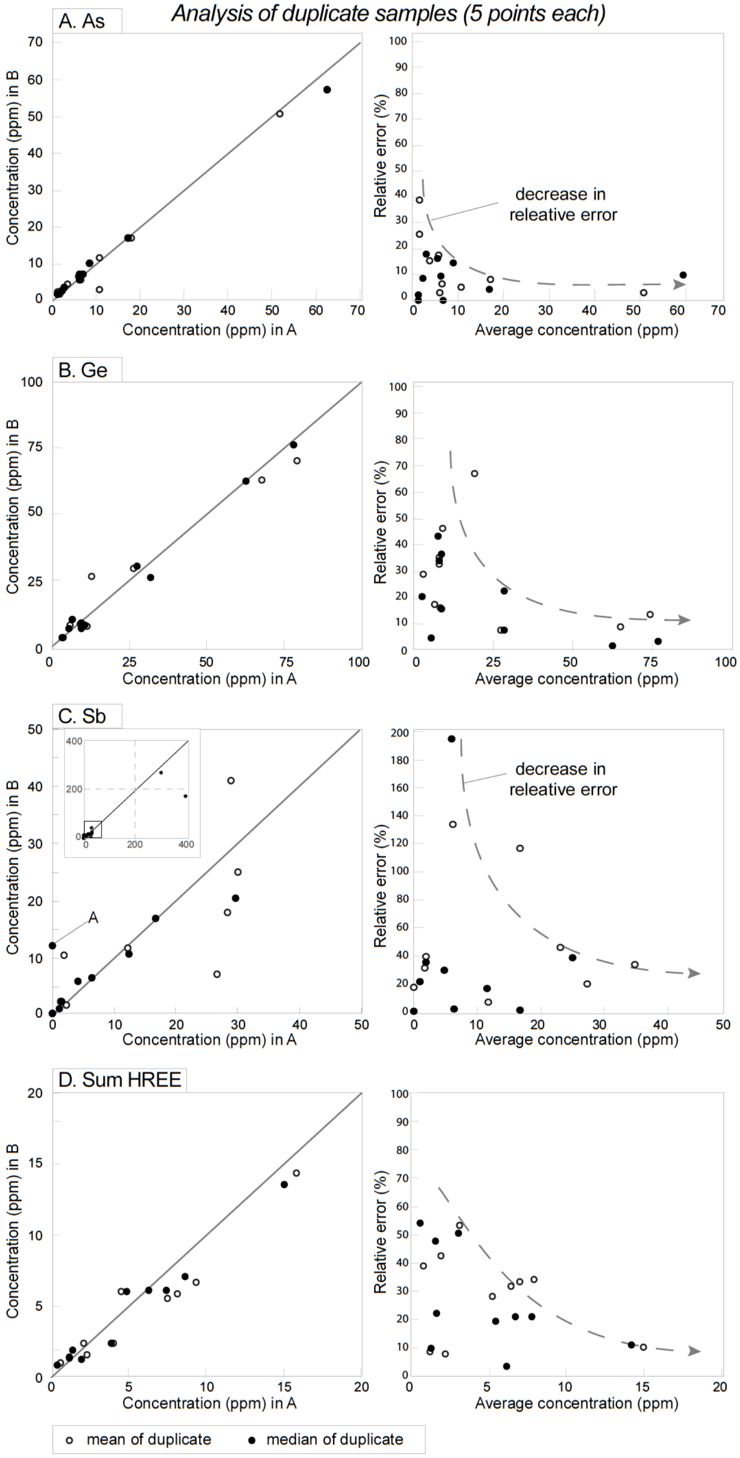

Figure 4-4. Cross-plot of duplicate A and B sample pairs (5 analysis points each), and estimated relative error % vs. average concentration. A. As. B. Ge. C. Sb. D Sum HREE. Relative error = (absolute difference between A-B) / (mean of A and B) expressed as %.

4.7 Results

4.7.1 Vein mineralogy and textures

Prehnite in veinlets is opaque to light mint-green colored in propylitic facies alteration. It typically forms fine-grained (~20 µm) aggregates, but locally occurs as coarse (>100 µm) crystals that exhibit compositional zoning in BSE images (Figs. 4-5A and B). Pumpellyite and epidote are locally intergrown with prehnite in propylitic veins. Discrete pumpellyite veinlets are locally sub-parallel to, and cross-cut prehnite veinlets in re-fractured veins. Aggregates of fine-grained (~20–50 µm) crystals characterize epidote in propylitic veins, but epidote is also locally intergrown with pumpellyite and prehnite (Fig. 4-5C). Epidote in sodic-calcic veins occurs as fine-grained aggregates of grains and as coarser interlocking crystal aggregates with abundant interstitial (vug) spaces (Figs. 4-5D–F). Younger quartz, prehnite, carbonate, pumpellyite, and locally clay minerals occlude the interstitial spaces (e.g., Figs. 4-5D and E). Some sodic-calcic veins are composed of multiple generations of epidote as indicated by cross-cutting, infilling, and replacement by compositionally distinct phases (Fig. 4-5F). Furthermore, compositional growth zones are locally truncated by younger mineral phases in some sodic-calcic veins (e.g., Fig. 4-5F).

All assemblages of epidote exhibit some degree of Fe-Al substitution, and compositional variation is evident in BSE images and in X-ray intensity maps (e.g., Fig. 4-5F and G). In coarser sodic-calcic epidote veins, sector zoning is common and localized Ti-enriched domains occur (Fig. 4- 5G); the other epidote-bearing facies lack these domains. Additionally, MnO % can vary in concentration by a factor of approximately ten at a sub-20 µm scale (e.g., Figs. 4-5E and G). With the exception of the epidote veins with white-mica–chlorite halos, sulfide minerals are absent from epidote and prehnite veins.

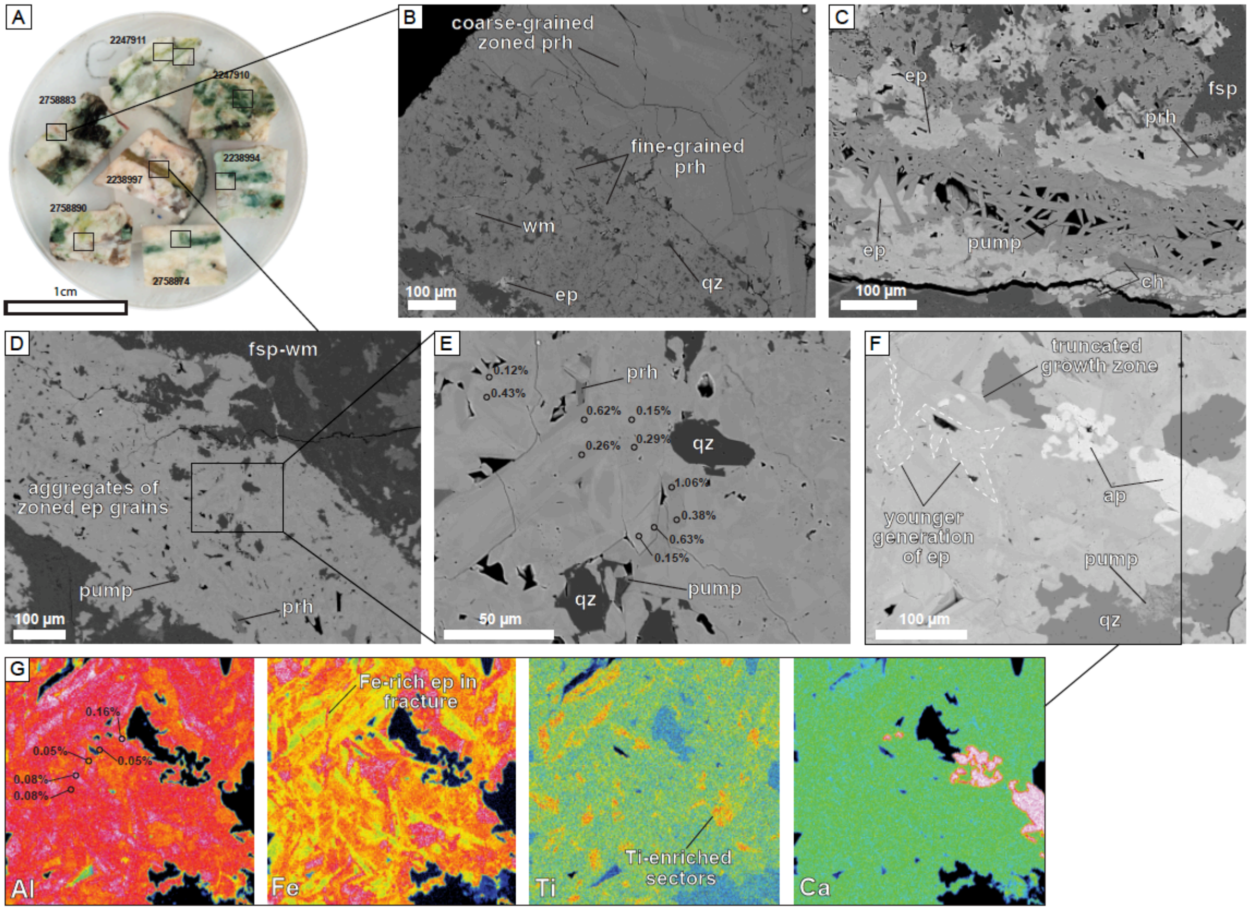

Figure 4-5. Compositional zoning in epidote and prehnite veins. A. Example of grain / sample mount used in this study. B. Coarse and compositionally zoned prehnite veinlet with fine-grained prehnite, epidote, and white-mica halo (2758883; propylitic). C. Patchy zoned epidote intergrown with coarse pumpellyite. Chlorite, epidote and prehnite in the halo (2245473; propylitic). D. Aggregate of zoned epidote subhedral and anhedral grains with interstitial (late) mineral inclusions of quartz, prehnite and pumpellyite (2238897; sodic-calcic). E. Inset from Fig. 4-5D illustrating the heterogeneous distribution of Mn in epidote (EMPA MnO % values; mean = 0.41 %; median = 0.34 %). F. Aggregates of epidote zoned grains with interstitial quartz and pumpellyite, and patches of apatite (2245302; sodic-calcic). G. X-ray intensity maps for Al, Fe, Ti and Ca of area shown in Fig. 4-5F. Note sector zoning in Fe-Al composition and Ti-enriched crystal sectors / zones, and low and homogenous Mn concentration.

4.7.2 Partitioning of elements

Several elements are enriched in epidote by one to two orders of magnitude relative to the whole-rock composition (Fig. 4-6). Of the elements enriched in epidote, Mn, Pb, Bi, and the metalloids (As, Ge and Sb) are of particular interest because they are pathfinder elements for porphyry Cu deposits (Halley et al., 2015). Prehnite has lower trace-element concentrations compared to epidote, but also shows enrichment in Mn, Pb, and Ge concentrations relative to whole-rock compositions (Fig. 4-6). Epidote is slightly enriched in REE's compared to whole-rock compositions.

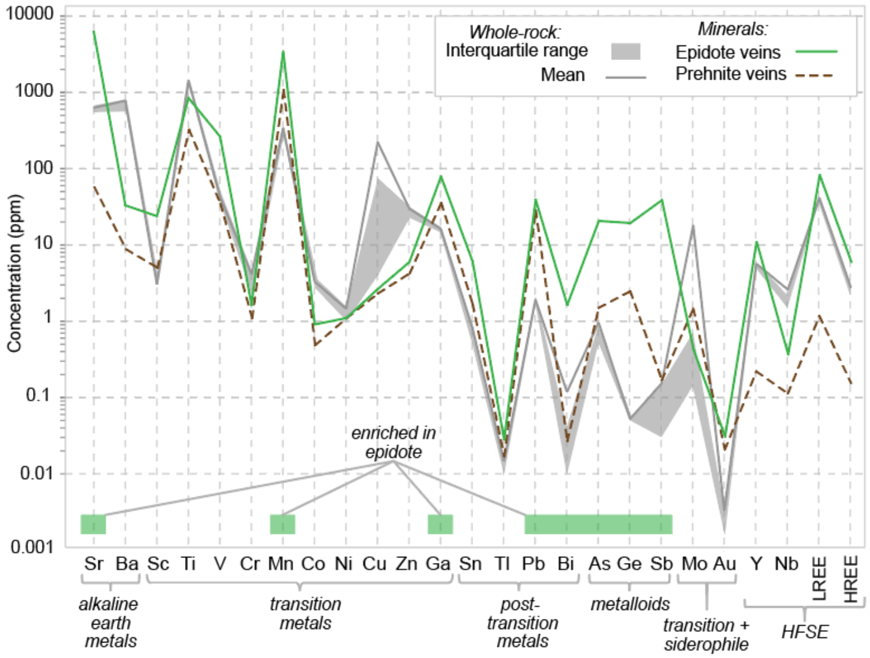

Figure 4-6. Comparison of epidote and prehnite LA-ICP-MS and whole-rock geochemical data. Strontium, Mn, Ga, Pb, As, Ge, and Sb concentrations are enriched by one to two orders of magnitude in epidote.

Epidote composition is influenced by how it manifests in a rock, i.e., whether in a vein or in an altered wall rock halo (Fig. 4-7). Some transition elements (Ni, Cu and Zn) are enriched by up to 5 times in epidote in alteration halos (hosted in mafic minerals) relative to the concentration in the epidote veins (samples 2245485). Epidote in the halo of sample 2245478 (hosted in plagioclase), however, has a similar concentration of Ni and Cu relative to the vein composition, but is enriched in Ba (Fig. 4-7). Two of the sample pairs have similar REE concentrations in the epidote textural sites, whereas in sample 2017KB007 the vein is enriched in REE relative to the epidote in the halo which is possibly replacing K-feldspar (Fig. 4-7). Critically, there is little difference between the pathfinder element (Pb, As, and Sb) concentrations between epidote textural sites (Fig. 4-7).

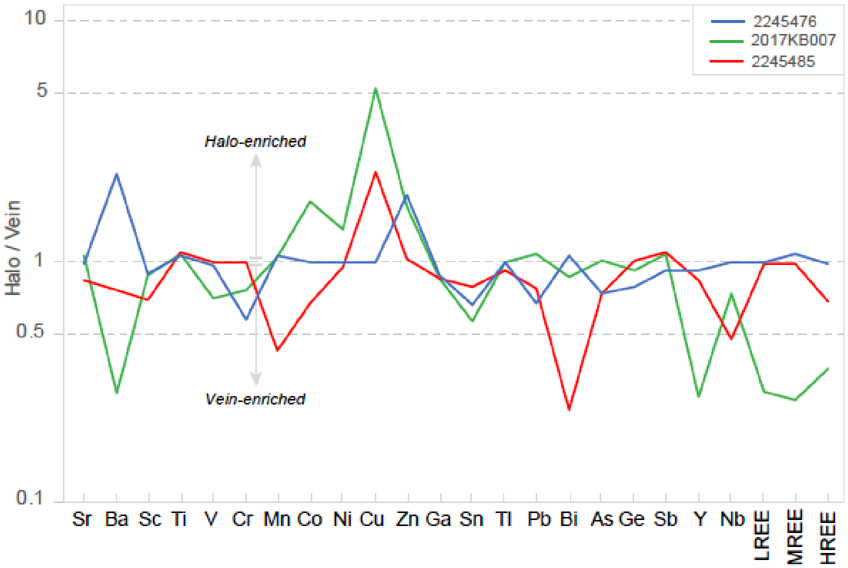

Figure 4-7. Comparison of the geochemistry in select epidote veins versus epidote occurring in the corresponding wall-rock alteration halo.

4.7.3 *Spatial variation in epidote and prehnite composition*

Zonation patterns can be detected in epidote and prehnite vein composition that form zones at varying distances from the HVC porphyry Cu centers. The elements selected for plotting are mostly enriched in epidote relative to whole-rock compositions, and are those in which at least 50 % of the determinations are greater than the LOD (Figs. 4-8 to 4-13). Median values are used to represent the composition of epidote and prehnite veins from individual samples. The median was chosen because it is not affected by outliers.

There is no clear zonation of Sr concentrations in epidote around the HVC porphyry Cu centers (Fig. 4-8). Strontium is lower in many samples within mapped domains of sodic-calcic facies (Figs. 4-8B) and some of the maximum values are from propylitic samples (Fig. 4-8C). Equally, no systematic zoning of Sr in prehnite is evident (Fig. 4-8D).

Within ~2–5 km distance from the porphyry Cu centers, numerous epidote veins have anomalously high concentrations of Mn (> 4450 ppm; >90th percentile; Figs. 4-9A-C). An Mn anomaly is detectable in prehnite even more distally than in epidote. The highest Mn concentration in prehnite veinlets is 5–7.5 km away from the Lornex Cu center (Fig. 4-9D). The Sc concentration is higher in several epidote veins along the fringes of sodic-calcic domains relative to the epidote close to Cu mineralization and distal samples (Fig. 4-10A). Titanium has variable, but generally higher, concentrations in epidote veins within 1–5 km of the Lornex and

Highmont porphyry Cu centers, these higher median Ti values are in contrast with those beyond that distance (Fig. 4-10B). Isolated Zn anomalies (>90th percentile) are dominantly found within ~ 2–4 km of Cu-mineralization (Fig. 4-10C). There is no consistent spatial variation in the concentration of Ga or Sn in epidote around the porphyry Cu centers (Figs. 4-10D and 4-11F). Anomalous levels of Pb in epidote (>50 ppm) and prehnite (>30 ppm) occur between ~3 and 8 km south of the Lornex porphyry Cu center (Figs. 4-11B and C). There is an isolated Pb-anomaly in the epidote vein at the southern margin of the batholith (Fig. 4-11B), this sample is cross-cut by chlorite-calcite veinlets with minor chalcopyrite that appears to be unrelated to the HVC porphyry centers. Epidote veins with high concentrations of Mn and Zn, and low concentrations of Pb zone outwards to epidote veins enriched in Pb-only. This systematic metal zoning in epidote veins occurs over ~8 km distance south of the Lornex Cu center (c.f., Figs. 4-9A, 4-10C and 4-11B), but not east of the Highmont porphyry center. The highest Bi concentrations occurs in some epidote veins within ~ 1.5 km of Cu-mineralization, but many other veins within this distance also have a low Bi concentration (Fig. 4-11D).

Epidote veins within ~2 km of Cu-mineralization have low-levels of As (~3–16 ppm), but beyond this distance, a few veins have anomalously high As (>50 ppm; >90th percentile; Fig. 4-12A). Isolated As highs occur in some epidote veins in mafic-rich host rocks. Arsenic in prehnite is predominately below detection, however, samples with concentrations above the LOD occur in the mafic rocks east of the Highmont porphyry center (Fig. 4-12B). A coherent domain of epidote veins with a moderate Ge anomaly (>17 ppm; >70th percentile) forms a halo around the porphyry centers for ~3 km but locally up to 5 km (Fig. 4-12C). Epidote veins with the highest median and maximum Sb values occur within ~4 km of the porphyry Cu centers (Fig. 4-12D).

The Y and sum REE concentration of epidote veins do not appear to vary systematically with distance from the porphyry Cu centers, but these elements are enriched in some veins from sodic-calcic domains (Fig. 4-13). The spatial association of epidote veins with anomalous Th and U is similar to that of the REE’s (Figs. 4-13C and D).

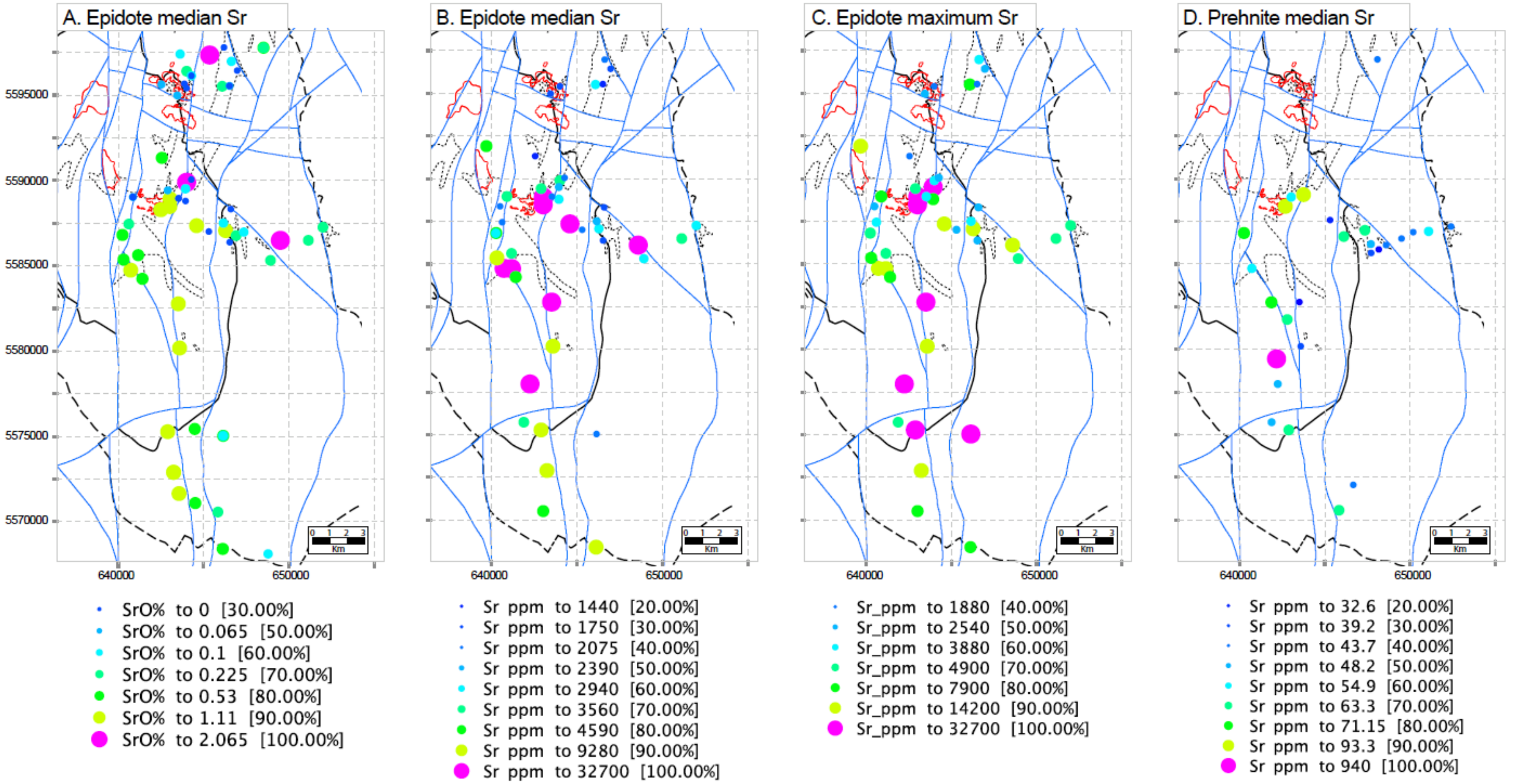

Figure 4-8. Epidote and prehnite Sr compositional maps. A. Median SrO % from EMPA. B. Epidote median Sr. C. Epidote maximum Sr. Prehnite median Sr.

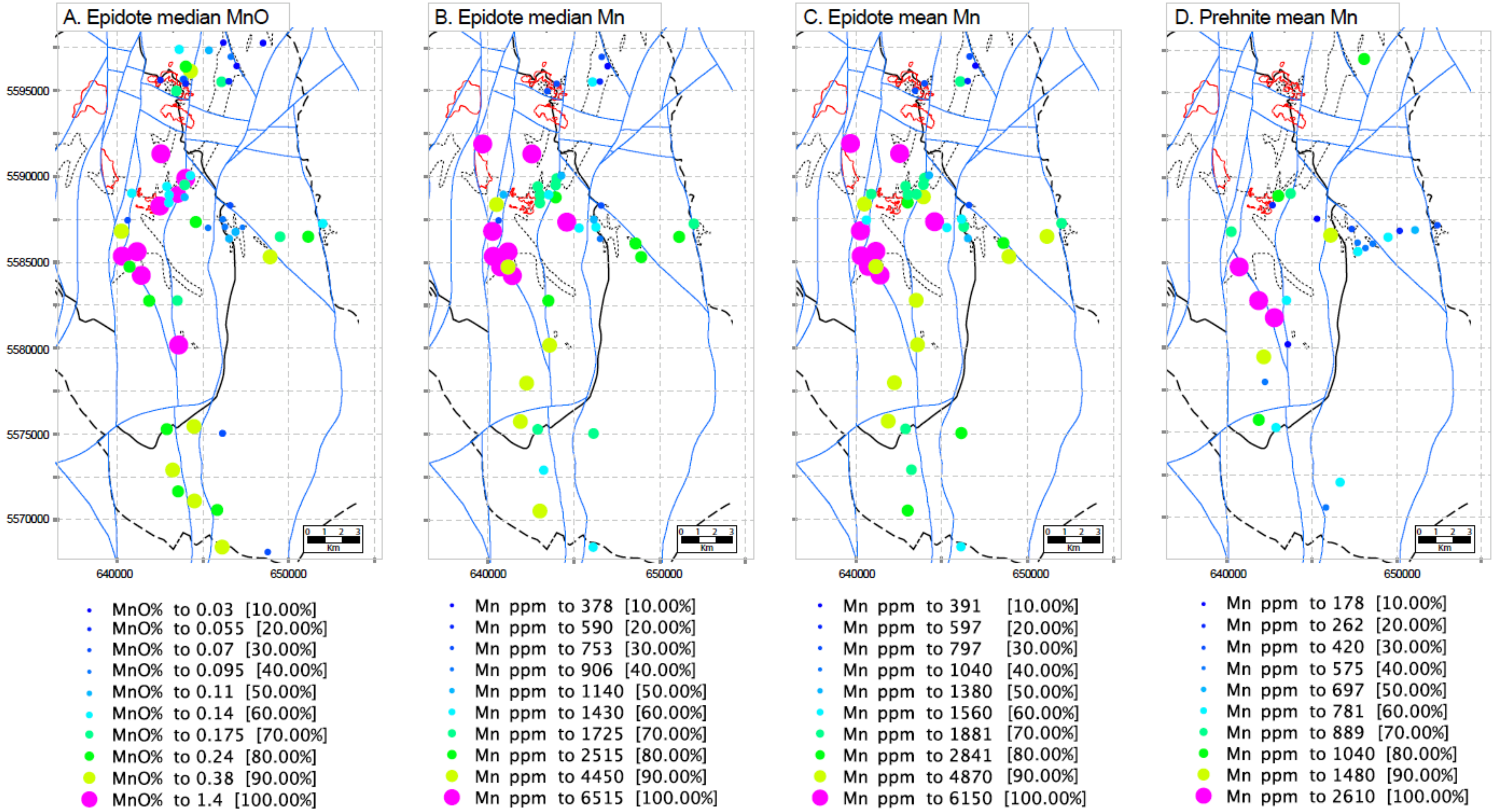

Figure 4-9. Epidote and prehnite Mn compositional maps. A. Epidote median MnO % from EMPA. B. Epidote median Mn. C. Epidote mean Mn. D. Prehnite mean Mn.

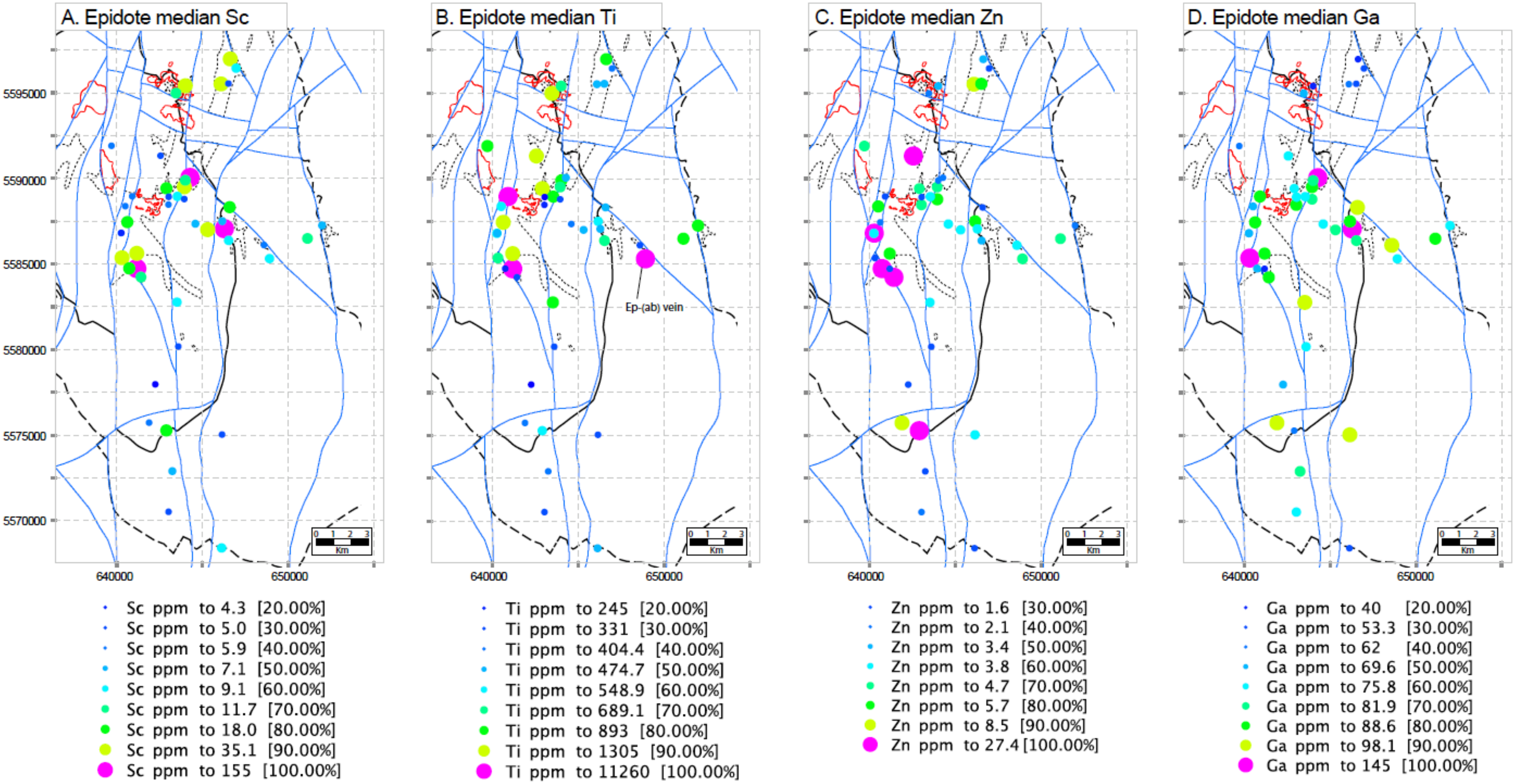

Figure 4-10. Epidote compositional maps. A. Median Sc. B. Median Ti. C. Median Zn. D. Median Ga.

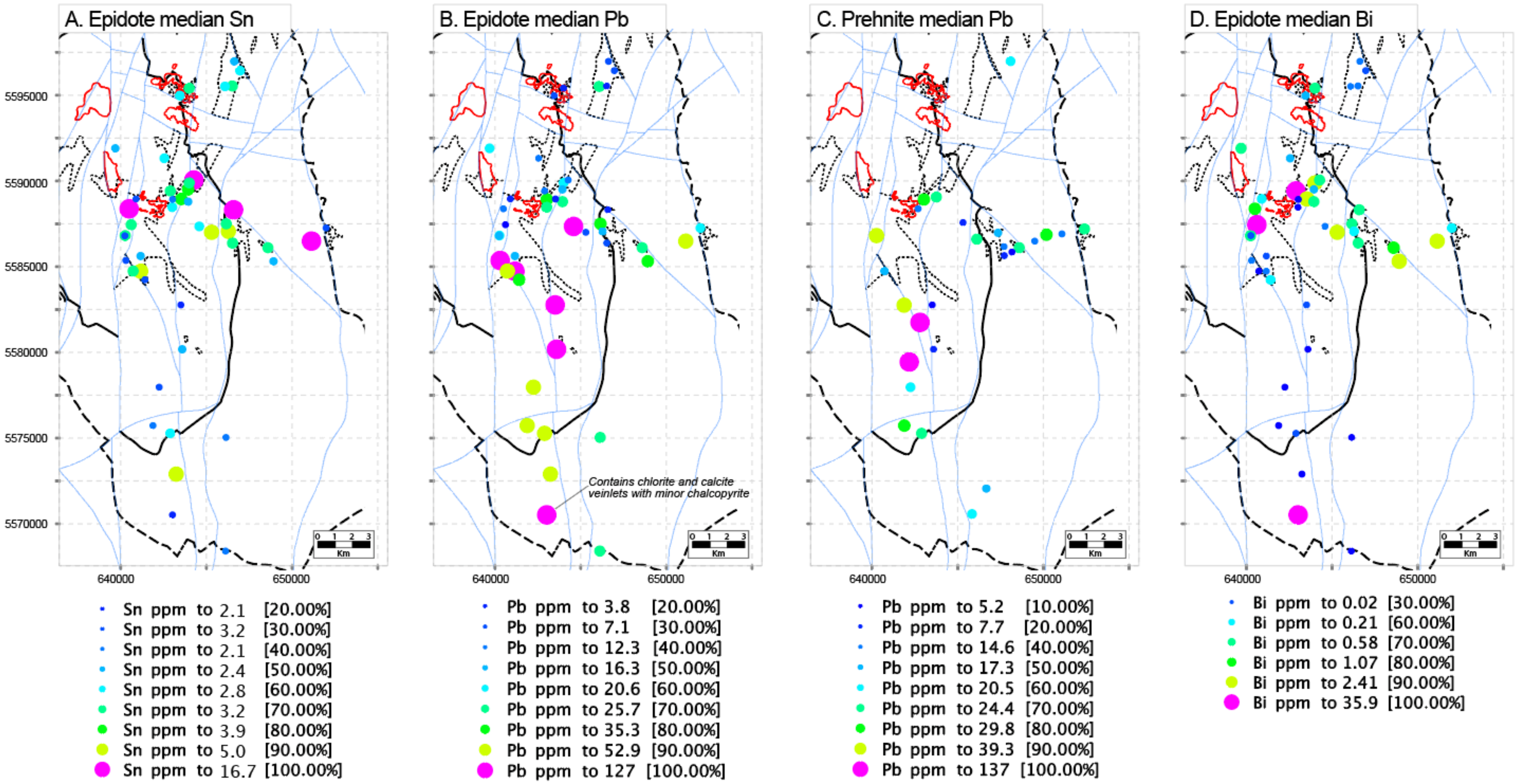

Figure 4-11. Epidote and prehnite compositional maps. A. Epidote median Sn. B. Epidote median Pb. C. Prehnite median Pb. D. Epidote median Bi.

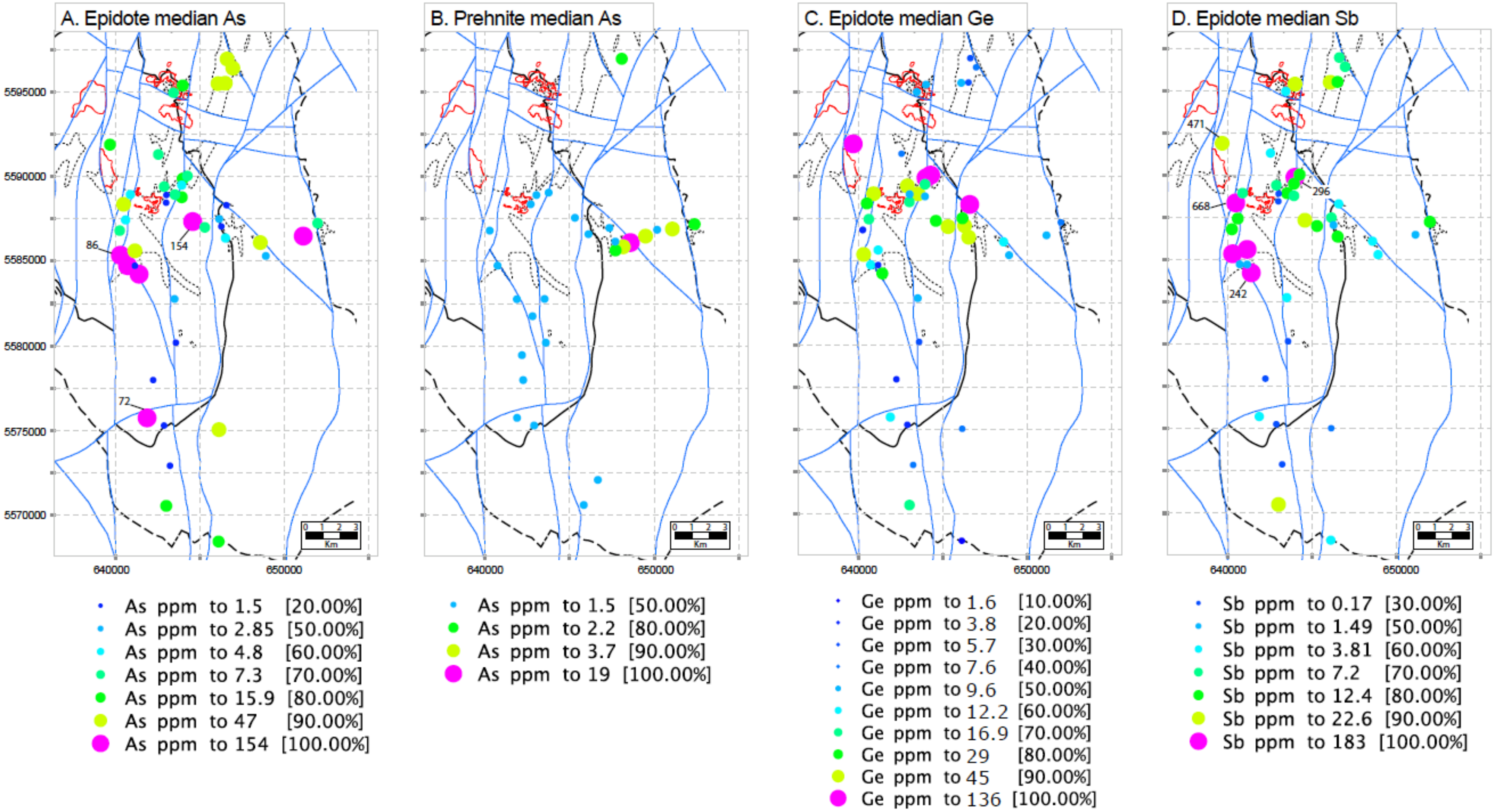

Figure 4-12. Epidote and prehnite compositional maps. A. Epidote median As (maximum values in the data set are labeled). B. Prehnite median As. C. Epidote median Ge. D. Epidote median Sb (maximum values in the data set are labeled).

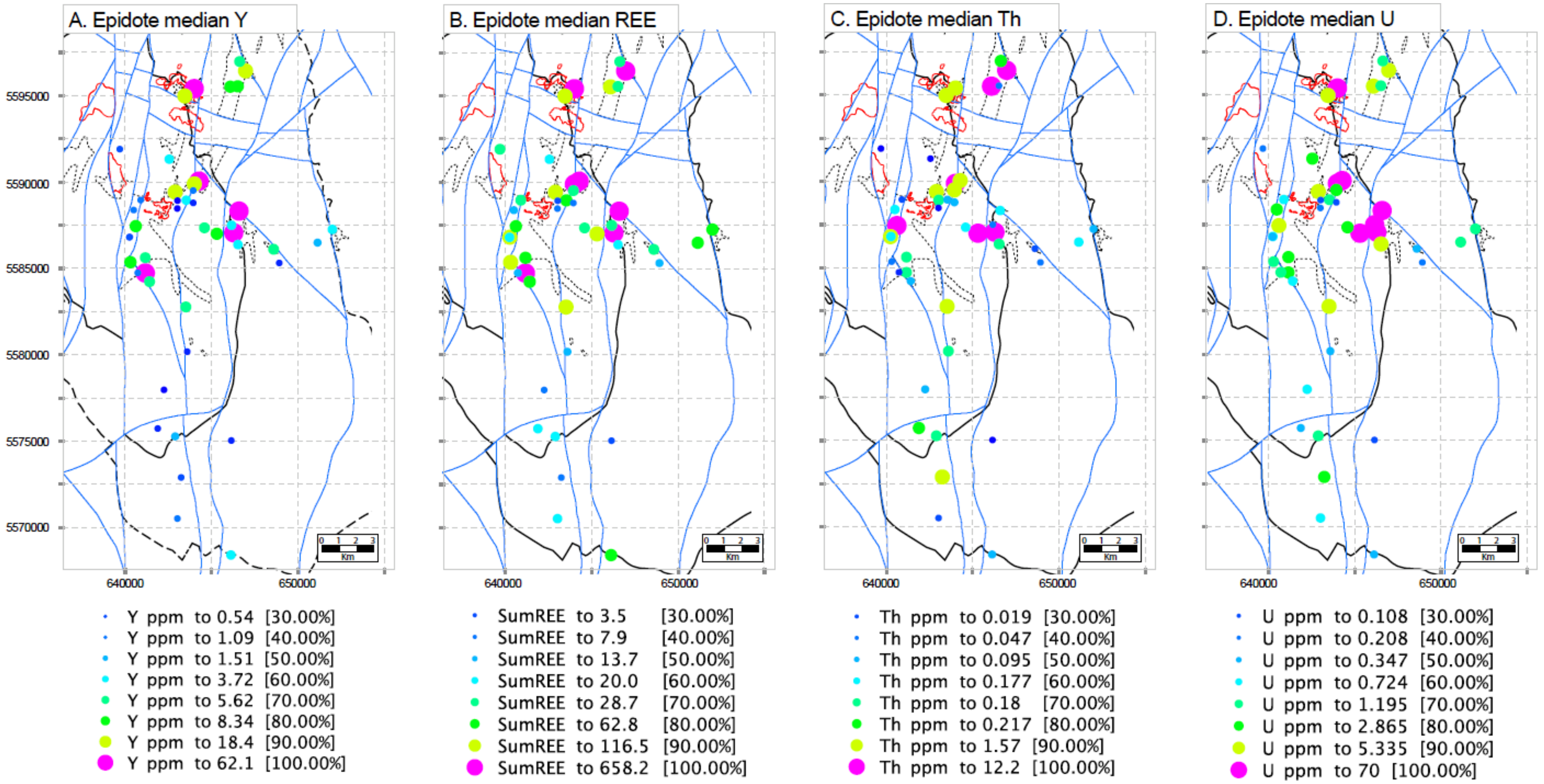

Figure 4-13. Epidote compositional maps. A. Epidote median Y. B. Epidote median REE. C. Epidote median Th. D. Epidote median U.

4.7.4 Variation in epidote composition due to host rock

In addition to distance from the porphyry Cu centers, the host rock exerts minor influence on the composition of epidote veins. There is no significant difference in the major-element composition of epidote due to host rock (e.g. Fig. 4-14), however, the median concentration of As in propylitic veins is slightly higher (~4 ppm) in the mafic-rich host rocks compared to mafic-poor rocks. Furthermore, numerous analyses of epidote from both propylitic sub-facies have As concentrations > 30 ppm (Fig. 4-15), but these veins occur in mafic-rich host rocks located 10–15 km away from the porphyry centers (e.g., the epidote-(K-feldspar) sub facies in Fig. 4-1D). Additionally, the median concentration of Mn in propylitic epidote veins hosted in mafic-poor rocks is slightly higher (~100 ppm) relative to veins hosted in mafic-rich rocks (Fig. 4-15). More significant than host rock effects, however, are the compositional differences related to alteration facies.

4.7.5 Variation in epidote composition related to alteration facies

On a per formula unit (pfu) basis, epidote in propylitic veins have lower Ca and higher Sr values compared sodic-calcic veins (Figs. 4-14; Table 4-6). The A2-site deficit caused by lower Ca content in propylitic epidote is largely balanced by an increase in Sr concentrations (Table 4-6; Fig. 4-14B). Despite exhibiting Fe-Al solid-solution and zoning (e.g., Fig. 4-5), the composition of epidote in all facies is indistinguishable, independent of host-rock composition, and has X_{Fe} values of ~0.2–0.3 (Fig. 4-14D). Epidote analyses with the highest concentration of Mn occur around the porphyry Cu systems (e.g., Fig. 4-9B), but are not attributable to a specific alteration facies (Fig. 4-15). The As concentration in epidote from propylitic facies is distinctly enriched relative to those in the sodic-calcic veins (Fig. 4-15), particularly the samples close to the porphyry centers (i.e., Fig. 4-12A). The > 80th percentile Sb values overlap for propylitic and sodic-calcic facies epidote, and these analyses are from samples within 2–4 km of the porphyry Cu-mineralization (i.e., Fig. 4-12D).

Sodic-calcic epidote veins overprinted by intense white-mica–chlorite alteration close to the porphyry centers have the highest As and Sb concentrations (Fig. 4-15). The Ge response in epidote from all facies is similar with the exception of a sub-population of epidote analyses from sodic-calcic veins (Fig. 4-15)– these are primarily from just three samples approximately 3 km east of Highmont (Fig. 4-12C). The epidote median Ti pfu values are similar for both the sodic-calcic and propylitic and facies, but the maximum values are higher in the former facies, consistent with observations from X-ray intensity maps (e.g., Fig 4-5G). A sub-population of sodic-calcic epidote vein analyses are enriched in U relative to the other analyses (Fig. 4-15).

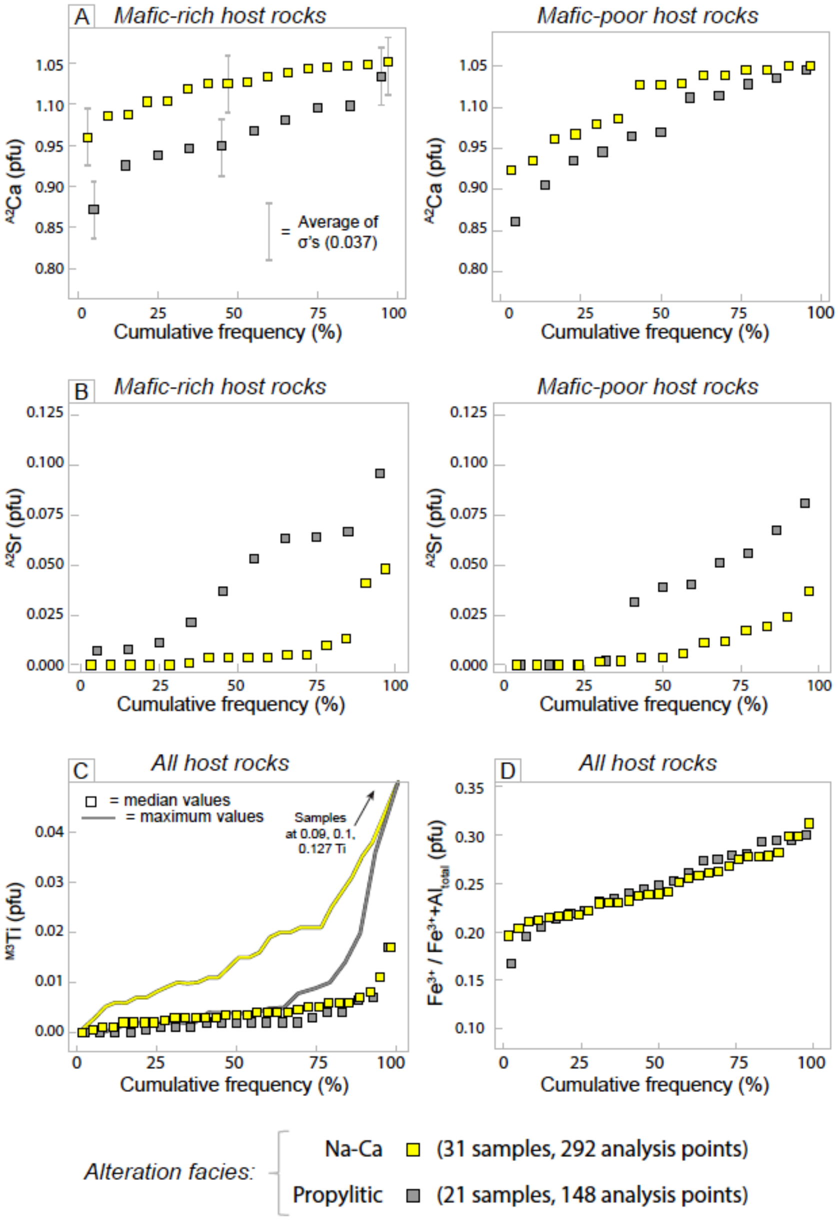

Figure 4-14. Electron microprobe epidote compositions cumulative frequency plots. A. Ca in epidote hosted in mafic-rich and mafic-poor host rocks. B. Sr in epidote hosted in mafic-rich and mafic-poor host rocks. C. Ti in epidote, all host rocks. D. Fe^{3+} / [Fe^{3+} + Al] (X_{Fe}), all host rocks. Pfu = per formulae unit. Normalization based on 9 cations and 1 OH anion and follows the site allocations of Armbruster et al. (2006).

Table 4-6. Representative electron microprobe analysis of epidote in Na-Ca and propylitically altered samples

Sample	15GL010	15KB056	15KB152	15KB182	15KB229	16KB017	15GL052	15GL064	15GL081	15KB156
Facies	Na-Ca	Na-Ca	Na-Ca	Na-Ca	Na-Ca	Propylitic	Propylitic	Propylitic	Propylitic	Propylitic
Texture	vein	vein	vein	vein	vein	vein	vein	vein	vein	vein
n of points	6	8	17	8	13	5	4	5	5	6
Wt. %	Median	Median	Median	Median	Median	Median	Median	Median	Median	Median
SiO_2%	37.62	37.525	37.48	37.29	37.7	37.4	37.51	37.84	37.11	37.465
TiO_2%	0.10	0.05	0.13	0.10	0.12	0.04	0.00	0.03	0.02	0.00
Al_2O_3%	25.09	23.84	25.14	23.00	25.07	22.64	24.51	25.28	24.27	22.37
Fe_2O_3%	10.94	11.69	10.78	13.23	11.12	13.82	11.60	11.13	12.01	14.59
MnO%	0.06	0.01	0.34	0.11	0.12	0.23	0.24	0.17	1.40	0.26
MgO%	0.13	0.00	0.22	0.00	0.08	0.79	1.46	0.88	1.11	1.43
CaO%	24.19	24.19	23.81	23.76	24.10	23.23	22.67	23.36	21.75	22.37
SrO%	0.13	0.00	0.22	0.00	0.08	0.79	1.46	0.88	1.11	1.43
Na_2O%	0.00	0.00	0.02	0.03	0.00	0.00	0.02	0.00	0.00	0.00
K_2O%	0.00	0.00	0.00	0.00	0.00	0.02	0.01	0.01	0.16	0.00
TOTAL%	98.25	97.29	98.14	97.51	98.39	98.96	99.45	99.58	98.94	99.90
H_2O calculated	1.90	1.88	1.90	1.88	1.91	1.87	1.89	1.90	1.87	1.87
TOTAL%	100.15	99.17	100.04	99.39	100.30	100.83	101.34	101.48	100.81	101.77

Normalization based on 9 cations and 1 OH

		Median	σ	Median	σ	Median	σ	Median	σ	Median	σ	Median	σ	Median	σ	Median	σ	Median	σ	Median	σ
T	Si	2.966	*0.014*	2.982	*0.017*	2.959	*0.014*	2.973	*0.009*	2.968	*0.029*	2.985	*0.006*	2.986	*0.010*	2.970	*0.007*	2.964	*0.019*	2.997	*0.004*
	Al	0.035	*0.014*	0.018	*0.017*	0.041	*0.014*	0.028	*0.009*	0.032	*0.021*	0.015	*0.006*	0.015	*0.010*	0.030	*0.007*	0.036	*0.018*	0.004	*0.003*
T total		**3.000**		**3.000**		**3.000**		**3.000**		**3.000**		**3.000**		**3.000**		**3.000**		**3.000**		**3.000**	
M2	Al	1.000	*0.000*	1.000	*0.000*	1.000	*0.000*	1.000	*0.000*	1.000	*0.000*	1.000	*0.000*	1.000	*0.000*	1.000	*0.000*	1.000	*0.000*	1.000	*0.000*
M3	Mn	0.004	*0.018*	0.001	*0.001*	0.021	*0.011*	0.007	*0.004*	0.007	*0.005*	0.015	*0.005*	0.017	*0.012*	0.010	*0.006*	0.021	*0.005*	0.010	*0.009*
	Mg	0.004	*0.004*	0.010	*0.010*	0.006	*0.005*	0.011	*0.006*	0.007	*0.017*	0.000	*0.001*	0.000	*0.002*	0.000	*0.004*	0.001	*0.008*	0.000	*0.002*
	Fe^{3+}	0.650	*0.092*	0.701	*0.134*	0.642	*0.084*	0.793	*0.085*	0.666	*0.116*	0.832	*0.091*	0.693	*0.117*	0.659	*0.048*	0.724	*0.028*	0.880	*0.024*
	Ti	0.006	*0.003*	0.003	*0.005*	0.008	*0.006*	0.006	*0.006*	0.007	*0.008*	0.002	*0.002*	0.000	*0.001*	0.002	*0.002*	0.001	*0.001*	0.000	*0.001*
	Al	0.325	*0.084*	0.268	*0.128*	0.322	*0.089*	0.181	*0.073*	0.312	*0.125*	0.146	*0.088*	0.280	*0.116*	0.330	*0.049*	0.257	*0.033*	0.110	*0.028*
M1	Al	0.951	*0.032*	0.953	*0.020*	0.986	*0.022*	0.950	*0.020*	0.963	*0.020*	0.982	*0.014*	0.995	*0.007*	0.980	*0.014*	1.000	*0.004*	0.999	*0.002*
	Fe^{3+}	0.000	*0.000*	0.000	*0.000*	0.000	*0.000*	0.000	*0.000*	0.000	*0.000*	0.000	*0.000*	0.000	*0.000*	0.000	*0.000*	0.000	*0.000*	0.000	*0.000*
M total		**2.939**		**2.935**		**2.985**		**2.947**		**2.962**		**2.977**		**2.984**		**2.981**		**3.004**		**2.999**	
A1	Ca	1.000	*0.000*	1.000	*0.000*	1.000	*0.000*	1.000	*0.000*	1.000	*0.000*	1.000	*0.000*	1.000	*0.000*	1.000	*0.000*	1.000	*0.000*	1.000	*0.000*
A2	Mn^{2+}	0.000	*0.015*	0.000	*0.000*	0.000	*0.022*	0.000	*0.000*	0.000	*0.006*	0.000	*0.000*	0.000	*0.003*	0.000	*0.040*	0.071	*0.037*	0.004	*0.010*
	K	0.000	*0.000*	0.000	*0.000*	0.000	*0.000*	0.000	*0.000*	0.000	*0.000*	0.002	*0.001*	0.001	*0.001*	0.001	*0.002*	0.016	*0.012*	0.000	*0.000*
	Sr	0.006	*0.006*	0.000	*0.001*	0.010	*0.006*	0.000	*0.002*	0.004	*0.005*	0.037	*0.007*	0.067	*0.027*	0.040	*0.041*	0.051	*0.019*	0.067	*0.015*
	Na	0.000	*0.002*	0.000	*0.003*	0.003	*0.003*	0.004	*0.006*	0.000	*0.006*	0.000	*0.002*	0.003	*0.008*	0.000	*0.005*	0.000	*0.000*	0.000	*0.000*
	Ca	1.046	*0.047*	1.046	*0.020*	1.004	*0.042*	1.047	*0.021*	1.027	*0.031*	0.981	*0.014*	0.936	*0.040*	0.970	*0.092*	0.861	*0.048*	0.926	*0.024*
A total		**2.052**		**2.046**		**2.017**		**2.051**		**2.031**		**2.020**		**2.006**		**2.011**		**1.999**		**1.996**	
Fe/Fe+Al(ltot)		0.218	*0.032*	0.238	*0.045*	0.215	*0.028*	0.269	*0.029*	0.223	*0.040*	0.280	*0.032*	0.232	*0.039*	0.219	*0.017*	0.240	*0.011*	0.294	*0.008*
Fe/(Fe+Al) M3		0.666	*0.088*	0.723	*0.131*	0.666	*0.090*	0.814	*0.078*	0.683	*0.127*	0.851	*0.091*	0.713	*0.118*	0.666	*0.050*	0.738	*0.033*	0.889	*0.027*
Charge, ideal = -26 (13O)		-25.924	*0.027*	-25.931	*0.035*	-25.916	*0.028*	-25.901	*0.024*	-25.930	*0.044*	-25.948	*0.008*	-25.950	*0.015*	-25.944	*0.015*	-25.926	*0.013*	-25.982	*0.013*

The concentration of Sb and As in epidote from HVC are, with the exception of a few samples, broadly positively correlated (Fig. 4-16A). Numerous data points at HVC have As values in excess of ~130 ppm but lack a corresponding Sb enrichment– these analyses are predominantly from epidote veins hosted in mafic-rich rocks towards the margins of the batholith, and do not contribute to the anomalous As domains adjacent the porphyry Cu centers (i.e., Fig. 4-12A). Conversely, several analyses are enriched in Sb (>10 ppm), but at detection limit for As (Fig. 4-16A). Germanium is also generally positively correlated with Sb concentration in epidote (Fig. 4-16B), however, a sub-set of sodic-calcic epidote analyses have >100 ppm Ge, but Sb values < ~ 10 ppm. The sum HREE and U concentrations in epidote from HVC broadly increase together (Fig. 4-16C). The median REE composition of epidote from sodic-calcic veins is higher than propylitic epidote veins at HVC, but both facies have large Eu anomalies (Fig. 4-16D).

4.7.6 Comparison to other geological environments

Analyses of epidote from greenschist- and blueschist-facies metamorphic rocks yielded Sb concentrations predominantly below the detection limit, and concentrations < 30 ppm for As and Ge (Figs. 4-16E and F), in contrast to the metalloid-enriched epidote in the HVC district. Additionally, these metamorphic epidotes lack Eu anomalies ($Eu_N/\sqrt{Sm_N \times Gd_N}$), and have high REE_N values relative to epidote in other environments (Figs. 4-16D)

Propylitic epidote veins from the Nicola batholith (Table 4-3; Fig. 4-1A), where there are no documented porphyry occurrences, contain < 10 ppm Sb and As, and have Ge concentrations below 10 ppm (Figs. 4-16E and F). Additionally, these veins have higher sum HREE values compared to most of the HVC propylitic samples (Fig. 4-16G). Epidote veins from the Nicola batholith, have a small Eu anomaly but are more REE-enriched than the HVC district epidote (Fig. 4-16D).

Epidote-calcite veins, with localized chalcopyrite / Cu-oxide blebs, in Nicola Group rocks adjacent the Nicola Batholith exhibit a similar concentration range of As, Ge, and Sb as the veins form the Nicola batholith (Figs. 4-16E and F), but have lower REE values (Figs. 4-16D and G). The epidote-calcite veins in Nicola Group rock have the lowest REE_N value and have a small Eu anomaly (Fig. 4-16D).

A few analyses of epidote in a sodic-calcic altered rock from the Yerington porphyry Cu district have Sb concentrations of 20–40 ppm, but most are characterized by <10 ppm As and Sb, and <15 ppm Ge (Figs. 4-16E and F). The epidote from Yerington, however, is distinctly enriched in U, similar to some sodic-calcic epidote from HVC, relative to epidote in the other geological environments (c.f., Figs. 4-16C and G). The sodic-calcic vein from Yerington is LREE-rich, HREE-poor (steep normalized slope), and has a moderate Eu anomaly (Fig. 4-16D).

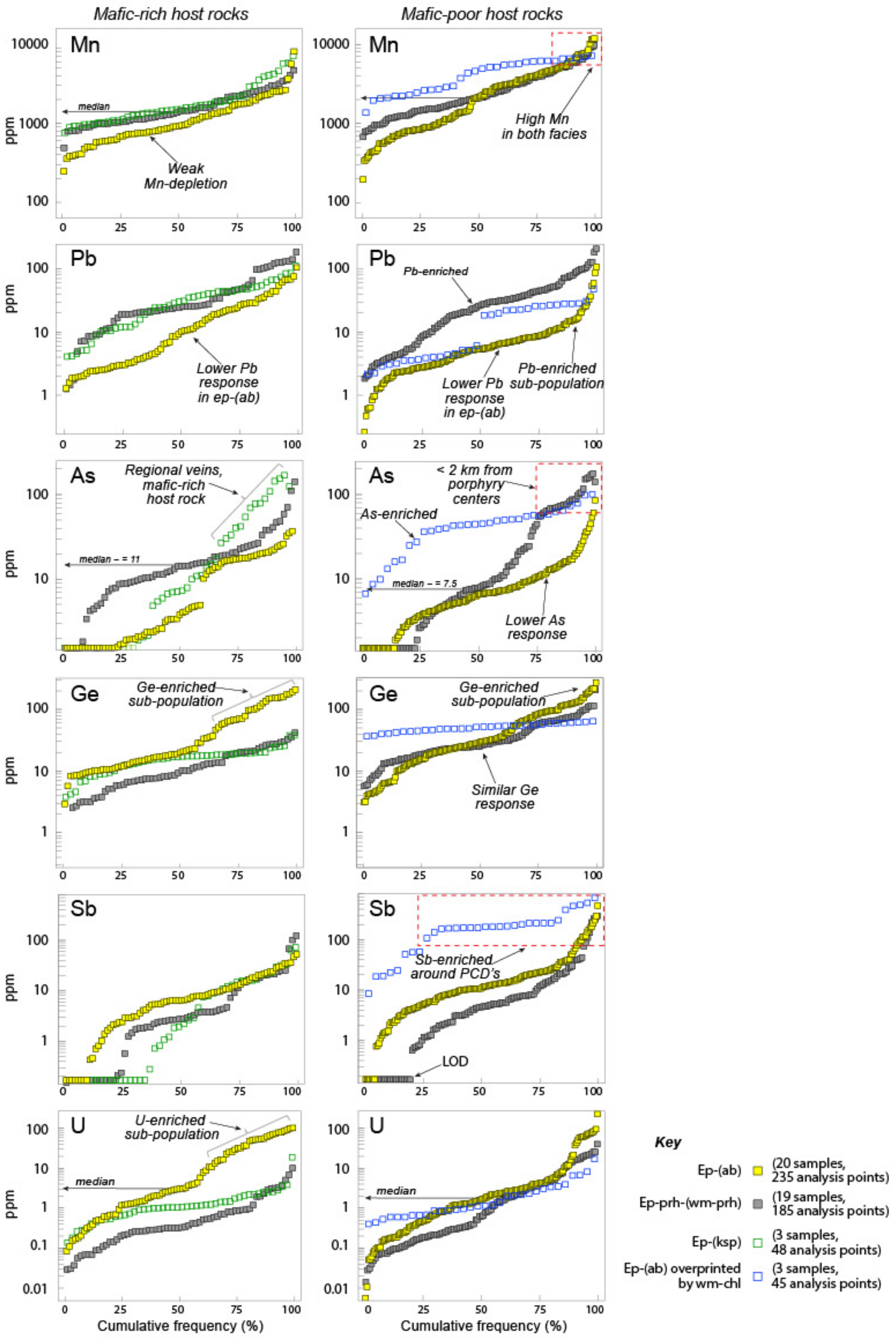

Figure 4-15. Epidote geochemistry by LA-ICP-MS cumulative frequency plots.

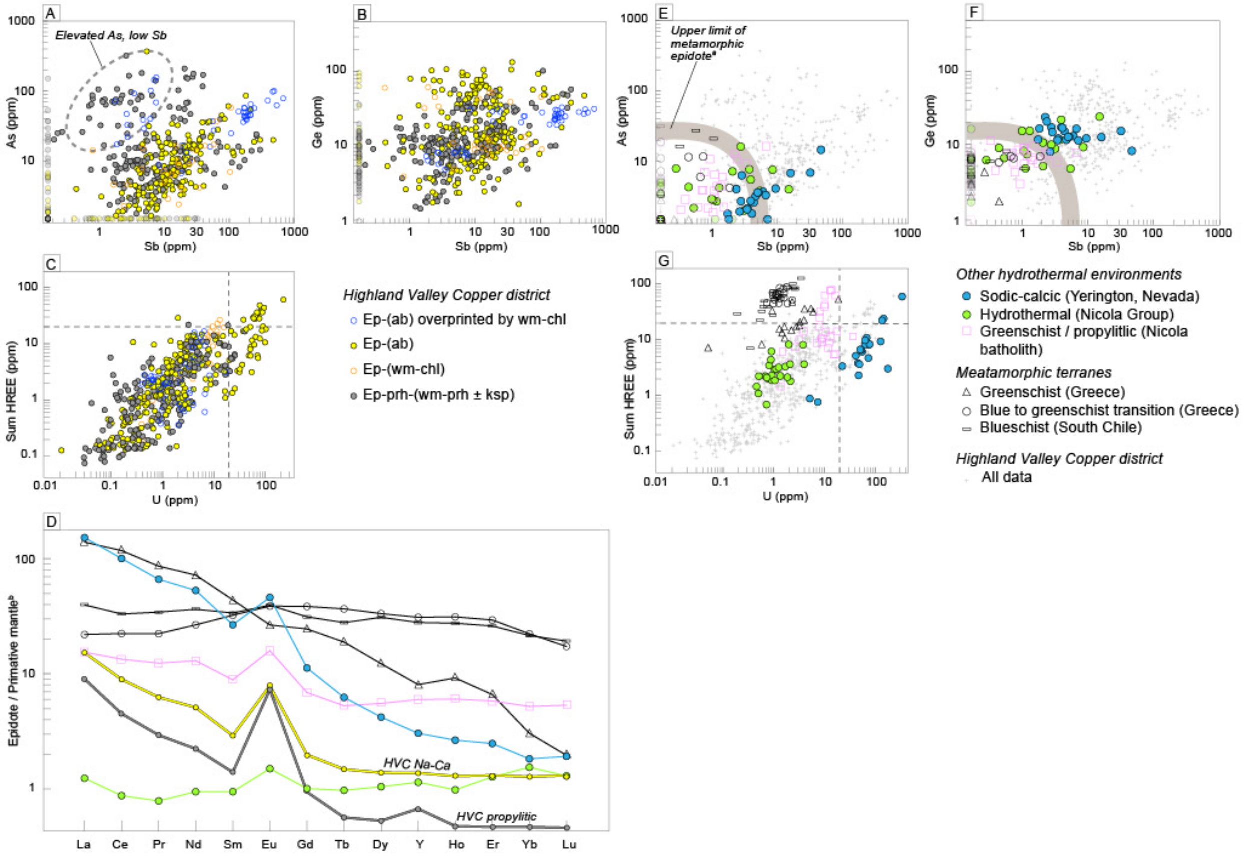

Figure 4-16. Epidote in porphyry Cu systems discrimination diagrams. A. Cross-plot of Sb and As for HVC samples, modified after Wilkinson et al. (2017). B. Cross-plot of Sb and Ge for HVC samples. C. Cross-plot of U and sum HREE value for HVC samples. D. Normalized REE compositions (median) of Na-Ca and propylitic epidote from HVC and other geological environments. E. Sb and As compositions of epidote from other geological environments. F. Sb and Ge compositions of epidote from other geological environments. F. Cross-plot of U and sum HREE value from other geological environments. G. Cross-plot of U and sum HREE value from other geological environments. [a]Wilkinson et al. (2017) is the source for the limit of metamorphic epidote boundary. [b]Sun and McDonough (1989).

4.8 Discussion

4.8.1 Controls on epidote chemistry

Variations in temperature, pH, oxygen and carbon dioxide fugacity, crystal-chemical constraints, and the bulk-rock and fluid chemistry affect the composition of epidote (Arnsason et al., 1993; Bird and Spieler, 2004; Frei et al., 2004). The similarity in the Fe-Al composition of epidote in sodic-calcic and propylitic veins (Fig. 4-14D) suggest the mineral precipitated under similar temperature, pH, oxygen and carbon dioxide fugacity conditions (Arnsason et al., 1993). The average X_{Fe} value of epidote in low-grade regional metamorphic rocks decreases with increasing metamorphic grade, however, the precise effects of temperature on epidote composition in multivariant natural assemblages is difficult to determine (Arnsason et al., 1993; Poli and Schmidt, 2004). The sodic-calcic alteration facies is interpreted to have formed over a higher, temperature range (~400–300°C) than the propylitic alteration (~350–200°C), thus although their range of X_{Fe} values is similar, an influence of temperature on trace-element composition cannot be excluded. The pH of the fluid controls the aqueous ligand species for Al and Fe to some extent, such that the X_{Fe} value can increase with increasing pH above ~300°C (Arnsason et al., 1993). In the presence of calcite and quartz, thermodynamic calculations suggest that epidote Fe-Al composition is highly sensitive to small changes in $f\mathrm{CO}_2$ in H_2O-rich fluids– causing complex compositional zoning (Bird and Helgeson, 1981; Arnsason et al., 1993). The effect of changing $f\mathrm{CO}_2$, however, is dependent on the accompanying assemblage and stoichiometry of the epidote-forming reaction (Arnsason et al., 1993). Crystal-chemical constraints and the composition of the fluids (cations and ligands) are inferred to be key controls of the trace-element composition of epidote in the HVC district.

Due to their similar ionic potential, Sb and As can substitute for divalent cations (e.g., Mg^{2+}, $Fe^{2+,}$ Mn^{2+}) in the M3 site, whereas the larger Ge^{4+} ion is thought to substitute for Si^{4+} in the T site (Railsback, 2003; Frei et al., 2004). The A-sites in epidote represent large irregular cavities between crosslinked octahedral chains, with the A2 site being larger and more distorted than A1 (Frei et al., 2004). The large-ion lithophile elements (i.e., Sr and Pb), U, Th, trivalent REE's, and possibly Bi^{3+}, can substitute for Ca^{2+} in the A-sites with concomitant replacement of two M-site ions (Al^{3+} and/or Fe^{3+}) for charge balance (Frei et al., 2004). Oxidizing conditions are required for porphyry Cu formation (Dilles et al., 2015; Richards, 2015), and propylitic alteration is characterized by assemblages containing Fe^{3+}-bearing minerals (Meyer and Hemley, 1967; Beane, 1982). Europium can occur in two valence states, Eu^{2+} and Eu^{3+} (Railsback, 2003). We interpret the positive Eu-anomalies in epidote to indicate oxidizing conditions in which Eu^{3+} (atomic radius = 1.03 Å) is available to substitute for Ca (atomic radius = 0.99 Å) in A-sites, with replacement of trivalent for divalent cations into the M sites to maintain charge balance (if even required for low levels of Eu– mean of ~ 2 ppm and maximum of 30 ppm). The valence state of Mn in our epidote analyses is unknown. Divalent Mn will substitute for Ca^{2+} in the A2, or in the M site for Fe^{3+} if trivalent (Frei et al., 2004). Other minerals formed in an assemblage with epidote may also affect the trace-element composition. For example, the availability of H_2S and pyrite formation is interpreted to affect the concentration of As, Sb, and Pb in epidote because these elements strongly partition to pyrite (Cooke et al., 2014a; Kusebauch et al., 2018). Partitioning of As, Sb, and Pb to pyrite instead of epidote may have occurred within ~ 2 km of the porphyry Cu centers as epidote veins are locally depleted in these elements within that distance.

Sodic-calcic alteration at HVC is interpreted to be the product of the in-flow and heating of seawater-derived fluids into the porphyry system (Chapter 3). Consequently, the presence of sodic-calcic and propylitic facies epidote veins in the GCB provides an opportunity to evaluate the influence of a non-magmatic fluid component on chemical dispersion in epidote around the porphyry centers. The difference in the concentration of Ca and Sr in sodic-calcic and propylitic epidote veins (i.e., Figs. 4-14A and B) is the result of feldspar alteration processes. The concentration of Sr in epidote is dependent on the Sr bulk-rock composition and presence of other Sr-bearing minerals such as calcic-plagioclase, titanite, apatite and calcite (Frei et al., 2004). In propylitic vein halos, plagioclase is typically altered to mixtures of Ca-poor plagioclase, albite, prehnite, calcite, and white-mica (Dilles and Einaudi, 1992; Plümper and Putnis, 2009; Djouka-Fonkwe et al., 2012; Chapter 2). Plagioclase in the GCB granodiorites contain an average of 1300 ppm Sr (D'Angelo, 2016) and is strongly altered within propylitic vein halos (e.g., Figs 4-2A to F). However, in the sodic-calcic vein halos, albite replaces K-feldspar and plagioclase is typically weakly affected. Thus, we interpret the higher Sr, and lower Ca, concentrations in the A2-site of propylitic epidote to be caused by a localized increase in availability of Sr via plagioclase-destructive alteration.

Sodic-calcic epidote at HVC is distinctly Pb-poor relative to propylitic epidote (e.g. Fig. 4-16). The lower Pb concentrations in sodic-calcic veins may reflect a higher temperature of formation, and / or is consistent with formation from an inward flowing, seawater-derived fluid, in which Pb would be soluble (Hemley and Hunt, 1992; Chapter 3). Sodic-calcic epidote is further distinguished from propylitic epidote by anomalously high U concentrations in some analysis (> 25 ppm) and a higher mean and median sum REE composition, characteristics that are similar to the sodic-calcic veins from Yerington (Figs. 4-16C and G). The REE composition of epidote is strongly affected by REE solubility in the fluid, which is function of the chloride and fluoride concentration (Frei et al., 2004; Williams-Jones, 2015). Additionally, the LREE's are more soluble than HREE's, and decreasing temperature or increasing pH decreases REE solubility (Migdisov et al., 2009; Williams-Jones, 2015). Thus, high salinity fluids can transport more REE's, and will fractionate the REE to varying degrees depending on the pH-buffering capacity of the host rocks (Williams-Jones, 2015). Uranium is generally more soluble in oxidizing alkaline fluids compared to reducing or acidic fluids (Kyser, 2013). Furthermore, pH and ligand species have a greater effect on U solubility than changes (decreases) in temperature (Kyser, 2013). Based on these solubility properties, we infer that the high concentration of U and REE's in some sodic-calcic veins reflects formation from an oxidized, saline, and alkaline fluid. Whether the REE and U are sourced locally (from altered rocks), MVP-derived, or transported from an external reservoir cannot be determined with this data-set.

Veins and altered rocks with high concentrations of As, Sb, and Bi in porphyry systems are generally thought to have formed from magmatic fluids (Sillitoe, 2010; Halley et al., 2015). Therefore, the Bi in localized Bi-enriched epidote veins within 1.5 km of the porphyry centers is inferred to be derived from magmatic volatile phase (MVP). Similarly, the Sb in the highly anomalous epidote samples (e.g. Fig. 4-12D), which peak between 2 to 4 km distance from the HVC porphyry (Fig. 4-17A), is interpreted to be sourced from MVP outflowing from the porphyry centers (e.g., Cooke et al. 2014). Above ~ 30 ppm the Sb concentration populations in sodic-calcic and propylitic facies epidote overlap (Fig. 4-15). The high Sb concentrations in sodic-calcic veins is somewhat at odds with the origin of this facies from an external fluid (Chapter 3). This study and analyses from central Baguio district, Philippines (Cooke et al. 2014), and the Mt Milligan porphyry Au-(Cu) system in BC (Jago et al. 2014) indicate that Sb is heterogeneously distributed in epidote. The cause of intra-sample variability in Sb concentration in epidote is unknown. We did not attempt to spatially resolve elemental deportment on a per analysis basis, but note that numerous sodic-calcic epidote veins exhibit compositional complexity and multiple generations of growth at a finer-scale than the laser diameter used for quantitative analysis (e.g. Figs. 4-5F and G). Thus, it is conceivable that the Sb anomalies in sodic-calcic epidote is related to a younger generation of epidote formed from MVP and unrelated to the external fluid. Alternatively, both fluids were present in the fracture around the time epidote was precipitating in these veins. A sub-set of propylitic samples are As-rich and Sb-poor and hosted in mafic-rich rocks ~12 km away from the porphyry centers (e.g., Figs. 4-12A and 4-16A). The mafic-rich GCB rocks have higher As concentrations than the mafic-poor rocks which host the porphyry centers (D'Angelo et al., 2017). Thus, the As in these As-enriched and Sb-poor propylitic epidote veins could potentially be locally sourced from the altered host rock rather than from MVP. Up to 10 ppm Ge has been reported in epidote from skarn systems (Bernstein, 1985), around the HVC porphyry centers the average Ge concentration is ~ 30 ppm and as high as 137 ppm. The more coherent distribution of Ge-enriched epidote veins around the Lornex and Highmont porphyry centers (e.g. Fig. 4-12C) compared to Sb and As in epidote suggests different mechanisms control its substitution for Si in T-sites– perhaps temperature.

Systematic metal zonation (Cu, Zn, Ag, Pb, Mn, Au) in veins is recognized in several porphyry districts (e.g., Bingham, Butte, Lepanto, Collahuasi, Morochoa), and is attributed to lateral MVP flow and precipitation from a progressively cooling H_2S-bearing fluid (Hemley and Hunt, 1992; Sillitoe, 2010; Seward et al., 2014; Catchpole et al., 2015). Epidote veins with high concentrations of Mn and Zn, but low concentrations of Pb, occur within a window of ~1.5 to 3 km south of the porphyry centers (e.g., Figs. 4-9A and 4-10C). From ~ 3 km to 6 km away from the porphyry centers, epidote veins are locally enriched in Pb, but not in Zn and Mn. The domain of prehnite with anomalous Mn concentrations is spatially-offset from the Mn-enriched epidote veins (c.f., Figs. 4-9B and C). Additionally, Pb-rich prehnite overlaps with and extends further than the Pb-rich epidote veins for up to 8 km south of the porphyry Cu centers. This metal and mineral zonation in propylitic veins is consistent with cooling and outward flow of a H_2S-poor MVP from the porphyry centers, or upwards from the peripheries of the underlying cupola (Cooke et al., 2014a). Systematic metal zonation is better developed in the veins south of the porphyry centers compared to those situated to the east. This asymmetry is interpreted to reflect paleo-fluid flow anisotropy.

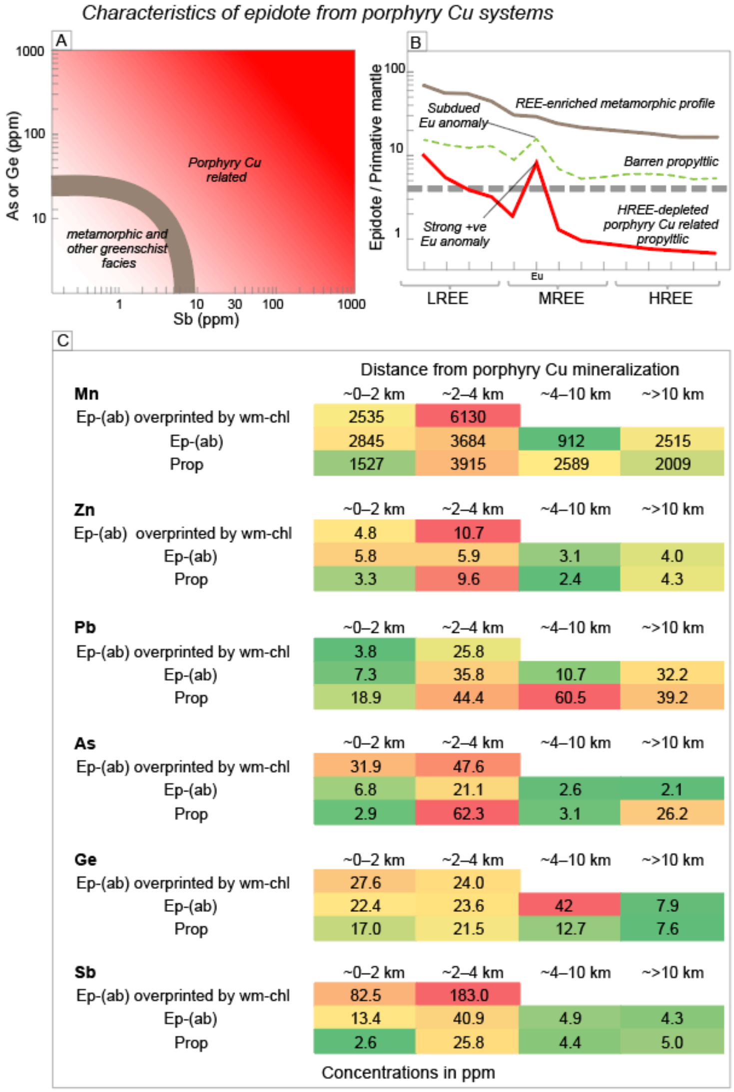

		~0–2 km	~2–4 km	~4–10 km	~>10 km
Mn	Ep-(ab) overprinted by wm-chl	2535	6130		
	Ep-(ab)	2845	3684	912	2515
	Prop	1527	3915	2589	2009
Zn	Ep-(ab) overprinted by wm-chl	4.8	10.7		
	Ep-(ab)	5.8	5.9	3.1	4.0
	Prop	3.3	9.6	2.4	4.3
Pb	Ep-(ab) overprinted by wm-chl	3.8	25.8		
	Ep-(ab)	7.3	35.8	10.7	32.2
	Prop	18.9	44.4	60.5	39.2
As	Ep-(ab) overprinted by wm-chl	31.9	47.6		
	Ep-(ab)	6.8	21.1	2.6	2.1
	Prop	2.9	62.3	3.1	26.2
Ge	Ep-(ab) overprinted by wm-chl	27.6	24.0		
	Ep-(ab)	22.4	23.6	42	7.9
	Prop	17.0	21.5	12.7	7.6
Sb	Ep-(ab) overprinted by wm-chl	82.5	183.0		
	Ep-(ab)	13.4	40.9	4.9	4.3
	Prop	2.6	25.8	4.4	5.0

Figure 4-17. A. Schematic illustrating the As, Ge and Sb composition of epidote from porphyry Cu systems. B. Schematic illustrating the normalized REE compositions prospective epidote from porphyry Cu occurrences and other geological environments. C. Summary of pathfinder elements that vector to HVC porphyry Cu centers. Warm colors indicate the highest element concentration domain, whereas cooler colors indicate low concentration domains.

4.8.2 *Recognizing epidote associated with porphyry Cu systems*

Pioneering work in the central Baguio porphyry-skarn district, Philippines, initially demonstrated that epidote outside of the pyrite halos is enriched in As and Sb (Cooke et al., 2014a). More recently Wilkinson et al. (2017) have added that epidote from metamorphic terranes have low As and Sb that contrast with the epidote enriched in these elements from porphyry Cu-(Mo), and to a lesser extent with epidote from Cu-(Au) systems. Furthermore, Cooke et al. (2014a) postulate that the most endowed (fertile) porphyries flux the most metals, and will thus have higher concentrations of pathfinder elements in their halos compared to weakly mineralized or barren porphyry occurrences.

Epidote veins from the fertile HVC porphyry district can be discriminated from epidote from other geological environments by a combination of compositional features: large positive Eu anomaly, low sum HREE concentration, moderate negative normalized REE slope, and analyses of ~ >30 ppm As and Ge, and >10 ppm Sb (Figs. 4-17A and B). Epidote from the Mt. Milligan alkalic porphyry Au-(Cu) deposit (British Columbia) is characterized by large positive Eu-anomalies, low HREE concentrations, and As and Sb contents that range between 10 and 60 ppm (Jago et al., 2014). High Bi and Pb may also be indicative of epidote from propylitic veins around porphyry Cu centers (Cooke et al., 2014a; this study).

The epidote-calcite veins in the Nicola Group volcanic rocks are weakly Cu-mineralized and are perhaps related to hydrothermal circulation caused by intrusion of the nearby Nicola batholith. As there are no known porphyry Cu occurrences in the Nicola batholith, those epidote vein samples are inferred to represent barren propylitic alteration related to late-stage fluid circulation in the batholith (e.g., Bergbauer and Martel, 1999; Bird and Spieler, 2004; Fig. 4-17B). These samples are real-world examples of propylitic facies alteration encountered in "grass-roots" exploration programs. Epidote veins from the Nicola batholith and Nicola Group country rock have moderate Eu anomalies implying oxidizing conditions, but lack the metalloid-element enrichment evident in epidote from the HVC district (e.g. Figs. 4-16A and B), and from other porphyry centers (Jago et al., 2014; Wilkinson et al., 2017).

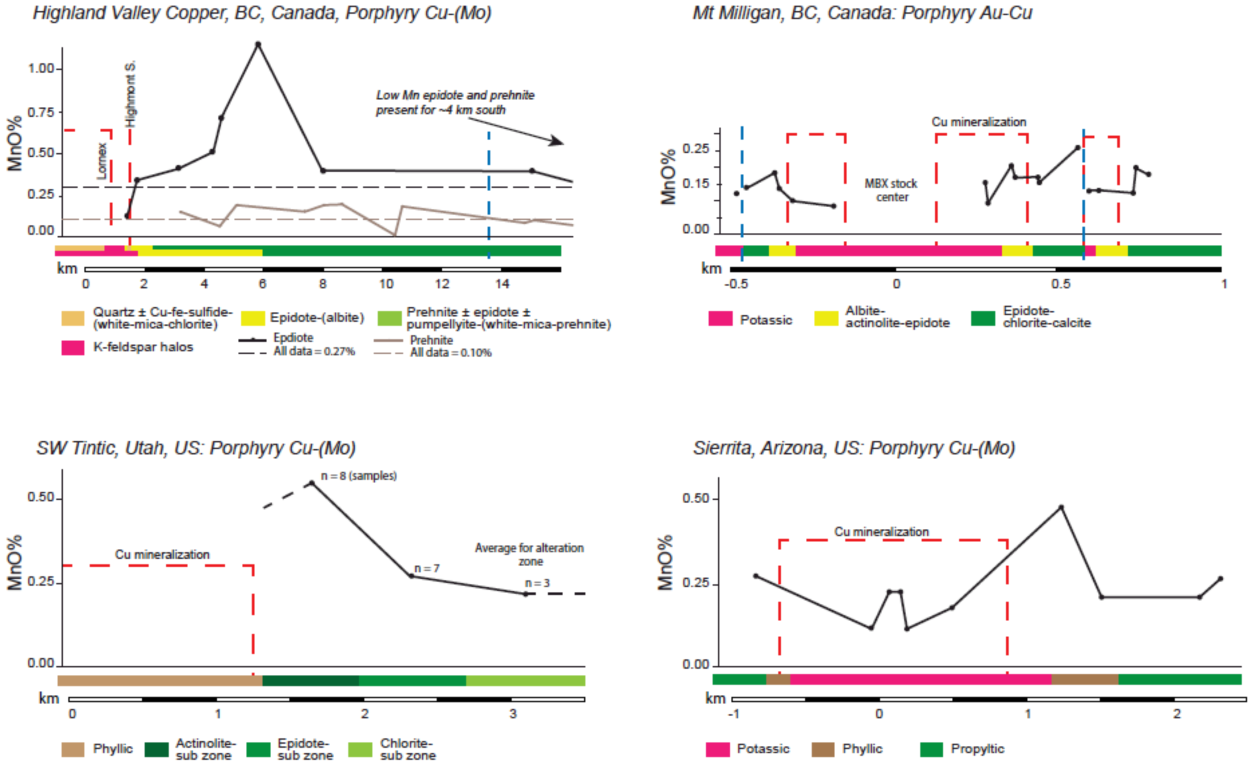

Figure 4-18. Manganese in epidote profiles outboard of porphyry Cu centers. Low Mn epidote occurs within and directly adjacent Cu-mineralization that transitions to high Mn shoulder anomalies, and then to lower Mn concentrations in background and distal epidote. Same vertical concentration scale for each porphyry occurrence, but variable lateral distance scale. HVC = EMPA data; Mt. Milligan alkalic porphyry Au-Cu deposit = LA-ICP-MS (Jago, 2008); SW Tintic porphyry Cu-(Mo) deposit = EMPA (Norman et al., 1991); Sierrita porphyry Cu-(Mo) deposit = EMPA (Fellows, 1976).

4.8.3 Vectoring to porphyry Cu centers

The data and interpretations presented in this study add to the recent advancements in the application of mineral geochemistry for vectoring to porphyry Cu centers (Cooke et al., 2014a; Wilkinson et al., 2015). Epidote vein compositions vary systematically with respect to distance from the HVC porphyry Cu centers (Fig. 4-17C). The highest concentrations of Bi are detected in epidote within ~1.5 km Cu-mineralization that occurs with potassic and white-mica–chlorite alteration in the porphyry centers. Depletion in some pathfinder elements (Pb, As, and Sb) occurs in propylitic veins close to the porphyry centers (Fig. 4-17A). Epidote veins are moderately enriched in Ge (>30 ppm) for up to 5 km around the porphyry centers (e.g. Fig. 4-12C). The elements Mn, Zn, As, and Sb are on average most enriched in epidote between 2 and 4 km of the porphyry centers, whereas Pb forms a larger halo in epidote of up to ~ 6 km (Fig. 4-17C). Additionally, in prehnite, Mn is anomalous in the veinlets between 3 and 6 km away from the porphyry centers, whereas Pb can be detected within a window of ~ 5.5 to 8 km distance (Fig. 4-17C). Critically, this study demonstrates that even with widely spaced samples the sequential enrichment of pathfinder elements in epidote and prehnite veins can be detected and used to vector to porphyry Cu centers.

The crystal structure of epidote is more favorable than prehnite for incorporation of trace elements (i.e. Fig. 4-6), both minerals, however, take-up anomalous amounts of Mn that can be measured by EMPA, making this element particularly useful in vectoring to Cu mineralization. Systematic variation in the Mn concentration of epidote with respect to Cu mineralization has been documented at several porphyry Cu deposits: SW Tintic, Utah; Sierrita, North Silver Bell, and Christmas mines in Arizona; Mt. Milligan, BC (Fellows, 1976; Ballantyne, 1981; Norman et al., 1991; Jago, 2008). Based on this study and patterns evident in the other porphyry systems, the Mn concentration in epidote increase inwards through propylitic alteration to a maximum at the transition from propylitic to higher-temperature assemblages, and then decrease sharply inward to Cu mineralized domains (i.e., Fig. 4-18).

4.9 Conclusions

The elements Mn, Pb, Bi, and the metalloids (As, Ge and Sb) are enriched in epidote relative to corresponding whole-rock compositions, similar to observations made by Cooke et al. (2014a), and are of particular interest because they are pathfinder elements for porphyry Cu deposits (Halley et al., 2015). Prehnite has lower trace-element concentrations compared to epidote, but is also enriched in Mn, Pb, and Ge relative to the host rock. Epidote in wall-rock alteration halos has a similar concentration of Pb, As, Ge, and Sb as the epidote in corresponding veins.

In the HVC district, epidote occurring with sodic-calcic facies can be distinguished from the epidote in propylitic veins by generally lower concentrations of Sr, Pb, and As, higher Ca content, and localized enrichment in U (~20–200 ppm) and REE’s.

Epidote veins from the fertile HVC porphyry district can be discriminated from the epidote occurring in metamorphic terranes, barren propylitic alteration, and other Cu mineralized non-porphyry Cu hydrothermal systems, by a combination of compositional features: large positive

Eu anomaly, low sum HREE concentration, moderate negative normalized REE slope, and principally by analyses of >30 ppm As and Ge, and >10 ppm Sb.

The highest Bi concentrations occur in some epidote veins within ~ 1.5 km of Cu-mineralization. Epidote veins within ~2 km of Cu-mineralization have low-levels of As (~3–16 ppm), but numerous samples between ~2 and 4 km have anomalously high As (>50 ppm). A coherent domain of epidote veins with a moderate Ge anomaly (>30 ppm) forms a halo around the porphyry centers for ~ 5 km (e.g. Fig. 4-12C). Epidote veins with the highest Sb values (~ >20 ppm) occur within ~4 km of the porphyry Cu centers (e.g. Fig. 4-12D). The elements Mn and Zn are on average most enriched (>6000 ppm and > 25 ppm, respectively) in epidote between 2 and 4 km of the porphyry centers, whereas Pb (~>120 ppm) forms a larger halo in epidote of up to ~ 6 km (Fig, 4-17A). Prehnite veinlets are enriched in Mn (>2500 ppm), and off-set from the Mn-rich epidote, between 3 and 6 km away from the porphyry centers, and high concentrations of Pb (~>130 ppm) can be detected within a window of ~ 5.5 to 8 km distance (e.g. Fig. 4-11B and C).

Critically, this study demonstrates that even with widely spaced samples the sequential enrichment of pathfinder elements in epidote and prehnite veins can be detected and used to vector to porphyry Cu centers.

The crystal structure of epidote is more favorable than prehnite for incorporation of trace elements (i.e. Fig. 4-6), both minerals, however, take-up anomalous amounts of Mn that can be measured by EMPA, making this element particularly useful in vectoring to Cu mineralization. Systematic variation in the Mn concentration of epidote with respect to Cu mineralization has been documented at several porphyry Cu deposits: SW Tintic, Utah; Sierrita, North Silver Bell, and Christmas mines in Arizona; Mt. Milligan, BC (Fellows, 1976; Ballantyne, 1981; Norman et al., 1991; Jago, 2008). Based on this study and patterns evident in the other porphyry systems, the Mn concentration in epidote increase inwards through propylitic alteration to a maximum at the transition from propylitic to higher temperature assemblages, and then decrease sharply inward to Cu mineralized domains (i.e., Fig. 4-18).

5 Variability of outcrop magnetic susceptibility and its relationship to the porphyry Cu centers in the Highland Valley Copper district

5.1 Introduction

Ground and airborne magnetic methods have long been used in porphyry Cu exploration at a wide range of scales (Nabighian et al., 2005) for the dual purpose of supporting geological interpretations, and for the direct detection of magnetic minerals that can be associated with mineralization (Holliday and Cooke, 2007). Typically, case studies have focused on aeromagnetic survey methodology and how magnetic intensity and derivative products relate to mineral deposits (Hoover et al., 1994; Nabighian et al., 2005; Reeves, 2005), or clusters of deposits at a regional scale (Behn et al., 2001). At the system-scale, porphyry Cu deposits can be characterized by roughly circular-shaped magnetic intensity lows, or torus-like lows around a central high (Holden et al., 2011; Clark, 2014). Rock magnetic susceptibility studies appear to be more focused on characterizing lithology (Hrouda et al., 2009; Gettings and Bultman, 2014), comparing instruments (Lee and Morris, 2013; Deng, 2015), or reconciling aeromagnetic anomalies (Austin and Foss, 2014). There have been a limited number of studies that use outcrop or drill hole magnetic susceptibility readings to characterize and map alteration features associated with hydrothermal systems (Lapointe et al., 1986; Hrouda et al., 2009; Mitchinson et al., 2013), information required for meaningful geophysical inversions (Oldenburg and Pratt, 2007).

The volume of hydrothermally altered rocks around Cu-Fe-sulfide mineralization in porphyry deposits is termed “the footprint”. An understanding of how veins and alteration relate to changes in host rock magnetic susceptibility in the porphyry Cu footprint is critical to developing better exploration tools. Four major porphyry Cu-(Mo) systems, hosted in the Late Triassic Guichon Creek batholith (GCB), occur in the Highland Valley Copper (HVC) district in British Columbia; Canada’s largest and longest operating Cu mine (Fig. 5-1; Ydon, 2007; Byrne et al., 2013; Sillitoe, 2013). We evaluate the relationship between outcrop magnetic susceptibility data and the alteration surrounding the prolific HVC mining district. We calculate ranges of uncertainty and show that the variability in magnetic susceptibility measurements at individual outcrops can be correlated to vein frequency and altered rock volume. We then up-scale this observation to a district data set of 1610 outcrops, and show how domains of higher magnetic variability, and susceptibility lows, define a footprint for the porphyry Cu systems at HVC. Our findings are significant to exploration because they show how commonly collected magnetic susceptibility data can potentially be used to map vein and alteration intensity in the porphyry Cu footprint. Additionally, this work provides some insight into the processes that cause changes in rock properties.

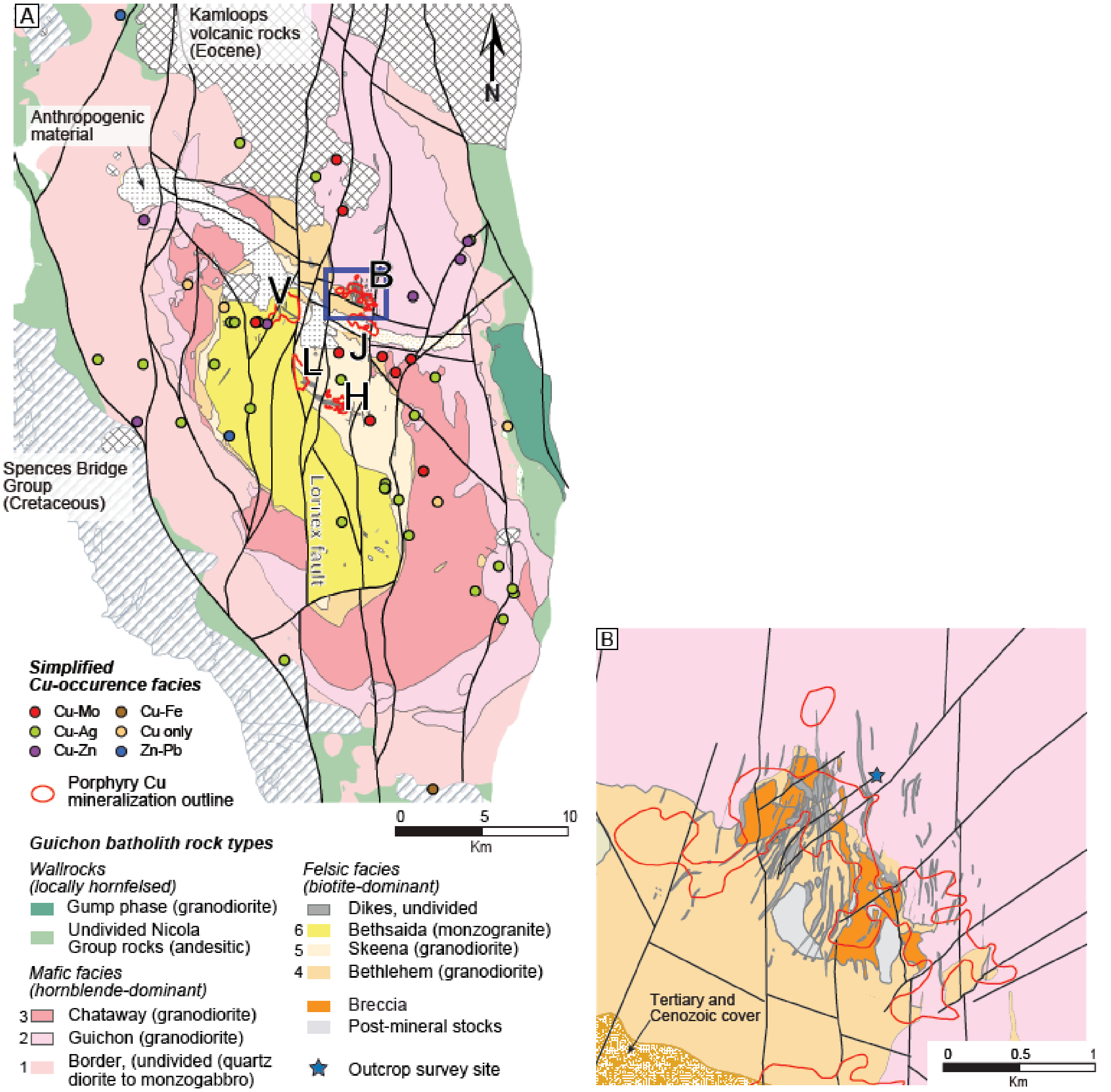

Figure 5-1. Study location maps. A. Guichon baholith geology and the Highlnd Valley Copper district. Blue frame indicates the location of Figure 5-1B. B = Bethlehem, H = Highmont, J = JA, L = Lornex, V = Valley. B. Geology of the Bethlehem deposit and location of the magnetic susceptibility study site. Lithology numbers refer to the major rock units in the district as shown in Figure 5-1A.

5.2 Porphyry Cu alteration zones and magnetic susceptibility

Porphyry Cu systems typically exhibit a predictable spatial and temporal distribution of alteration minerals that is the result of a common thermal and chemical evolution (Seedorff et al., 2005). The deep and central part of the system is characterized by potassic alteration that zones upwards to sericitic (fine-grained white-mica), and then into advanced argillic alteration. Additionally, at deep levels potassic alteration can zone laterally to sodic-calcic or propylitic alteration, whereas at intermediate and shallow levels the peripheral alteration comprises propylitic and intermediate argillic or argillic assemblages, respectively (Seedorff et al., 2005; Sillitoe, 2010). Thus, the plan-view distribution of alteration facies is partly a function of erosional level. The host rocks to porphyry Cu systems are commonly andesitic volcanic rocks and / or intermediate composition intrusions that are magnetite-bearing (Clark, 1999; Sillitoe, 2010; Clark, 2014).

Physical property analysis of drill core from calc-alkalic porphyry Cu systems in British Columbia show that quartz-sericite-bearing alteration assemblages have lower magnetic susceptibilities when compared to their intrusive and volcanic host rocks (Mitchinson et al., 2013). Propylitic alteration can also affect primary magnetite resulting in lower susceptibilities (Clark, 1999). Potassic assemblages can be associated with susceptibility highs or lows depending on whether secondary magnetite is formed during alteration, or the primary magnetite is destroyed (Seedorff et al., 2005; Mitchinson et al., 2013). Detailed mineralogical work at the Escondida porphyry, in northern Chile, shows that destruction of Fe-Ti oxide minerals and a two-order of magnitude reduction in bulk susceptibility occurs in a broad domain of pervasive quartz-sericite and argillic alteration around inner potassic assemblages (Riveros et al., 2014). In contrast, the highest bulk susceptibility values in the Escondida porphyry system came from centrally located potassic and chlorite-sericite altered rocks in which coarser secondary magnetite grains occur (Riveros et al., 2014). In-situ measurements of hydrothermally altered rocks from several other Chilean porphyry Cu deposits are associated with localized high-variability of natural remanence and susceptibility when compared to samples from regional intrusions (Tapia et al., 2016). The studies of the magnetic properties of rocks in and around porphyry Cu deposits demonstrate that hydrothermal alteration can affect Fe–Ti oxide mineralogy and abundances and subsequently modify host rock paleomagnetic natural remanence and susceptibilities (Mitchinson et al., 2013; Riveros et al., 2014; Tapia et al., 2016). Critically, the assessment of rock magnetic properties and petrology provide a link to the empirical observation that many porphyry systems, at the system-scale, are characterized by roughly circular-shaped magnetic intensity lows, or torus-like lows around a concomitant central high (Holden et al., 2011; Clark, 2014). Furthermore, magmatic-hydrothermal processes in porphyry Cu deposits are interpreted to cause high short-range variance in magnetic properties that are potentially in high contrast to the distal country rocks (Tapia et al., 2016).

We hypothesize that hydrothermal alteration around porphyry Cu systems can be characterized by not only lower susceptibilities, but also by a higher degree of magnetic variation than is normal for the typical porphyry Cu system host rocks (volcanic and intrusive). At HVC we test whether the variation in magnetic susceptibility readings at individual outcrops can be related to vein and alteration intensity, and critically, whether a measure of susceptibility variation forms a district-scale footprint that is spatially associated with the porphyry Cu centers. Underlying caveats, however, are that a set of outcrop susceptibility measurements is taken within a single rock type, that vein fill and altered rock halos have a different response than the host rock, and that the exposure has not undergone extensive weathering and oxidation. A detailed investigation of the link between alteration mineralogy and changes in the protolith magnetic properties is beyond the scope of this contribution.

5.3 Background Geology

The allochthonous Quesnel terrane in the Canadian Cordillera is characterized by Mesozoic island-arc assemblages comprised of volcanic and sedimentary rocks and associated intrusions (Coney et al., 1980). Several plutons in the Quesnel terrane are genetically and spatially related to porphyry Cu deposit formation (Logan and Mihalynuk, 2014). The Late Triassic I-type calc-alkalic GCB intruded the Nicola Group volcano-sedimentary rocks between approximately 211 to 207 Ma, prior to docking with ancestral North America, and hosts the HVC district (Byrne et al., 2013; Nelson et al., 2013; D’Angelo et al., 2017). Exposure and aeromagnetic data indicate the GCB is approximately 25 by 65 km in size with a north-northwest-elongated ellipsoidal geometry near the surface (Ager et al., 1972; McMillan, 1985a). Several texturally, compositionally, and temporally distinct intrusive rocks occur in the GCB (Northcote 1969; McMillan 1976; D’Angelo, 2016.). Older marginal and equigranular mafic-rich diorites and granodiorites transition to younger, centrally located, in-equigranular to porphyritic mafic-poor granodiorites (Fig. 5-2A). The HVC porphyry centers formed between ~209 and 207 Ma and are hosted in the mafic-poor granodiorites in the center of the batholith (D'Angelo et al., 2017). Four porphyry Cu centers compose the HVC district– Bethlehem, J.A., Valley-Lornex, and Highmont (Byrne et al., 2013). Numerous Cu-occurrence of various size and tenor also occur throughout the GCB (McMillan et al., 2009). The Valley-Lornex porphyry center has the largest footprint and is the best endowed system in the HVC district (Fig. 5-1; Byrne et al., 2013). Post-Cu mineralization regional-scale faulting has off-set geological contacts and segmented the once contiguous Valley-Lornex porphyry Cu center (Hollister et al., 1975; McMillan, 1976; Lesage et al., 2019).

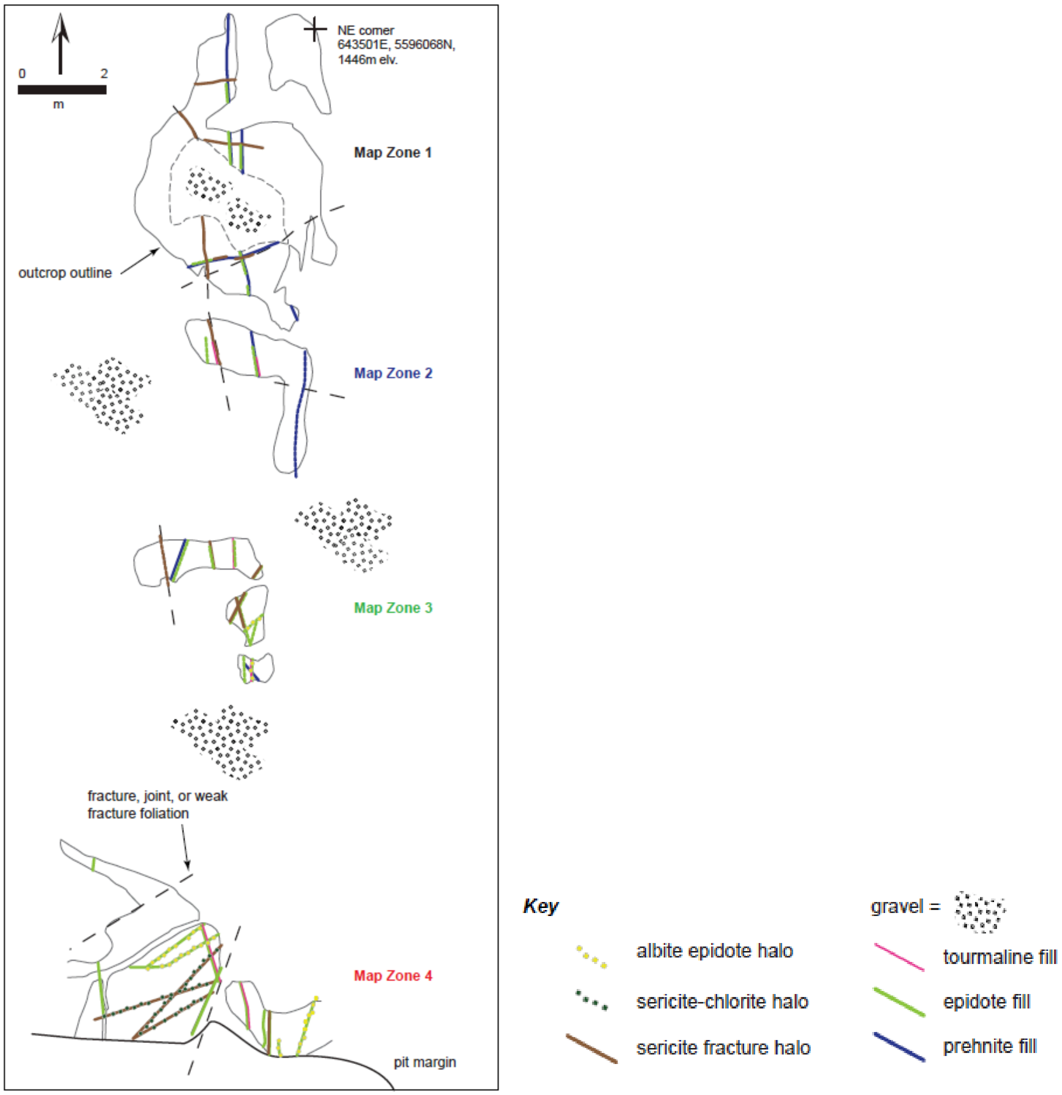

Figure 5-2. Geological map of the magnetic susceptibility variability study site at Bethlehem. The host rock is Guichon facies (unit 2 in Figure 5-1B). The map zones correspond to results shown in Table 5-2. Gravel is mostly anthropogenic.

In the HVC porphyry centers, chalcopyrite, bornite, and localized molybdenite occurs with 1) veinlets and discontinuous fracture fill of quartz with K-feldspar halos (potassic); 2) quartz with coarse-grained muscovite halos (coarse-muscovite); and with 3) pervasive and fracture-controlled fine-grained sericite–chlorite alteration (McMillan, 1985; Byrne et al., 2013; Lesage et al., 2016). Peripheral to the porphyry Cu-mineralization alteration is restricted to generally narrow 1–3 cm halos around a low density of prehnite and / or epidote veinlets (Lesage et al., 2016; Byrne et al., 2017). Epidote ± actinolite veins with K-feldspar-destructive albite halos (sodic-calcic) occur in a ~0.5–1.5 km-wide north-northeast-elongated domain in the northeast portion of the batholith, and in a ~ 3 km wide domain that extends for ~ 7 km south of Lornex and Highmont (Byrne et al., 2017). Veinlets of prehnite ± epidote ± pumpellyite with plagioclase-destructive, K-feldspar-stable, sericite–prehnite halos (propylitic) are the most common and widely distributed alteration facies in the batholith. The highest density of propylitic veinlets is centered on the porphyry systems, but this facies is present out to the margins of the batholith (Byrne et al., 2017).

5.4 Methodology

5.4.1 Data collection

Magnetic susceptibility measurements were collected using KT-10 magnetic susceptibility meters at outcrops adjacent to the Bethlehem pit, and throughout the district. Teck Resources limited provided district-scale outcrop susceptibility measurements from its property, which was augmented by data collected by the Canadian Mining Innovation Council (CMIC) Footprints Project researchers (Lesher et al., 2017). There are 1610 outcrops with susceptibility measurements in the district data set for the GCB, with a minimum of 5 readings at each outcrop. Measurement points were collected at approximately 0.5 m intervals with no particular emphasis on where alteration veins were located. The KT-10's were operated in non-pin measurement mode, zeroed in the air between measurements, and readings taken on flat outcrop surfaces utilizing the whole face of the meter to reduce instrumentation error (Lee and Morris, 2013; Deng, 2015). The KT-10 exhibits no significant temporal or thermal drift in non-pin measurement mode (<2%) and individual readings are within 1.4 % of the expected value (Deng, 2015). We infer that the uncertainty associated with utilizing data from multiple instruments over several years is less significant than instrument error, and the uncertainty associated with averaging multiple readings across an outcrop. The latter source of uncertainty is investigated below.

To permit direct comparison of the lithology, vein and alteration features, unobscured flat outcrops with minimum lichen cover adjacent with Bethlehem pit were chosen as the study site (Figs. 5-1B, 5-2, and 5-3A). The outcrop was divided into four zones from the farthest (north) to closest to the pit wall margin (south); a distance of approximately 25m (Figs. 5-2 and 5-3A). Ten measurement sets of ten measurements each were completed in each of the four zones, resulting in a total of four hundred magnetic susceptibility measurements. Uncertainty and reproducibility of magnetic susceptibility geometric mean and coefficient of variation are estimated from repeat measurement sets of the same outcrops.

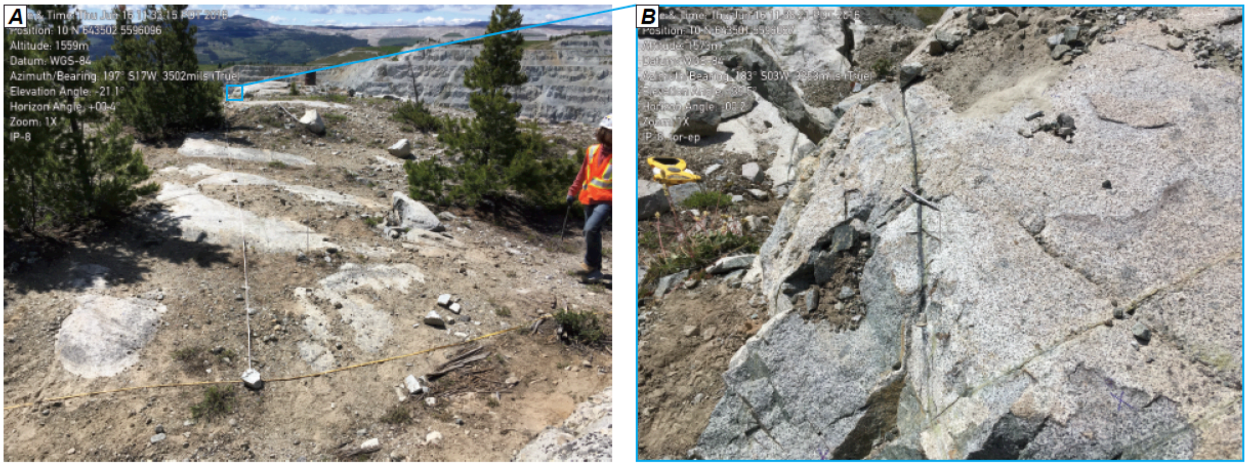

Figure 5-3. The Bethlehem study site. A. View looking south towards map zone 4. B. A portion of map zone 4 showing a tourmaline vein with a sericite halo.

5.4.2 Data processing

Bulk magnetic susceptibility in igneous rocks has a lognormal distribution and the geometric mean is a more meaningful term for assessing the difference between rocks than using the arithmetic calculation (Latham et al., 1989). Lapointe et al. (1984) used log transformed magnetic susceptibility and cumulative frequency plotted on a probability scale to effectively test for disparate magnetic response populations related to alteration. Subsequently, the $\log_{10}$ magnetic susceptibility, geometric mean, standard deviation and coefficient of variation, and the cumulative frequency of various geological populations have been calculated. Coefficient of variation is a unit-less measurement of dispersion of a single variable calculated from the ratio of the standard deviation to the mean. Coefficient of variation allows for a better measure of dispersion than the standard deviation for variables with different means. Geometric coefficient of variation (Kirkwood, 1979) is used to describe the dispersion of lognormal data. Equations used are provided in Appendix 5-A.

5.4.3 Geostatistical interpolants

Two interpolant methods in *Esri's ArcGIS Geostatistical Analyst* were used to model regional outcrop magnetic data: Empirical Bayesian Kriging (EBK) and Inverse Distance Weighted (IDW). Empirical Bayesian Kriging is a probabilistic interpolation method that accounts for the error in estimating the underlying semivariogram through repeated automated simulations (Krivoruchko, 2012). Selected modeling criterion for the EBK interpolant are: log transformation of the coefficient of variation values; exponential fit for the semivariogram curve; and a 200 m cell size.

The IDW interpolant is a deterministic model which assumes that each measured point has a local influence that diminishes with distance (ESRI, 2017). The interpolation determines average cell values using a linearly weighted combination of a set of sample points, and the weight is a function of inverse distance raised to a power (Watson and Philip, 1985). It gives greater weights to points closest to the prediction location, and the weights diminish as a function of distance (Watson and Philip, 1985). Selected modeling criterion for the IDW interpolant are: inverse distance raised to the power of 4 (nearby data have more influence); 200 m cell size; 1000 m search radius; and a 0.2 smoothing factor.

The interpolant raster products were converted to polygons for ease of symbolizing and to display with additional data sets. The coefficient of variation values are symbolized using the percentiles intervals: 0-60th, 60-65th, 65-70th, 70-75th, 75-80th, 80-85th, 85-90th, 90-95th, 95-97th, and >97th. The rationale for the chosen intervals is presented below. The outcrop magnetic susceptibility interpolant was symbolized using geometric intervals.

5.5 Results

5.5.1 Bethlehem study site geology

The host rock at the Bethlehem study site is the Guichon granodiorite, a homogenous, equigranular, hornblende, biotite and magnetite bearing granodiorite (D'Angelo, 2016). Veinlets containing prehnite ± epidote with weak sericite–chlorite ± prehnite alteration halos are common in map zone 1. Tourmaline veinlets (Fig. 5-3B) increases towards the pit margin and appear to be cross-cut and / or re-opened by prehnite-bearing veins (zone 2). Fractures with discontinuous epidote fill and sericite–chlorite halos are more common in zone 3, where a few epidote veins with albite halos are also found. Zone 4, at the pit margin, contains sulfide veinlets with limonite–sericite–chlorite alteration halos and has more epidote veins with albite halos than the other zones. Epidote veins with albite halos cross-cut tourmaline-epidote veins, and the sulphide veinlets. The measured vein frequency and volume of altered rock show an increase towards the Bethlehem pit margin and mineralization (Fig. 5-2; Table 5-1).

5.5.2 Bethlehem study site magnetic susceptibility and relationship to mapped veins

Magnetic susceptibility values at the Bethlehem study site range between 0.6×10^{-3} and 70×10^{-3} SI, and the data has a negative-skew distribution (Fig. 5-4). Three populations within the data are evident and these correspond to the magnetic response from 1) least altered rock, 2) rock with fractures with sericite–chlorite halos, and 3) rock fractures with albite halos (Fig. 5-4). The magnetic susceptibility response for unaltered Guichon granodiorite ranges between approximately 26×10^{-3} SI and 45×10^{-3} SI (Fig. 5-4). Exposures with veins with a sericite–chlorite halo have a lower response than unaltered host rock, but veins with albite halos have the lowest susceptibility (Figure 4). All the alteration at the margin of the Bethlehem pit is associated with a decrease in magnetic susceptibility relative to the protolith.

The cumulative frequency of the magnetic susceptibilities from each map zone was calculated to assess at which values the zones differ (Fig. 5-5). A decrease in magnetic susceptibility from zone 1 to zone 4 is evident (Fig. 5-5). The four zones have a similar response between approximately 26×10^{-3} SI and 45×10^{-3} SI which corresponds to unaltered rock measurements. Below approximately 26×10^{-3} SI, however, there is an inflection in the probabilities and the populations for each map zone diverge (Fig. 5-5). Overall map zone 4 has the lowest magnetic susceptibility and contrasts with the response for zone 1 (Table 5-1; Fig. 5-

5). Below approximately 26x10^{-3} SI, the magnetic susceptibility response for map zones 2 and 3 sit between that of zones 1 and 4.

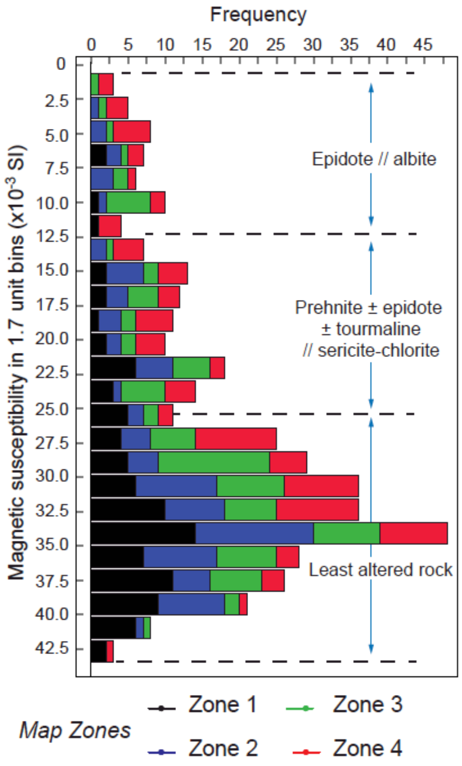

Figure 5-4. Frequency distribution of all magnetic susceptibility readings at the Bethlehem study outcrop site (*n* = 399; one outlier removed for clarity at 70x10^{-3}). Alteration mineralogy = vein fill // alteration halo. Magnetic response boundaries between alteration facies and fresh rock are overlapping and approximate.

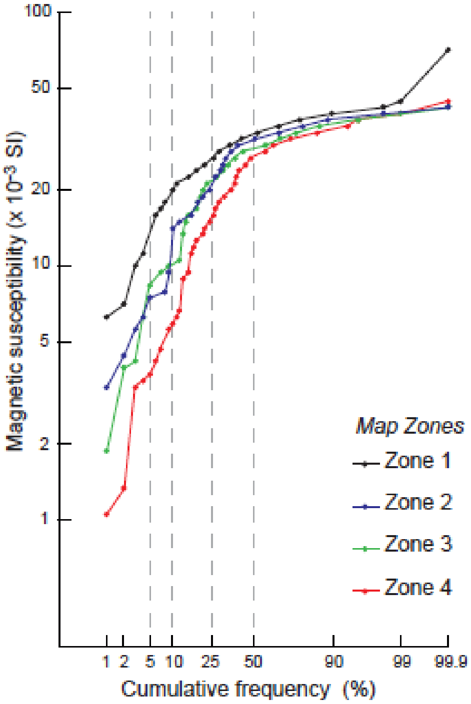

Figure 5-5. Comparison of map zone magnetic susceptibility measurements (log scale) versus their cumulative frequency (probability scale) at the Bethlehem study site.

The changes in magnetic susceptibility response correlate with changes in vein frequency and estimated altered rock volume. Based on the magnetic susceptibility geometric mean per map zone (*n* = 100 per map zone), a decrease from 29.8x10^{-3} to 19.6x10^{-3} SI towards the pit margin occurs (Table 5-1; Fig. 5-6). The decrease in magnetic susceptibility geometric mean corresponds to an increase in vein frequency and volume of altered rock (Fig. 5-6). The geometric coefficient of variation has been calculated for each map zone (Table 5-1; Fig. 5-6). The coefficient of variation increases towards the pit margin and has a positive correlation with vein frequency and volume of altered rock, and a negative correlation with mean magnetic susceptibility (Fig. 5-6).

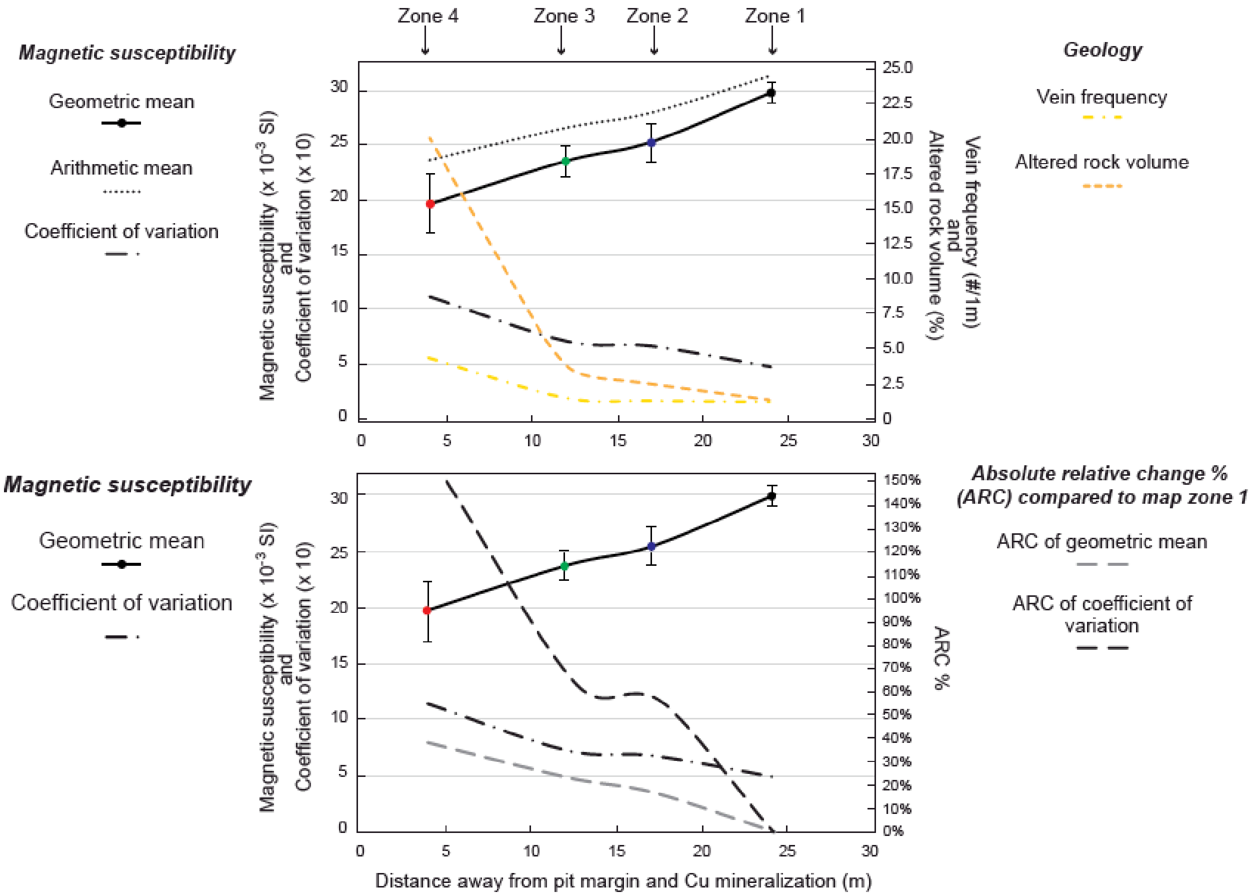

Figure 5-6. Profiles of vein and alteration data, and magnetic susceptibility readings as a function of distance from the pit margin at the Bethlehem study site. Data points colored by outrop map zone indicated in Figure 5-2. Geometric mean uncertainty whiskers correspond to values in Table 5-1. Altered rock volume = vein fill width plus visible alteration halo width multiplied by the vein frequency per meter.

Table 5-1. Summary of vein and alteration halo and magnetic susceptibility measurements at the Bethlehem study site.

	Zone 4	**Zone 3**	**Zone 2**	**Zone 1**
Total vein frequency	4.3	1.5	1.3	1.2
Vein fill plus alteration halo (cm)	4.5	2.3	2.0	1.2
Total altered volume % (per m)	19.4	3.4	2.6	1.4
Max distance from pit wall	4	12	17	24
Area of map zone (m^2)	11.3	3.5	3.8	13.8
Magnetic susceptibility ($x10^{-3}$ SI) arithmetic mean	23.6	26.6	28.0	31.4
Magnetic susceptibility ($x10^{-3}$ SI) geometric mean	19.6	23.5	25.3	29.8
Arithmetic Stdev.	10.6	9.3	9.8	9.0
Geometric Stdev.	2.1	1.7	1.7	1.4
Range	42.9	39.0	37.8	64.6
IQR	16.7	11.6	13.2	11.0
Min	0.6	1.9	3.2	6.3
Max	43.5	40.9	41.0	70.9
Arithmetic CV	0.45	0.35	0.35	0.28
^{k}Geometric CV	1.07	0.70	0.67	0.42

^{k}Geometric CV = CV_k = $e^{\sigma ln} - 1$, where σ is σ_g (Kirkwood, 1979)
IQR = inter quartile range
Stdev. = standard deviation

By comparing the magnetic susceptibility geometric data of each zone to the corresponding values for map zone 1, an absolute relative change term (ARC%) can be used to measure the relative change as a function of distance from the pit margin. The ARC% of the magnetic susceptibility means between zone 1 and 4 is ~34%, however, the ARC% of their coefficient of variation is ~154%, a considerably stronger signal. The ARC% of the magnetic susceptibility mean and coefficient of variation values for zones 2 and 3 lie between that of zones 1 and 4 (Table 5-2; Fig. 5-6).

Table 5-2. Absolute relative change of map zones 4, 3 and 2 compared to map zone 1.

	1 vs 4	**1 vs 3**	**1 vs 2**	**1 vs 1**
Magnetic susceptibility (x10^{-3} SI) geometric mean ARC%	34.2%	21.0%	15.1%	0.0%
Geometric CV ARC%	153.6%	64.3%	58.0%	0.0%
Arithmetic CV ARC%	56.0%	21.5%	22.0%	0.0%

ARC% = absolute relative change = x-reference value / reference value*100

5.5.3 Uncertainty and reproducibility

Repeatability of measurements refers to the variation in repeat measurements made on the same subject under identical conditions. Individual magnetic susceptibility measurements were collected from the same outcrop but were not taken in exactly the same location. Consequently, this analysis of uncertainty refers to reproducibility; the variation in measurements made on a subject under changing conditions. By collecting ten sets of ten magnetic susceptibility measurements for each of the mapped zones (Fig. 5-2) the reproducibility (standard error) of outcrop means by this data collection method can be assessed (Table 5-3).

Table 5-3. Standard error associated with magnetic susceptibility measurements (x10^{-3} SI).

	Zone 4	**Zone 3**	**Zone 2**	**Zone 1**
Mean of Mag. Sus. GeoMeans* (n =10)	19.9	24.0	25.4	29.8
Stdev. of means	3.7	1.9	2.6	1.3
Standard Error (SE)	1.2	0.6	0.8	0.4
SE at 95% CI (9 DF)	2.6	1.3	1.9	0.9
Uncertainty (error) % of GeoMean Mag. Sus. @ 10 measurements	13.3%	5.6%	7.3%	3.0%
Uncertainty (error) % of GeoCV. @ 10 measurements	17.9%	12.7%	10.6%	11.8%

*Susceptibility in x10^{-3} SI
Average standard error % of the geometric mean from the 4 map zones = 7.3%. *t* = 2.62 at 95% CI.
Abbreviations: CI = confidence interval; DF= degrees of freedom, GeoCV = geometric coefficient of variation, GeoMean = geometric mean, Mag. Sus. = magnetic susceptibility, SE = standard error, Stdev. = arithmetic standard deviation.

At a confidence interval of 95% and 9 (n-1) degrees of freedom, the average standard error of the geometric mean from 10 magnetic susceptibility measurements from the 4 map zones is

7.3% (Table 5-3). Embedded in the uncertainty of geometric mean calculation is the instrumentation error. However, uncertainty is also dependent on the outcrop variability, thus the most altered outcrop (map zone 4) has the highest uncertainty at ~13% of the mean compared to just 3% in zone 1 (Table 5-3). The average standard error for the repeat values of the coefficient of variation from the four maps zones is 13.2%. A similar increase in uncertainty of the coefficient of variation is observed from map zone 1 to map zone 4 (Table 5-3). Increasing the number of measurements included in the calculations reduces uncertainty, however, at 10 readings within ~10m^2 area of moderately altered rock (~20 volume %) an acceptable level of uncertainty (~13–18%) for the mean and coefficient of variation is achieved (Table 5-3).

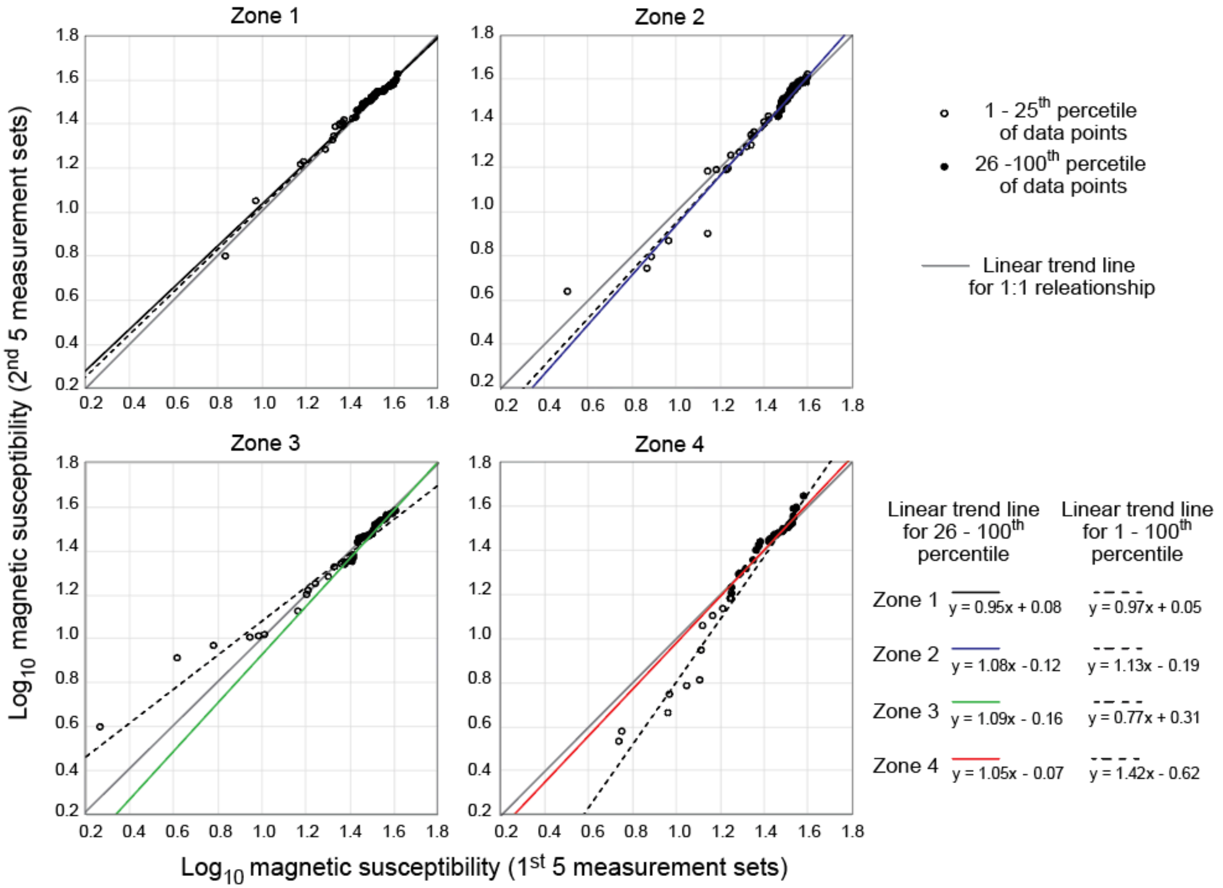

Log$_{10}$ magnetic susceptibility (1st 5 measurement sets)

Figure 5-7. Minimum-maximum plots for the four map zones. The data has been siloed into the 1st 50 measurements versus the 2nd 50 measurements. The black line indicates a 1:1 relationship.

An alternative and visual way to evaluate the reproducibility of magnetic susceptibility measurements, and subsequent mean and coefficient of variation, is to test the data on minimum-maximum plots (Fig. 5-7). The 100 data points per map zone were split into the first 50 and second 50 measurements and then organized from minimum to maximum value for crossplotting on log scale (Fig. 5-7). Perfectly reproducible data would plot on the 1:1 line. The minimum-maximum plots show no systematic bias across the 4 map zones. Excluding the lower quartile of susceptibility values greatly improves the correlation between measurements sets (Fig. 5-7), particularly for map zones 3 and 4, indicating that low susceptibility values are the primary contributor to outcrop variability and uncertainty of the mean.

5.6 Up-scaling to the district porphyry footprint

5.6.1 Estimation of altered rock volume from mapping data

The orientation, vein fill width, alteration halo width, vein frequency per meter, and mineralogy are recorded for vein sets exposed in 743 outcrops in the Guichon Creek batholith. The vein fill and alteration halo widths were added and then multiplied by their corresponding frequency per meter. This product was then summed for each vein set, independent of mineralogy and orientation, to estimate the altered rock volume percentage (%) at each individual outcrop. The frequency distribution of altered rock volume % for outcrops in the Guichon Creek batholith has a log normal distribution (Fig. 5-8).

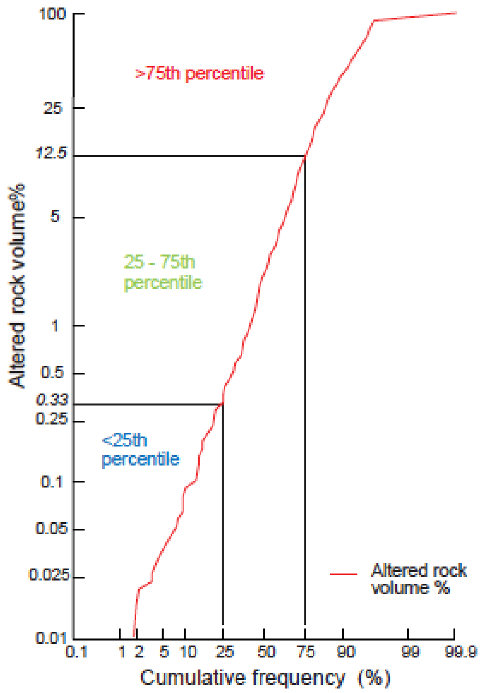

Figure 5-8. Regional outcrop altered rock volume % (log scale) versus their cumulative frequency (probability scale). Percentile breaks and color scheme are referenced to Figure 5-8. *n* = 743.

5.6.2 Outcrop magnetic susceptibility data and relationship to altered rock volume %

Results from the outcrop study site at Bethlehem demonstrate that as the altered rock volume % increases the magnetic susceptibility variability also increases. There is a similar relationship between the altered rock volume % and the corresponding magnetic susceptibility geometric mean and coefficient of variation in the district outcrop data set (Figs. 5-9 and 5-10). Figure 5-9 includes all rock facies in the batholith and has not been filtered to exclude outcrops of aplite dikes (~1% of data; low susceptibility) or rocks with abundant mafic-rich inclusions (unknown proportion of data; typically, high susceptibility). Outcrops that occur within the first quartile (<0.33 vol. %) of the altered rock volume population have the highest magnetic susceptibility geometric mean and lowest coefficient of variation response (Fig. 5-9). The inverse is true for outcrops in the fourth quartile of altered rock volume (>12.6 vol. %; Fig. 5-9). Each of the altered rock volume populations show an inflection close to $15x10^{-3}$ SI that likely relates to a switch to susceptibility responses dominated by alteration (Fig. 5-9A). A sample of outcrops in order of decreasing distance from the Highmont porphyry center are presented in Figure 5-10. This outcrop selection shows how magnetic response can differ with altered rock volume percent, alteration facies, and distance from the porphyry Cu center.

Hand samples of the least altered host rocks in the GCB show a wide range of magnetic susceptibilities from the oldest peripheral mafic-rich rocks (units 1-3; Table 5-4) to the younger centrally located mafic-poor rocks (units 4-6; Table 5-4; Fig. 5-9A). The standard deviation of the least altered rock sample suites also decreases from the marginal mafic facies to the inner more felsic facies from $\sim 20x10^{-3}$ SI to $5x10^{-3}$ SI, respectively. The cumulative frequency curves in Figure 5-9A do not differentiate between host-rock facies, however, the plot can be broken into three response domains based on the expected susceptibilities of the least altered samples of the host rocks:

1. fresh rocks with geometric mean $>50x10^{-3}$ SI;
2. a mix of fresh and altered rocks with susceptibilities between ~15 and $50x10^{-3}$ SI;
3. altered rocks and aplite, or leucocratic dikes, that have a low magnetic susceptibility geometric mean $< \sim 15x10^{-3}$ SI.

Magnetite addition associated with potassic alteration is very rare at Highland Valley (McMillan, 1985a; Byrne et al., 2013; Lesage et al., 2016), thus the outcrops with $>50x10^{-3}$ SI susceptibility are interpreted to reflect primary magmatic features and localized increase in Fe-Ti mineral content, although some component of hydrothermal magnetite cannot be ruled out.

Table 5-4. Median magnetic susceptibility and standard deviation of sub-sampled drill cores from hand samples of least altered host rocks.

Host rocks	Unit number	n	*Median susceptibility ($x10^{-3}$ SI)	Standard deviation
Bethsaida	6	62	20.01	5.58
Skeena	5	17	26.69	8.43
Bethlehem	4	11	27.41	10.64
Chataway	3	17	36.25	15.13
Guichon	2	49	38.47	7.52
Border	1	13	40.00	21.74

Measured at the Geological Survey of Canada - Pacific using the Sapphire SI2B susceptibility meter, which is accurate to 10-7 SI. Magnetic susceptibility measurements are made on 2.2 cm long cylindrical cores that are 2.5 cm in diameter, drilled from hand samples.

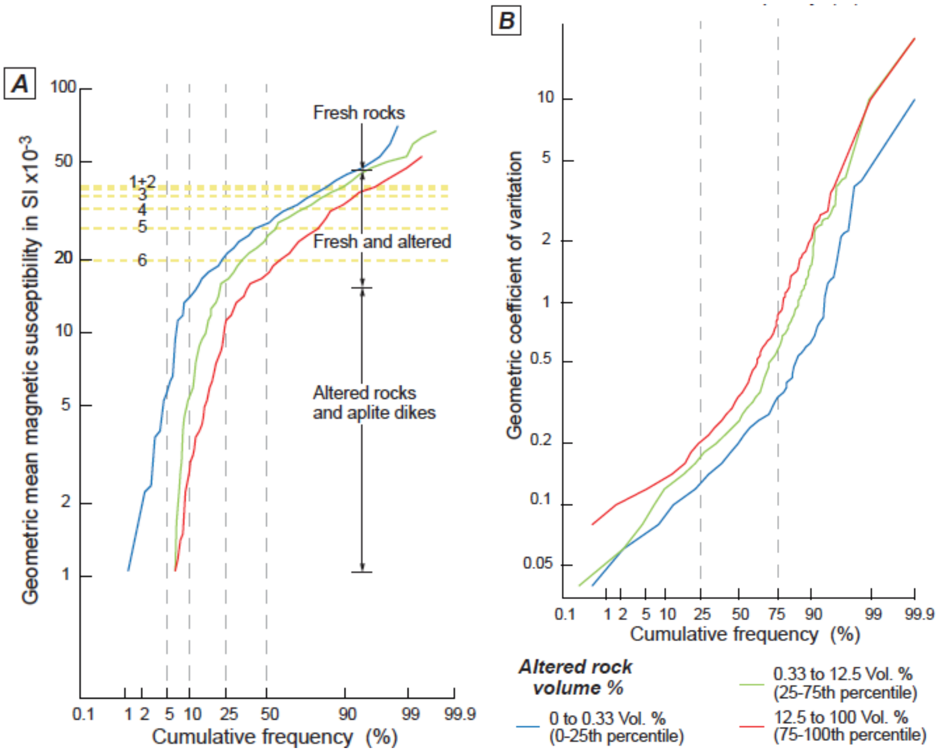

Figure 5-9. Regional outcrop magnetic susceptibility data. A Geometric mean magnetic susceptibility data (log scale) versus cumulative frequency (probability scale) symbolized by altered rock volume percentile groups. Orange colored dashed lines are the median magnetic susceptibility values for intrusive facies in the Guichon batholith (Table 5-4); older marginal mafic facies = 1, 2 and 3, and inner more felsic facies = 4, 5 and 6. B. Coefficient of variation (log scale) versus cumulative frequency (probability scale). Outcrop n = 743, and measurement n = 6061.

Figure 5-10. Altered outcrop examples. A. Guichon granodiorite cut by prehnite veinlets with weak sericite-prehnite-vermiculite alteration halos. B. Skeena granodiorite cut by epidote-prehnite veinlet with sericite-prehnite halo. C. A portion of an outcrop of Skeena granodiorite cut by sulphide-limonite veinlets with coarse muscovite alteration halos. Alt. Vol. = altered rock volume; CV = coefficient of variation; MS = magnetic susceptibility.

A total of 1160 outcrops with an average of 7.2 magnetic susceptibility measurements per outcrop are included in histogram and cumulative frequency plots (Fig. 5-11), and in subsequent spatial interpolants (Figs. 5-12 and 5-13). Several small inflections in the coefficient of variation frequency curve are evident (blue arrows; Fig. 5-11A). These breaks are used to symbolize data and the spatial interpolants.

The data points on a cross-plot of the district outcrop geometric mean and coefficient of variation values form an approximate inverted U-shape (Fig. 5-11B). Based on these coefficient of variation and mean susceptibility values, and the groupings established in Figure 5-9A, they district outcrop magnetic data can be split into four general response domains (Fig. 5-11B):

1. fresh and weakly altered outcrops that have susceptibilities >15x x10^{-3} SI and a coefficient of variation less than 0.395, or 70th percentile of the data (Low CV, High MS);
2. outcrops with high variability and susceptibilities >15x x10^{-3} SI (High CV, High MS);
3. outcrops with high variability and low susceptibilities <15x x10^{-3} SI (High CV, Low MS);
4. outcrops that have both low variability and <15x x10^{-3} SI susceptibility (Low CV, Low MS)

A high density of outcrops with a coefficient of variation >0.395 occur around the Valley, Lornex, Highmont, and, to a lesser extent, Bethlehem porphyry centers compared to elsewhere in the district (green and orange symbols; Fig. 5-12A). There is insufficient outcrop data around J.A. and south of Bethlehem to make meaningful inferences for that area. Numerous Cu occurrences, as well as some distal alteration zones, are also associated with outcrops of high magnetic coefficient of variation. The group of low variability and low susceptibility outcrops can be attributed to fresh host rocks with atypically low susceptibility (e.g. aplite), or pervasively altered outcrops in which insufficient primary magnetite remains to provide higher contrast variability (Fig. 5-11B). A cluster of low susceptibility low variability outcrops occurs southwest of the Cu mineralization outline for Valley, and at Lornex (red symbols; Fig. 5-12A). Several additional clusters of low susceptibility low variability outcrops occur in the batholith outboard of the HVC porphyry centers and Cu occurrences. The spatial and geological context for these features is discussed below using interpolant maps and location labels.

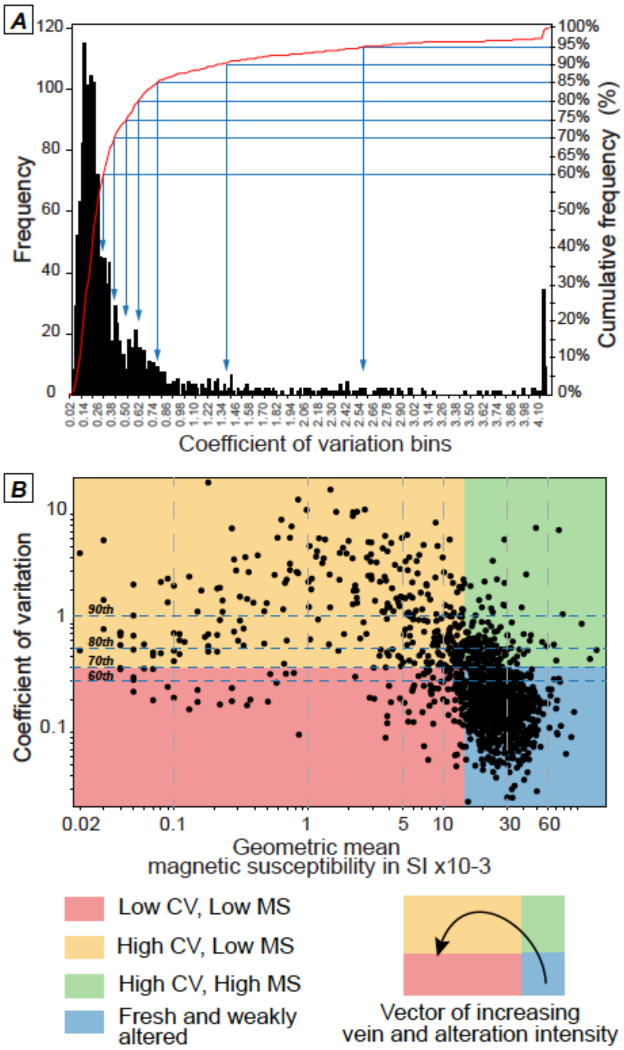

Figure 5-11. A. Histogram and cumulative frequency distribution of regional outcrop magnetic susceptibility coefficient of variation (log scale). The spike at ~99% is because outcrops with coefficient of variation >4.1 are included in the same bin range. The blue arrows indicate the percentile breaks used to symbolize the data points and geostatistical interpolants shown in Figure 5-12. B. Outcrop geometric mean versus coefficient of variation. The colored boxes indicate the magnetic response domains based on coefficient of variation and susceptibility. Outcrop n =1610 and measurement n = 11432.

5.7 Geostatistical interpolants

There is a paucity of data from in the Valley and Lornex porphyry centers themselves, however, outcrop susceptibility domains less than ~10x10^{-3} SI characterize the rocks directly adjacent Cu-mineralization (Fig. 5-12B). Surrounding these susceptibility lows, and extending for up to 5 km distance, are domains of high magnetic variability, or a mix of high-and-low variability outcrops (IDW interpolant; Fig. 5-12C). For ~5 km southwest of the Cu mineralization at Valley there is a heterogeneous domain comprising high-and-low variability outcrops, beyond which the response is mostly less than 0.302 (<60th percentile value; Figs. 5-12C and 5-13A). The outcrops east and south of Lornex and Highmont have a more homogenous coefficient of variation response in excess 0.506 (>75th percentile; Fig. 5-12C). Small and isolated coefficient of variation domains of > 0.772 are associated with Cu occurrences and alteration outboard of the porphyry systems (e.g., >85th percentile anomalies labelled 1-10 in Fig. 5-12C). The EBK predictive interpolant detects a broad coefficient of variation anomaly composed of >0.395 (70th percentile value) that overlaps with and extends beyond the porphyry Cu centers for up to ~4 km (Fig. 5-13B). The EBK interpolant is less sensitive to the small isolated coefficient of variation highs surrounded by lower response outcrops evident in the IDW interpolant. Two orientations are apparent in the kriged interpolant (Fig. 5-13B); a northwest long-axis and a northeast-trending short-axis. Some artefacts are present at the peripheries of the EBK model (e.g. areas marked “e” in Fig 5-13B), where the extrapolation is at the limit of information and the data envelope is one-sided. Additionally, an anomalous area across the Lornex fault directly northeast of Valley is driven by a single data point and is subsequently less reliable (marked “s” in Fig. 5-13B).

Anomaly 1, apparent in both coefficient of variation interpolants (Figs. 5-12C and 5-13B), is extrapolated to extend under post-mineral volcanic cover, and is also close to historically mined Cu occurrences (Highland and Transvaal; McMillan et al., 2009). Outcrops with low susceptibility and low variation are also present in the area around anomaly 1. Anomaly 2 is associated with a domain of strong fracture controlled albite alteration, a regional-scale structure, and two minor Cu occurrence (BX and Hat-Outrider; McMillan et al., 2009). Anomaly 3 is hosted in mafic-rich rocks at the margin of the batholith and is driven by several magnetite-destructive, weakly Cu-Zn-mineralized fault zones (Dansey showing; McMillan et al., 2009), and widespread, but low density, epidote replacement halos on fractures. Anomaly 4 is at the edge of the batholith at the contact with Nicola volcaniclastic rocks, and appears to be associated with locally altered rocks in faults at a small Cu occurrence (Fidler showing; McMillan et al., 2009). Anomaly 5 refers to a northeast-trending array of Cu-showings that are spatially associated with localized susceptibility lows and higher variability outcrops. From south to north the Cu occurrences are Bornite ridge, Malachite Hill, and Jericho (McMillan et al., 2009). Anomaly 6 is associated with several north trending structures associated quartz-sulphide veins with well-developed sericite-chlorite halos (Yubet showing; McMillan et al., 2009). Anomaly 7, south of Yubet, comprises a susceptibility low and variation high. Mapping in this area indicates the susceptibility low is caused by porphyry and aplite dikes, and the variability high is caused by structurally focused domains of fractures with sericite-prehnite halos, and subordinate epidote veins with albite halos (Lesage et al., 2016). Anomaly 8 is primarily a susceptibility low caused by relatively fresh Bethsaida granodiorite which has a lower Mg# than typical for this unit elsewhere in the batholith. The coefficient of variation high directly west of the susceptibility low at anomaly 8 is being driven by one strongly anomalous outcrop. Anomalies 9 (Empire) and 10 (Alwin) are past-producing mines that exploited high-grade chalcopyrite-bornite mineralization in quartz-carbonate veins, and in sulphide pods hosted in shear zones (McMillan et al., 2009 and references there in). Muscovite alteration associated with these Cu-occurrences is restricted to ~0.1–1 m wide halos around related structures.

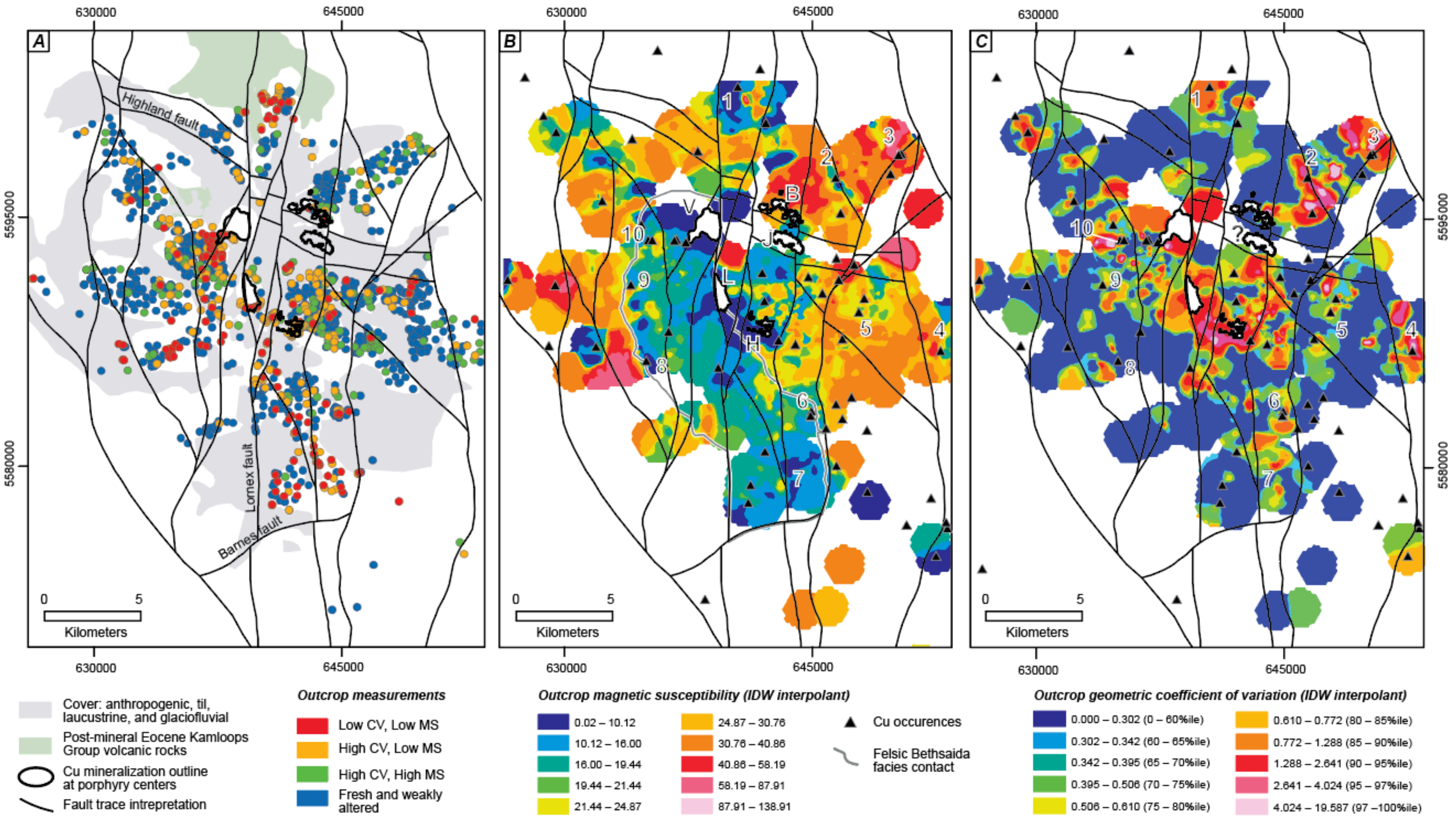

Figure 5-12. Magnetic susceptibility domain map and models. A. Outcrop data points symbolized by their coefficient of variation and susceptibility response groups (i.e., Figure 5-9), and the distribution of post-mineral cover and volcanic rocks. B. Inverse distance weighted (IDW) interpolant of outcrop magnetic susceptibility and the location of the Cu occurrences. Letters indicate the porphyry Cu systems in the Highland Valley district: B = Bethlehem, H = Highmont, J = JA, L = Lornex and V = Valley. C. Inverse distance weighted (IDW) interpolant (displayed as polygons) of outcrop geometric coefficient of variation. Numbers on the maps relate to anomalies noted in the text Model parameters and additional annotation explanation are given in the main body text. Number of data points (outcrops) shown is 1610. %ile = percentile. Structural interpretation from Lesage et al. (2016).

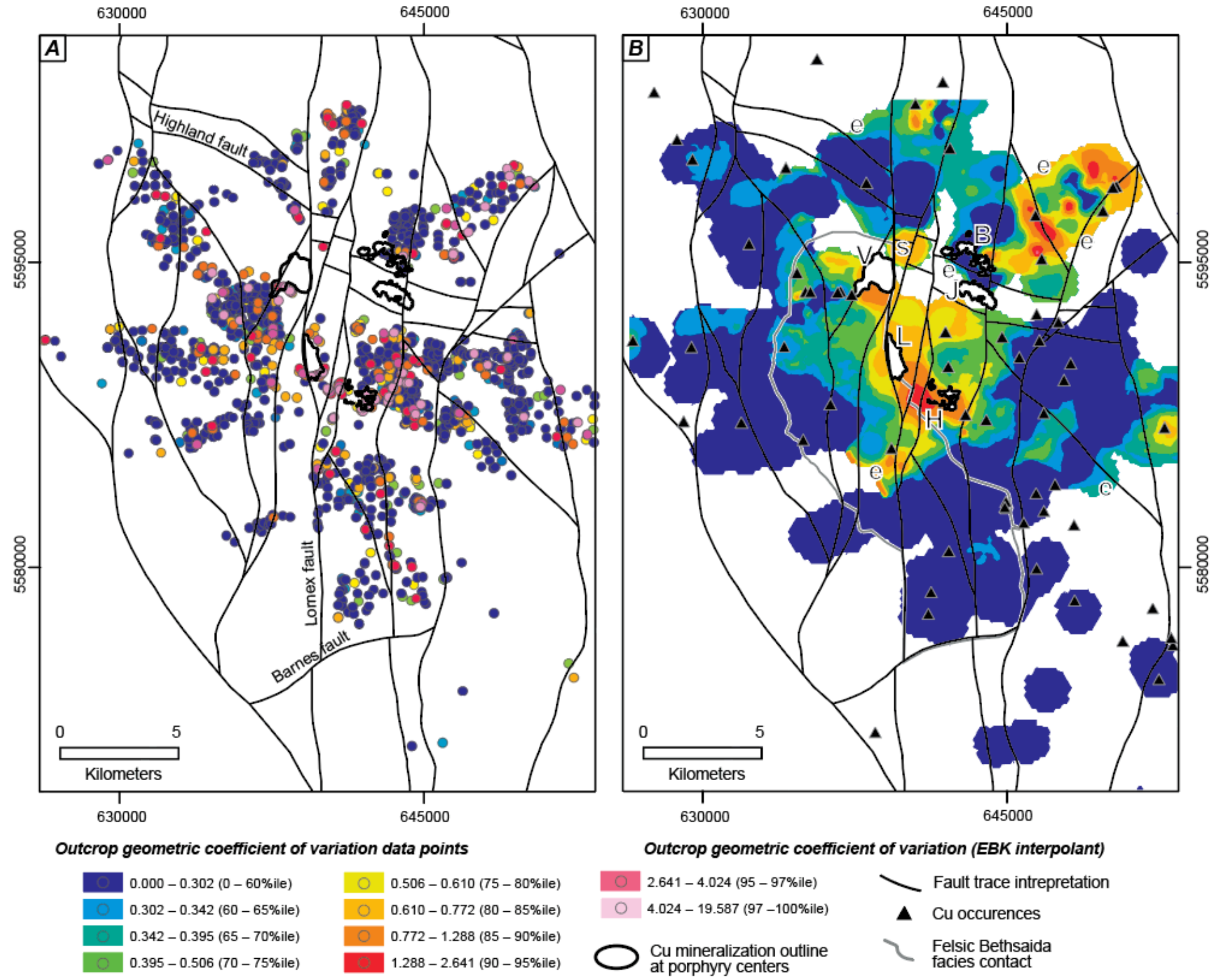

Figure 5-13. Data map and model. A. Outcrop data points symbolized by geometric coefficient of variation. B. Empirical Bayesian Kriging (EBK) predictive interpolant (displayed as polygons) of outcrop coefficient of variation and location of Cu occurrences. Letters indicate the porphyry Cu systems in the Highland Valley district: B = Bethlehem, H = Highmont, J = J.A., L = Lornex and V = Valley. Model parameters and additional annotation explanation are given in the main body text. Coefficient of variation data points (outcrops) = 1610. %ile = percentile.

5.8 Discussion

5.8.1 Alteration and magnetic susceptibilities

The mean and coefficient of variation of outcrop magnetic susceptibility measurements can be used to assess alteration intensity in the HVC porphyry Cu footprints. Outcrops with a coefficient of variation greater than ~0.4 and susceptibilities below ~15x10^{-3} SI have a high probability of being altered (e.g., Fig. 5-11B). Between susceptibilities of ~15 and 40x10^{-3} SI there is a mix of altered and unaltered rocks that requires sorting by host-rock to differentiate.

Subsequently, it is the measure of variability that provides a less ambiguous proxy for alteration intensity because it is not affected by overlapping ranges in protolith susceptibilities. Additionally, the magnitude of change in the coefficient of variation value of least altered outcrops compared to those within ~4 km of the Valley porphyry center is greater than the corresponding change in susceptibilities (Table 5-5). It is important to note, however, that in outcrops with a coefficient of variation greater than ~0.4 and susceptibility between 15 and 40×10^{-3} SI, a subordinate portion of the dispersion could also be caused by high susceptibility readings taken over rare magnetite-rich mafic inclusion, as opposed to lows due to alteration.

Table 5-5. Absolute relative change in magnetic response towards the Valley porphyry center

Coefficient of variation		
Distal	Proximal	ARC
[1]0.302	0.506	68%
[2]0.302	0.772	156%

Magnetic susceptibility ($\times 10^{-3}$ SI)		
[3]Distal	Proximal	ARC
20	10	50%
20	5	75%

[1] 60th to 75th percentile
[2] 60th to 85th percentile
[3] Least altered Bethsaida outboard of the Valley Cu mineralization
ARC = absolute relative change = x-reference value/reference value

Domains of outcrops with elevated coefficient of variation are interpreted to be primarily caused by alteration focused in fractures sets related to cooling in the pluton and permeability generated by the porphyry Cu systems. Hydrothermal alteration processes, focused in and adjacent to fractures, are interpreted to have decreased host rock susceptibilities by either oxidation of primary magnetite or metasomatic removal of Fe-Ti oxides, or a combination of these processes (Mitchinson et al., 2013; Riveros et al., 2014). The relationship between increasing alteration intensity and altered rock volume, and the corresponding outcrop magnetic response can be modeled as an inverted U-shaped vector through magnetic susceptibility and coefficient of variation space (inset in Fig. 5-11B). This vector has 4 stages:

1. incipient fracturing, vein fill, and development of alteration halos initially increases outcrop magnetic heterogeneity and coefficient of variation without a significant reduction in mean susceptibility;
2. higher fracture density and interconnectivity further increases coefficient of variation but also causes a distinct reduction in mean susceptibility;
3. a sufficient volume of rock is altered to further reduce the mean susceptibility, but also begin to re-homogenize the magnetic response causing a decrease in coefficient of variation (downward inflection in the arrow in Fig 5-11B);
4. at very high fracture density and when fracture halos overlap (pervasive alteration), the outcrop has a homogenously low mean susceptibility, and subsequent low coefficient of variation.

5.8.2 Geostatistical interpolants

In the GCB, the coefficient of variation of outcrop-scale magnetic susceptibility measurements is a proxy for abundance of fracture controlled magnetite destructive alteration. When modeled, the coefficient of variation increases towards Cu mineralization and generally corresponds with higher altered rock volume % estimated from mapping. A larger and more coherent domain of >75th percentile coefficient of variation is present east of the Lornex and Highmont porphyry centers compared to the area directly west of Valley (Fig. 5-12C). This disparate response is perhaps a function of alteration facies. The rocks west of Valley are cut by K-feldspar ± chalcopyrite veinlets with narrow (1-3mm) K-feldspar halos, and subordinate fractures with sericite-chlorite halos (Lesage et al., 2016). Whereas the areas east and south of Lornex, and northeast of Highmont have a higher abundance of fractures with well-developed halos of sericite-chlorite, and fractures with albite halos (Lesage et al., 2016; Byrne et al., 2017). Aeromagnetic data indicates a magnetic low over well mineralized and strongly altered portions of the Valley and Lornex porphyry centers (Ager et al., 1972; McMillan, 1985a). Thus, although there is a paucity of outcrop magnetic data from within the Cu centers themselves, we infer that they have homogenous and low susceptibilities, and a corresponding low coefficient of variation.

Northwest and northeast trending coefficient of variation anomalies are evident in the IDW and EBK interpolants. These trends are consistent with the orientation of Cu mineralization and porphyry dikes in the Highland Valley district (Byrne et al., 2013). The interpolants in Figures 5-12 and 5-13 are unconstrained by lithological or fault boundaries. A second composite IDW interpolant constrained to major fault block boundaries was also generated (Appendix 5-B), but does not differ significantly from the geologically unconstrained IDW interpolant shown in Figure 5-12C.

5.9 Conclusions and Implications

Our work shows that information relating to alteration can be leveraged from outcrop magnetic data, which can be easily collected at all stages in an exploration programme (Clark et al., 1992).

Domains of outcrops that exhibit coefficient of variation >0.3 extend 1–4 km away from the porphyry centers at HVC and form a larger footprint than magnetic susceptibility lows.

Measuring outcrop magnetic susceptibility coefficient of variation and mapping the anomalies is a valid method to delineate high variability magnetic signal around porphyry Cu systems caused by alteration (Fig. 5-14), and potentially provides a vector to Cu-mineralization.

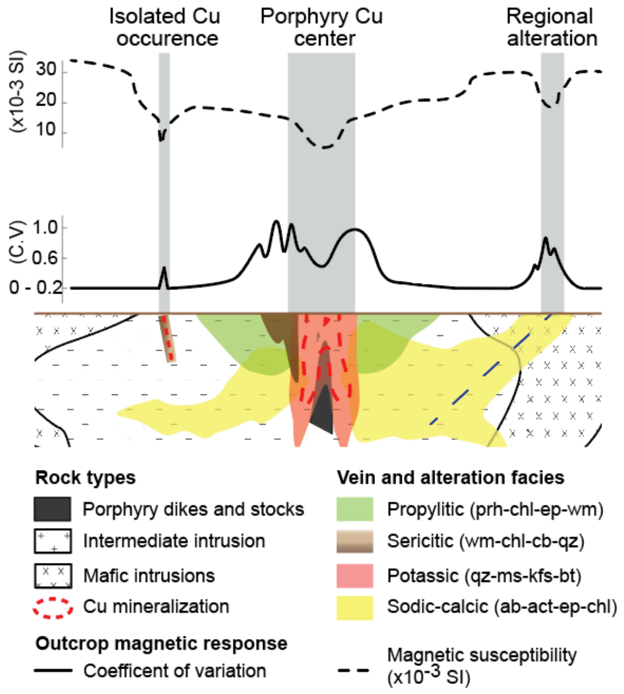

Figure 5-14. Schematic diagram illustrating outcrop magnetic coefficient of variation and susceptibility profiles of the calc-alkalic Cu-(Mo) porphyry systems in the Highland Valley Copper district. Act = actinolite; bt = biotite; cb = carbonate mineral; chl = chlorite; ep = epidote; kfs = K-feldspar; ms = muscovite (coarse grained); prh = prehnite; qz = quartz; wm = fine-grained white-mica (sericite).

Mapping outcrop magnetic susceptibility coefficient of variation could be useful data to accompany, and be a proxy for, vein density and mineral assemblage mapping. Susceptibility variation anomalies should be reviewed in conjunction with lithological and alteration information in order to differentiate those associated with 1) favorable alteration facies and 2) mineral vectors towards porphyry mineralization, from 3) less prospective regional alteration features (Fig. 5-14), and 4) localized increase in primary Fe-Ti mineral concentration.

Uncertainty in the mean and coefficient of variation values from 10 susceptibility measurements per ~10 m^2 size outcrop is generally < 15% in altered rocks. The number of measurements per outcrop should be scaled accordingly.

6 Conclusions

Numerous studies have investigated the anatomy and formation of the well mineralized portions (~500–4000 m^2) of porphyry Cu deposits (Seedorff et al., 2005; Sillitoe, 2010, and references there in). Far fewer studies have focused on material-transfer, mineralogical, or isotope systematics to assess the relative roles of magmatic, meteoric, seawater, and formation fluids in the development the weakly altered rocks that form the larger footprint (~ 10–100 km^2) of the magmatic-hydrothermal centers (Dilles et al., 2000; Djouka-Fonkwe et al., 2012; Cooke et al., 2014a; Halley et al., 2015). The GCB lithological framework (McMillan, 1976; D'Angelo et al., 2017), and HVC porphyry center geology (McMillan, 1985a; Byrne et al., 2013) are well established, but there has been a dearth of work on the distal expressions of the system. This study aimed to determine the diagnostic features of the rocks and minerals peripheral to the prolific HVC district. Specifically, how, to what degree, and to what distance are the rocks outside of the porphyry centers altered and metasomatized? Critical to how the footprint formed are the fluids present. Was there an external fluid present peripheral to, and locally in, the magmatic-hydrothermal porphyry Cu centers, and what was its origin? We also characterized the trace chemistry of epidote and prehnite veinlets in the GCB to test for compositional characteristics related to the porphyry systems. The results of this study have implications for exploration models (footprints), and the genesis of porphyry Cu systems.

The main conclusions are organised by components of the porphyry footprint: 1) material-transfer, 2) mineral chemistry, 3) changes in magnetic susceptibility, and 4) fluid sources. The implications for porphyry Cu genesis and exploration, and potential future lines of enquiry are also presented.

6.1 New insights into material-transfer in the porphyry footprint

- Several alteration facies and domains were determined from mapping, feldspar staining and shortwave infrared imaging: K-feldspar halos (potassic), epidote veins with K-feldspar destructive albite halos (sodic-calcic), quartz and coarse-grained muscovite veins and halos (early-halo), fine-grained white-mica–chlorite veins and halos (white-mica–chlorite), and two sub-facies of propylitic alteration comprising: 1) prehnite veinlets with white-mica–

chlorite–prehnite halos, and 2) veins of epidote ± prehnite with halos of chlorite and patchy K-feldspar, which only occurs in mafic host rocks near the batholith margins.

- K-feldspar alteration is easily detectable with staining, but generally only caused weak alkali metasomatism. A domain of this facies east of Valley is, however, characterized by intermittent quartz addition and higher than background Cu and Ag concentrations with concomitant K/Th highs, for up to 2 km away from the Valley pit.
- Sodic-calcic alteration is characterized by Na metasomatism and formation of albite ± fine-grained white-mica after primary K-feldspar. Sodic-calcic alteration forms a large (~34 km^2) asymmetrically zoned footprint around the HVC porphyry Cu centers. Rocks affected by sodic-calcic alteration have low K, high Sr/Ba, elevated H_2O concentrations, and are locally depleted in Fe, Cu, and to a lesser extent Zn, relative to fresh rocks.
- Cu-bearing early-halo and fine-grained white-mica–chlorite alteration is distinguished by well-developed, feldspar-destructive, white-mica formation (indicated by 2CNK/Al values <0.8), Ca-depletion, K-enrichment, hydration, and localized calcite and quartz addition. This alteration and material-transfer is spatially limited to within ~400 m the HVC porphyry Cu centers, to a few district Cu occurrences, and, less commonly, locally in structures up to ~ 4 km away from the Lornex porphyry center.
- Propylitic alteration did not cause sufficient material-transfer of the major rock-forming elements to be confidently distinguished from protolith compositions. The K for K-feldspar alteration in the halos of epidote ± prehnite veins is interpreted to be sourced from chlorite altered biotite and is restricted to mafic host rocks at the margins of the batholith. This facies is likely unrelated to porphyry Cu genesis.
- Water- and calcite-enriched propylitic and sodic-calcic altered rocks form the largest coherent lithogeochemical footprint to the mineralization in the HVC district (~60 km^2). The least altered rocks and background propylitic alteration have whole-rock $\delta^{13}C$ values between approximately -25 and -21 ‰ and low calcite content (< 0.15 wt. %). The porphyry centers generally contain >0.75 wt. % calcite and have $\delta^{13}C$ values > -10 ‰. Up to 6 km away from Cu mineralization, propylitic, sodic-calcic, and a few least altered rocks have $\delta^{13}C$ values between -11 and -7 ‰ that contrast with lower whole-rock $\delta^{13}C$ values in more distal locations. The calcite is interpreted to have formed via CO_2 degassing from a late-

stage magmatic volatile phase (MVP) that contained ~1.6 mol. % CO_2 in H_2O, and cross-cut sodic-calcic altered rocks peripheral to Cu mineralization.

- Feldspar staining and shortwave infrared spectral results reveal weak and cryptic alteration that did not cause sufficient material-transfer to be confidently distinguished from protolith compositions with lithogeochemical analyses. Molar element ratio diagrams are an effective way to assess mineral changes and measure material-transfer caused by alteration processes, but are dependent on correct protolith assignment. Mineral-normative schemes using loss on ignition, C and S data can be used to calculate rock H_2O and calcite content and potentially help differentiate propylitic alteration in other porphyry districts.

6.2 Mineral chemistry in the porphyry footprint

- Epidote veins from the fertile HVC porphyry district can be discriminated from epidote from other geological environments by a combination of compositional features: large positive Eu anomaly, low sum HREE concentration, moderate negative normalized REE slope, and analyses of >30 ppm As and Ge, and >10 ppm Sb. The positive Eu anomaly in epidote is attributed to the prevalence of Eu^{3+} over Eu^{2+}, which is readily substituted for Ca in the A-site of epidote, caused by the oxidizing conditions that are a prerequisite for porphyry Cu formation (Dilles et al., 2015) and consistent with the oxidized minerals in propylitic assemblages (Cooke et al., 2014a).
- In the HVC district, epidote occurring with sodic-calcic facies can be distinguished from the epidote in propylitic veins by generally lower concentrations of Sr, Pb, and As, higher Ca content, and localized enrichment in U (~20–200 ppm) and REE's.
- The highest concentrations of Bi are detected in epidote within ~1.5 km Cu-mineralization, and potassic and white-mica–chlorite alteration. Depletion in some pathfinder elements (Pb, As, and Sb) occurs in propylitic veins close to the porphyry centers. A coherent domain of epidote veins with a moderate Ge anomaly (>30 ppm) forms a halo around the porphyry centers for up to 5 km. Epidote veins with the highest Sb values (~ >20 ppm) occur within 2–4 km of the porphyry Cu centers.
- The elements Mn and Zn are on average most enriched (>6000 ppm and > 25 ppm, respectively) in epidote between 2 and 4 km of the porphyry centers, whereas Pb (~>120 ppm) forms a larger halo in epidote of up to ~ 6 km. Prehnite veinlets are enriched in Mn

(>2500 ppm), and off-set from the Mn-rich epidote, between 3 and 6 km away from the porphyry centers, and high concentrations of Pb (~>130 ppm) can be detected within a window of ~ 5.5 to 8 km distance.

- Manganese anomalies in epidote surrounding the HVC district, and several other porphyry Cu-(Mo, Au) deposits, are detectable with EMPA. The Mn concentration in epidote increase inwards through propylitic alteration to a maximum at the transition from propylitic to higher temperature assemblages, and then decrease sharply inward to Cu mineralized domains.

6.3 Changes in magnetic susceptibility in the porphyry footprint

- The density of fracture-controlled, magnetite-destructive, alteration veins and halos have a positive correlation with the corresponding outcrops magnetic susceptibility coefficient of variation (CV). These values increase in tandem until the outcrop is homogenously altered and has a low geometric mean susceptibility ($<10\times10^{-3}$ SI), at which point the CV decrease to background fresh rock levels (0-0.2).
- Modeling of outcrop magnetic susceptibility data shows that domains of outcrop with coefficient of variation of >0.3 extend 1–4 km away from the porphyry centers, whereas pronounced susceptibility lows of $<10\times10^{-3}$ SI have a smaller footprint centered on the Cu-mineralization.
- With some caveats, variability in outcrop magnetic susceptibility provides a signal that corresponds to vein and alteration intensity that can potentially be used to vector to porphyry centers, and delineate high variability magnetic signal genetically related porphyry Cu centers (e.g., Tapia et al., 2016).

6.4 Fluid sources in the porphyry footprint

- Fracture-controlled sodic-calcic alteration comprising epidote ± actinolite ± tourmaline veins with halos of K-feldspar-destructive albite (1–20 X_{An}) ± fine-grained white-mica ± epidote occurs in the HVC district. Sodic-calcic alteration is important because it forms a large asymmetric footprint (34 km^2) around the porphyry Cu centers.
- Tourmaline in sodic-calcic veins have a wide compositional range primarily caused by Fe-Al_{-1} substitution, but generally have > 2 Fe per formulae unit, higher than tourmaline in

potassic and white-mica–chlorite veins. Tourmaline $\delta^{11}B_{fluid}$ values range from 4.2 to 18.3 ‰. The highest $\delta^{11}B_{fluid}$ values are from a quartz-tourmaline-specularite cemented breccia with albite altered clast rinds at the Highmont porphyry center. The $\delta^{11}B_{fluid}$ values > ~ 10 ‰ indicate a source rich in ^{11}B, such as seawater or seawater-derived formation water in submarine volcano-sedimentary country rocks.

- Estimates of $\delta^{18}O_{fluid}$ and δD_{fluid} values of epidote and tourmaline veins from sodic-calcic domains range from 3.0 to 8.2 ‰ and -40.6 to -3.9 ‰, respectively, which contrasts with the dominantly magmatic fluid values from Cu-mineralized potassic and white-mica alteration facies. Isotopic exchange between average GCB host rock and seawater at low water–rock ratio (<0.1) can produce fluid compositions consistent with the fluids in equilibrium with most of Na-Ca facies minerals.
- The $^{87}Sr/^{86}Sr_{inital}$ values of strongly sodic-calcic altered rocks range from 0.703416 to 0.703508, higher than the values of fresh and potassically altered rocks. Modeling suggests that this shift can be caused by up to 3 % Sr from Triassic seawater.
- Ingress and heating of seawater, or seawater-derived formation fluid from Nicola Group submarine rocks, towards the HVC porphyry cupolas is interpreted to have caused sodic-calcic alteration in the GCB. Alteration occurred along sheeted fracture sets at low water–rock ratio. Metasomatic exchange of K for Na, localized removal of Fe and Cu, and a paucity of cogenetic secondary quartz is consistent with progressively heating of a saline fluid (Dilles and Einaudi, 1992; Hemley and Hunt, 1992; Monecke et al., 2018). Due to the lower ionic potential of K relative to Fe and Cu (Railsback, 2003), alteration occurring at low water–rock ratio might preferentially remove the more mobile ion.
- Outflow of MVP from the porphyry Cu centers coupled with CO_2-degassing generated calcite veinlets, localized calcite-bearing propylitic and white-mica–chlorite alteration, and ^{13}C-enriched rocks peripheral to Cu mineralization. Propylitic alteration predominantly overprinted sodic-calcic rocks in the HVC district. The sodic-calcic altered rocks received a late MVP flux that is recorded as a series of cross-cutting calcite veinlets that is related to porphyry Cu genesis.
- The pathfinder metals and metalloids in epidote are interpreted to be primarily sourced from outflowing H_2S-depleted, thermally retrograding, MVP emanating from the porphyry Cu centers or from the fringes of the subjacent cupola (i.e., Cooke et al., 2014). Upward and

outflowing fluids favored permeable structural corridors and did not occur concentrically around the porphyry Cu centers.

- High intra-sample $\delta^{11}B$ variation (>3 ‰) exhibited by the tourmaline in the locally Cu mineralized Highmont breccia indicate that magmatic and seawater-derived fluids were locally mixing in the porphyry centers.
- The range $\delta^{18}O_{fluid}$ and δD_{fluid} values of sodic-calcic and propylitic minerals, and the D-enrichment of some Cu-mineralized white-mica–chlorite facies minerals, implies seawater-derived fluid and MVP (or an admixture of both) were present in the porphyry footprint. Similarly, the high concentration of As and Sb in some sodic-calcic epidote suggests that a MVP and seawater-derived fluid were mixing, or present in fractures at different times.

6.5 Implications for exploration for porphyry systems

Several key factors determine the nature of alteration peripheral to porphyry Cu centers. Prevailing models for propylitic alteration invoke the heating of meteoric fluids surrounding potassic alteration and Cu mineralization (Bowman et al., 1987; Norman et al., 1991; Sillitoe, 2010). The trace-element composition of chlorite and epidote and fluid-rock interaction models, however, indicate that a cooling MVP will also generate propylitic alteration (Reed et al., 2013; Cooke et al., 2014a; Wilkinson et al., 2015). Furthermore, isotope and fluid inclusion studies have shown that saline formation water (Dilles et al., 1992) and seawater or seawater-derived (Chivas et al., 1984;(Jones, 1974) Orovan et al., 2018; Chapter 3) fluids can be entrained into a porphyry system. Consequently, the characteristics of the alteration peripheral to porphyry Cu centers will depend on the relative contributions from 1) the MVP flux and 2) an external fluid. The salinity, and thermal evolution of the external fluid will control alteration products and metasomatism. Inflow and heating of a saline fluid will cause K, Fe, and Cu removal, and Na ± Ca addition over a range of water-rock ratio (Dilles et al., 1995; Chapters 2 and 3). Whereas heating of ambient or circulating meteoric water (variably evolved) in wall rocks causes hydration but is dominantly isochemical at the low water-rock ratio conditions outside of the magmatic-hydrothermal centers (Reed, 1997; Urqueta et al., 2009). The cooling and outflow of spent MVP can produce locally intense non-isochemical propylitic alteration via the redistribution of certain elements (Ca, Sr, Fe, Co, As, Sb) depleted from the porphyry core (Pacey et al., 2016; Ahmed et al., 2019). To summarize, variations in 1) the relative proportions of the disparate fluids and their salinity, 2) their flow-paths and thermal evolution, 3) timing of incursion into the porphyry system, 4) water-rock ratio, and 5) the host-rock bulk composition are identified as the key factors affecting the footprints of porphyry Cu systems. Furthermore, exposure level (e.g., Halley et al., 2015) and paleo-geography should be considered in the exploration for porphyry Cu systems.

Seawater-derived fluids can infiltrate batholiths and porphyry systems at deep levels (4–5 km) in the crust. Based on the geological setting of the HVC systems, subtle metasomatic albite alteration caused by seawater-derived fluids may be more common in porphyry districts hosted in low-lying coastal and island-arcs than is currently recognized.

The minerals commonly occurring in propylitic alteration can form from a variety of processes unrelated to magmatic-hydrothermal systems, i.e., lower greenschist-facies (Hacker et al., 1992) and barren geothermal systems (Bird et al., 1984). Whole-rock C isotope compositions can be used to discriminate prospective alteration peripheral to porphyry Cu centers related to late-stage CO_2 degassing from a MVP, as demonstrated in this study and in the Collahuasi district (Djouka-Fonkwe et al., 2012). Similarly, distinct compositional features can be used to discriminate the epidote formed within the porphyry footprint from the epidote occurring with barren propylitic alteration.

The Mn halos in epidote and prehnite veinlets, detected with EMPA, can be used to vector to porphyry Cu centers, and could be a useful precursor data before trace geochemical analysis.

Collectively these results demonstrate methodologies and approaches that will be useful in elucidating hydrothermal footprints in porphyry Cu systems globally. The tools and models presented are ideal for the exploration of partially exposed or buried porphyry targets in which the maximum information, and value, should be extracted from available bedrock samples.

6.6 Future work

This study demonstrates how whole-rock C isotope analysis can be used to detect carbonate formed from MVP. Continuous-Flow Isotope Ratio Mass Spectrometry (CF-IRMS) is an accurate and precise technique that is required to measure the C isotope composition of rocks with low total C (0.1 wt. %), but data collection is slow and relatively expensive (~$60 per sample). As detection limits improve, infrared absorption laser spectroscopy (Barker et al., 2013) could potentially be applied to rapidly and cost-effectively measure the C isotope composition of carbonate in rock pulps to discriminate propylitic alteration around porphyry Cu centers.

Pairing the SIMs B isotope data with in situ O isotope analysis would provide additional insights to the fluids attending tourmaline formation– do these disparate isotope systems record the same processes and support the same conclusions?

In-situ O isotope analysis of epidote from propylitic and sodic-calcic veins from various locations around the HVC porphyry systems could help resolve the relative contributions of magmatic and non-magmatic fluids, and their potential mixing, to the “green rocks” surrounding the Cu centers.

A study of the S isotope composition of sulfate minerals in the porphyry centers at HVC would complement available sulfide mineral S isotope data, and test whether seawater SO_4 was the S source for the late-stage anhydrite and gypsum veins in the porphyry centers (McMillan, 1985a). The latter would have implications for the role of seawater-sourced fluids during the low temperature late-stages of the magmatic-hydrothermal system.

This study demonstrated moderate degrees of intra-sample variability (~ 20 % relative error) in the concentrations of some pathfinder element, particularly Sb, in epidote. Hot cathodoluminescent mapping could help reveal stages of epidote growth related to different events, if present. The crystallographic controls (i.e. sector zoning) on trace element deportment in epidote and prehnite are not well understood. Element mapping by synchrotron X-ray fluorescence spectroscopy, or laser ablation inductively coupled plasma mass spectrometry would be helpful in understanding the processes controlling fine-scale variation in epidote composition.

Bibliography

Ager, C.A., McMillan, W.J., and Ulrych, T.J., 1972, Gravity magnetics and geology of the Guichon Creek batholith: British Columbia Department of Mines and Petroleum Resources, Bulletin 62, 31 p.

Ager, C.A., Ulrych, T.J., and McMillan, W.J., 1973, A gravity model for the Guichon Creek batholith, south-central British Columbia: Canadian Journal of Earth Sciences, v. 10, p. 920–935, doi: 10.1139/e73-081.

Ahmed, A.D., Hood, S.B., Gazley, M.F., Cooke, D.R., and Orovan, E.A., 2019, Interpreting element addition and depletion at the Ann Mason porphyry-Cu deposit, Nevada, using mapped mass balance patterns: Journal of Geochemical Exploration, v. 196, p. 81–94, doi: 10.1016/j.gexplo.2018.09.009.

Ali, S.H., Giurco, D., Arndt, N., Nickless, E., Brown, G., Demetriades, A., Durrheim, R., Enriquez, M.A., Kinnaird, J., Littleboy, A., Meinert, L.D., Oberhänsli, R., Salem, J., Schodde, R., et al., 2017, Mineral supply for sustainable development requires resource governance: Nature, v. 543, no. 7645, p. 367–372, doi: 10.1038/nature21359.

Alva-Jimenez, T., 2011, Variation in hydrothermal muscovite and chlorite composition in the Highland Valley Porphyry Cu-Mo District, British Columbia, Canada: M.Sc. Thesis, University of British Columbia, 249 p.

Arancibia, O.N., and Clark, A.H., 1996, Early magnetite-amphibole-plagioclase alteration-mineralization in the Island Copper porphyry copper-gold- molybdenum deposit, British Columbia: Economic Geology, v. 91, p. 402–438.

Armbruster, T., Bonazzi, P., Akasaka, M., Bermanec, V., Chopin, C., Gieré, R., Heuss-Assbichler, S., Liebscher, A., Menchetti, S., Pan, Y., and Pasero, M., 2006, Recommended nomenclature of epidote-group minerals: European Journal of Mineralogy, v. 18, no. 5, p. 551–567, doi: 10.1127/0935-1221/2006/0018-0551.

Arnsason, J.G., Bird, D.K., and Liou, J.G., 1993, Variables controlling epidote composition in hydrothermal and low-pressure regional metamorphic rocks, *in* Hock, V. and Koller, F. eds., 125 years Knappenwand, Proceedings of a symposium held in Salzburg, Austria, Abhandlungen der Geologischen Bundesanstalt, p. 17–25.

Austin, J.R., and Foss, C.A., 2014, The Paradox of Scale: Reconciling magnetic anomalies with rock magnetic properties for cost-effective mineral exploration: Journal of Applied Geophysics, v. 104, p. 121–133, doi: 10.1016/j.jappgeo.2014.02.018.

Ballantyne, G.H., 1981, Chemical and mineralogical variations in propylitic zones surrounding porphyry copper deposits: Ph.D. thesis, Salt Lake City, University of Utah, 208 p.

Barker, S., Dipple, G., Hickey, K., Lepore, W., and Vaughan, J., 2013, Applying stable isotopes to mineral exploration: teaching an old dog new tricks: Economic Geology, v. 108, no. 1, p. 1–9.

Barth, S., 1993, Boron isotope variations in nature: a synthesis: Geologische Rundschau, v. 82, no. 4, p. 640–651, doi: 10.1007/BF00191491.

Barton, M.D., 2014, Iron Oxide (–Cu–Au–REE–P–Ag–U–Co) Systems, *in* Turekian, K. and Holland, H.D. eds., Treatise on Geochemistry: Second Edition, Elsevier, Oxford, p. 515–541.

Barton, M.D., Johnson, D.A., and Zurcher, L., 2000, Phanerozoic iron oxide(-REE-Cu-Au-U) systems in southwestern North America and their origins, *in* Fe oxide-Cu-Au deposits; a discussion of critical issues and current developments, James Cook University, p. 5–11.

Battles, D.A., and Barton, M.D., 1995, Arc-related sodic hydrothermal alteration in the western US: Geology, v. 23, no. 10, p. 913–916, doi: 10.1130/0091-7613(1995)023<0913:ARSHAI>2.3.CO;2.

Beane, R.E., 1982, Hydrothermal alteration in silicate rocks, *in* Titley, S.R. ed., Advances in Geology of the Porphyry Copper Deposits, Southwestern North America, University of Airzona, Tuscon.

Behn, G., Camus, F., Carrasco, P., and Ware, H., 2001, Aeromagnetic signature of porphyry copper systems in northern Chile and its geologic implications: Economic Geology, v. 96, no. 2, p. 239–248, doi: 10.2113/gsecongeo.96.2.239.

Bergbauer, S., and Martel, S.J., 1999, Formation of joints in cooling plutons: Journal of Structural Geology, v. 21, no. 7, p. 821–835, doi: 10.1016/S0191-8141(99)00082-6.

Berger, G., and Velde, B., 1992, Chemical parameters controlling the propylitic and argillic alteration process: European Journal of Mineralogy, v. 4, no. 6, p. 1439–1454.

Bergey, W.R., Carr, J.M., and Reed, A.J., 1971, Highmont Copper-Molybdenum Deposits, Highland Valley, British Columbia, *in* Canadian Institute of Mining and Metallurgy, Bulletin 64, p. 68–76.

Bernstein, L.R., 1985, Germanium geochemistry and mineralogy: Geochimica et Cosmochimica Acta, v. 49, no. 11, p. 2409–2422, doi: 10.1016/0016-7037(85)90241-8.

Bird, D.K., and Helgeson, H.C., 1981, Chemical interaction of aqueous solutions with epiodte-feldspar mineral assemblages in geological systems. II, Equilibrium constrants in metamoprhic/geothermal processes: American Journal of Science, v. 281, p. 576–614.

Bird, D.K., Schiffman, P., Elders, W.A., Williams, A.E., and McDowell, S.D., 1984, Calc-silicate mineralization in active geothermal systems: Economic Geology, v. 79, no. 4, p. 671–695, doi: 10.2113/gsecongeo.79.4.671.

Bird, D.., and Spieler, A.., 2004, Epidote in Geothermal Systems, *in* Reviews in Mineralogy & Geochemistry 56, p. 235–300.

Bowman, J.R., Parry, W.T., Kropp, W.P., and Kruer, S. a., 1987, Chemical and isotopic evolution of hydrothermal solutions at Bingham, Utah: Economic Geology, v. 82, no. 2, p. 395–428, doi: 10.2113/gsecongeo.82.2.395.

Briskey, J.A., 1980, Geology, Petrology, and Geochemistry of the Jersey, East Jersey, Huestis, and Iona Porphyry Copper-Molybdenum Deposits, Highland Valley, Britsh Columbia: University of British Columbia, 427 p.

Briskey, J.A., and Bellamy, J.R., 1976, Bethlehem Coppers's Jersey, East Jersey, Huestis and Iona Deposits, *in* Sutherland Brown, A. ed., Porphyry Deposits of the Canadian Cordillera, Canadian Institute of Mining and Metallurgy, Special Volume 15, p. 105–119.

Byrne, K., Lesage, G., Gleeson, S.A., and Lee, R.G., 2017, Large-Scale Sodic-Calcic Alteration Around Porphyry Copper Systems: Examples from the Highland Valley Copper District, Guichon Batholith, South-Central British Columbia: Geoscience BC Summary of Activities 2016, p. 213–222.

Byrne, K., Stock, E., Ryan, J., Johnson, C., Nisenson, J., Alva-Jimenez, T., Lapointe, M., Stewart, H., Grubisa, G., and Sykora, S., 2013, Porphyry Cu-(Mo) deposits in the Highland Valley District, South Central British Columbia, *in* Logan, J.M. and Schroeter, T. eds., Society of Economic Geologists, Guidebook Series, v. 44, Society of Economic Geologists, p. 99–116.

Carten, R.B., 1986, Sodium-calcium metasomatism: chemical, temporal, and spatial relationships at the Yerington, Nevada porphyry copper deposit.: Economic Geology, v. 81, no. 6, p. 1495–1519, doi: 10.2113/gsecongeo.81.6.1495.

Casselman, M.J., McMillan, W.J., and Newman, K.M., 1995, Highland Valley porphyry copper deposits near Kamloops, British Columbia: A review and update with emphasis on the Valley deposit, *in* Schroeter, T.G. ed., Porphyry deposits of the Northwestern Cordillera of North America, Special Volume 46, Canadian Institute of Mining and Metallurgy, p. 161–191.

Catanzaro, E.J., Champion, C.E., Garner, E.L., Maienko, G., Sappenfield, K.M., and Shields, W.R., 1970, Boric acid: Isotopic and assay standard reference materials: National Bureau of Standards (US) Special Publication 260-17, 70 p.

Catchpole, H., Kouzmanov, K., Putlitz, B., Seo, J.H., and Fontboté, L., 2015, Zoned Base Metal Mineralization in a Porphyry System: Origin and Evolution of Mineralizing Fluids in the Morococha District, Peru: Economic Geology, v. 110, no. 1, p. 39–71, doi: 10.2113/econgeo.110.1.39.

Cathles, L.M., 1977, Analysis of the cooling of intrusives by groundwater convection which includes boling: Economic Geology, v. 72, no. 5, p. 804–826.

Chapman, J., Plouffe, A., and Ferbey, T., 2015, Tourmaline Chemistry as a Tool for Porphyry Exploration: The Woodjam Cu-Au Deposits, Central British Columbia: Round-up 2015, Poster, p. 1.

Chaussidon, M., and Albarède, F., 1992, Secular boron isotope variations in the continental crust: an ion microprobe study: Earth and Planetary Science Letters, v. 108, no. 4, p. 229–241, doi: 10.1016/0012-821X(92)90025-Q.

Chester, R., 2000, Marine Geochemistry: Blackwell Publishers, London.

Chivas, A.R., O'Neil, J.R., and Katchan, G., 1984, Uplift and submarine formation of some Melanesian porphyry copper deposits: Stable isotope evidence: Earth and Planetary Science Letters, v. 68, p. 326–334.

Clark, D.A., 2014, Magnetic effects of hydrothermal alteration in porphyry copper and iron-oxide copper-gold systems: A review: Tectonophysics, v. 624–625, p. 46–65, doi: 10.1016/j.tecto.2013.12.011.

Clark, D.A., 1999, Magnetic petrology of igneous intrusions: implications for exploration and magnetic interpretation: Exploration Geophysics, v. 30, no. 2, p. 5–26, doi: 10.1071/EG999005.

Clark, D.A., and Emerson, D.W., 1991, Notes on rock magnetization characteristics in applied geophysical studies: Exploration Geophysics, v. 22, no. 3, p. 547–555.

Clark, D.A., French, D.H., Lackie, M.A., and Schmidt, P.W., 1992, Magnetic petrology: application of integrated rock magnetic and petrological techniques to geological interpretation of magnetic surveys: Exploration Geophysics, v. 23, no. 2, p. 65, doi: 10.1071/EG992065.

Collins, A.C., 2010, Mineralogy and geochemistry of tourmaline in contrasting hydrothermal systems: Copiapo area, northern Chile: M.Sc. Thesis, The University of Arizona, 225 p.

Colpron, M., Nelson, J.A.L., and Murphy, D.C., 2007, Northern Cordilleran terranes and their interactions through time: GSA Today, v. 17, no. 4, p. 4–10, doi: 10.1130/GSAT01704-5A.1.

Coney, P.J., Jones, D.L., and Monger, J.W.H., 1980, Cordilleran suspect terranes: Nature, v. 288, p. 329–333.

Cooke, D.R., Baker, M., Hollings, P., Sweet, G., Zhaoshan, C., Danyushevsky, L., Gilbert, S., Zhou, T., White, N.C., Gemmell, J.B., and Inglis, S., 2014a, New Advances in Detecting the Distal Geochemical Footprints of Porphyry Systems: Epidote Mineral Chemistry as a Tool for Vectoring and Fertility Assessments: Building Exploration Capability for the 21st Century, Society of Economic Geologist, Special Publication Series, v. 18, p. 127–152.

Cooke, D.R., Hollings, P., Wilkinson, J.J., and Tosdal, R.M., 2014b, Geochemistry of Porphyry Deposits, *in* Holland, H.D. and Turekian, K.K. eds., Treatise on Geochemistry: Second Edition, Elsevier Ltd., p. 357–381.

Corriveau, L., Williams, P.J., and Mumin, A.H., 2010, Alteration Vectors to IOCG Mineralization from Uncharted Terranes to Deposits, *in* Corriveau, L. and Mumin, A.H. eds., Exploring for Iron Oxide Copper-Gold Deposits: Canada and Global Analogues: Geological Association of Canada, Short Course Notes, No. 20, Geological Association of Canada, p. 89–110.

D'Angelo, M., 2016, Geochemistry, petrography and mineral chemistry of the Guichon Creek and Nicola batholiths, southcentral British Columbia Michael: M.Sc. Thesis, Lakehead University, 435 p.

D'Angelo, M., Alfaro, M., Hollings, P., Byrne, K., Piercey, S., and Creaser, R.A., 2017, Petrogenesis and magmatic evolution the Guichon Creek Batholith: Implications for the Highland Valley porphyry Cu ± (Mo) district, southcentral British Columbia: Economic Geology, v. 112, p. 1857–1888, doi: 10.5382/econgeo.2017.4532.

Davies, J.F., and Whitehead, R.E., 2006, Alkali-alumina and MgO-alumina molar ratios of altered and unaltered rhyolites: Exploration and Mining Geology, v. 15, no. 1–2, p. 75–88, doi: 10.2113/gsemg.15.1-2.75.

Deer, W.A., Howie, R.A., and Zussman, J., 2009, Layered Silicates Excluding Micas and Clay Minerals (Volume 3B): The Geological Society of London.

Deng, D.N., 2015, A comparative study of hand-held magnetic susceptibility instruments: M.Sc. Thesis, Laurentian University, 207 p.

Digel, S.G., and Gordon, T.M., 1995, Phase relations in metabasites and pressure-temperature conditions at the prehnite-pumpellyite to greenschist fades transition, Flin Flon, Manitoba Canada: Geological Society of America Special Paper 296, p. 67–80.

Dilles, J.H., and Einaudi, M.T., 1992, Wall-Rock Alteration and Hydrothermal Flow Paths about the Ann-Mason Porphyry Copper Deposit, Nevada-A 6-Km Vertical Reconstruction: Economic Geology, v. 87, p. 1963–2001.

Dilles, J.H., Einaudi, M.T., Proffett, J.M., and Barton, M.D., 2000, Overview of the Yerington porphyry copper district: magmatic to nonmagmatic sources of hydrothermal fluids, their flowpaths, alteration affects on rocks, and Cu-Mo-Fe-Au ores: Society of Economic Geologist, Post-meeting Field Conference, v. 32, p. 55–66.

Dilles, J.H., Farmer, G.L., and Field, C.W., 1995, Sodium-calcium alteration by non-magmatic saline fluids in porphyry copper deposits: Results from Yerington, Nevada, *in* Thompson, J.F.H. ed., Magmas, fluids, and ore deposits: Mineralogical Association of Canada Short Course, v. 23, Mineralogical Association of Canada, p. 309–338.

Dilles, J.H., Kent, A.J.R., Wooden, J.L., Tosdal, R.M., Koleszar, A., Lee, R.G., and Farmer, L.P., 2015, Zircon compositional evidence for sulfur degassing from ore-forming arc magmas: Economic Geology, v. 110, p. 241–251, doi: 10.2113/econgeo.110.1.241.

Dilles, J.H., Solomon, G.C., Taylor, H.P., and Einaudi, M.T., 1992, Oxygen and hydrogen isotope characteristics of hydrothermal alteration at the Ann-Mason porphyry copper deposit, Yerington, Nevada: Economic Geology, v. 87, no. 1, p. 44–63, doi: 10.2113/gsecongeo.87.1.44.

Djouka-Fonkwe, M.L., Kyser, K., Clark, A.H., Urqueta, E., Oates, C.J., and Ihlenfeld, C., 2012, Recognizing propylitic alteration associated with porphyry Cu-Mo deposits in lower greenschist facies metamorphic terrain of the Collahuasi district, northern Chile-implications of petrographic and carbon isotope relationships: Economic Geology, v. 107, no. 7, p. 1457–1478, doi: 10.2113/econgeo.107.7.1457.

Elshkaki, A., and Graedel, T.E., 2013, Dynamic analysis of the global metals flows and stocks in electricity generation technologies: Journal of Cleaner Production, v. 59, p. 260–273, doi: https://doi.org/10.1016/j.jclepro.2013.07.003.

Elshkaki, A., Graedel, T.E., Ciacci, L., and Reck, B., 2016, Copper demand, supply, and associated energy use to 2050: Global Environmental Change, v. 39, p. 305–315, doi: 10.1016/j.gloenvcha.2016.06.006.

Erdmer, P., Moore, J.M., Heaman, L., Thompson, R.I., Daughtry, K.L., and Creaser, R. a, 2002, Extending the ancient margin outboard in the Canadian Cordillera: record of Proterozoic crust and Paleocene regional metamorphism in the Nicola horst, southern British Columbia: Canadian Journal of Earth Sciences, v. 39, no. 11, p. 1605–1623, doi: 10.1139/e02-072.

ESRI, 2017, 3D Analysts toolbox: How IDW works: Arc Map 10.3, p. 1.

Faure, G., and Mensing, T.M., 2005, Isotopes principles and applications: Wiley & Sons Inc., New Jersey.

Fellows, M., 1976, Composition of epidote from porphyry copper deposits: M.Sc. Thesis, The University of Arizona, 205 p.

Franz, G., and Liebscher, A., 2004, Physical and Chemical Properties of the Epidote Minerals. An Introduction: Reviews in Mineralogy and Geochemistry, v. 56, p. 1–81, doi: 10.2138/gsrmg.56.1.1.

Frei, D., Liebscher, A., Franz, G., and Dulski, P., 2004, Trace Element Geochemistry of Epidote Minerals: Reviews in Mineralogy and Geochemistry, v. 56, p. 553–605, doi: 10.2138/gsrmg.56.1.553.

Garwin, S., 2002, The geologic setting of intrusion-related hydrothermal systems near the Batu Hijau porphyry copper-gold deposit, Sumbawa, Indonesia: Society of Economic Geologists Special Publication 9, p. 333–366.

Gettings, M.E., and Bultman, M.W., 2014, Magnetic susceptibility data for some exposed bedrock in the western conterminous United States: Data Series 804, U.S. Geological Survey, p. 5.

Giggenbach, W.F., 1992, Magma degassing and mineral deposition in hydrothermal systems along convergent plate boundaries: Economic Geology, v. 87, p. 1927–1944.

Grant, J.A., 2005, Isocon analysis: A brief review of the method and applications: Physics and Chemistry of the Earth, v. 30, no. 17–18 SPEC. ISS., p. 997–1004, doi: 10.1016/j.pce.2004.11.003.

Grant, J.A., 1986, The isocon diagram a simple solution to Gresens' equation for metasomatic alteration: Economic Geology, v. 81, no. 8, p. 1976–1982, doi: 10.2113/gsecongeo.81.8.1976.

Greenlaw, L., 2014, Surface lithogeochemistry of the Relincho porphyry Copper-Molybdenum deposit , Atacama Region, Chile: M.Sc. Thesis, University of British Columbia, 135 p.

Hacker, B.R., Ernst, W.G., and Barton, M.D., 1992, Metamorphism, Geochemistry and Origin of Magnesian Volcanic- Rocks, Klamath Mountains, California: Journal of Metamorphic Geology, v. 10, p. 55–69, doi: 10.1111/j.1525-1314.1992.tb00071.x.

Halley, S.W., Dilles, J.H., and Tosdal, R.M., 2015, Footprints: Hydrothermal Alteration and Geochemical Dispersion Around Porphyry Copper Deposits: SEG Newsletter, No. 100, p. 12–17.

Harris, A.C., Golding, S.D., and White, N.C., 2005, Bajo de la Alumbrera Copper-Gold Deposit: Stable Isotope Evidence for a Porphyry-Related Hydrothermal System Dominated by Magmatic Aqueous Fluids: Economic Geology, v. 100, no. 5, p. 863–886, doi: 10.2113/gsecongeo.100.5.863.

Hawthorne, F.C., Oberti, R., Harlow, G.E., Maresch, W.V., Martin, R.F., Schumacher, J.C., and Welch, M.D., 2012, Nomenclature of the amphibole supergroup: American Mineralogist, v. 97, p. 2031–2048.

Hedenquist, J.W., Simmons, S.F., Giggenbach, W.F., and Eldridge, C.S., 1993, White Island, New Zealand, volcanic-hydrothermal system represents the geochemical environment of high-sulfidation Cu and Au ore deposition: Geology, v. 21, no. 8; 8, p. 731–734, doi: 10.1130/0091-7613(1993)021<0731:WINZVH>2.3.CO;2.

Heier, K.S., 1962, Trace elements in feldspars - A review: Norks Geologisk Tidsskrift, v. 42, p. 415–454.

Hemley, J.J., and Hunt, J.P., 1992, Hydrothermal ore-forming processes in the light of studies in rock-buffered systems; II, Some general geologic applications: Economic Geology, v. 87, no. 1, p. 23–43, doi: 10.2113/gsecongeo.87.1.23.

Henley, R.W., and McNabb, A., 1978, Magmatic vapor plumes and ground-water interaction in porphyry copper emplacement: Economic Geology, v. 73, no. 1, p. 1–20, doi: 10.2113/gsecongeo.73.1.1.

Henry, D.J., Novák, M., Hawthorne, F.C., Ertl, A., Dutrow, B.L., Uher, P., and Pezzotta, F., 2011, Nomenclature of the tourmaline-supergroup minerals: American Mineralogist, v. 96, no. 5–6, p. 895–913, doi: 10.2138/am.2011.3636.

Hervig, R.L., Moore, G.M., Williams, L.B., Peacock, S.M., Holloway, J.R., and Roggensack, K., 2002, Isotopic and elemental partitioning of boron between hydrous fluid and silicate melt: American Mineralogist, v. 87, no. 5–6, p. 769–774, doi: 10.2138/am-2002-5-620.

Holden, E.J., Fu, S.C., Kovesi, P., Dentith, M., Bourne, B., and Hope, M., 2011, Automatic identification of responses from porphyry intrusive systems within magnetic data using image analysis: Journal of Applied Geophysics, v. 74, no. 4, p. 255–262, doi: 10.1016/j.jappgeo.2011.06.016.

Holliday, J.R., and Cooke, D.R., 2007, Advances in Geological Models and Exploration Methods for Copper ± Gold Porphyry Deposits, *in* Proceedings of Exploration 07: Fifth Decennial International Conference on Mineral Exploration, p. 791–809.

Hollister, V.F., Allen, J.M., Anzalone, S.A., and Seraphim, R.H., 1975, Structural evolution of porphyry mineralization at Highland Valley, British Columbia: Canadian Journal of Earth Sciences, v. 12, p. 807–820.

Hoover, D.B., Klein, D.P., and Campbell, D.C., 1994, Geophysical methods in exploration and mineral environmental investigations: Field Geophysics, v. 53, no. 9, p. 1689–1699, doi: 10.1017/CBO9781107415324.004.

Hövelmann, J., Putnis, A., Geisler, T., Schmidt, B.C., and Golla-Schindler, U., 2010, The replacement of plagioclase feldspars by albite: Observations from hydrothermal experiments: Contributions to Mineralogy and Petrology, v. 159, no. 1, p. 43–59, doi: 10.1007/s00410-009-0415-4.

Hrouda, F., Chulapacova, M., and Chadima, M., 2009, Terraplus: The use of magnetic susceptibility of rocks in geological exploration: Terraplus, Geophysical Equipment Supplier, 25 p.

Hunt, J.A., Baker, T., and Thorkelson, D.J., 2007, A eeview of Iron Oxide Copper-Gold deposits, with focus on the Wernecke Breccias, Yukon, Canada, as an example of a non-magmatic end member and implications for IOCG genesis and classification: Exploration and Mining Geology, v. 16, no. 3–4, p. 209–232, doi: 10.2113/gsemg.16.3-4.209.

Jago, C.P., 2008, Metal-and alteration-zoning, and hydrothermal flow paths at the moderately-tilted, silica-saturated Mt. Milligan Cu-Au alkalic porphyry deposit: M.Sc. Thesis, University of British Columbia, 227 p.

Jago, C., Tosdal, R., Cooke, D., and Harris, A., 2014, Vertical and lateral variation of mineralogy and chemistry in the Early Jurassic Mt. Milligan alkalic porphyry Au-Cu deposit, British Columbia, Canada: Economic Geology, v. 109, p. 1005–1033, doi: 10.2113/econgeo.109.4.1005.

Jambor, J.L., and Delabio, R.N., 1978, Distribution of hydrothermal clay minerals in the Valley copper porphyry deposit, Highland Valley, British Columbia: The Geological Survey of Canada, paper 77-9.

Jennings, K., and Schodde, R., 2016, From mineral discovery to production: Society of Economic Geologist, Newsletter, No. 105, p. 20–24.

Jochum, K.P., Nohl, U., Herwig, K., Lammel, E., Stoll, B., and Hofmann, A.W., 2007, GeoReM: A new geochemical database for reference materials and isotopic standards: Geostandards and Geoanalytical Research, v. 29, no. 3, p. 333–338, doi: 10.1111/j.1751-908X.2005.tb00904.x.

Jones, M.B., 1974, Hydrothermal Alteration and Mineralization of the Valley Copper Deposit, Highland Valley, British Columbia: PhD. Thesis, Oregon State University, 280 p.

Kirkwood, T.B.L., 1979, Geometric means and measures of dispersion: Biometrics, v. 35, no. 4, p. 908–909.

Kobylinski, C., Hattori, K., Smith, S., and Plouffe, A., 2016, Mineral chemistry of greenrock alteration associated with the porphyry Cu-Mo mineralization at the Gibraltar deposit, south central British Columbia, Canada., *in* Joint Meeting of Geological Association of Canada, Mineralogical Association of Canada (GAC-MAC), Whitehorse, Yukon, p. 2.

Kowalski, P.M., and Wunder, B., 2018, Boron isotope fractionation among vapor–liquids–solids–melts: Experiments and atomistic modeling, *in* Marschall, H.R. and Foster, G. eds., Boron Isotopes. Advances in Isotope Geochemistry, p. 33–69.

Krivoruchko, K., 2012, Empirical Bayesian Kriging: ArcUser 15, ESRI Press, v. Fall 2012, p. 6–10.

Kusebauch, C., Oelze, M., and Gleeson, S.A., 2018, Partitioning of arsenic between hydrothermal fluid and pyrite during experimental siderite replacement: Chemical Geology, v. 500, p. 136–147, doi: https://doi.org/10.1016/j.chemgeo.2018.09.027.

Kyser, K., 2013, Uranium Ore Deposits, *in* Holland, H.D. and Turekian, K.K. eds., Treatise on Geochemistry: Second Edition, Elsevier Ltd., p. 489–513.

Lang, J., Stanley, C., Thompson, J.F.H., and Dunne, K., 1995, Na-K-Ca magmatic-hydrothermal alteration in alkalic porphyry Cu-Au deposits, British Columbia, *in* Thompson, J.F.H. ed., Magmas, Fluids and Ore Deposits, Mineralogical Association of Canada, p. 339–366.

Lapointe, P., Chomyn, B.A., Morris, W.A., and Coles, R.L., 1984, Significance of magnetic susceptibility measurements from the Lac Du Bonnet Batholith, Manitoba, Canada: Geoexploration, v. 22, no. 3–4, p. 217–229, doi: 10.1016/0016-7142(84)90013-9.

Lapointe, P., Morris, W.A., and Harding, K.L., 1986, Interpretation of magnetic susceptibility: a new approach to geophysical evaluation of the degree of rock alteration: Canadian Journal of Earth Science, v. 23, p. 393–401.

Latham, A.G., Harding, K.L., Lapointe, P., Morris, W.A., and Balch, S.J., 1989, On the lognormal distribution of oxides in igneous rocks, using magnetic susceptibility as a proxy for oxide mineral concentration: Geophysical Journal International, v. 96, no. 1, p. 179–184, doi: 10.1111/j.1365-246X.1989.tb05259.x.

Leake, B.E., Woolley, A.R., Arps, C.E.S., Birch, W.D., Gilbert, M.C., Grice, J.D., Hawthorne, F.C., K., Ato, A., Kisch, H.J., Krivovichev, V.G., Linthout, K., Laird, J.J., Mandarino, Maresch, W.V., et al., 1997, Nomenclature of amphiboles: Report of the subcommittee on amphiboles of the International Mineralogical Association commission on new minerals and mineral names: Mineralogical Magazine, v. 61, p. 295–321.

Lee, R.G., Byrne, K., Angelo, M.D., Hart, C.J.R., Hollings, P., Gleeson, S.A., and Alfaro, M. *In Review*, Assessing the fertility of the Guichon Creek batholith, south-central B.C., through chemical composition of zircon: Economic Geology, p. 54.

Lee, M.D., and Morris, W.A., 2013, Comparison of magnetic-susceptibility meters using rock samples from the Wopmay Orogen, Northwest Territories, Canada: Geological Survey of Canada, Technical Note 5, p. 7.

Lesage, G., Byrne, K., Lypaczewski, P., Lee, R.G., and Hart, C.J.R., 2016, Characterizing the district-scale alteration surrounding a large porphyry Cu system: The footprint of Highland Valley Copper, British Columbia, *in* GAC-MAC Abstracts, June 1-3, 2016, v. 39, Whitehorse, Yukon, p. 52.

Lesage, G., Byrne, K., Morris, W.A., Enkin, R.J., Lee, R.G., Mir, R., and Hart, C.J.R., 2019, Interpreting regional 3D fault networks from integrated geological and geophysical data sets: An example from the Guichon Creek batholith, British Columbia: Journal of Structural Geology, v. 119, p. 93–106, doi: https://doi.org/10.1016/j.jsg.2018.12.007.

Lesher, M., Hannington, M., Galley, A., Ansdell, K., Astic, T., Banerjee, N., Beauchamp, S., Beaudoin, G., Bertelli, M., Bérubé, C., Beyer, S., Blacklock, N., Byrne, K., Cheng, L.Z., et al., 2017, Integrated Multi-Parameter Exploration Footprints of the Canadian Malartic Disseminated Au, McArthur River-Millennium Unconformity U, and Highland Valley Porphyry Cu Deposits:

Preliminary Results from the NSERC-CMIC Mineral Exploration Footprints Resea, *in* Tschirhart, V. and Thomas, M.D. eds., Proceedings of Exploration 17: Sixth Decennial International Conference on Mineral Exploration, p. 325–347.

Liebscher, A., Meixner, A., Romer, R.L., and Heinrich, W., 2005, Liquid-vapor fractionation of boron and boron isotopes: Experimental calibration at 400°C/23 MPa to 450°C/42 MPa: Geochimica et Cosmochimica Acta, v. 69, no. 24, p. 5693–5704, doi: 10.1016/j.gca.2005.07.019.

Liou, J.G., 1971, Synthesis and Stability Relations of Prehnite, Ca2Al2Si3O10(OH)2: The American Mineralogist, v. 56, p. 507–531.

Locock, A.J., 2014, An Excel spreadsheet to classify chemical analyses of amphiboles following the IMA 2012 recommendations: Computers and Geosciences, v. 62, p. 1–11, doi: 10.1016/j.cageo.2013.09.011.

Logan, J.M., and Mihalynuk, M.G., 2014, Tectonic controls on early Mesozoic paired alkaline porphyry deposit belts (Cu-Au ± Ag-Pt-Pd-Mo) within the Canadian Cordillera: Economic Geology, v. 109, no. 4, p. 827–858, doi: 10.2113/econgeo.109.4.827.

Lypaczewski, P., and Rivard, B., 2018, Estimating the Mg# and AlVI content of biotite and chlorite from shortwave infrared reflectance spectroscopy: Predictive equations and recommendations for their use: International Journal of Applied Earth Observation and Geoinformation, v. 68, p. 116–126.

Madeisky, H.E., and Stanley, C.R., 1993, Lithogeochemical exploration of metasomatic zones associated with volcanic-hosted massive sulfide deposits using pearce element ratio analysis: International Geology Review, v. 35, no. 12, p. 1121–1148, doi: 10.1080/00206819309465580.

Des Marais, D.J., and Moore, J.G., 1984, Carbon and its isotopes in mid-oceanic basaltic glasses: Earth and Planetary Science Letters, v. 69, no. 1, p. 43–57, doi: 10.1016/0012-821X(84)90073-6.

Marschall, H.R., Meyer, C., Wunder, B., Ludwig, T., and Heinrich, W., 2009, Experimental boron isotope fractionation between tourmaline and fluid: Confirmation from in situ analyses by secondary ion mass spectrometry and from Rayleigh fractionation modelling: Contributions to Mineralogy and Petrology, v. 158, no. 5, p. 675–681, doi: 10.1007/s00410-009-0403-8.

Marschall, H.R., Wanless, V.D., Shimizu, N., Pogge von Strandmann, P.A.E., Elliott, T., and Monteleone, B.D., 2017, The boron and lithium isotopic composition of mid-ocean ridge basalts and the mantle: Geochimica et Cosmochimica Acta, v. 207, p. 102–138, doi: 10.1016/j.gca.2017.03.028.

Marshall, L.J., and Oliver, N.H.S., 2008, Constraints on hydrothermal fluid pathways within Mary Kathleen Group stratigraphy of the Cloncurry iron-oxide-copper-gold District, Australia: Precambrian Research, v. 163, p. 151–158, doi: 10.1016/j.precamres.2007.08.016.

de Martin, B.J., Reves-Sohn, R.A., Canales, J.P., and Humphris, S.E., 2007, Kinematics and geometry of active detachment faulting beneath the Trans-Atlantic geotraverse (TAG) hydrothermal field on the Mid-Atlantic Ridge: Geology, v. 35, no. 8, p. 711–714, doi: 10.1130/G23718A.1.

Massey, N.W.D., MacIntyre, D.G., Desjardins, P.J., and Cooney, R.T., 2005, Digital geology map of British Columbia. B.C.: Digital Geology Map, Geofile 2005-1, p. Geofile 2005-1.

Masterman, G.J., Cooke, D.R., Berry, R.F., Walshe, J.L., Lee, A.W., and Clark, A.H., 2005, Fluid chemistry, structural setting, and emplacement history of the Rosario Cu-Mo porphyry and Cu-Ag-Au epithermal veins, Collahuasi district, northern Chile: Economic Geology, v. 100, p. 835–862.

McMillan, W.J., 1977, Geological Fieldwork 1977: Geological Fieldwork 1977, British Columbia Geological Survey, p. 26–36.

McMillan, W.J., 1976, Geology and genesis of the Highland Valley ore deposits and the Guichon Creek batholith, *in* Southerland Brown, A. ed., Porphyry Deposits of the Canadian Cordillera, Canadian Institute of Mining and Metallurgy, Special Volume 15, p. 85–104.

McMillan, W.J., 1985a, Geology and ore deposits of the Highland Valley camp (A. J. Sinclair, Ed.): Field Guide and Reference Manual Series, Geological Association of Canada.

McMillan, W.J., 1985b, J.A. Deposit, *in* Sinclair, J.A. ed., Geology and Ore Deposits of the Highland Valley Camp, Geological Association of Canada, Field Guide and Reference Manual Series, p. 63–74.

McMillan, W.J., 1974, Stratigraphic section from the Jurassic Ashcroft Formation and Triasccis Nicola Group contiguous to the Guichon Creek batholith: Geological Fieldwork 1974, British Columbia Geological Survey, p. 27–34.

McMillan, W.J., Anderson, R.G., Chen, R., and Chen, W., 2009, Geology and mineral occurrences (MINFILE), the Guichon Creek batholith and Highland Valley porphyry copper district, British Columbia: Open file 6079, Geological Survey of Canada, 2 p.

McMillan, W.J., Thompson, J.F.H., Hart, C.J.., and Johnston, S.T., 1995, Regional geological and tectonic setting of porphyry deposits in British Columbia and Yukon Territory, *in* Schroeter, T.G. ed., Porphyry Deposits of the Northwestern Cordillera of North America, Canadian Institute of Mining and Metallurgy, p. 46–57.

Meyer, C., and Hemley, J.J., 1967, Wall rock alteration, *in* Barnes, H.L. ed., Geochemistry of hydrothermal ore deposits, Holt, Rinehart, and Winston, Inc, New York, p. 166–235.

Meyer, C., Wunder, B., Meixner, A., Romer, R.L., and Heinrich, W., 2008, Boron-isotope fractionation between tourmaline and fluid: An experimental re-investigation: Contributions to Mineralogy and Petrology, v. 156, no. 2, p. 259–267, doi: 10.1007/s00410-008-0285-1.

Migdisov, A.A., Williams-Jones, A.E., and Wagner, T., 2009, An experimental study of the solubility and speciation of the rare earth elements (III) in fluoride- and chloride-bearing aqueous solutions at temperatures up to 300°C: Geochimica et Cosmochimica Acta, v. 73, p. 7087–7109.

Mihalynuk, M.G., Diakow, L.J., Friedman, R.M., and Logan, J.M., 2016, Chronology of southern Nicola arc stratigraphy and deformation: British Columbia Geological Survey, Geological Fieldwork 2015, Paper 2016-1, p. 31–63.

Mitchinson, D.E., Enkin, R.J., and Hart, C.J.R., 2013, Linking Porphyry Deposit Geology to Geophysics via Physical Properties: Adding Value to Geoscience BC Geophysical Data: Geoscience BC Report 2013-14, p. 116.

Monecke, T., Monecke, J., Reynolds, T.J., Tsuruoka, S., Bennett, M.M., Skewes, W.B., and Palin, R.M., 2018, Quartz solubility in the H2O-NaCl system: A framework for understanding vein formation in porphyry copper deposits: Economic Geology, v. 113, no. 5, p. 1007–1046, doi: 10.5382/econgeo.2018.4580.

Moore, J.M., 2000, Nicola Horst, southern British Columbia: window into the pre-Triassic margin of North America? : Geological Survey of Canada, Current Research 2000-A16, 6 p.

Morgan, G.B., and London, D., 1989, Experimental reactions of amphibolite with boron-bearing aqueous fluids at 200 MPa : implications for tourmaline stability and partial melting in mafic rocks: Contributions to Mineralogy and Petrology, v. 102, p. 281–297.

Mortimer, N., 1986, Late Triassic, arc-related, potassic igneous rocks in the North American Cordillera: Geology, v. 14, p. 1035–1038.

Mortimer, N., 1987, The Nicola Group: Late Triassic and early Jurassic subduction related volcanism in British Columbia: Canadian Journal of Earth Sciences, v. 24, p. 2521–2536.

Moss, T.J., 2010, Petrography and lithogeochemistry of the Quebrada Blanca copper-molybdenum deposit, Region I, Chile: M.Sc. Thesis, Acadia University, 258 p.

Nabighian, M.N., Grauch, V.J.S., Hansen, R.O., Lafehr, T.R., Li, Y., Peirce, J.W., Phillips, J.D., and Ruder, M.E., 2005, 75th Anniversary The historical development of the magnetic method in exploration: Geophysics, v. 70, no. 6, p. 33–61, doi: 10.1190/1.2133784.

Nelson, J.L., Colpron, M., and Israel, S., 2013, The Cordillera of British Columbia, Yukon, and Alaska: Tectonics and Metallogeny, *in* Colpron, M., Bissig, T., Rusk, B.G., and Thompson, J.F.H. eds., Tectonics, Metallogeny, and Discovery-the North American Cordillera and similar accretionary settings, Society of Economic Geologists, Special Publication 17, p. 53–109.

Norman, D.K., Parry, W.T., and Bowman, J.R., 1991, Petrology and geochemistry of propylitic alteration at southwest Tintic, Utah: Economic Geology, v. 86, no. 1, p. 13–28, doi: 10.2113/gsecongeo.86.1.13.

Northcote, K.E., 1969, Geology and geochronology of the Guichon Creek batholith: Bulletin 56, British Columbia Department of Mines and Petroleum Resources, v. 56, p. 77.

Norton, D.L., 1979, Transport phenomena in hydrothermal systems: the redistribution of chemical components around cooling magmas: Bulletin of Mineralogy, v. 102, p. 471–486.

Ohmoto, H., 1972, Systematics of sulfur and carbon isotopes in hydrothermal ore deposits: Economic Geology, v. 67, no. 5, p. 551–578, doi: 10.2113/gsecongeo.67.5.551.

Ohmoto, H., and Rye, R.O., 1974, Hydrogen and oxygen isotopic compositions of fluid inclusions in the Kuroko Deposits, Japan: Economic Geology, v. 69, no. 6, p. 947–953, doi: 10.2113/gsecongeo.69.6.947.

Ohmoto, H., and Rye, R.O., 1979, Isotopes of sulfur and carbon, *in* Barnes, H.L. ed., Geochemistry of Hydrothermal Ore Deposits, John Wiley & Sons, New York, p. 509–567.

Olade, M.A., 1974, Bedrock geochemistry of porphyry copper deposits, Highland Valley, British Columbia: Ph.D Thesis, University of British Columbia, 531 p.

Olade, M.. A., and Fletcher, W.K., 1976a, Distribution of sulphur and sulphide-iron and copper in bedrock assocaited with porphyry copper deposits, Highland Valley, British Columbia: Journal of Geochemcial Exploration, v. 5, p. 21–30.

Olade, M.A., and Fletcher, W.K., 1975, Primary dispersion of rubidium and strontium around porphyry copper deposits, Highland Valley, British Columbia: Economic Geology, v. 70, p. 15–21, doi: 10.2113/gsecongeo.70.1.15.

Olade, M.A., and Fletcher, W.K., 1976b, Trace element geochemistry of the Highland Valley and

Guichon Creek Batholith in relation to porphyry copper mineralization: Economic Geology, v. 71, p. 733–748, doi: 10.2113/gsecongeo.71.4.733.

Oldenburg, D., and Pratt, D.A., 2007, Geophysical inversion for mineral exploration: A decade of progress in theory and practice, *in* Proceedings of Exploration 07: Fifth Decennial International Conference on Mineral Exploration, p. 61–95.

Orovan, E.A., Cooke, D.R., Harris, A.C., Ackerman, B., and Lawlis, E., 2018, Geology and Isotope Geochemistry of the Wainaulo Cu-Au Porphyry Deposit, Namosi District, Fiji: Economic Geology, v. 113, p. 133–161, doi: 10.5382/econgeo.2018.4546.

Osatenko, M.J., and Jones, M.B., 1976, Valley Copper, *in* Sutherland Brown, A. ed., Porphyry Deposits of the Canadian Cordillera, Canadian Institute of Mining and Metallurgy, Special Volume 15, p. 130–143.

Pacey, A., Wilkinson, J.J., Boyce, A.J., and Cooke, D.R., 2016, Propylitic alteration and metal mobility in porphyry systems: a case study of the Northparkes Cu-Au deposits, NSW, Australia: Applied Earth Science, v. 125, no. 2, p. 93–93, doi: 10.1080/03717453.2016.1166660.

Palmer, M., and Swihart, G., 1996, Boron isotope geochemistry: an overview, *in* Grew, E. and Anovitz, L. eds., Boron: mineralogy, petrology and geochemistry, Reviews in Mineralogy Vol. 33, Mineralogical Society of America, Washington, p. 709–744.

Paton, C., Hellstrom, J., Paul, B., Woodhead, J., and Hergt, J., 2011, Iolite: Freeware for the visualisation and processing of mass spectrometric data.: Journal of Analytical Atomic Spectrometry, v. 26, no. 12, p. 2508–2511, doi: http://doi.org/10.1039/c1ja10172b.

Pineau, F., and Javoy, M., 1983, Carbon isotopes and concentrations in mid-ocean ridge basalts: Earth Planet. Sci. Lett., v. 62, p. 239–257.

Plümper, O., and Putnis, A., 2009, The complex hydrothermal history of granitic rocks: Multiple feldspar replacement reactions under subsolidus conditions: Journal of Petrology, v. 50, no. 5, p. 967–987, doi: 10.1093/petrology/egp028.

Poli, S., and Schmidt, M.W., 2004, Experimental subsolidus studies on epidote minerals, *in* Reviews in Mineralogy & Geochemistry 56, p. 171–195.

Pollard, P.J., 2001, Sodic(-calcic) alteration in Fe-oxide-Cu-Au districts: An origin via unmixing of magmatic H2O-CO2- NaCl-CaCl2 ± KCl fluids: Mineralium Deposita, v. 36, p. 93–100.

Preto, V.A., 1979, Geology of the Nicola Group between Merritt and Princeton: Bulletin 69, British Columbia Ministry of Energy, Mines and Petroleum Resources, p. 100.

Proffett, J.M., 2009, High Cu grades in porphyry Cu deposits and their relationship to emplacement depth of magmatic sources: Geology, v. 37, no. 8, p. 675–678, doi: 10.1130/G30072A.1.

Putnis, A., 2015, Transient porosity resulting from fluid–mineral interaction and its consequences: Reviews in Mineralogy and Geochemistry, v. 80, p. 1–23, doi: 10.2138/rmg.2015.80.01.

Radetzki, M., 2009, Seven thousand years in the service of humanity-the history of copper, the red metal: Resources Policy, v. 34, no. 4, p. 176–184, doi: 10.1016/j.resourpol.2009.03.003.

Railsback, L.B., 2003, An earth scientist's periodic table of the elements and their ions: Geology, v. 31, p. 737–740.

Ray, G.E., Dawson, G.L., and Webster, I.C.L., 1996, The stratigraphy of the Nicola Group in the Hedley district, British Columbia, and the chemistry of its intrusions and Au skarns: Canadian Journal of Earth Science, v. 33, p. 1105–1126.

Reed, M.H., 1997, Hydrothermal alteration and its relationship to ore fluid composition, *in* Barnes, H.L. ed., Geochemistry of hydrothermal ore deposits, John Wiley and Sons, New York, p. 303–365.

Reed, A.J., and Jambor, J.L., 1976, Highmont: Linearly zoned copper-molybdenum porphyry deposits and their significance in the genesis of the Highland Valley ores, *in* Sutherland Brown, A. ed., Porphyry Deposits of the Canadian Cordillera, Canadian Institute of Mining and Metallurgy, Special Volume 15, p. 163–181.

Reed, M.H., Rusk, B.G., and Palandri, J., 2013, The Butte magmatic-hydrothermal system: One fluid yields all alteration and veins: Economic Geology, v. 108, p. 1379–1396.

Reeves, C., 2005, Aeromagnetic Surveys. Principles, Practice & Interpretation: Earthworks, Geosoft.

Richards, J.P., 2011, Magmatic to hydrothermal metal fluxes in convergent and collided margins: Ore Geology Reviews, v. 40, no. 1, p. 1–26, doi: http://dx.doi.org.login.ezproxy.library.ualberta.ca/10.1016/j.oregeorev.2011.05.006.

Richards, J.P., 2015, The oxidation state, and sulfur and Cu contents of arc magmas: implications for metallogeny: Lithos, v. 233, p. 27–45, doi: http://dx.doi.org.login.ezproxy.library.ualberta.ca/10.1016/j.lithos.2014.12.011.

Richards, J.P., and Mumin, A.H., 2013, Magmatic-hydrothermal processes within an evolving Earth: Iron oxide-copper-gold and porphyry Cu ± Mo ± Au deposits: Geology, v. 41, p. 767–770, doi: 10.1130/G34275.1.

Riedell, K.B., and Proffett, J.M., 2014, Batholithic and early halo type Cu-Mo deposits: Geological Society of America, 2014 annual meeting & exposition, (46), 6, p. 606.

Riveros, K., Veloso, E., Campos, E., Menzies, A., and Véliz, W., 2014, Magnetic properties related to hydrothermal alteration processes at the Escondida porphyry copper deposit, northern Chile: Mineralium Deposita, v. 49, no. 6, p. 693–707, doi: 10.1007/s00126-014-0514-7.

Roy, B., and Clowes, R.M., 2000, Seismic and potential-field imaging of the Guichon Creek batholith, British Columbia, Canada, to delineate structures hosting porphyry copper deposits: Geophysics, v. 65, no. 5, p. 1418, doi: 10.1190/1.1444831.

Rusk, B.G., Reed, M.H., and Dilles, J.H., 2008, Fluid Inclusion evidence for magmatic-hydrothermal fluid evolution in the porphyry copper-molybdenum deposit at Butte, Montana: Economic Geology, v. 103, no. 2, p. 307–334, doi: 10.2113/gsecongeo.103.2.307.

Rusk, B.G., Reed, M.H., Dilles, J.H., Klemm, L.M., and Heinrich, C.A., 2004, Compositions of magmatic hydrothermal fluids determined by LA-ICP-MS of fluid inclusions from the porphyry copper–molybdenum deposit at Butte, MT: Chemical Geology, v. 210, no. 1–4, p. 173–199, doi: http://dx.doi.org/10.1016/j.chemgeo.2004.06.011.

Russell, K., and Stanley, C.R., 1990, Theory and application of pearce element ratios to geochemical data analysis, *in* Geological Association of Canada, Short Course Volume 8., p. 1–324.

Schiarizza, P., 2017, Ongoing stratigraphic studies in the Nicola Group: Stump Lake – Salmon River area, south-central British Columbia: Geological Fieldwork 2016, British Columbia Ministry of

Energy and Mines, v. 2017–1, p. 17–33.

Schiarizza, P., 2016, Toward a regional stratigraphic framework for the Nicola Group: Preliminary results from the Bridge Lake – Quesnel River area: Geological Fieldwork 2015, British Columbia Ministry of Energy and Mines, v. 2016–1, p. 12–30.

Schodde, R., 2014, The global shift to undercover exploration; How fast? How effective?, *in* Society of Economic Geologists, SEG 2014: Building Exploration Capability for the 21st Century, Keystone, Colorado.

Seedorff, E., Barton, M.D., Stavast, W.J.A., and Maher, D.J., 2008, Root zones ofporphyry systems: extending the porphyry model to depth: Economic Geology, v. 103, p. 939–956.

Seedorff, E., Dilles, J.H., Proffett, J.M., Einaudi, M.T., Zurcher, L., Stavast, W.J.A., Johnson, D.A., and Barton, M.D., 2005, Porphyry Deposits: Characteristics and Origin of Hypogene Features, *in* Hedenquist, J.W., Thompson, J.F.H., Goldfarb, R.J., and Richards, J.P. eds., Economic Geology 100th Anniversary Volume, Society of Economic Geologists, p. 251–298.

Seward, T., Williams-Jones, A.E., and Migdisov, A.A., 2014, The chemistry of metal transport and deposition by ore-forming hydrothermal fluids, *in* Holland, H.D. and Turekian, K.K. eds., Treatise on Geochemistry: Second Edition, Elsevier Ltd., p. 29–57.

Shanks, W.C., 2014, Stable Isotope Geochemistry of Mineral Deposits, *in* Holland, H.D. and Turekian, K.K. eds., Treatise on Geochemistry: Second Edition, Elsevier Ltd., p. 59–85.

Sheppard, S.M.F., Nielsen, R.L., and Taylor, H.P., 1971, Hydrogen and oxygen isotope ratios in minerals from porphyry copper deposits: Economic Geology, v. 66, no. 4, p. 515–542, doi: 10.2113/gsecongeo.66.4.515.

Sillitoe, R.H., 2013, Metallogenic and regulatory inequalities around the Northern Pacific rim: Implications for discovery, *in* Society of Economic Geologists, Whistler 2013: Geoscience for Discovery, Whistler, British Columbia.

Sillitoe, R.H., 2010, Porphyry copper systems: Economic Geology, v. 105, no. 1, p. 3–41, doi: 10.2113/gsecongeo.105.1.3.

Smith, M.P., and Yardley, B.W.D., 1996, The boron isotopic composition of tourmaline as a guide to fluid processes in the southwestern England orefield: An ion microprobe study: Geochimica et Cosmochimica Acta, v. 60, no. 8, p. 1415–1427, doi: 10.1016/0016-7037(96)00007-5.

Stanley, C., 2011, Pearce and general element ratio diagrams: Molar scatterplots allowing rigorous investigation of material transfer in geochemical systems, *in* 25th International Applied Geochemistry Symposium 2011, International Applied Geochemistry, ROVANIEMI-LAPLAND, p. C10.3.

Stanley, C.., and Madeisky, H.E., 1994, Lithogeochemical exploration for hydrothermal ore deposits using Pearse element ratio analysis, *in* Lentz, D.R. ed., Alteration and Alteration Processes associated with Ore-forming Systems, Geological Association of Canada, Short Course Notes, v. 11, p. 193–211.

Stevenson, R., 2015, Stable isotopes of hydrothermal carbonate minerals in the Butte porphyry-lode deposits, Montana: Graduate Theses & Non-These, Montana Tech of the University of Montana, 95 p.

Sun, W., and McDonough, W., 1989, Chemical and isotopic systematics of oceanic basalts: Implications for mantle composition and processes: Geological Society, London, Special Publications, v. 42, p. 313–345, doi: 10.1144/GSL.SP.1989.042.01.19.

Sutherland, B.A., 1976, Morphology and classification, *in* Sutherland, B.A. ed., Porphyry deposits of the Canadian Cordillera: Canadian Institute of Mining and Metallurgy, Special Volume 15, p. 44–51.

Tapia, J., Townley, B., Córdova, L., Poblete, F., and Arriagada, C., 2016, Hydrothermal alteration and its effects on the magnetic properties of Los Pelambres, a large multistage porphyry copper deposit: Journal of Applied Geophysics, v. 132, p. 125–136, doi: 10.1016/j.jappgeo.2016.07.005.

Taylor, B.E., 1986, Magmatic volatiles: Isotopic variation of C, H, and S, *in* Valley, J.W., Taylor, H.P., and O'Neil, J.R. eds., Reviews in Mineralogy, Vol. 16, Mineralogical Society of America, p. 185–226.

Taylor, H.P., 1979, Oxygen and hydrogen isotope relationships in hydrothermal mineral deposits, *in* Barnes, H.L. ed., Geochemistry of Hydrothermal Ore Deposits, John Wiley & Sons, New York, p. 236–277.

Taylor, H.P., and Sheppard, S.M.F., 1986, Igneous rocks: I. Processes of isotopic fractionation and isotope systematics, *in* Valley, J.W., Taylor, H.P., and O'Neil, J.R. eds., Stable isotopes in high temperature geological processes, Reviews in Mineralogy, Vol. 16, Mineralogical Society of America, p. 227–272.

Teck, 2018, Annual Information Form 2017: Teck Resources Limited, 124 p.

Thompson, J.F.H., 2016, The future of mineral exploration, *in* AMEBC Round-Up 2016, Abstracts Technical Sessions, Vancouver.

Tilton, J.E., and Lagos, G., 2007, Assessing the long-run availability of copper: Resources Policy, v. 32, no. 1, p. 19–23, doi: https://doi.org/10.1016/j.resourpol.2007.04.001.

Tosdal, R.M., and Richards, J.P., 2001, Magmatic and structural controls on the development of porphyry Cu±Mo±Au deposits, *in* Reviews in Economic Geology Vol. 14: Structural Controls on Ore Genesis, p. 157–181.

Tremba, E.L., Faure, G., Katsikatsos, G.C., and Summerson, C.H., 1975, Strontium isotope composition in the Tethys Sea, Euboea, Greece: Chemical Geology, v. 16, p. 109–120.

Trumbull, R.B., and Slack, J.F., 2018, Boron isotopes in the continental crust: granites, pegmatites, felsic volcanic rocks, and related ore deposits, *in* Marschall, H.R. and Foster, G.L. eds., Advances in Isotope Geochemistry - Boron Isotopes - The Fifth Element, Springer-Verlag, Hiedelberg, Berlin.

Ulrich, T., and Heinrich, C.A., 2001, Geology and alteration geochemistry of the porphyry Cu-Au deposit at Bajo de la Alumbrera, Argentina: Economic Geology, v. 96, p. 1719–1742, doi: 10.2113/gsecongeo.97.8.1865.

Urqueta, E., Stanley, C.R., Clark, A.H., Oates, C.J., and Kyser, T.K., 2009, Lithogeochemistry of the Collahuasi porphyry Cu-Mo and epithermal Cu-Ag (-Au) cluster, northern Chile: Pearce element ratio vectors to ore: Geochemistry: Exploration, Environment, Analysis, v. 9, no. 1, p. 9–17, doi: 10.1144/1467-7873/07-169.

Vennemann, T.W., Muntean, J.L., Kesler, S.E., O'Neil, J.R., Valley, J.W., and Russell, N., 1993, Stable isotope evidence for magmatic fluids in the Pueblo Viejo epithermal acid sulfate Au-Ag deposit, Dominican Republic: Economic Geology, v. 88, p. 55–71.

Warren, I., Simmons, S.F., and Mauk, J.L., 2007, Whole-rock geochemical techniques for evaluating hydrothermal alteration, mass changes, and compositional gradients associated with epithermal Au-Ag mineralization: Economic Geology, v. 102, p. 923–948.

Watson, D.F., and Philip, G.M., 1985, A Refinement of Inverse Distance Weighted Interpolation: Geoprocessing, v. 2, p. 315–327.

Weis, P., 2014, The physical hydrology of ore-forming magmatic-hydrothermal systems: Building Exploration Capability for the 21st Century, Society of Economic Geologist, Special Publication Series, v. 18, p. 59–75.

Wheeler, R.S., Browne, P.R.L., and Rodgers, K.A., 2001, Iron-rich and iron-poor prehnites from the Way Linggo epithermal Au-Ag deposit, southwest Sumatra, and the Heber geothermal field, California: Mineralogical Magazine, v. 65, no. June, p. 397–406, doi: 10.1180/002646101300119475.

Wilburn, D.R., Stanley, K.A., and Karl, N.A., 2015, Exploration Review: Mining Engineering, Annual Review 2014, p. 16–38, doi: www.miningengineeringmagazine.com.

Wilkinson, J.J., Chang, Z., Cooke, D.R., Baker, M.J., Wilkinson, C.C., Inglis, S., Chen, H., and Gemmell, J.B., 2015, The chlorite proximitor: A new tool for detecting porphyry ore deposits: Journal of Geochemical Exploration, v. 152, p. 10–26, doi: 10.1016/j.gexplo.2015.01.005.

Wilkinson, J.J., Cooke, D.R., Baker, M.J., Chang, Z., Wilkinson, C.C., Chen, H., Fox, N., Hollings, P., White, N.C., Gemmell, J.B., Loader, M.A., Pacey, A., Sievwright, R.H., Hart, L.A., et al., 2017, Porphyry indicator minerals and their mineral chemistry as vectoring and fertility tools- Application of indicator mineral methods to bedrock and sediments, *in* Thomas, V.T. and M.D. ed., Proceedings of Exploration 17, p. 67–77.

Williams-Jones, A.E., 2015, The hydrothermal mobility of the rare earth elements, *in* Simandl, G.J. and Neetz, M. eds., Symposium on Strategic and Critical Materials Proceedings, British Columbia Ministry of Energy and Mines British Columbia Geological Survey, p. 119–123.

Williams, P.J., Barton, M.D., Johnson, D.A., Fontbote, L., De Haller, A., Mark, G., Oliver, N.H.S., and Marschik, R., 2005, Iron oxide copper-gold deposits: Geology, space-time distribution, and possible modes of origin, *in* Hedenquist, J.W., Thompson, J.F.H., Goldfarb, R.J., and Richards, J.P. eds., Economic Geology 100th Anniversary Volume, Society of Economic Geologists, p. 371–405.

Wilson, A.J., Cooke, D.R., and Harper, B.R., 2003, The Ridgeway gold-copper deposit: A high-grade alkalic porphyry deposit in the Lachlan fold belt, New South Wales, Australia: Economic Geology, v. 98, p. 1637–1666.

Wood, D., 2018, Transforming the business of gold exploration: adapting to deeper exploration: SEG Newsletter, No. 112, p. 62.

Wood, D., 2016, We must change exploration thinking in order to discover future orebodies: SEG Newsletter, No. 105, p. 16–19.

Xavier, R.P., Wiedenbeck, M., Trumbull, R.B., Dreher, A.M., Monteiro, L.V.S., Rhede, D., de Araújo, C.E.G., and Torresi, I., 2008, Tourmaline B-isotopes fingerprint marine evaporites as the source of high-salinity ore fluids in iron oxide copper-gold deposits, Carajás Mineral Province (Brazil): Geology, v. 36, no. 9, p. 743–746, doi: 10.1130/G24841A.1.

Yavuz, F., Iskenderoglu, A., and JIang, S.-Y., 1999, Tourmaline compositions from the Salikvan porphyry Cu-Mo deposit and vicinity, Northeastern Turkey: The Canadian Mineralogist, v. 37, p. 1007–1023.

Ydon, J.W., 2007, An overview of the economic and geological contexts of Canada's major mineral deposit types, *in* Goodfellow, W.D. ed., Mineral Deposits of Canada: A Synthesis of Major Deposit-Types, District Metallogeny, the Evolution of Geological Provinces, and Exploration Methods, Geological Association of Canada, Mineral Deposits Division, Special Publication No. 5, p. 3–48.

List of Appendices

Appendix 2-A: Additional methodology information, and carbonate EMPA.

Appendix 2-B: Sulfur-bearing mineral species in peripheral alteration–PER plots.

Appendix 2-C: Data and plots to supplement Figure 2-16.

Appendix 3-A: Additional methodology information, and sample list.

Appendix 3-B: Mineral-fluid fractionation factors for D and O isotopes and additional information.

Appendix 4-A: Additional methodology information, and sample list and images.

Appendix 4-A: Equations used and supplementary models.

List of Supplemental data files provided in the Education and Research Archive

Supplemental data 2-A: Lithogeochmical and rock slab alteration data.

Supplemental data 2-B: Material-transer / element gain and loss calculations.

Supplemental data 2-C: Whole-rock C isotope data (CF-IR-MS).

Supplemental data 3-A: Boron isotope data (SIMS).

Supplemental data 3-B: Radiogenic Sr isotope data (TIMS).

Supplemental data 3-C: Chlroite EMPA.

Supplemental data 3-D: Feldspar EMPA.

Supplemental data 3-E: Amphibole EMPA.

Supplemental data 4-A: Epidote and prehnite EMPA.

Supplemental data 4-B: LA-ICP-MS results.

Supplemental data 4-C: LA-ICP-MS QAQC analysis.

Appendix 2-A

Methodologies

Lithogeochemical Analytical Methodology

Lithogeochemical analyses were undertaken at ACME Analytical Laboratory (now Bureau Veritas Laboratories), Vancouver, Canada using Method G4A-G4B. Sample submittals were accompanied by a number of external matrix-matched pulp standards, coarse blanks, and pulp duplicate request, which were in addition to those used by the analytical facility in order to ensure quality control. Sample preparation consisted of a 70% crush to 10 mesh with a 500–1000 g cut being pulverized. A 0.2 g sample split was fused at 1000°C with 1.5 g of an 80:20 lithium metaborate/tetraborate mix. The cooled bead was digested in 100 mL of 5% HNO_3. ICP-ES analysis determines major element concentrations reported as the common oxides. The same whole rock fusion solution was analyzed by ICP-MS (Perkin Elmer Elan 6000) to determine absolute concentrations of trace elements using the following methods. Method 1F-MS: A 1 g subsample was digested in 6 mL of hot (95°C) modified Aqua Regia (1:1:1 $HCl:HNO_3:H_2O$) for 1 hour, cooled and made to 20 mL volume with 5% HCl. The solution was analyzed by ICP-MS (Perkin Elmer Elan 6000 or 9000). Method G3B: A 30 g sample split was custom mixed with PbO fire assay fluxes and fired for 45 minutes at 1050°C. Molten Pb + slag was poured into an iron mold, cooled and Pb button recovered. Heating at 950°C in a MgO cupel rendered a Ag ± Au, Pt, Pd dore bead. The bead was parted in hot HNO3, digested by adding HCl and aspirated into a Jarrel Ash Atomcomp 875 ICP-ES to determine Au, Pt and Pd. Upper limits = 10 ppm. Method G7TD: A 0.5 g sample split was digested in 20 mL of 4-Acid solution ($HNO_3:HClO_4:HF:H_2O$) at 200°C and taken to dryness. The residue was dissolved in 16 mL of 50% HCl at ~95°C for 1 hour then made to volume in a 100 mL volumetric flask with 5% HCl. ICP-ES analysis determines total Ni. Loss on Ignition (LOI) is report as % weight loss on a 1 g split ignited at 1000°C. LECO combustion analysis was used to determine total C and S on a 0.2 g sample split which is heated and combusted in the presence of pure oxygen. During the process, C and S are oxidized to form CO_2 and SO_2 and measured with an element analyzer.

Lithogeochemical Data and Quality Assurance (QA) and Quality Control (QC)

Blanks, pulp duplicates, and standard reference material (SRM) were inserted at a rate of 1 in 30 samples each. Blank material used is a coarse crushed granodiorite purchased in bulk from an aggregate supplier and tested numerous times in unsure homogeneity of low level metal content (carry over contamination during sample preparation). Pulp duplicates were requested to test how homogenous unknown rock pulps are (lab sample prep). Accuracy was evaluated by using matrix matched Guichon Creek batholith pulps (SRM) developed by Teck for use in evaluating in resource estimate assay data.

The following quality control rules were applied to all analytical sample batches included in this study. Coarse blank material has Cu and Mo values below 10 times the detection limit (10 ppm) for Cu and Mo (by 1F-MS). Requested duplicate pulp pairs plotted on min-max plots are all within 10 % relative error of each other for the rock forming elements, indicating that rocks pulps were well homogenized and digestion techniques are consistent. Collectively the SRM pulps, inserted within analytical batch, indicate an acceptable lab bias (< 4 %) for major elements relative to the accepted values determined from round-robin testing.

Shortwave Infrared (SWIR) Imaging Spectrometry

Rock slabs were acquired using a Specim SisuROCK imaging spectromter (University of Alberta) which operated in the shortwave infrared wavelength (λ) range (1000–2500 nm), at a variable spatial resolution of 0.2-1.0 mm/pixel. Absorption positions were retrieved from the second derivative of interpolated spectra, as described in Lypaczewski and Rivard (2018). In this paper, whether coarse or fine-grained, the terms sericite, white-mica, and muscovite are collective termed white-mica. The term white-mica used in this contribution encompasses the minerals and mineral groups of muscovite, illite, smectite. The exact position of the 2200nm Al_2-OH absorption feature is correlated to white-mica Al^{VI} content, which reflects the level of Tschermak substitution, and physicochemical conditions under which the mineral formed (Herman et al., 2001; Swayze et al. 2014, Halley et al., 2015). In this study, this absorption feature of white-mica is classified as short (2190–2198nm), intermediate (2198–2204 nm), and long (2204-2214 nm). This classification is based on the response of white-mica in fracture halos, or the background response if no discrete vein halo is present. Prehnite was identified from the SWIR spectra based on a distinct absorption feature appearing at 1476 nm, and kaolinite is identified by the presence of an absorption around 2160 nm.

Feldspar Staining

Slab staining was performed in the Mineral Deposit Research Unit wet-chemical heavy-mineral separates lab in the Department of Earth and Ocean Sciences at the University of British Columbia. The staining was carried out under a fume hood using the required personal safety equipment: latex and long heavy duty rubber gloves, lab coat and HF-resistant rubber apron, safety glasses and face shield with throat guard, and a HF burn kit (Ca gluconate gel).

Procedure

The following work-flow was used to test for the presence of K-feldspar, Ca-component in plagioclase, carbonate and prehnite (Laniz et al., 1964; McMonigle, 2015):

1) Rock samples were cut on a diamond saw into approximately 2 cm thick by 10 x 10 cm rock slabs.
2) The slabs were labeled and photographed prior to staining.
3) The slabs were etched in 45-52% solution of HF in shallow bath for 60 seconds than rinsed in two water baths.
4) A 7% solution of Amaranth (~66 g in 1 l distilled water) was prepared and placed in shallow bath. The etched rocks slabs were dipped face down in the bath for 10 s before being rinsed off in multiple baths and set at an angle to air drying under the fume hood.
5) A 20% solution of Sodium Colbaltinitrite (~20 g for every 100 ml distilled water) was placed in a shallow bath. The rinsed and dried bath was dipped in the bath for ten seconds before a final rinse and drying for 20 minutes.
6) The stained face was photographed.

Interpretation of staining colors

Primary K-feldspar stains yellow and is distinguished from secondary K-feldspar based on morphology and distribution in the rock slab. Primary K-feldspar is predominantly hosted in groundmass and is interstitial to euhedral plagioclase crystals, whereas secondary K-feldspar forms linear features associated with fractures and replaces plagioclase in patches. The absence of yellow-staining, in K-feldspar-bearing protolith, indicates K-feldspar-destructive albite alteration. In unaltered and weakly white-mica–prehnite dusted plagioclase crystals the calcic component stains a pink to red color. Plagioclase that appears milky white in hand specimen and turbid in transmitted light (due to fine-grained white-mica inclusions) does not take the stain as completely, or at all, compared to fresh plagioclase. Albite does not stain with Amaranth. Similarly, strongly albitized plagioclase does not stain pink, thus the absence of pink-purple Amaranth stain indicates modification of plagioclase. Veins and calcite and prehnite stain a distinct pink color.

Whole-rock C isotope analysis

In addition to the 133 unknowns 10% analyses each of the following were analyzed: 1) certified reference materials and secondary standards 2) random duplication of unknown samples and 3) blanks. Total carbon content and isotope ratio (δ13Ctotal) includes all forms of carbon present in each sample.

δ13Ctotal values are reported using the delta (δ) notation in units of permil (‰) relative to Vienna Pee Dee Belemnite (VPDB) international standard, with a precision of 0.2‰. Precision ‰ is based upon duplicate sample analyses. Accuracy ‰ is based upon primary or secondary standard.

Electron Microprobe Analyses of Carbonate Minerals

Electron microprobe analyses (EPMA) was performed during several analytical sessions using the CAMECA SX100 at the Electron Microprobe Laboratory at the University of Alberta. Wavelength dispersive spectrometry (WDS) was carried out to primarily identify the major and minor chemistry of silicate alteration minerals in the Guichon Creek batholith, however, where present, carbonate minerals were also analyzed. For the WDS the EPMA beam was operated in spot mode at an accelerating voltage of 20 kV, a probe current of 20 nA, and a beam diameter between 1–5 µm. Unknowns were analyzed at a peak count time of 30 s and background count time of 30 s. Standards were analyzed for 20–30 s on peak. Data reduction was completed using the "PAP" f(rZ) method (Pouchou and Pichoir, 1985). The standards used are listed in table G1 and carbonate mineral results in table G2.

Table 2-A-1. EMPA standards

Element/Line	Crystal	OnPeak Time	OffPeak Time	Standard
Na ka	LTAP	30	30	$NaAlSi_3O_8$ albite VA 131705
Ca ka	PET	30	30	Plagioclase (labradorite) 115900
K ka	LPET	30	30	$KAlSi_3O_8$ sanidine Itrongay
Si ka	TAP	30	30	$CaMgSi_2O_6$ diopside Wakefield
Fe ka	LLIF	30	30	Fe_2SiO_4 fayalite Rockport
Mg ka	LTAP	30	30	Frank Smith pyrope garnet
Ti ka	PET	30	30	$SrTiO_3$
Sr la	LPET	30	30	$SrTiO_3$
Al ka	TAP	30	30	Frank Smith pyrope garnet
Mn ka	LLIF	30	30	$(Mn,Fe)_3Al2Si_3O_{12}$ spessartine, Navegadora Mine

Table 2-A-2. Carbonate mineral EMPA analysis

Sample ID	2245281	2245281	2245301	2245301	2245301	2242942	2245427	2245287	2242945	2242945	2242945	2242945
Analysis Pt.	1	2	1	2	3	1	1	1	1	2	4	5
(wt. %)												
FeO	0.51	0.31	0.46	0.5	0.64	0.06	0.27	0.96	0.07	0.07	1.3	1.48
MnO	0.02	0.02	0.99	0.89	1.02	0.03	0.8	0.81	0.15	0.19	0.58	0.58
MgO	0.07	0.07	0.32	0.19	0.39	0.1	0.44	0.24	0.03	0	0.17	0.33
CaO	54.03	54.28	52.61	55.71	52.57	55.63	59.81	60.16	58.78	59.45	56.28	57.22
SrO	0	0	0	0	0	0	0	0	0.11	0	0	0
CO_2	42.8	42.88	42.53	44.79	42.71	43.82	48.08	48.57	46.35	46.82	45.51	46.53
Total	97.43	97.56	96.91	102.08	97.33	99.64	109.4	110.74	105.49	106.53	103.84	106.14
(a.p.f.u)												
Fe	0.007	0.004	0.007	0.007	0.009	0.001	0.003	0.012	0.001	0.001	0.017	0.019
Mn	0	0	0.014	0.012	0.015	0	0.01	0.01	0.002	0.003	0.008	0.008
Mg	0.002	0.002	0.008	0.005	0.01	0.002	0.01	0.005	0.001		0.004	0.008
Ca	0.991	0.993	0.971	0.976	0.966	0.996	0.976	0.972	0.995	0.997	0.971	0.965
Sr									0.001			
Alteration facies early	Ep-(ab)	Ep-(ab)	Ep-(ab)	Ep-(ab)	Ep-(ab)	Ep-(ab)	Ep-(ab)	Ep-(ab)	Ep-(ab)	Ep-(ab)	Ep-(ab)	Ep-(ab)
Alteration facies late	Prh-(wm-prh)	Prh-(wm-prh)				Prh-(wm-prh)	Prh-(wm-prh)	Tur-(wm-chl*)	Tur-(wm-chl*)	Tur-(wm-chl*)	Tur-(wm-chl*)	Tur-(wm-chl*)

Atoms per formula unit (a.p.f.u) is based on normalization to 5 atoms and assumes one CO_3. Mineral abbreviations: ab = albite, bt = biotite, chl = chlorite, ep = epidote, Kfs = K-feldspar, prh = prehnite, wm = white-mica, wm-chl* = white-mica–chlorite alteration facies described in the main body text, and tur = tourmaline.

Table 2A-2. Continued

Sample ID	2245333	2228247	2234412	2245328	2245328	2245328	2245328	2247902	2247902	2234402	2234402	2234402
Analysis Pt.	1	1	1	1	2	3	4	1	2	1	2	3
(wt. %)												
FeO	0.21	0.1	0.79	0.03	0.03	0.02	0.01	0.35	0.11	0.11	0.09	0.1
MnO	0	0.13	0.19	0.28	0.3	0	0	1.61	0.33	0.13	0.15	0.13
MgO	0	0.02	0.79	0.1	0.09	0.01	0.03	0.19	0.02	0	0	0
CaO	54.1	59.96	54.22	55.38	58.75	53.28	53.43	55.23	55.9	56.83	57.35	57.02
SrO	0	0	0	0.24	0.37	0.82	0.83	0	0	0	0	0
CO2	42.59	47.22	44.02	43.87	46.57	42.19	42.32	44.77	44.16	44.75	45.16	44.89
Total	96.9	107.43	100.01	99.9	106.11	96.32	96.62	102.15	100.52	101.82	102.75	102.14

a.p.f.u												
Fe	0.003	0.001	0.011	0	0	0	0	0.005	0.002	0.002	0.001	0.001
Mn		0.002	0.003	0.004	0.004			0.022	0.005	0.002	0.002	0.002
Mg		0	0.02	0.002	0.002	0	0.001	0.005	0			
Ca	0.997	0.997	0.967	0.991	0.99	0.991	0.991	0.968	0.993	0.997	0.997	0.997
Sr				0.002	0.003	0.008	0.008					
Alteration facies early	Tur-(wm-chl*)	Bt	Ep-(Kfs)	Ep-(Kfs)	Ep-(Kfs)	Ep-(Kfs)	Ep-(Kfs)	Ep-(ab)	Ep-(ab)	Wm-chl*	Wm-chl*	Wm-chl*
Alteration facies late	Ep-(ab)	Ab	Tur-(wm-chl*)	Prh-(wm-prh)	Prh-(wm-prh)	Prh-(wm-prh)	Prh-(wm-prh)	Prh-(wm-prh)	Prh-(wm-prh)	Prh-(wm-prh)	Prh-(wm-prh)	Prh-(wm-prh)

Halley, S.W., Dilles, J.H., and Tosdal, R.M., 2015, Footprints: Hydrothermal Alteration and Geochemical Dispersion Around Porphyry Copper Deposits: SEG Newsletter, No. 100, p. 12–17.

Laniz, R. V., Stevens, R.E., and Norman, M.B., 1964, Staining of Plagioclase Feldspars and Other Minerals with F.D. and C. Red no. 2: GEOLOGICAL SURVEY PROFESSIONAL PAPER 501, v. 501–B, p. B152–B153.

Lypaczewski, P., & Rivard, B., 2018, Estimating the Mg# and Al^{VI} content of biotite and chlorite from shortwave infrared reflectance spectroscopy: Predictive equations and recommendations for their use. International Journal of Applied Earth Observation and Geoinformation, 68, 116-126.

McMonigle, M.D., 2015, Feldspar Staining of the Plutonic Rocks of the Salinian Terrane: College of Marin, Kentfield, California, 1-8 p.

Pouchou, I.L., Pichoir, F., 1985, "PAP" (ϕ–ρ–Z) procedure for improved quantitative microanalysis. In: ARMSTRONG IT (ed) Microbeam Analysis. San Francisco Press, San Francisco, p. 104–106.

Swayze, G. A., Clark, R. N., Goetz, A. F., Livo, K. E., Breit, G. N., Kruse, F. A., ... & Stoffregen, R. E. (2014). Mapping advanced argillic alteration at Cuprite, Nevada, using imaging spectroscopy. *Economic Geology*, *109*(5), 1179-1221.

Appendix 2-B

Sulfur species in altered rocks from the GCB

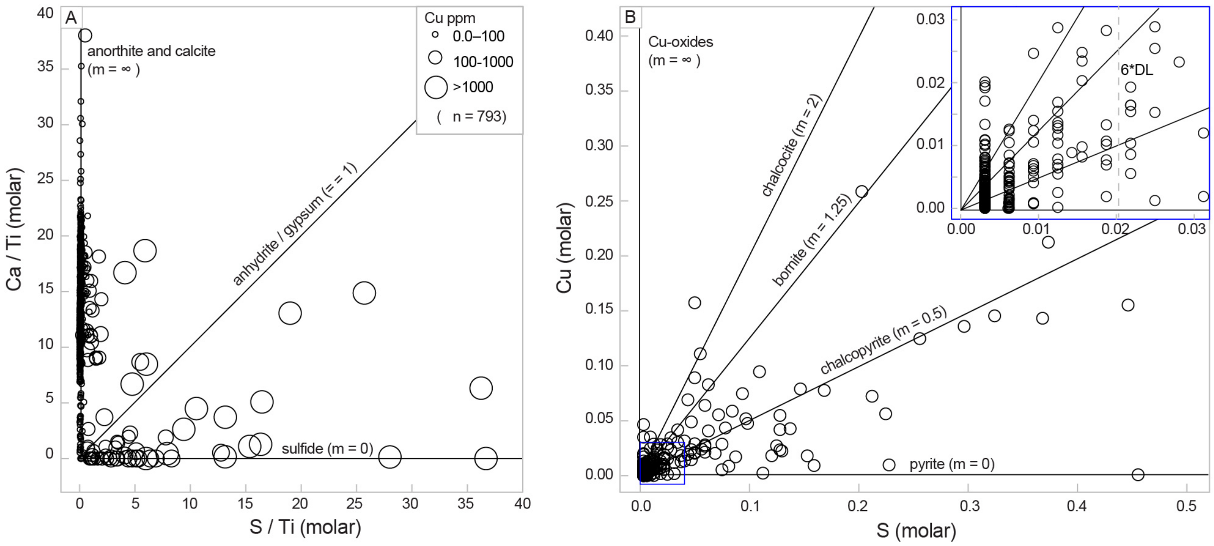

Figure 2-B-1. A. Ca /Ti versus S /Ti from lithogeochemistry with mineral control lines. Sulfur present in Guichon Creek batholith rocks is dominantly sulphide minerals. B. Cu versus S with sulfide mineral species control lines. Approximately 90% of data have S below the limit of detection

Appendix 2-C

Supplementary data for Figure 2-16.

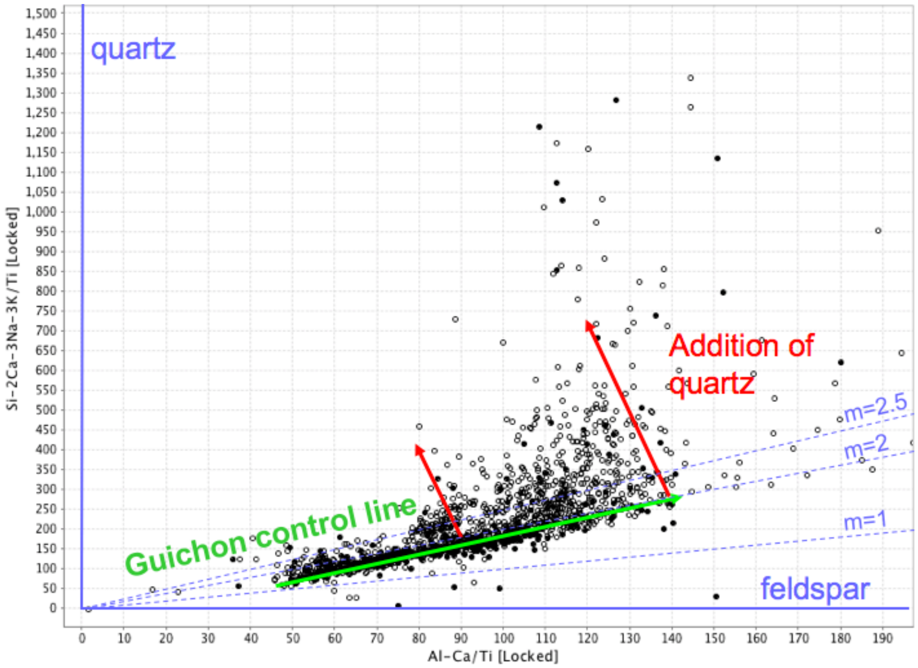

Figure 2-C-1. Al-Ca/Ti versus Si-2Ca-3Na-3K/Ti PER diagram, with quartz and feldspar control lines, modified after Moss (2011). Least altered Guichon Creek rocks cluster around a line of m = 1.9. Rocks fractionated upwards along the Guichon control line from Border to Bethsaida facies. Solid circle are samples with rock slab characterization. Open circles are Teck Resource ltd. data.

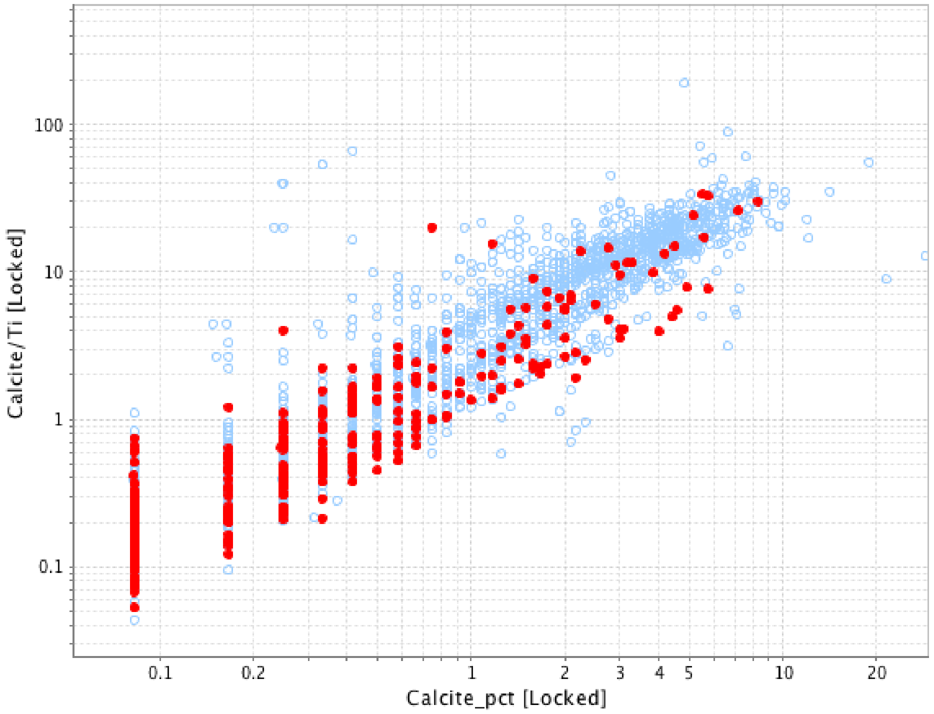

Figure. 2-C-2. Calcite wt. % versus calcite/Ti$_{(molar)}$. Note the positive correlation between the terms. The solid red data points correspond to the data points shown on the map in Figure 2-16B. The blue hollow points are additional samples that were used to hand contour the >0.75 wt. % calcite domain.

Appendix 3-A

Table 3-A-1. Sample matrix

Station	East	North	EMPA Data					Isotope data	
			Feldspar	Epidote	Amphibole	Chlorite	Tourmaline	D&O	B
2758647	637469	5593388				ch			
2014GL153	629621	5591817						D&O	
2015GL-V11-13	638278	5594000						D&O	
2015GL010	640611	5587446		ep				D&O	
2015GL051	641410	5584234				ch			
2015GL052	641872	5582754		ep					
2015GL064	643512	5582769		ep					
2015GL081	643590	5580180		ep					
2015KB_B14-015_202.6	643452	5594980		ep				D&O	
2015KB022	644003	5596400			amph	ch			
2015KB030	645350	5597348			amph	ch			
2015KB041	643873	5595660	fsp			ch			

2015KB043A	646623	5596976						D&O	
2015KB046	644282	5596132				ch			
2015KB047	643621	5597401	fsp			ch	tur		
2015KB056	646965	5596434	fsp	ep	amph		tur	D&O	B
2015KB060	646190	5597794	fsp		amph	ch			
2015KB062	646709	5596976		ep				D&O	
2015KB069	650192	5599013					tur		B
2015KB087-SB	648506	5597775	fsp		amph	ch	tur	D&O	B
2015KB093	647553	5598812					tur		B
2015KB102	646085	5595515		ep				D&O	
2015KB103A	646516	5595539					tur	D&O	
2015KB111	648084	5596986	fsp		amph	ch		D&O	
2015KB120	652400	5587195				ch			
2015KB136	651134	5586490				ch			
2015KB144	650179	5586864				ch			
2015KB145	649496	5586489				ch			
2015KB152	648917	5585313						D&O	
2015KB152-SA	648917	5585313		ep					
2015KB154	648591	5586106		ep					
2015KB156	648164	5585853		ep					
2015KB168	647703	5586167				ch			
2015KB169A	647351	5586974		ep		ch			
2015KB169B	647351	5586974	fsp	ep		ch			
2015KB171	646588	5588317		ep				D&O	
2015KB178	646900	5586768	fsp		amph	ch			
2015KB180	646281	5587062		ep				D&O	
2015KB182	646525	5586377		ep				D&O	
2015KB184	646156	5587500				ch			
2015KB210	645303	5587005			amph	ch			
2015KB213	643998	5589888				ch			
2015KB216	644272	5590052	fsp			ch			
2015KB218	642894	5589418		ep				D&O	
2015KB229B	643531	5588947	fsp	ep	amph			D&O	
2015KB243	642548	5591322				ch			
2015KB250	639686	5591903				ch			
2015KB266	642490	5588280	fsp		amph	ch	tur		B
2015KB270	642180	5588281					tur		B
2015KB276	640869	5589062						D&O	
2015KB278	640854	5589025	fsp	ep				D&O	
2016KB001	634116	5590894						D&O	
2016KB008	644892	5583047						D&O	
2016KB010	652564	5574416					tur	D&O	
2016KB016	644478	5575437		ep					
2016KB017	642892	5575277		ep					
2016KB018	641882	5575729				ch			

2016KB019	646143	5575035	ep		ch			
2016KB023	643239	5572898			ch			
2016KB035	645835	5570571	ep					
2016KB041	643020	5570520			ch			
2016KB042	644507	5571095	ep					
2016KB047	648777	5568118		amph	ch	tur		B
2016KB048	646119	5568409	ep		ch			
2016KB061	640492	5588376	ep				D&O	
BC14124	637058	5591933			ch			
BC14187	635424	5592724			ch			
BC14213	636570	5591263			ch			
BC14318	632722	5597417			ch			
B13-130_293m	642527	5595700			ch		D&O	
BETH_NORTH	640514	5601872	ep		ch		D&O	
MD004	634574	5586650			ch			
MD060	640557	5598038			ch			

Feldspar Staining

Slab staining was performed in the Mineral Deposit Research Unit wet-chemical heavy-mineral separates lab in the Department of Earth and Ocean Sciences at the University of British Columbia. The staining was carried out under a fume hood using the required personal safety equipment: latex and long heavy duty rubber gloves, lab coat and HF-resistant rubber apron, safety glasses and face shield with throat guard, and a HF burn kit (Ca gluconate gel).

Procedure

The following work-flow was used to test for the presence of K-feldspar, Ca-component in plagioclase, carbonate and prehnite (Laniz et al., 1964; McMonigle, 2015):

1. Rock samples were cut on a diamond saw into approximately 2 cm thick by 10 x 10 cm rock slabs.
2. The slabs were labeled and photographed prior to staining.
3. The slabs were etched in 45-52% solution of HF in shallow bath for 60 seconds than rinsed in two water baths.
4. A 7% solution of Amaranth (~66 g in 1 l distilled water) was prepared and placed in shallow bath. The etched rocks slabs were dipped face down in the bath for 10 s before being rinsed off in multiple baths and set at an angle to air drying under the fume hood.
5. A 20% solution of Sodium Colbaltinitrite (~20 g for every 100 ml distilled water) was placed in a shallow bath. The rinsed and dried bath was dipped in the bath for ten seconds before a final rinse and drying for 20 minutes.
6. The stained face was photographed.

Interpretation of staining colors

Primary K-feldspar stains yellow and is distinguished from secondary K-feldspar based on morphology and distribution in the rock slab. Primary K-feldspar is predominantly hosted in groundmass and is interstitial to euhedral plagioclase crystals, whereas secondary K-feldspar forms linear features associated with fractures and replaces plagioclase in patches. The absence of yellow-staining, in K-feldspar-bearing protolith, indicates K-feldspar-destructive albite alteration. In unaltered and weakly white-mica–prehnite dusted plagioclase crystals the calcic component stains a pink to red color. Plagioclase that appears milky white in hand specimen and turbid in transmitted light (due to fine-grained white-mica inclusions) does not take the stain as completely, or at all, compared to fresh plagioclase. Albite does not stain with Amaranth. Similarly, strongly albitized plagioclase does not stain pink, thus the absence of pink-purple Amaranth stain indicates modification of plagioclase. Veins and calcite and prehnite stain a distinct pink color.

Lithogeochemical Analytical Methodology

Lithogeochemical analyses were undertaken at ACME Analytical Laboratory (now Bureau Veritas Laboratories), Vancouver, Canada using Method G4A-G4B. Sample submittals were accompanied by a number of external matrix-matched pulp standards, coarse blanks, and pulp duplicate request, which were in addition to those used by the analytical facility in order to ensure quality control. Sample preparation consisted of a 70% crush to 10 mesh with a 500–1000 g cut being pulverized. A 0.2 g sample split was fused at 1000°C with 1.5 g of an 80:20 lithium metaborate/tetraborate mix. The cooled bead was digested in 100 mL of 5% HNO_3. ICP-ES analysis determines major element concentrations reported as the common oxides. The same whole rock fusion solution was analyzed by ICP-MS (Perkin Elmer Elan 6000) to determine absolute concentrations of trace elements using the following methods. Method 1F-MS: A 1 g subsample was digested in 6 mL of hot (95°C) modified Aqua Regia (1:1:1 $HCl:HNO_3:H_2O$) for 1 hour, cooled and made to 20 mL volume with 5% HCl. The solution was analyzed by ICP-MS (Perkin Elmer Elan 6000 or 9000). Method G3B: A 30 g sample split was custom mixed with PbO fire assay fluxes and fired for 45 minutes at 1050°C. Molten Pb + slag was poured into an iron mold, cooled and Pb button recovered. Heating at 950°C in a MgO cupel rendered a Ag ± Au, Pt, Pd dore bead. The bead was parted in hot HNO_3, digested by adding HCl and aspirated into a Jarrel Ash Atomcomp 875 ICP-ES to determine Au, Pt and Pd. Upper limits = 10 ppm. Method G7TD: A 0.5 g sample split was digested in 20 mL of 4-Acid solution ($HNO_3:HClO_4:HF:H_2O$) at 200°C and taken to dryness. The residue was dissolved in 16 mL of 50% HCl at ~95°C for 1 hour then made to volume in a 100 mL volumetric flask with 5% HCl. ICP-ES analysis determines total Ni. Loss on Ignition (LOI) is report as % weight loss on a 1 g split ignited at 1000°C. LECO combustion analysis was used to determine total C and S on a 0.2 g sample split which is heated and combusted in the presence of pure oxygen. During the process, C and S are oxidized to form CO_2 and SO_2 and measured with an element analyzer.

Lithogeochemical Data and Quality Assurance (QA) and Quality Control (QC)

Blanks, pulp duplicates, and standard reference material (SRM) were inserted at a rate of 1 in 30 samples each. Blank material used is a coarse crushed granodiorite purchased in bulk from an aggregate supplier and tested numerous times in unsure homogeneity of low level metal content (carry over contamination during sample preparation). Pulp duplicates were requested to test how homogenous unknown rock pulps are (lab sample prep). Accuracy was evaluated by using matrix matched Guichon Creek batholith pulps (SRM) developed by Teck for use in evaluating in resource estimate assay data.

The following quality control rules were applied to all analytical sample batches included in this study. Coarse blank material has Cu and Mo values below 10 times the detection limit (10 ppm) for Cu and Mo (by 1F-MS). Requested duplicate pulp pairs plotted on min-max plots are all within 10% relative error of each other for the rock forming elements, indicating that rocks pulps were well homogenized and digestion techniques are consistent. Collectively the SRM pulps, inserted within analytical batch, indicate an acceptable lab bias (< 4 %) for major elements relative to the accepted values determined from round-robin testing.

Electron Microprobe Analyses

Electron microprobe analyses (EPMA) was performed during several analytical sessions using the CAMECA SX100 at the Electron Microprobe Laboratory at the University of Alberta. Wavelength dispersive spectrometry (WDS) was carried out to primarily identify the major and minor chemistry of silicate alteration minerals. For the WDS the EPMA beam was operated in spot mode at an accelerating voltage of 20 kV, a probe current of 20 nA, and a beam diameter between 1–5 µm. Unknowns were analyzed at a peak count time of 30 s and background count time of 30 s. Standards were analyzed for 20–30 s on peak. Data reduction was completed using the "PAP" f(rZ) method (Pouchou and Pichoir, 1985). The standards used are listed in Table A1 and carbonate mineral results in Table A2.

Table 3-A-2. EMPA standards

Element/Line	Crystal	OnPeak Time	OffPeak Time	Standard
Na ka	LTAP	30	30	$NaAlSi_3O_8$ albite VA 131705
Ca ka	PET	30	30	Plagioclase (labradorite) 115900
K ka	LPET	30	30	$KAlSi_3O_8$ sanidine Itrongay
Si ka	TAP	30	30	$CaMgSi_2O_6$ diopside Wakefield
Fe ka	LLIF	30	30	Fe_2SiO_4 fayalite Rockport
Mg ka	LTAP	30	30	Frank Smith pyrope garnet
Ti ka	PET	30	30	$SrTiO_3$
Sr la	LPET	30	30	$SrTiO_3$
Al ka	TAP	30	30	Frank Smith pyrope garnet
Mn ka	LLIF	30	30	$(Mn,Fe)_3Al2Si_3O_{12}$ spessartine, Navegadora Mine

Hydrogen and Oxygen isotope analysis

QFIR quality assurance and control protocols include generating 10% analyses each of the following: 1) certified reference materials and secondary standards 2) random duplication of unknown samples and 3) blanks. Precision, in permil notation (‰) is based upon duplicate sample analyses. Accuracy is based upon primary or secondary standard analyses and is as follows: δD of 1.5‰ and $\delta^{18}O$ of 0.1‰.

For hydrogen in silicate minerals, samples were weighed into silver capsules, degassed for 1 hour at 100°C then crushed and loaded into a zero-blank auto sampler. The hydrogen isotopic composition was measured using a Thermo-Finnigan thermo-combustion elemental analyzer (TC/EA) coupled to a Thermo-Finnigan Delta^{Plus} XP Continuous-Flow Isotope-Ratio Mass Spectrometer (CF-IRMS). δD values are reported using delta (δ) notation in permil (‰), relative to Vienna Standard Mean Ocean Water (VSMOW), with a precision of 3‰.

Oxygen from silicate minerals was extracted from 5 mg samples at 550-600°C according to the conventional BrF5 procedure of Clayton and K Mayeda (1963) and analyzed via dual inlet on a Thermo-Finnigan Delta^{Plus} XP Isotope-Ratio Mass Spectrometer (IRMS). $\delta^{18}O$ values are reported using the delta (δ) notation in units of permil (‰) relative to Vienna Standard Mean Ocean Water (VSMOW) international standard, with a precision of 0.1‰.

Boron isotope analysis

The B isotope analyses were done with a nominal 13 kV, 5 nA ^{16}O– primary beam focused to a 5 µm spot on the sample surface. Each analysis was preceded by a 60 s pre-burn on a 10 × 10 µm raster to remove the gold coating and establish stable sputtering conditions. Positive secondary ions were extracted using a +10 kV potential applied to the sample holder. A 400 µm diameter contrast aperture, a 3000 µm field aperture and a 50 V energy window were used without application of a voltage offset. The instrument was operated at a mass resolving power of M/ΔM ≈ 2400, which is sufficient to separate the ^{11}B+ from the ^{10}B^{1} H+ mass station (ΔM = 900) and ^{10}B^{+} from the ^{9}Be^{1} H^{+} mass stations (ΔM = 1400). Faraday cup multi-collection was applied for simultaneous measurement of ^{10}B and ^{11}B. Each analysis comprised 20 mass scans (4 blocks of 5 measurements), resulting in a total analysis time of about 3 min.

To determine instrumental mass fractionation (IMF) and monitor analytical quality we used the matrix-matched reference materials of Harvard 112566 (schorl, ^{11}B/^{10}B = 3.9931) and Harvard 108796 (dravite, ^{11}B/^{10}B = 4.0169). All standard, unknown, and IMF results are in Supplemental material 3-B.

Strontium isotope analysis

Whole rock powders were then dissolved in Teflon beakers using an 8 ml (4:1) mixture of 29 M HF – 15 M HNO_3. After five days of digestion, the solutions were evaporated to dryness and re-dissolved in 6M HCl for three days. Samples were dried down and re-dissolved in 1.0 ml of 2.5 M HCL before being loaded onto a column containing cation exchange resin AG-50W-X8, H+ form, (200-400 mesh) to isolate a Sr fraction. The Sr fraction was evaporated to dryness and then taken up in 3M HNO_3 and loaded onto a column containing Eichrom© Sr resin to separate out the Sr and remove Rb and other remaining elements. Sr was loaded onto a single tungsten filament with 2 μL of Sr activator. Strontium isotopic compositions were determined using a multi-collector Finnigan Mat 262 mass spectrometer in static mode for concentration determination, and dynamic mode for isotopic composition determination. Reproducibility of the Sr isotope analyses were evaluated using the standard NBS-987 with an accepted value = 0.710240. Mean ^{87}Sr/^{86}Sr value for NBS-987 standard reference material for 20 runs (n=20) was 0.710233 with a standard deviation of 0.000013 (1σ). Sr ratios were normalized to ^{88}Sr/^{86}Sr = 8.375202 and measured values were adjusted to the NBS-987 standard (accepted value=0.710240).

Appendix 3-B

Appendix 3-B

Oxygen (1000lnα Mineral-Fluid)

	Fractionation temperature (C°)									Reference
	200	*250*	*300*	*350*	*400*	*450*	*650*	*700*	*750*	
Plagioclase (An = 0.35)		6.1	4.5	3.3	2.3	1.5	-0.5	-0.8	-1.0	O'Neil, J.R.; and Taylor, H.P. Jr. (1967) The oxygen isotope and cation exchange chemistry of feldspars; Amer. Mineral. 52, 1414-1437
K-feldspar							0.5	0.1	-0.2	O'Neil, J.R.; and Taylor, H.P. Jr. (1967) The oxygen isotope and cation exchange chemistry of feldspars; Amer. Mineral. 52, 1414-1438
Biotite							-2.6	-2.7	-2.5	Bottinga, Y.; and Javoy, M. (1973) Comments on oxygen isotope geothermometry; Earth Plan. Sci. Lett. 20, 250-265
Quartz		9.5	7.4	5.8	4.6	3.6	1.5	1.2	0.9	Clayton; R.N.; O'Neil, J.R.; and Mayeda, T.K. (1972) Oxygen isotope exchange between quartz and water; J. Geophys. Res. 77, 3057-3067
Albite		6.9	5.2	3.9	2.8	2.0				O'Neil, J.R.; and Taylor, H.P. Jr. (1967) The oxygen isotope and cation exchange chemistry of feldspars; Amer. Mineral. 52, 1414-1437
Albite		6.0	4.4	3.3	2.4					Zheng, Y.F. (1993) Calculation of oxygen isotope fractionation in hydroxyl-bearing silicates; Earth. Plan. Sci. Lett. 120, 247-262
Albite		7.7	5.8	4.4	3.2					Bottinga, Y.; and Javoy, M. (1973) Comments on oxygen isotope geothermometry; Earth Plan. Sci. Lett. 20, 250-265
Tourmaline		4.2	2.8	1.8	1.1	0.5				Zheng, Y.F. (1993) Calculation of oxygen isotope fractionation in hydroxyl-bearing silicates; Earth. Plan. Sci. Lett. 120, 247-263
Epidote		2.2	1.0	0.2	-0.4	-0.8	-1.4			Zheng, Y.F. (1993) Calculation of oxygen isotope fractionation in hydroxyl-bearing silicates; Earth. Plan. Sci. Lett. 120, 247-263
Chlorite		1.0	0.1	-0.7	-1.3					Wenner, D.B.; and Taylor, H.P. Jr. (1971) Temperatures of serpentinization of ultramafic rocks based on 18O/16O fractionation between coexisting serpentine and magnetite; Contrib. Mineral. Petrol. 32, 165-185
Hornblende							-2.3	-2.3	-2.2	Zheng, Y.F. (1993) Calculation of oxygen isotope fractionation in hydroxyl-bearing silicates; Earth. Plan. Sci. Lett. 120, 247-263
Prehnite	5.7	3.8	2.4	1.4						Zheng, Y.F. (1993) Calculation of oxygen isotope fractionation in hydroxyl-bearing silicates; Earth. Plan. Sci. Lett. 120, 247-262
Actinolite			0.0	-0.7	-1.2	-1.5				Zheng, Y.F. (1993) Calculation of oxygen isotope fractionation in hydroxyl-bearing silicates; Earth. Plan. Sci. Lett. 120, 247-263
Muscovite		4.8	3.4	2.2	1.4	0.7				O'Neil, J.R.; and Taylor, H.P. Jr. (1969) Oxygen isotope equilibrium between muscovite and water; J. Geophys. Res. 74, 6012-6022

Hydrogen (1000lnα Mineral-Fluid)

	Fractionation temperature (C°)									**Reference**
	200	*250*	*300*	*350*	*400*	*450*	*650*	*700*	*750*	
Biotite							-27.8	-25.3	-23.2	Suzuoki, T.; and Epstein, S. (1976) Hydrogen isotope fractionation between OH-bearing minerals and water; Geochim. Cosmochim Acta 40, 1229-1240
Tourmaline			-54.7	-42.0	-31.9	-23.9				Kotzer, T.G.; Kyser, T.K.; King, R.W.; and Kerrich, R. (1993) An empirical oxygen- and hydrogen-isotope geothermometer for quartz-tourmaline and tourmaline-water; Geochim. Cosmochim. Acta 57, 3421-3426
Epidote		-27.9	-33.6	-38.0	-41.4	-44.1	-51.0			Chacko T., Riciputi L.R., Cole D.R. & Horita J. (1999) A new technique for determining equilibrium hydrogen isotope fractionation factors using the ion microprobe: Application to the epidote-water system. Geochimica et Cosmochimica Acta, 63, p. 1-10.
Chlorite		-37.5	-35.3	-33.5	-32.2	-31.1				Graham, C.M.; Atkinson, J.; and Harmon, R.S. (1984) Hydrogen isotope fractionation in the system chlorite-water; NERC 6th progress report of research 1981-1984, NERC Pub. Ser. D., 25, 99. 139
Hornblende							-20.1	-17.3	-14.9	Suzuoki, T.; and Epstein, S. (1976) Hydrogen isotope fractionation between OH-bearing minerals and water; Geochim. Cosmochim Acta 40, 1229-1240
Prehnite	-40.5	-37.5	-35.3	-33.5	-32.2	-31.1				Graham, C.M.; Atkinson, J.; and Harmon, R.S. (1984) Hydrogen isotope fractionation in the system chlorite-water; NERC 6th progress report of research 1981-1984, NERC Pub. Ser. D., 25, 99. 139
Actinolite		-37.5	-35.3	-33.5	-32.2	-31.1				Graham, C.M.; Atkinson, J.; and Harmon, R.S. (1984) Hydrogen isotope fractionation in the system chlorite-water; NERC 6th progress report of research 1981-1984, NERC Pub. Ser. D., 25, 99. 139
Muscovite		-61.7	-48.2	-37.8	-29.7	-23.2				Suzuoki, T.; and Epstein, S. (1976) Hydrogen isotope fractionation between OH-bearing minerals and water; Geochim. Cosmochim Acta 40, 1229-1240

Modal mineralogy and mineral weighted 1000 lnα values used for calculate the initial fluids composition in equilibrium with rocks of the GCB

	Fresh rock modal abundance (%)					Formation temperature (C°)	Weighted D 1000 ln α	Weighted O 1000 ln α
	Plagioclase (An = 35)	K-feldspar	Quartz	Biotite	Hornblende			
Guichon	50	13	19	7	10	750	-0.8	-18.9
Chataway	54	11	21	5	9	750	-0.7	-17.9
Bethlehem	62	8	18	6	6	700	-0.5	-21.3
Skeena	59	10	23	4	5	700	-0.4	-20.9
Bethsaida	52	11	29	7	1	700	-0.2	-23.2

Whole-rock D and O isotope results for least altered host rocks

Station	Host rock			Measured values		Temperature (C°)	Calculated	
		Al/Ti	Si/Ti	δD ‰	δ^{18}O ‰		δD ‰	δ^{18}O ‰
2013MD044	Guichon	45	138	-74.6	6.4	750	-51.5	7.2
2013MD043	Chataway	51	161	-77.5	6.7	750	-51.8	7.4
2013MD049	Bethlehem	68	223	-86.2	8.3	700	-64.8	8.8
2013MD072	Skeena	86	302	-84.1	7.5	700	-58.8	7.9
2013MD034	Skeena	78	259	-81.9	8.0	700	-61.1	8.4
2015GL010	Bethsaida	112	425	-99.5	7.1	700	-76.3	7.4
2013MD069	Bethsaida	98	353	-79.4	9.4	700	-56.2	9.6
2013MD073	QFPM	159	635	-87.0	8.6	700	-61.7	7.9

Table 3-B-3. Modal mineralogy and mineral weighted 1000 lnα values used for calculate the initial fluids composition in equilibrium with rocks of the GCB

Host Rock	Fresh rock modal abundance (%)					Formation temperature (C°)	Weighted D 1000 ln α	Weighted O 1000 ln α
	Plagioclase (An = 35)	K-feldspar	Quartz	Biotite	Hornblende			
Guichon	50	13	19	7	10	750	-0.8	-18.9
Chataway	54	11	21	5	9	750	-0.7	-17.9
Bethlehem	62	8	18	6	6	700	-0.5	-21.3
Skeena	59	10	23	4	5	700	-0.4	-20.9
Bethsaida	52	11	29	7	1	700	-0.2	-23.2

Table 3-B-4. Whole-rock D and O isotope results for least altered host rocks

				Measured values			Calculated	
Station	Host rock	Al/Ti	Si/Ti	δD ‰	δ^{18}O ‰	Temperature (C°)	δD ‰	δ18O ‰
2013MD044	Guichon	45	138	-74.6	6.4	750	-51.5	7.2
2013MD043	Chataway	51	161	-77.5	6.7	750	-51.8	7.4
2013MD049	Bethlehem	68	223	-86.2	8.3	700	-64.8	8.8
2013MD072	Skeena	86	302	-84.1	7.5	700	-58.8	7.9
2013MD034	Skeena	78	259	-81.9	8.0	700	-61.1	8.4
2015GL010	Bethsaida	112	425	-99.5	7.1	700	-76.3	7.4
2013MD069	Bethsaida	98	353	-79.4	9.4	700	-56.2	9.6
2013MD073	QFPM	159	635	-87.0	8.6	700	-61.7	7.9

Appendix 4-A

Methodologies

Feldspar Staining

Slab staining was performed in the Mineral Deposit Research Unit wet-chemical heavy-mineral separates lab in the Department of Earth and Ocean Sciences at the University of British Columbia. The staining was carried out under a fume hood using the required personal safety equipment: latex and long heavy duty rubber gloves, lab coat and HF-resistant rubber apron, safety glasses and face shield with throat guard, and a HF burn kit (Ca gluconate gel).

The following work-flow was used to test for the presence of K-feldspar, Ca-component in plagioclase, carbonate and prehnite (Laniz et al., 1964; McMonigle, 2015):

1. Rock samples were cut on a diamond saw into approximately 2 cm thick by 10 x 10 cm rock slabs.
2. The slabs were labeled and photographed prior to staining.
3. The slabs were etched in 45-52% solution of HF in shallow bath for 60 seconds than rinsed in two water baths.
4. A 7% solution of Amaranth (~66 g in 1 l distilled water) was prepared and placed in shallow bath. The etched rocks slabs were dipped face down in the bath for 10 s before being rinsed off in multiple baths and set at an angle to air drying under the fume hood.
5. A 20% solution of Sodium Colbaltinitrite (~20 g for every 100 ml distilled water) was placed in a shallow bath. The rinsed and dried bath was dipped in the bath for ten seconds before a final rinse and drying for 20 minutes.
6. The stained face was photographed.

Interpretation of staining colors

Primary K-feldspar stains yellow and is distinguished from secondary K-feldspar based on morphology and distribution in the rock slab. Primary K-feldspar is predominantly hosted in groundmass and is interstitial to euhedral plagioclase crystals, whereas secondary K-feldspar forms linear features associated with fractures and replaces plagioclase in patches. The absence of yellow-staining, in K-feldspar-bearing protolith, indicates K-feldspar-destructive albite alteration. In unaltered and weakly white-mica–prehnite dusted plagioclase crystals the calcic component stains a pink to red color. Plagioclase that appears milky white in hand specimen and turbid in transmitted light (due to fine-grained white-mica inclusions) does not take the stain as completely, or at all, compared to fresh plagioclase. Albite does not stain with Amaranth. Similarly, strongly albitized plagioclase does not stain pink, thus the absence of pink-purple

Amaranth stain indicates modification of plagioclase. Veins and calcite and prehnite stain a distinct pink color.

Electron Microprobe Analyses

Electron microprobe analyses (EPMA) was performed during several analytical sessions using the CAMECA SX100 at the Electron Microprobe Laboratory at the University of Alberta. Wavelength dispersive spectrometry (WDS) was carried out to primarily identify the major and minor chemistry of silicate alteration minerals in the Guichon Creek batholith, however, where present, carbonate minerals were also analyzed. For the WDS the EPMA beam was operated in spot mode at an accelerating voltage of 20 kV, a probe current of 20 nA, and a beam diameter between 1–5 µm. Unknowns were analyzed at a peak count time of 30 s and background count time of 30 s. Standards were analyzed for 20–30 s on peak. Data reduction was completed using the "PAP" f(rZ) method (Pouchou and Pichoir, 1985). The standards used are listed in table G1 and carbonate mineral results in table 4-A-1

Table 4-A-1. EMPA standards

Element/Line	Crystal	OnPeak Time	OffPeak Time	Standard
Na ka	LTAP	30	30	NaAlSi$_3$O$_8$ albite VA 131705
Ca ka	PET	30	30	Plagioclase (labradorite) 115900
K ka	LPET	30	30	KAlSi$_3$O$_8$ sanidine Itrongay
Si ka	TAP	30	30	CaMgSi$_2$O$_6$ diopside Wakefield
Fe ka	LLIF	30	30	Fe$_2$SiO$_4$ fayalite Rockport
Mg ka	LTAP	30	30	Frank Smith pyrope garnet
Ti ka	PET	30	30	SrTiO$_3$
Sr la	LPET	30	30	SrTiO$_3$
Al ka	TAP	30	30	Frank Smith pyrope garnet
Mn ka	LLIF	30	30	(Mn,Fe)$_3$Al2Si$_3$O$_{12}$ spessartine, Navegadora Mine

Grain and sample mounts

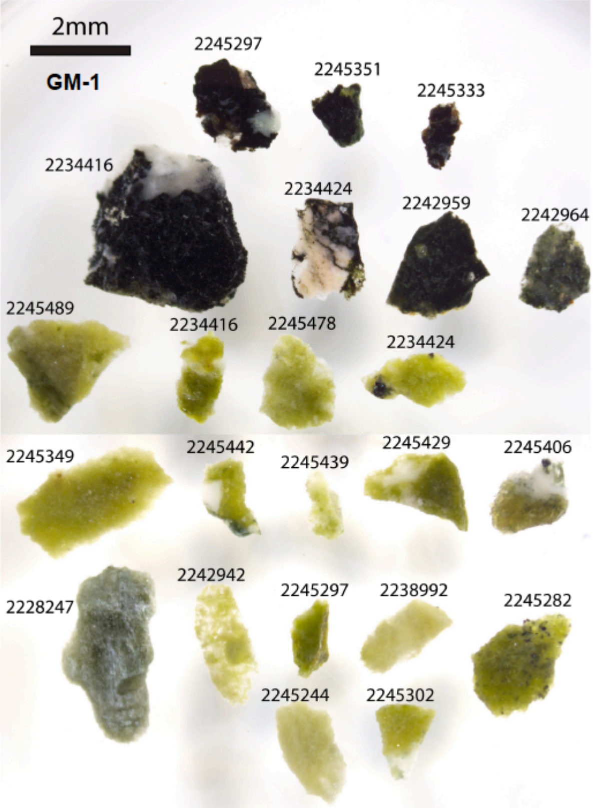

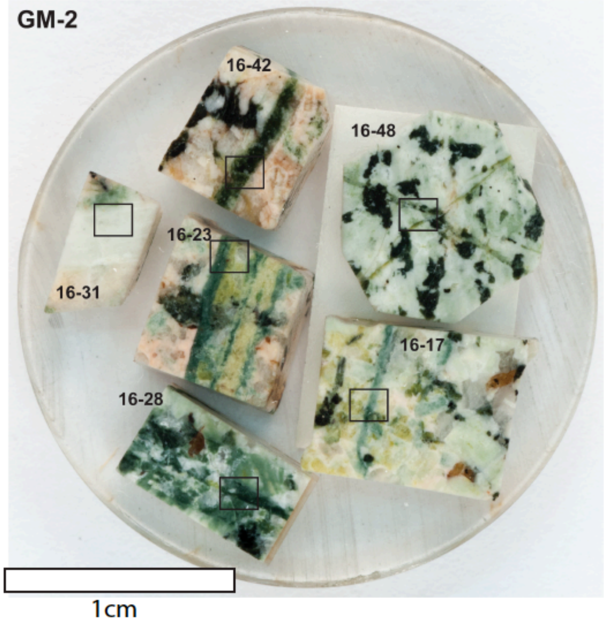

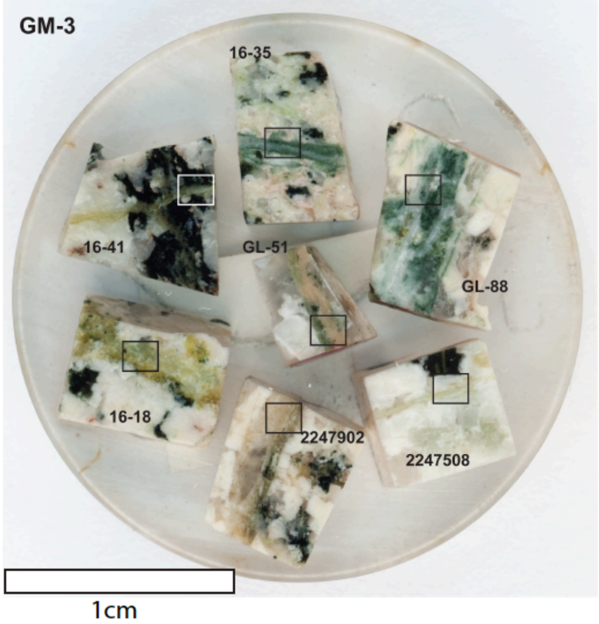

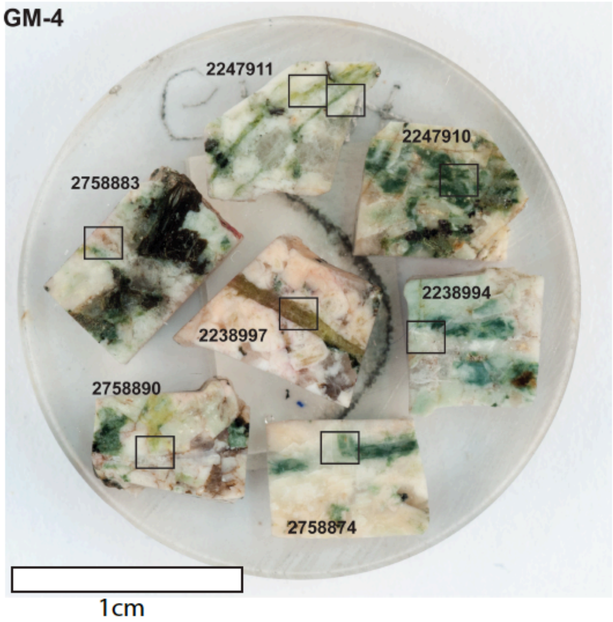

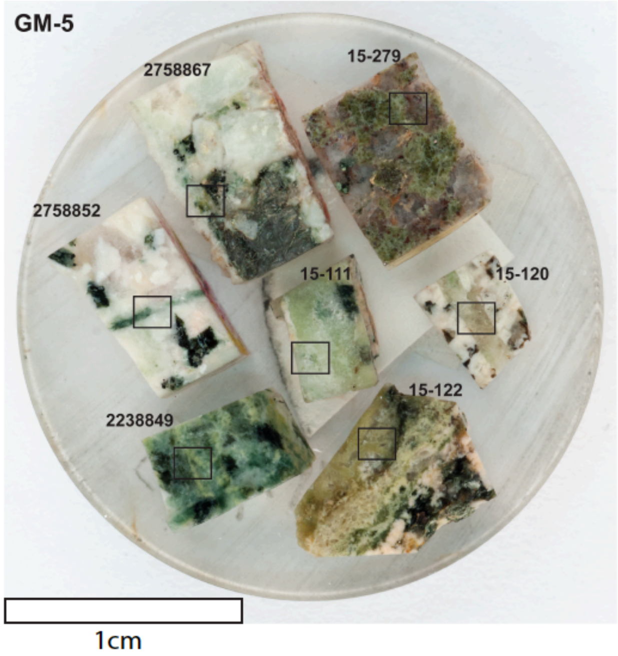
GM-5
2758867
15-279
2758852
15-111
15-120
15-122
2238849
1cm

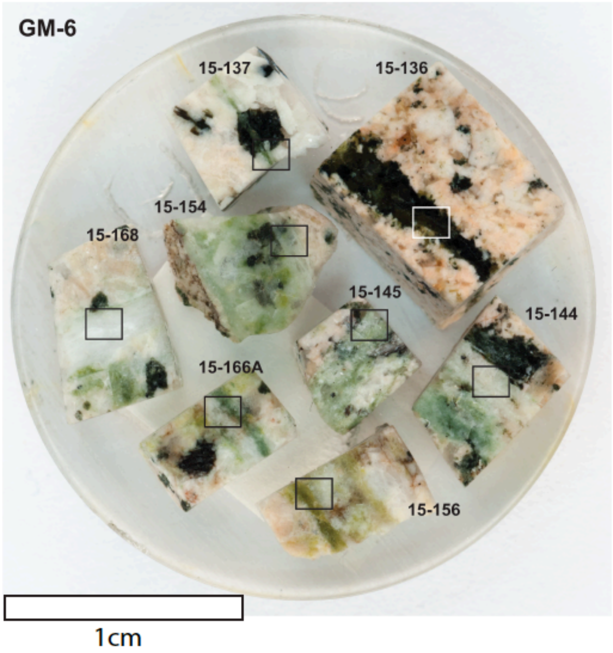
GM-6
15-137
15-136
15-154
15-168
15-145
15-144
15-166A
15-156
1cm

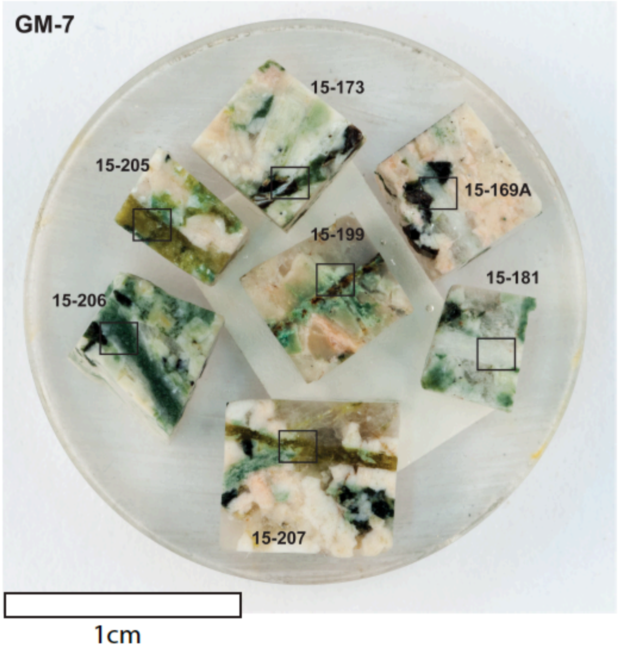
GM-7
15-173
15-205
15-169A
15-199
15-181
15-206
15-207
1cm

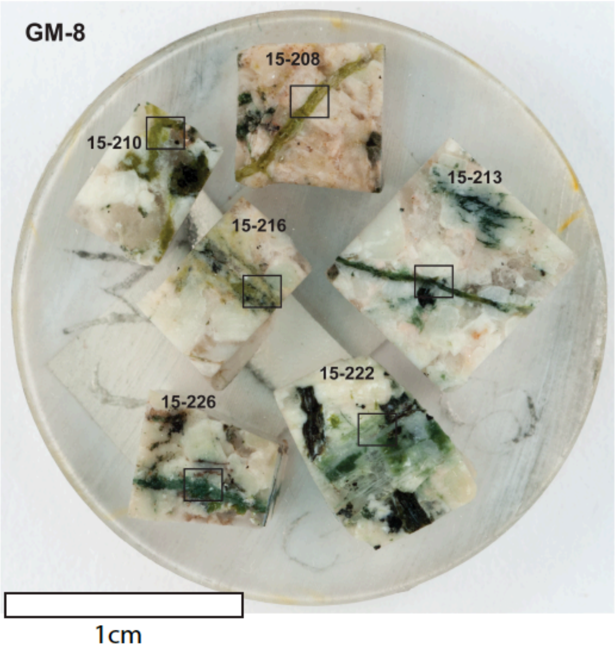
GM-8
15-208
15-210
15-213
15-216
15-222
15-226
1cm

Samples from other geological environments

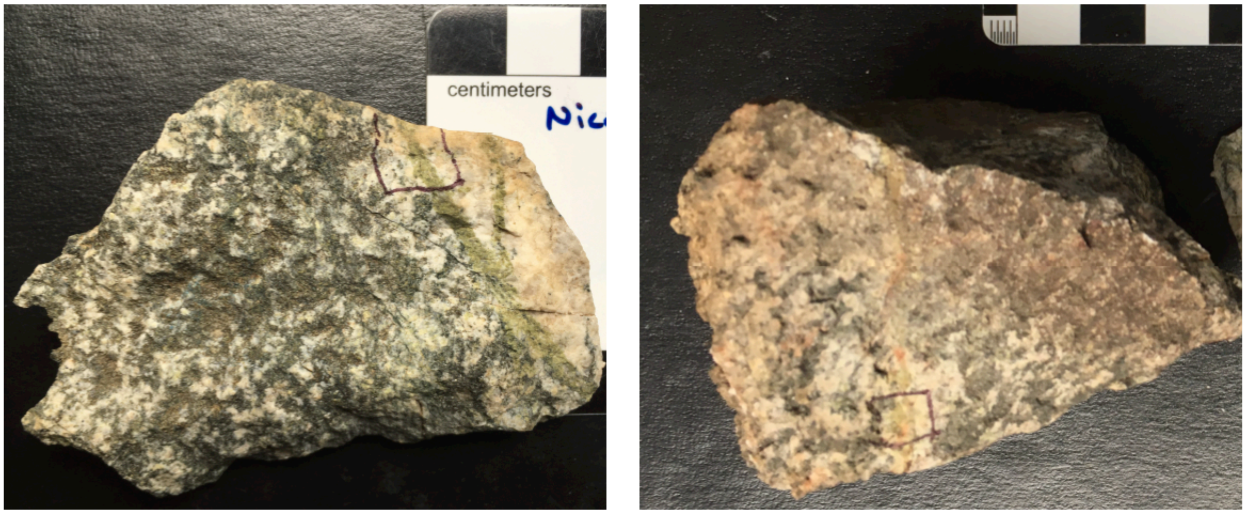

Nicola Batholith, southern BC. Epidote veins with localized bleached halos. Strong selective replacement of mafic minerals by chlorite. Weakly foliated quartz diorite. ***Greenschist / propylitic.***

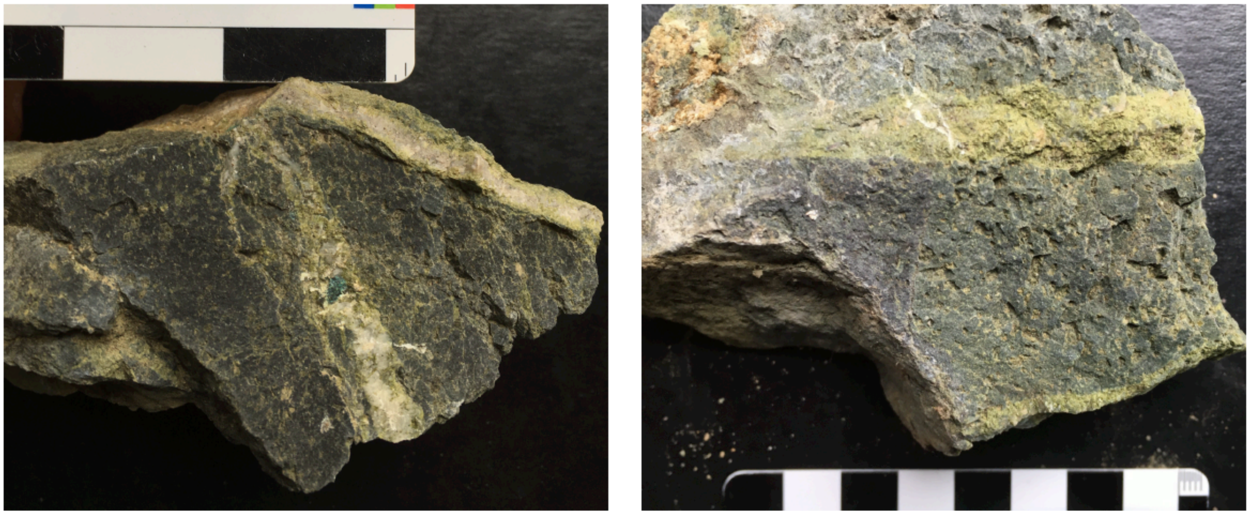

Nicola Group augite-phyric basaltic-andesite volcaniclastic rock (Group 3), Southern BC. Outcrop location is adjacent the Nicola batholith. Epidote and epidote-calcite veins with localized Cu-oxide (after chalcopyrite). Strong selective replacement of mafic minerals by epidote andc chlorite. Groundmass alerted to mixtures of fine-grained white-mica and chlorite. ***Hydrothermal / propylitic.***

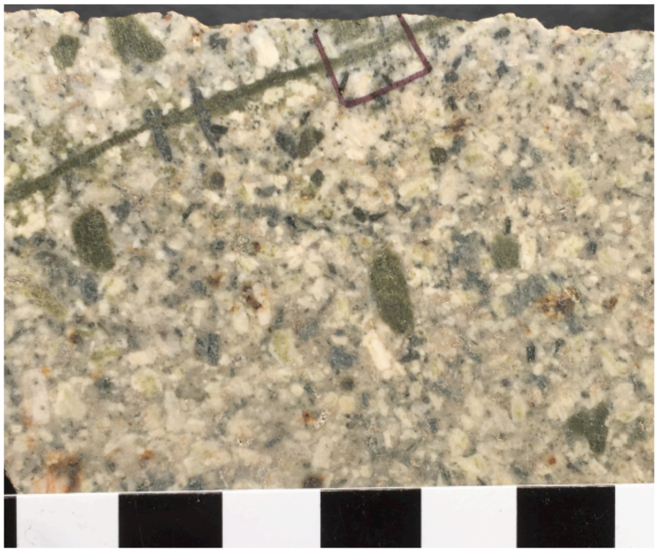

Yerington batholith porphyry Cu district, Nevada, US. Epidote vein with albite alteration and selective replacement of hornblende and primary K-feldspar by epidote and chlorite with accessory titanite. ***Sodic-calcic alteration*** adjacent potassic zone.

Appendix 5-A

Equations used

- x = measurand.
- μ = arithmetic mean or average.
- σ = arithmetic standard deviation.
- μ_g = geometric mean = $\sqrt[n]{x^1.x^2.x^3..x^n}$, which is also equal to the anti-logarithm of the arithmetic mean of the log-transformed distribution
- σ_g = geometric standard deviation $= e\sqrt{\frac{\sum_{xi=1}^{n}\left(ln\frac{xi}{\mu_g}\right)^2}{n}}$. The e and ln functions can be replaced with $10^{\wedge}$ and $\log_{10}$, when $\log_{10}$ transformation has been used, but the substitution does not affect the σ_g value.
- Simple CV = Simple coefficient of variation (relative standard deviation) = $CV_s = \frac{\sigma}{\mu}$. CV is a standardized measure of dispersion of a probability distribution or frequency distribution.
- Geometric CV = $CV_k = e^{\sigma_{ln}} - 1$, where σ is σ_g (Kirkwood, 1979).
- Geometric $CV_t = \sqrt{e^{\sigma_{ln}^2} - 1}$

- Standard error of the mean = $SE_{\bar{x}} = \frac{\sigma}{\sqrt{n}}$, where $\bar{x}$ = mean of the means, σ is the standard deviation of the means, and n = the number of repeat mean estimates (repeat measurement sets).
- ARC = absolute relative change = (x-reference value / reference value)*100

Additional IDW interpolants

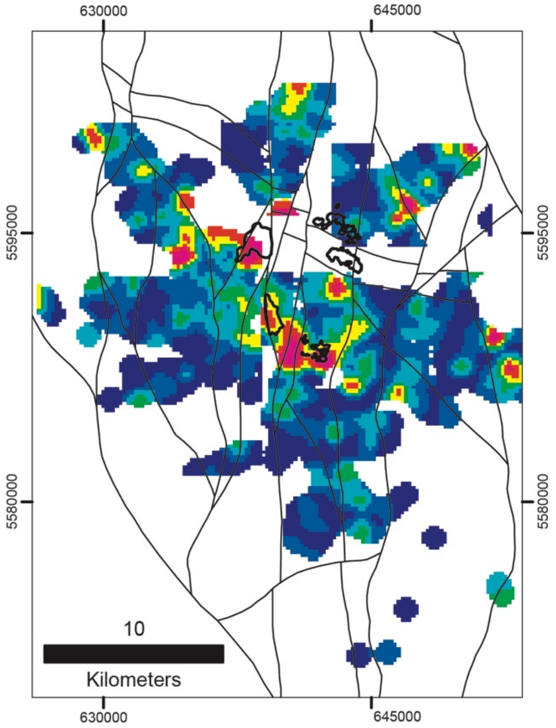

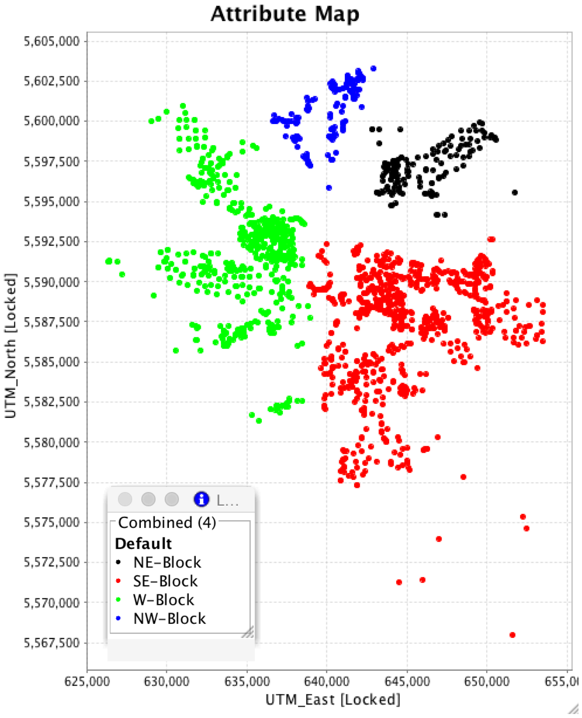

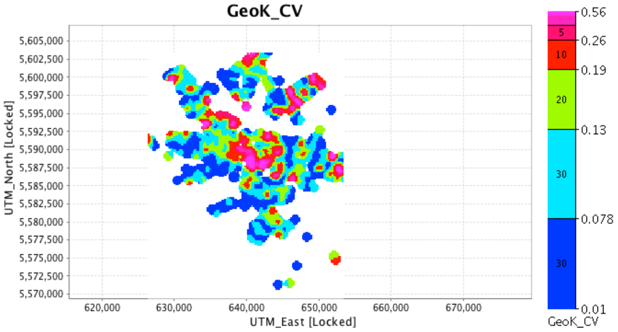

GeoK_CV

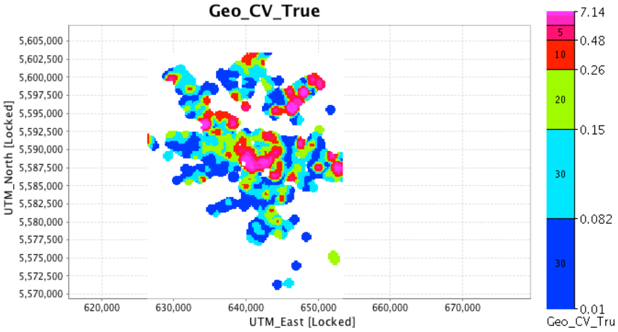

Geo_CV_True

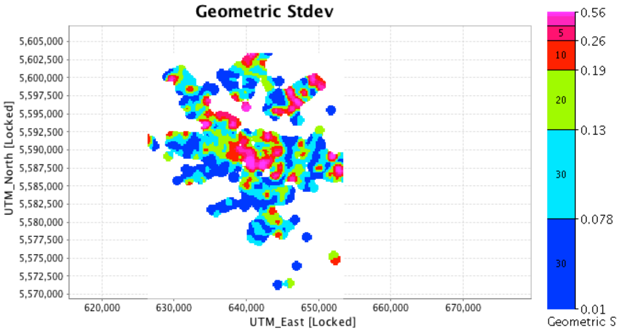

Geometric Stdev

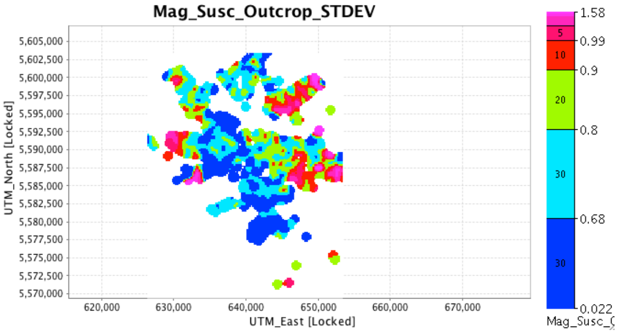

Mag_Susc_Outcrop_STDEV